

Department of Engineering, Cardiff University



Exploiting the properties of graphene to improve the mechanical and functional properties of ceramic-based materials

Joseph Alemzadeh

Submitted for the degree of
Doctor of Philosophy (PhD)

January 2024



Supervisory Team

Prof. Samuel Evans

Dr Victoria Garcia Rocha

Prof. Oliver Williams

Abstract

Since the isolation of graphene in 2004, it has received the attention of numerous research groups across the world. Being the subject of a Nobel Prize in Physics in 2010, its incorporation into high-performance composites has grown increasingly due to its attractive qualities. Ceramic materials have been a promising candidate for graphene integration because of their inherent brittleness and poor resistance to fracture. Taking inspiration from natural materials that exhibit intricate architectures, researchers have managed to exploit possibilities to arrange graphene throughout ceramic microstructures to create highly-ordered ceramic-graphene materials. However, this is not without its challenges during processing which include the dispersion of graphene-related materials and the scalability of production.

This research investigated a novel processing route which utilises advanced fabrication techniques to create bulk ceramic-graphene composites. This began with freeze-casting 30 mm alumina scaffolds that exhibit directionally-aligned pores between 20 – 70 μm in diameter. Prior to infiltration with water-based suspensions of graphene oxide, selected alumina materials were pre-sintered at 900 $^{\circ}\text{C}$ in air to remove casting additives and provide some mechanical strength through particle coalescence. Once infiltrated, alumina-graphene oxide scaffolds undergo Spark Plasma Sintering at 1300 $^{\circ}\text{C}$ to rapidly consolidate the composite scaffolds into dense compacts, whilst simultaneously transforming graphene oxide into reduced graphene oxide. The resulting microstructure consists of highly-oriented reduced graphene oxide throughout alumina layers between 0.5 – 7 μm thickness. The composite material was found to be 80 % tougher, 20 % stronger, and electrically active when compared to monolithic alumina.

Acknowledgements

This fully experimental project was supported by the EPSRC and conducted during the COVID-19 pandemic, requiring strong mental fortitude to overcome adversities faced during this period.

First and foremost, thank you to Dr Victoria Garcia Rocha for providing the opportunity to carry out this EPSRC-funded research over the past four years. Her support and guidance, predominantly from overseas, has been vital. I must also express my gratitude to Prof. Samuel Evans for consistently providing the opportunity to meet on a regular basis and for engaging in several of the practical aspects. Their in-house assistance has been paramount in obtaining new practical skills. Both academics have been an exceptional help throughout the writing process, and I would not have reached submission if it were not for their guidance. Further thanks are given to Prof. Gao Min (Lab Manager) and Prof. Oliver Williams (3rd supervisor) who have been extremely supportive during my experimental work and provided additional perspectives on the academic working environment.

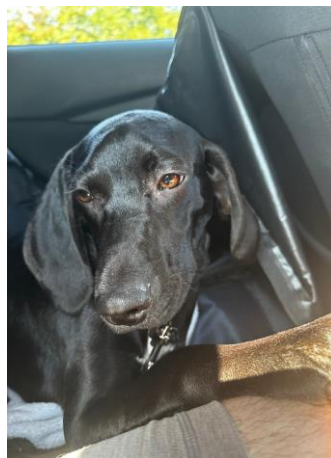
There are some academic staff within the Department of Engineering that I would also like to mention by name; these people have been truly brilliant (besides my supervisory team) and deserve to be mentioned here as it has been a pleasure working alongside them. Dr Julian Steer occupies an office next to my laboratory and has heard all the highs (and the lows) of my work. I am very grateful for the time he has given me during this project. Dr Christopher Harrison has worked in several laboratories that I have conducted research in and has been a fantastic source for multiple conversations. I have thoroughly appreciated their companionship over the course of this research. Prof. Emmanuel Brousseau and Dr Daniel Zabek have been exceptionally helpful during my utilisation of scanning electron microscopy. Without them I would not have been able to train other colleagues and students to use the equipment which

I have wholly enjoyed engaging in. I must also give enormous thanks to technical support staff from the mechanical, civil, and electrical workshops: Stephen Roberts, Malcolm Seaborne, Darren Peterson, Denley Slade, Richard Thomas, Ian King, Carl Wadsworth, Jeffrey Rowlands, Samuel Moeller, and Garry Shipley (to name only a handful). I will fondly remember the conversations that I have had with these people: both academic-related, and those that have been shared over a few drinks. I must also mention my colleagues that have shared the same workspaces as myself. Primarily, huge thanks are given to Dr Guillermo Menendez Rodriguez for showing me the ropes across the departmental facilities; not only have they provided academic support, but his companionship throughout the COVID-19 pandemic was vastly significant. Dr Sukhwinder Singh, Dr Mohammad Alnajideen, Dr Martin Eze, Dr Abdulhamid Mahmud Atia and Abdulaziz Alghlaigah have all played supportive roles within the working environment. I wish them all the best in their future endeavours.

Finally, all of this would not have been possible without the support from my family: my mother Jacqueline, father Kazem, brother Daniel and Louise, his girlfriend. Further thanks go to Mr Emyr Gillett and Mr Maxwell Cutler for being true friends for several years: they have kept my head level for a long time and may that continue for many more years. All these people deserve more recognition than a few lines on a piece of paper. A special mention goes to Pud, Theo, and a pigeon that I have befriended who have acted as emotional support mascots over the course of the writing period.



Pud



Theo



Table of Contents

Aims and Objectives.....	1
Chapter 1 Introduction	2
1.1 Structural ceramics	2
1.1.1 Powder processing of ceramics	4
1.1.2 Sintering techniques.....	5
1.1.3 Mechanical properties.....	9
1.1.3.1 Hardness	9
1.1.3.2 Flexural strength	11
1.1.3.3 Fracture mechanics and fracture toughness	12
1.2 Composites and ceramic-based materials	16
1.3 Natural materials	19
1.3.1 Nacre and structural hierarchy	19
1.3.2 Fabrication techniques towards bio-inspired materials	22
1.4 Graphene-reinforced materials.....	27
1.4.1 Graphene and graphene-related materials	27
1.4.2 Graphene as fillers in ceramic-based materials.....	29
1.4.2.1 Ceramic-graphene materials with random dispersion of filler	31
1.4.2.2 Architectural design within ceramic-graphene materials	37
Chapter 2 Experimental procedure	41
2.1 Overview of processing strategy	41
2.1.1 Preparation of ceramic suspensions.....	44
2.1.2 Freeze-casting/-drying of ceramic materials.....	45
2.1.3 Pre-sintering of ceramic materials	47
2.1.4 Infiltration of porous, ceramic materials with graphene oxide	48
2.1.5 Spark Plasma Sintering of ceramic-based materials	49
2.2 Overview of characterisation techniques	51
2.2.1 Particle size analysis.....	52
2.2.2 Thermogravimetric analysis	52

2.2.3	Viscosity	53
2.2.4	Optical microscopy	53
2.2.5	Scanning electron microscopy	54
2.2.6	Raman spectroscopy	56
2.2.7	X-ray diffraction	58
2.2.8	μ -computed tomography	60
2.3	Testing of material properties	62
2.3.1	Specimen preparation	62
2.3.2	Densities of fabricated materials	64
2.3.2.1	Bulk density	64
2.3.2.2	Density through Archimedes' principle	64
2.3.3	Vickers hardness	65
2.3.4	Fracture toughness	66
2.3.5	Flexural strength	68
2.3.6	Electrical conductivity	70
2.3.7	Thermal conductivity	71
Chapter 3 Fabrication of large alumina scaffolds with directional porosity and the consolidation of alumina		72
3.1	Optimising internal architecture of large, freeze-cast alumina scaffolds	72
3.1.1	Preparation of alumina suspensions	74
3.1.1.1	Selection and characterisation of raw alumina	74
3.1.1.2	Verification of the dispersion of starting alumina powder	78
3.1.2	Processing ceramic scaffolds through unidirectional freeze-casting	81
3.1.2.1	Appearance and densities of freeze-cast alumina scaffolds	81
3.1.2.2	Effect of pre-sintering alumina scaffolds	83
3.1.3	Understanding internal architecture of large freeze-cast materials	85
3.1.3.1	Architectural features of freeze-cast structures	86
3.1.3.2	Visualisation through μ -computed tomography	89
3.2	Exploring the consolidation of alumina via Spark Plasma Sintering	92
3.2.1	Optimising the consolidation parameters of as-received alumina	92
3.2.1.1	Preliminary sintering conditions	92
3.2.1.2	Influence of sintering temperature	95

3.2.2	Consequences of sintering freeze-cast, alumina scaffolds	100
3.3	Discussion.....	103
3.3.1	On the fabrication of freeze-cast alumina with directionally-aligned architecture	103
3.3.2	Selection of optimal solid loading of freeze-cast alumina for further processing	105
3.3.3	Consolidation of alumina through Spark Plasma Sintering.....	106
3.4	Concluding remarks	108
Chapter 4 Infiltration of alumina scaffolds using graphene oxide suspensions and their consolidation by Spark Plasma Sintering		109
4.1	Optimisation of the concentration of GO suspensions.....	110
4.2	Physicochemical features of graphene oxides	113
4.3	Infiltrating porous ceramic materials with water-based suspensions of graphene oxide	119
4.3.1	Preparation of graphene oxide suspensions	120
4.3.2	Optimisation of the infiltration method for depositing graphene oxides within porous ceramics	122
4.4	Consolidation of alumina-GO pre-forms through Spark Plasma Sintering	127
4.4.1	Sintering and density of alumina-rGO materials.....	127
4.4.2	Microstructural evaluation of alumina-rGO composites.....	132
4.5	Discussion.....	138
4.5.1	Characterisation of GO batches.....	138
4.5.2	Infiltration process and extent of GO deposition.....	139
4.5.3	Evidence for rGO in ceramic-based composites	141
4.6	Concluding remarks	143
Chapter 5 Mechanical and functional properties of alumina-based materials		144
5.1	Mechanical properties	145
5.1.1	Vickers hardness.....	145
5.1.2	Flexural strength.....	149
5.1.3	Indentation fracture toughness.....	151
5.2	Functional behaviour.....	154
5.2.1	Thermal conductivity.....	154

5.2.2	Electrical conductivity	156
5.3	Discussion	159
5.3.1	Mechanical behaviour	159
5.3.2	Electrical and thermal transport	165
5.4	Concluding remarks	169
Chapter 6	Potential applications of alumina-rGO composites	170
6.1	Ring-shaped components	170
6.2	Blade-like tools	172
6.3	Heat-shielding	173
6.4	Electrical signalling	173
6.5	Structural health monitoring in layered components.....	174
Conclusions	176
Future work	178
References	181

List of Figures

Figure 1.1 – Diagram of a general powder processing route to fabricating ceramic components and lists of advanced manufacturing techniques.	4
Figure 1.2 – Illustration of the sintering process at various stages. Adapted from Wheat, Vlasea and Hinebaugh. ²⁵	7
Figure 1.3 – Diagram of a Spark Plasma Sintering chamber.	8
Figure 1.4 – Various indentation geometries used to measure hardness in materials. Brinell and Rockwell indentations are produced with ball or cone shaped indenters respectively, hence their similar deformation patterns.	10
Figure 1.5 – Illustrations of three- and four-point flexure testing. Arrows represent an applied load.	12
Figure 1.6 – The different independent modes of fracture. Adapted from Huda et al. ⁴⁶	13
Figure 1.7 – Diagram illustrating the change in fracture toughness with increasing specimen thickness, giving rise to the plane stress and plane strain conditions. Adapted from Anderson. ⁴³	15
Figure 1.8 – A diagram of intrinsic and extrinsic toughening mechanisms that have been identified during crack propagation in front of the crack tip and in the wake of the crack. Taken from Ritchie. ⁶⁹	18
Figure 1.9 – Diagram of the structural hierarchy found in sheet nacre. It has been demonstrated from this work that there are 5 levels of hierarchy on various length scales. Taken from Bhushan and Sun. ⁷⁷	20
Figure 1.10 – A schematic of how the solidification front forms in unidirectional freezing at the bottom of a freeze-casting mould, generating aligned solvent crystals between the suspended solid particles. Adapted from Su et al. ¹¹⁴	24
Figure 1.11 – SEM images of alumina/PMMA composites which demonstrate its similarities to the natural material nacre. Scale bars – left = 100 μm , right = 3 μm . Taken from Ritchie et al. ⁸⁹	25

Figure 1.12 – Illustration of the graphene motif being utilised as a building block for other carbon-based allotropes. Taken from Geim and Novoselov. ¹²⁰	27
Figure 1.13 – Chemical structures of graphene, GO, and rGO. Taken from Lee and Park et al. ¹³⁴	29
Figure 1.14 – Diagram of design considerations whilst undertaking the fabrication of ceramic-graphene materials.....	30
Figure 1.15 – Analysis of 1466 document results from the phrase “ceramic AND graphene AND composite” using the Scopus search bar (as of 10th Dec 2023). Top) frequency of documents published from 2004 – 2023. Bottom) frequency of documents published from the top ten different countries/territories.....	32
Figure 1.16 – SEM images illustrating the microstructures of alumina-based materials. Left) monolithic alumina. Right) alumina-rGO composite, which illustrates the refinement of alumina grains in the sintered composite sample. Adapted from Fan et al. ¹⁴²	34
Figure 1.17 – SEM images depicting the microstructure of an alumina-graphene composite. Left) the well-dispersed nature of graphene nanosheets within the alumina matrix. Right) the existence of pores at the interfaces between ceramic grains and graphene nanosheets. Adapted from Jiang et al. ¹⁴³	35
Figure 1.18 – Left) microstructure depicted in SiC/graphene composites processed using Spark Plasma Sintering. Right) fracture surface of a composite illustrating the occurrence of crack branching in three dimensions. Adapted from Sedlák et al. ¹⁴⁴ ..	36
Figure 1.19 – Left) microstructure of alumina-FLG composite containing 5 vol.% of filler. Right) HRTEM image depicting the presence of FLG within the ceramic matrix. Adapted from Sun et al. ¹³⁷	37
Figure 1.20 – Fracture surfaces of alumina-rGO composite with 0 – 0.75 wt.% addition of filler. The red circles indicate pores found in the monolithic material. Adapted from Wang and Bi et al. ⁹³	39
Figure 2.1 – Illustration of the processing strategy designed for creating alumina-graphene materials.	41
Figure 2.2 – Chemical structure of the dispersing agent DOLAPIX CE64.	42
Figure 2.3 – Schematic of the ultrasonic apparatus used in dispersing ceramic-based suspensions.....	44

Figure 2.4 – Schematic of the custom freeze-casting set-up.	45
Figure 2.5 – Closed and expanded drawings of the PTFE mould, fabricated by fused deposition modelling, used in the freeze-casting process.	47
Figure 2.6 – Plot of the pre-sintering program for porous, ceramic scaffolds with remaining casting additives.	48
Figure 2.7 – Left) photograph of SPS Type HP D10-SD and chiller unit. Right) graphitic components used to assemble 30 mm die sets.....	50
Figure 2.8 – Illustration of the characterisation techniques utilised at various stages of the processing strategy.	51
Figure 2.9 – Diagram of the possible interactions that can occur after electrons penetrate the surface composition of a sample.	55
Figure 2.10 – Left) illustration of scattering processes. Right) Jablonski energy level diagram for the associated changes in vibrational energy.	57
Figure 2.11 – Typical Raman spectra obtained for graphene-related materials between 0 and 3500 cm^{-1} . Adapted from Álvarez and López-Ramón et al. ¹³¹	58
Figure 2.12 – Illustration of Bragg diffraction. Note that the second X-ray “wave” follows a path that includes an extra distance of $2d\sin\theta$	59
Figure 2.13 – Diagram illustrating the lengths to be measured for evaluating the indentation fracture toughness caused by a Vickers indenter.	67
Figure 2.14 – Illustration of two common types of cracking patterns seen in hard materials after indentation. Taken from Žmak et al. ¹⁹⁰	68
Figure 3.1 – Diagram of the developed processing route towards ceramic-graphene materials. The orientation of mechanical and functional testing on sectioned specimens is also illustrated. The dashed face indicates where Vickers indentations would be created for measuring the hardness and fracture toughness. Red lines indicate the direction in which the electrical/thermal behaviour was measured.	73
Figure 3.2 – Left) SEM image of as-received BA15-W alumina. Scale bar = 50 μm . Inset – higher magnification at the surface of an agglomerate. Scale bar = 1 μm . Right) SEM of individual grains after ultrasonic dispersion. Scale bar = 500 nm....	76
Figure 3.3 – Particle size distribution of as-received BA15-W alumina powder.	76
Figure 3.4 – X-ray diffraction pattern of as-received BA15-W alumina powder with ICDD reference 00-005-0712 for comparison.	77

Figure 3.5 – Particle size distribution of a 30 wt.% BA15-W suspension processed with various periods of direct ultrasonication. The dashed line represents the size distribution of the raw alumina powder without any sonication. 79

Figure 3.6 – Particle size distributions of BA15-W suspensions with various ceramic loadings after processing with direct ultrasonication for 5 minutes. The dashed line represents the size distribution of the raw alumina powder..... 80

Figure 3.7 – Particle size distribution of a 30 wt.% alumina suspension without the addition of dispersant after processing with direct ultrasonication for 5 minutes. The 6 scans are not processed to illustrate changes to the particle sizes over time, beginning with the result in blue. 81

Figure 3.8 – Photographs of alumina scaffolds after freeze-drying. **Left)** comparison of a 25 wt.% alumina scaffold with a 2 pence coin. **Middle)** view of surface that is exposed from mould. **Right)** view of surface that contacts the copper bottom inside the mould..... 82

Figure 3.9 – Photographs illustrating inconsistencies in the geometries of some of the ceramic scaffolds cast from moderate ceramic loadings. 83

Figure 3.10 – Masses of freeze-cast alumina scaffolds before and after pre-sintering at 900 °C for 30 mins in air for a range of ceramic loadings. It should be noted that the result at 27.5 wt.% ceramic loading is indicative of only one specimen..... 84

Figure 3.11 – Calculated densities and porosities of freeze-cast alumina cast alumina for a range of ceramic loadings..... 85

Figure 3.12 – SEM images of freeze-cast architecture produced from a 25 wt.% alumina suspension. **Left)** low magnification image through the CS axis. Scale bar = 500 µm. **Middle)** high magnification image that exhibits the surface roughness of ceramic lamellae. Scale bar = 100 µm. Red, dashed lines represent FD. **Right)** diagram representing the three planes that were defined. 87

Figure 3.13 – SEM image of a freeze-cast scaffold illustrating how the pore size and lamellae thickness was measured. Scale bar = 50 µm. This was conducted for 25, 35, and 40 wt.% alumina scaffolds. 88

Figure 3.14 – Frequency distribution of the lamellae thicknesses within the core region of some porous, alumina scaffolds. 88

Figure 3.15 – a) photograph of a 25 wt. % alumina scaffold. b), c) and d) cross-sectional μ -CT images of the alumina scaffold along various planes. e) and f) μ -CT 3D reconstructions of the alumina scaffold. The dashed white line in a) represents the direction of freezing.	89
Figure 3.16 – Left) 3D reconstruction of the core region of the alumina scaffold. Right) high-resolution, cross-sectional image illustrating the dense, solid region that exists in freeze-cast materials.	90
Figure 3.17 – SEM images of alumina sintered using SPS from as-received powder at 1300 °C, 60 MPa, 100 °Cmin ⁻¹ heating rate, natural cooling, a 1 min dwell. Top) overall fracture surface. Scale bar = 1 mm. Black arrows represent the direction of pressing. Bottom) high magnification image. Scale bar = 10 μ m.	93
Figure 3.18 – Photographs illustrating the comparison between sintered alumina specimens. Left) preliminary sintering conditions. Right) modified conditions using a continuous DC pulse sequence, lower pressure, and lower heating/cooling rates. Scale bar = 10 mm.	94
Figure 3.19 – Plot of calculated porosities for alumina specimens sintered with SPS at different temperatures.	96
Figure 3.20 – Plot of piston speed versus temperature up to the dwell from the SPS programs used for alumina specimens sintered with increasing temperature. The remaining conditions were 50 MPa, 50 Cmin ⁻¹ heating/cooling rates, 5 min dwell...	97
Figure 3.21 – SEM images of alumina specimens sintered from as-received powder at various temperatures. a) 1200 °C. b) 1300 °C. c) 1400 °C. Scale bars = 5 μ m. Insets illustrate the visual appearance of 30 mm specimens. The dashed, red circles highlight some porous regions found in the microstructure.	98
Figure 3.22 – Measured grain sizes from the microstructures of alumina specimens sintered with increasing temperature via SPS.	99
Figure 3.23 – X-ray diffraction pattern of BA15-W alumina sintered at 1300 °C with as-received BA15-W powder for comparison.	100
Figure 3.24 – SEM images of a freeze-cast alumina scaffold cast from a 27.5 wt.% suspension sintered using SPS at 1300 °C, 60 MPa, 100 °Cmin ⁻¹ heating rate, natural cooling, and 1 min dwell. Top) overall fracture surface. Scale bar = 1 mm. Bottom) high magnification image. Scale bar = 5 μ m.	101

Figure 4.1 – SEM images of rGO-reinforced alumina composites sintered at 1300 °C that were fabricated by drop casting and vacuum-assisted infiltration of alumina scaffolds with different water-based GO suspensions. **a)** 22.5Al₂O₃:0.025GO, **b)** 25Al₂O₃:0.1GO, **c)** 25Al₂O₃:0.25GO. Scale bars = 1 mm. The images shown in Fig. 4.1a and 4.1b were taken with secondary electron signals, whilst Fig. 4.1c was captured with in-line, back-scattered electrons. 111

Figure 4.2 – Top) OM image of deposited flakes of GO_{supplier} on Si-SiO₂(300 nm). Scale bar = 20 μm. Inset illustrates GO agglomerates. Scale bar = 20 μm. **Bottom)** frequency distribution for the size of GO_{supplier} flakes. 114

Figure 4.3 – Top) OM images of dispersed flakes of GO_{custom}. Scale bars = 20 μm. **Bottom)** frequency distribution for the size of GO_{custom} flakes. 115

Figure 4.4 – Raman spectra of GO_{supplier}, GO_{custom} and graphite. 116

Figure 4.5 – XRD pattern of GO_{supplier}, GO_{custom} and graphite. 118

Figure 4.6 – Viscosity measurements provided for various suspensions of graphene oxide and water for comparison at a shear rate of 50 s⁻¹. 121

Figure 4.7 – Images of a 40 wt.% alumina scaffold that has been drop-cast with a 0.025 wt.% suspension of GO_{supplier}. **Left)** infiltrated scaffold. **Right)** core section of the specimen that illustrates the deposition of GO_{supplier} through FD axis..... 122

Figure 4.8 – Unsuccessful test of an alumina scaffold infiltrated with a 0.25 wt.% GO_{supplier} suspension using vacuum-assisted infiltration. **Left)** before the infiltration procedure. Scale bar = 10 mm. **Right)** scaffold destroyed after the infiltration process. Larger cracks are highlighted with thin, white arrows. 124

Figure 4.9 – Images of 25 wt.% alumina scaffolds vacuum-infiltrated with a 0.25 wt.% GO_{supplier} suspension. **Left)** a whole scaffold with no physical changes. **Right)** a scaffold with which the dense region of material has been removed. Scale bars = 10 mm. 125

Figure 4.10 – Images of 25 wt.% alumina scaffolds vacuum-infiltrated with a 0.25 wt.% GO_{custom} suspension. **Left)** a whole scaffold. **Right)** a scaffold with the dense region of material has been removed. Scale bars = 10 mm. 126

Figure 4.11 – Photographs of alumina-GO material prior to the SPS consolidation. **Left)** free-standing scaffold after the freezing and drying process that followed

infiltration. Scale bar = 10 mm. **Right)** fitting the composite entity within a 30 mm graphite mould for the SPS procedure. 128

Figure 4.12 – Plot of piston speed versus temperature up to the dwell from the SPS programs used for alumina and 25Al₂O₃:0.25GO specimens sintered with 1300 °C, 50 MPa, 50 °Cmin⁻¹ heating/cooling rates, 5 min dwell..... 129

Figure 4.13 – Plot of TGA curves to determine carbon content within 25Al₂O₃:0.25GO composites. 130

Figure 4.14 – SEM images of the microstructure of alumina-0.8rGO at various length scales **a)** 38x magnification. Scale bar = 1 mm. **b)** 200x magnification. Scale bar = 200 µm. **c)** 5000x magnification. Scale bar = 10 µm..... 132

Figure 4.15 – Measured grain sizes from the microstructures of alumina-based materials sintered at 1300 °C via Spark Plasma Sintering. 133

Figure 4.16 – Raman spectrum of alumina-0.8rGO material sintered at 1300 °C and GO_{supplier} for comparison. 135

Figure 4.17 – X-ray diffraction pattern of alumina-0.8rGO sintered at 1300 °C and BA15-W alumina for comparison. 137

Figure 4.18 – SEM images of two sections of an alumina-0.8rGO composite sintered at 1300 °C, 50 MPa, 50 °Cmin⁻¹ heating/cooling rates, 5 min dwell. **Left)** a typical homogenous region of the composites. **Right)** inhomogeneity of the arranged rGO reinforcement within the core of the specimen. Scale bars = 50 µm..... 141

Figure 5.1 – Illustration of the specimens produced from disc-shaped, sintered materials to produce square- and bar-shaped specimens for mechanical and functional testing..... 144

Figure 5.2 – Optical micrographs of the FD-PD plane of alumina-based materials polished to a 1 µm finish, and Vickers indentations created using a 2 kg load. **a)** monolithic alumina. **b)** alumina-0.8rGO. **c)** monolithic alumina after indentation. **d)** alumina-0.8rGO after indentation. Scale bars = 50 µm. 146

Figure 5.3 – Calculated hardness values at various loads for alumina-based materials sintered at 1300 °C, 50 MPa, 50 °Cmin⁻¹ heating/cooling rates, 5 min dwell. 147

Figure 5.4 – SEM images of alumina-0.8rGO across two different planes to illustrate the homogeneity in rGO reinforcement. **Left)** FD-PD plane. **Right)** PD-CS. Scale bars = 50 µm..... 148

Figure 5.5 – Microhardness values of alumina-0.8rGO (at 0.5 kg load) through two different orientations, representing regions that were indented between or through visible areas of rGO..... 148

Figure 5.6 – SEM images of the <99% T.D fracture surfaces illustrating the differences in their microstructures. **a)** monolithic alumina. **b)** alumina-0.8rGO. **c)** and **d)** step-like morphology of alumina-0.8rGO after failure. Scale bars = 50 μm 150

Figure 5.7 – SEM images of Vickers indentation patterns at a load of 30 kg on alumina and alumina-0.8rGO cross sections. **Left)** monolithic alumina. **Right)** alumina-0.8rGO. Scale bars = 200 μm . The red arrow indicates the FD axis. The dashed white lines illustrate which cracks were taken into consideration to calculate the fracture toughness. 151

Figure 5.8 – Calculated VIF values at various indentation loads using the Palmqvist and Anstis formulae for alumina-based materials sintered at 1300 $^{\circ}\text{C}$, 50 MPa, 50 $^{\circ}\text{Cmin}^{-1}$ heating/cooling rates, 5 min dwell..... 153

Figure 5.9 – Plot of the out-of-plane thermal conductivity at increasing temperatures for alumina-based materials..... 156

Figure 5.10 – Illustration of the orientation that 2-probe resistivity measurements were conducted along. The dashed lines represent the electric field lines that would be generated due to electrical transport. 157

Figure 5.11 – Optical micrographs of material surfaces before and after polishing which illustrate the radial-median cracks produced from Vickers indentations (made at 30 kg). **a)** monolithic alumina before polishing, **b)** alumina-0.8rGO before polishing. **c)** monolithic alumina after polishing. **d)** alumina-0.8rGO after polishing. Scale bars = 200 μm 162

Figure 5.12 – High magnification SEM images of alumina-0.8rGO after Vickers indentation and flexure strength testing. **a)** crack deflection, **b)** crack bridging and rGO debonding, **c)** crack branching and intergranular fracture, **d)** pull-out of matrix and reinforcement. Scale bars = 5 μm . Higher contrast thresholds were set in **c)** and **d)** so that exposed ceramic grains were in view..... 164

List of Tables

Table 2.1 – Table of parameters set for the freeze-casting procedure.....	46
Table 2.2 – Table of grinding and polishing steps taken to prepare ceramic-based materials for various mechanical tests – it should be noted that a different surface was utilised for each successive polishing step.	63
Table 3.1 – List of trace elements and their concentrations found in BA15-W (provided by the manufacturer).	75
Table 3.2 – Table of density measurements for alumina specimens sintered with increasing temperature.....	96
Table 4.1 – Densities of alumina and alumina-rGO materials sintered using SPS at 1300 °C. The theoretical density is provided (in red).	131
Table 5.1 – Flexural strength values for alumina-based materials sintered at 1300 °C, 50 MPa, 50 °Cmin ⁻¹ heating/cooling rates, 5 min dwell.	149
Table 5.2 – Calculated specific heat capacity relationships for alumina-based materials.	155
Table 5.3 – Table of in-plane electrical resistivities and conductivities at ambient conditions for alumina-based materials sintered at 1300 °C, 50 MPa, 50 °Cmin ⁻¹ , 5 min dwell. Literature data for monolithic alumina from Centeno et al. is included for comparison.....	158

List of Acronyms

Abbreviation	Definition
ASTM	American Society for Testing and Materials
BSE	Backscattered Electron
CAD	Computer-aided Design
CMC	Ceramic Matrix Composite
CT	Computed Tomography
CVD	Chemical Vapour Deposition
DC	Direct Current
EDM	Electrical Discharge Machining
EMI	Electromagnetic Interference
ET	Electromagnetic Testing
FDM	Fused Deposition Modelling
FLG	Few-layer Graphene
GO	Graphene Oxide
GRM	Graphene-related Material
HRTEM	High-resolution Transmission Electron Microscopy
ICP-OES	Inductively Coupled Plasma Optical Emission Spectroscopy
IPA	Isopropanol
ISO	International Organisation for Standardisation
LEFM	Linear Elastic Fracture Mechanics
MASC	Magnetically-assisted Slip Casting

MLG	Multi-layer Graphene
MWCNT	Multi-walled Carbon Nanotubes
μ -CT	Micro-computed Tomography
NDE	Non-destructive Evaluation
OM	Optical Microscopy
PECS	Pulsed Electric Current Sintering
PMMA	Polymethyl Methacrylate
PSA	Particle Size Analysis
PTFE	Polytetrafluoroethylene
PVA	Polyvinyl Alcohol
R&D	Research and Development
rGO	Reduced Graphene Oxide
SE	Secondary Electron
SENB	Single-edge Notched Beam
SEVNB	Single-edge V-notched Beam
SLM	Selective Laser Melting
SLS	Selective Laser Sintering
SPS	Spark Plasma Sintering
T.D	Theoretical Density
TEM	Transmission Electron Microscopy
TGA	Thermogravimetric Analysis
VIF	Vickers Indentation Fracture
XPS	X-ray Photoelectron Spectroscopy
XRD	X-ray Diffraction

Aims and Objectives

The aim of this work is to provide insight into developing a water-based processing route towards alumina-graphene materials that possess structurally-ordered components inspired by the natural material, nacre. This novel methodology utilises a combination of freeze-casting and water-based infiltration, followed by Spark Plasma Sintering to create layers of ceramic and graphene-like material. Graphene has received lots of attention as a reinforcing phase (akin to the organic phase in nacre) because of its exceptional mechanical and functional traits, whilst researchers have taken inspiration from natural materials due to their intricate and well-ordered architectures that enhance their performance beyond randomly-ordered materials. The following objectives have been derived to assist in achieving this goal:

- Prepare water-based suspensions of alumina powder with varying solid content to freeze-cast large scaffolds with directional porosity
- After pre-sintering, evaluate scaffolds through microscopy studies and select candidates that possess desirable architectural features that most closely mimic nacre
- Prepare water-based suspensions of a graphene precursor and assess the effectiveness of infiltrating porous alumina to form alumina-graphene materials
- Carry out Spark Plasma Sintering to rapidly consolidate the alumina-graphene composite then assess its physical properties and the obtained microstructure
- Perform mechanical and functional tests on the composite material, with an emphasis on the fracture toughness
- Evaluate the mechanical and functional performance of the composite and relate it to its microstructure and provide comparisons against a monolithic counterpart

Chapter 1 Introduction

1.1 Structural ceramics

Structural ceramics are typically inorganic, non-metallic materials that are primarily implemented in load-bearing applications.¹⁻³ Before modern extraction and processing techniques, objects were constructed from readily available natural sources such as sands, soils, and animal products. Crude clays, cements and glass were generated from the resources. Since the turn of the 20th century, fabrication routes to creating structural materials have rapidly advanced and in turn the performance of materials during service has improved.⁴⁻⁶ This was predominantly due to the limited availability of raw materials in combination with difficulties in attaining high temperatures (>1000 °C) during many periods of ancient history.

Candidates that can fulfil the role of a structural ceramic display high compressive strength, hardness, and melting points. Many are also resistant to chemical attack and can sustain physical degradation due to their excellent abrasive qualities.^{1,2,7} Such examples are zirconia (ZrO_2), alumina (Al_2O_3), silicon carbide (SiC), boron nitride (BN), tungsten carbide (WC), and silicon nitride (Si_3N_4).^{1,3} Some of these materials possess high thermal and electrical conductivities, non-toxicity, and low densities. Others are developed because the raw materials are inexpensive and readily available, e.g., processing of alumina from bauxite ore during the Bayer process.⁸ Due to the abundance of structural ceramics with a combination of enticing properties, a plethora of applications is possible, including automotive parts (brakes, spark plugs), bearings, biomedical implants, blade-like tools (cutting tools, turbine blades), body armour, and nuclear equipment.^{2,3,9-12}

However, the main drawback with implementing structural ceramics is with regards to their brittleness which arises due to poor fracture toughness.^{7,13-15} They exhibit a low resistance to fracture which is detrimental in materials that experience little to no plastic deformation upon reaching their yielding point. As a result, ceramic materials do not exhibit ductile behaviour and can fail in a catastrophic manner. Failure can also arise from stresses related to thermal shock if the material is in service at elevated temperatures.^{16,17} If the fracture characteristics of ceramics can be improved, then this family of materials would be extremely attractive to utilise for applications in which they would normally suffer.

1.1.1 Powder processing of ceramics

Fig. 1.1 illustrates a general and basic processing route to fabricate ceramic components based on powder processing,^{2,18} plus a variety of casting techniques that have been developed over the past few decades. These are split into two categories: conventional manufacturing, and additive manufacturing which focuses on creating materials using a bottom-up approach, i.e., layer-by-layer fabrication.^{19,20} The latter has been loosely classified into three categories. Forming and finishing intricate ceramic components can require numerous steps, requiring both time and cost considerations.²

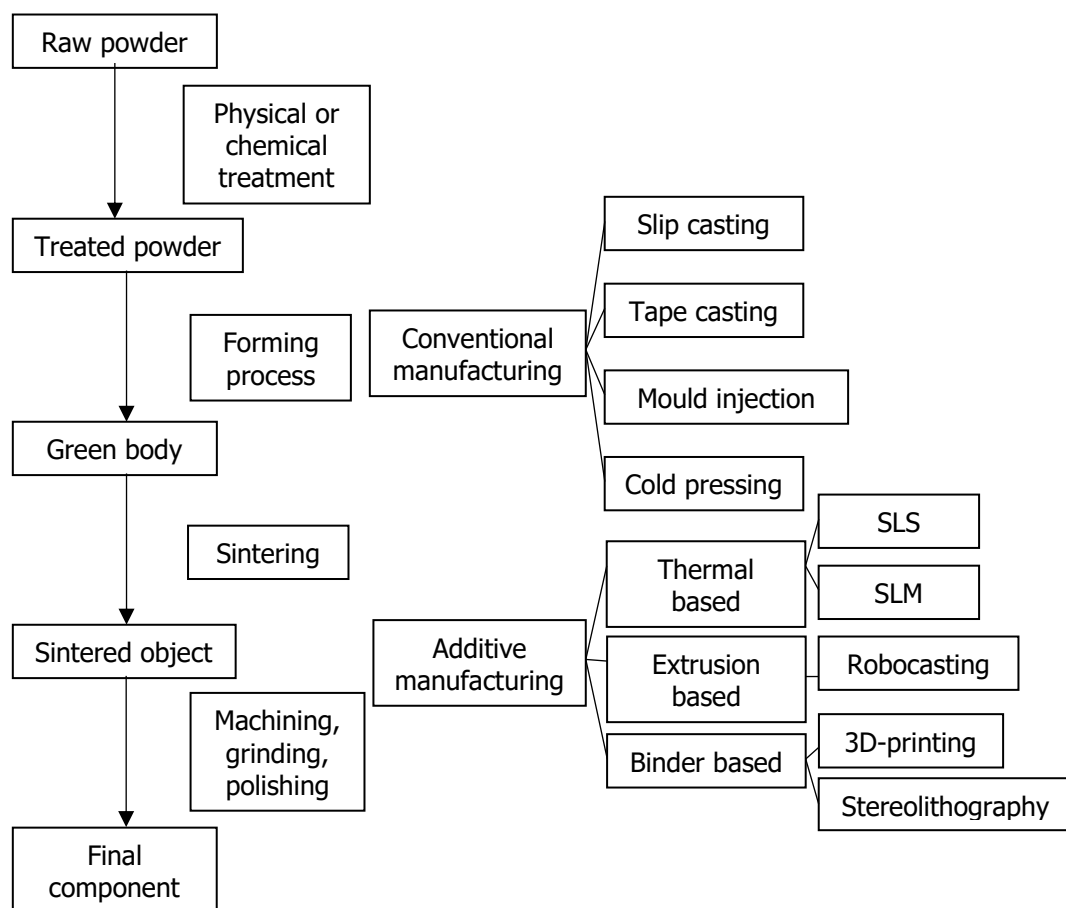


Figure 1.1 – Diagram of a general powder processing route to fabricating ceramic components and lists of advanced manufacturing techniques.

Common industrial routes to producing ceramic components typically start with raw materials in the form of particulates.² Raw material may be treated physically, e.g., through milling, or chemically as an initial step. Solid and liquid additives can improve the following step: forming, which could be as simple as cold pressing powder between a die set. Depending on moisture content, different casting techniques can be utilised to create objects of varying geometric complexity. Cast objects are referred to as “green bodies”. If the green body still retains moisture (or additives) after casting then a drying step would be necessary, where shrinkages in volume may take place. A sintering step causes binding and coalescence of neighbouring particles at elevated temperatures to densify the component, generating the final microstructure that the material will exhibit. However, a major issue with the casting of ceramics can be the introduction of defects in the material such as internal impurities, or external scratching from machining.^{2,18,21}

1.1.2 Sintering techniques

Sintering refers to the consolidation of loose particles into one solid mass through heat-treatment and is a vital step in the fabrication of ceramic components to densify the final object once it has been cast. The thermodynamic driving force of this irreversible process is a decrease in surface energies when particles are fusing together, during which the total surface area decreases whilst total particle size increases.^{22,23} This can be mathematically expressed, shown in Equation 1.1.

$$\delta G = \delta\gamma_E A + \gamma_E \delta A \quad \textbf{Equation 1.1}$$

Where G is the associated Gibbs free energy of the system, γ_E is the interfacial surface energy, and A is the interfacial surface area between particles. What this illustrates is that sintering behaviour is influenced by the starting particle size and their morphology (spheres, platelets etc.), plus the dwelling temperature.²³ Changes in the surface

energy ($\delta\gamma_E$) relate to the densification of the solid whilst changes in the interfacial area (δA) relate to grain growth mechanisms.^{22,24} There are 3 primary stages to the process of sintering. Initially, particles form necks between one another which simultaneously reduces the number of grain boundaries present. During the intermediate stages, there is a large extent of volumetric diffusion towards the necks of particles – this causes pores to take on a more tubular appearance, however the majority are still connected to the external environment (open porosity).²⁵ Additional sintering mechanisms such as grain boundary diffusion and migration are also present throughout this period. This intermediate stage is where most of the densification occurs for powder systems.^{23,25,26} The final stage of sintering is where grain growth predominates, reducing the extent of the now closed porosity as pores no longer reach the material's surface.²³ Although, once pores are closed there is typically some microscopic voids that remain: these "microvoids" can drastically alter to the final behaviour of a ceramic component.^{2,12} Therefore, it is imperative to control the sintering parameters to obtain dense ceramics, especially for structural applications. Fig. 1.2 provides an illustrative summary of the main sintering steps.

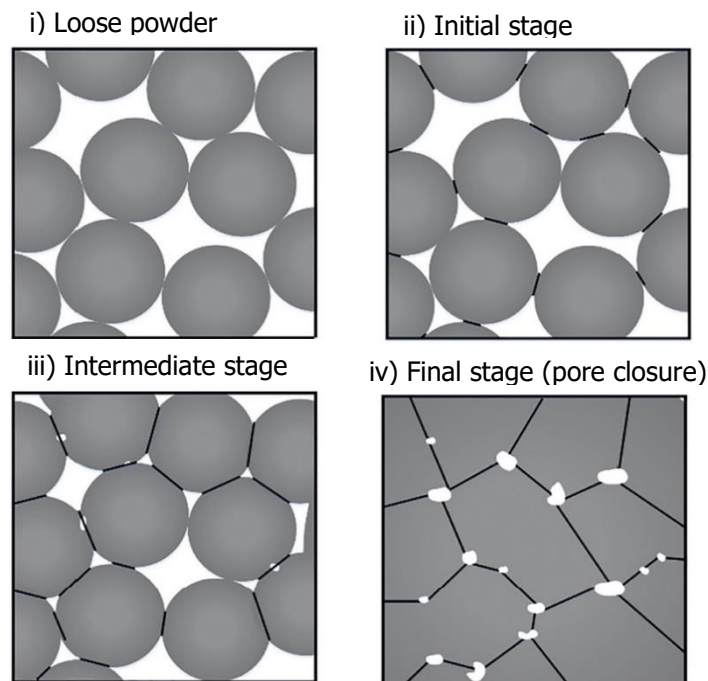


Figure 1.2 – Illustration of the sintering process at various stages. Adapted from Wheat, Vlasea and Hinebaugh.²⁵

A reduction in the overall porosity and an enhancement in properties such as mechanical strength or electrical/thermal conductivity are typical outcomes of the procedure. Optimisation of the sintering conditions enables for tailoring the final phase of a particular material, its porosity, or suppression of grain growth.^{27–30} The input of energy during sintering comes from an elevated temperature, however pressure or an imposed electric field can also exact additional forces on the material. Therefore, sintering that utilises only temperature to consolidate materials can be referred to as conventional sintering. Advanced sintering techniques such as SPS and PECS utilises an electric current whilst simultaneously applying uniaxial pressure to the green body.^{31,32}

Field-assisted sintering is considered advantageous over conventional sintering due to improved densification at lower temperatures and faster acquisition times (minutes

rather than hours). SPS (Fig. 1.3) has been utilised extensively within Materials Science as a tool for consolidating engineering materials such as metals and their alloys, polymers, and semiconductors.^{32–34} This method has also been of great interest for fabricating structural ceramics with improved densities and therefore mechanical behaviour. Fully densified alumina with a grain size between 300 – 500 nm has been sintered at 1150 °C through SPS with dwell times between 10 – 15 minutes, but included dopant amounts of magnesium oxide to suppress the grain growth.³⁵ Pure tungsten carbide and aluminium nitride can be densified using field-assisted techniques without the use of additives.³²

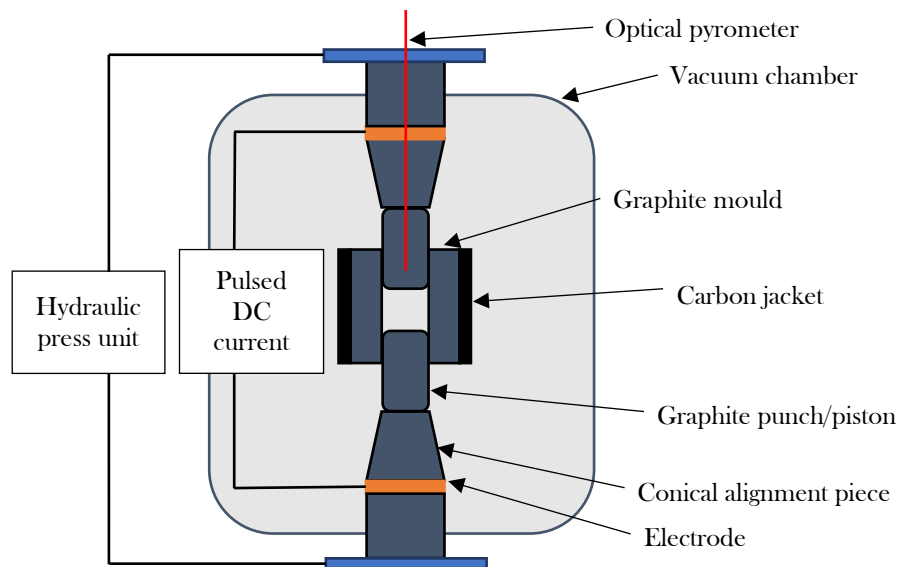


Figure 1.3 – Diagram of a Spark Plasma Sintering chamber.

These enhancements can be related to the atomistic mechanisms occurring at different stages during sintering: firstly, the use of uniaxial pressure creates additional contact points between neighbouring particles and influences the morphology of the contacting regions; a second factor is that additional diffusion mechanisms such as grain boundary sliding and plastic deformation arise from the additional pressure.³⁶ Grain boundary migration and diffusion also occur more readily in the intermediate and final stages of sintering, greatly reducing pore sizes trapped between the solid

grains – this is vital in processing ceramics in which their microstructures contain flaws of minimal size.

1.1.3 Mechanical properties

Attractive mechanical traits that structural ceramics can exhibit have already been stated: namely, high hardness and compressive strengths. Although, it has been mentioned that their limitations predominantly stem from a poor fracture toughness and ability to resist crack propagation. The following sub-sections provide some background regarding hardness, flexure strength, and fracture toughness. This includes definitions, methods of testing, and some of the working principles on which they are based on.

1.1.3.1 Hardness

Hardness can be defined as a material's ability to resist localised deformation whilst a load is applied.^{15,37} The underlying theory is based on solid mechanics: more precisely, the mechanistic movement of individual atoms within a crystal lattice as the bonds between break and re-form. Crystalline structures also contain imperfections including point defects (vacancy and interstitial sites), line defects such as dislocations, and interfacial defects for which an example may be grain boundaries.¹⁵ Dislocations arise from the misalignment of crystallographic planes of atoms, and if disrupted by a concentration of stress slipping (and therefore deformation) within crystallographic planes can be induced. Although, in structural ceramics, their ionic bonds are extremely rigid and like-charged ions would repel each other if close together.³⁷ Therefore, slipping of neighbouring crystal planes is inhibited in ceramics and ultimately leads to separation of material with limited or no plastic deformation.

Hardness testing may aim to characterise the bulk hardness of a material, or the hardness in localised regions of a material's microstructure, termed the microhardness.¹⁵ This type of testing, that utilises far lower loads than bulk hardness measurements, and is also useful for testing thin samples and coatings.³⁸ This could be to probe orientation effects of singular grains or diffusion gradients which may alter the hardness values obtained from a polycrystalline material.³⁸ Therefore, hardness is measured with different methods that depend on the geometry, thickness, i.e., a thin surface coating, or a thicker material, and composition of the specimen that will be tested. Indentation or scratch hardness are the two most common types of hardness measurement – the former measures a resistance based on a constant compressive force, whilst the latter technique provides an indication on the deformation resistance due to friction with a sharp object.^{15,39} Early tests were established on the grounds that one material could scratch another, and later during the early 1800s an arbitrary scale was formed by Friedrich Mohs to index the hardness of materials: the Mohs scale.⁴⁰ For reference, 1 was assigned to talc on the soft end of the scale, whilst 10 refers to diamond. Quantitative measurements that revolve around indentation hardness include the use of diamond-based indenters with different geometries such as Vickers, Knoop, Rockwell, and Brinell.¹⁵ Geometries of these indentations are shown in Fig. 1.4.

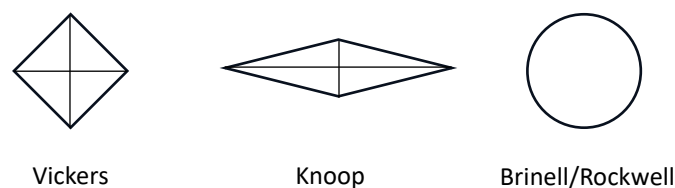


Figure 1.4 – Various indentation geometries used to measure hardness in materials. Brinell and Rockwell indentations are produced with ball or cone shaped indenters respectively, hence their similar deformation patterns.

All have their advantages and disadvantages when applied to different materials. For hard materials like ceramics, Brinell measurements are avoided as they form spherical deformation patterns which can induce severe cracking within the specimen and lower the measured value of hardness.¹⁵ Generally, Vickers and Knoop indenters are applied to measure the microhardness of brittle materials due to their simplistic geometry and limited edge cracking. Many testing procedures have been standardised in ASTM and ISO based on measuring a variety of materials that include soft materials like some metals and polymeric materials, and harder materials that include structural ceramics.

1.1.3.2 Flexural strength

Flexural strength (also called bending strength, or modulus of rupture) is defined as the stress in a material as it reaches failure.^{15,41} The most common method to evaluate this material property is the three-point flexure test, in which a bar-shaped specimen is held in a fixture that possess one support above and two below the specimen. A load is applied on the top contacting support which places a compressive stress on the top face of the material, whilst simultaneously creating a tensile force on the bottom.¹⁵ A four-point fixture, which possesses two supports on the load-bearing face, may be preferred whilst testing brittle materials due to the uniform interaction of stress concentrations with internal flaws across a larger volume.^{41,42} These flaws are primarily microvoids that remain after the sintering process, discussed in Section 1.1.2. The difference in supporting positions for these two testing fixtures is illustrated in Fig. 1.5. Failure occurs once the formed tensile stress overcomes the bending strength of the specimen. In materials such as metals failure would be accompanied by yielding and plastic deformation to accommodate the applied forces.¹⁵ However, in brittle materials like ceramics this failure is sudden, and sometimes catastrophic in larger specimens, because they exhibit little to no plastic deformation once fracture initiates.



Figure 1.5 – Illustrations of three- and four-point flexure testing. Arrows represent an applied load.

1.1.3.3 Fracture mechanics and fracture toughness

The study of fracture mechanics is related to understanding the propagation (and initiation) of cracks throughout materials. It has been mentioned that defects such as small flaws, or microvoids, may be imposed on the material which may greatly lower performance of the final product. Growth of these flaws during service may cause unexpected and catastrophic failure, so it is imperative to analyse flaws that may be liable as crack initiation sites.¹⁷ This is primarily conducted utilising solid mechanics to calculate the driving force of a propagating crack at its tip, and experimental testing data to determine the material's resistance to fracture. Ultimately, the field of fracture mechanics aims to characterise an imposed load on a crack; the goal being to utilise one parameter to fully describe the loading state.⁴³

For a crack to propagate, energy is typically provided to the material in the form of an imposed strain such as shearing. Irwin discovered that any loading state was formed from a combination of three, independent stress intensity factors.⁴⁴ Fig. 1.6 depicts that a crack can propagate as a result of this strain in one of three ways: i) through tension (crack-opening), ii) through shearing (in-plane sliding), or iii) through torsional strain (out-of-plane sliding).⁴³ During this time, Irwin also realised that some materials exhibit a resistance to crack extension during propagation. Such 'R-curves' are plots of fracture toughness parameters as a function of the size of the propagating crack.⁴⁵

The failure of brittle materials such as ceramics is predominantly characterised with the Mode I stress intensity factor, denoted by the symbol K_{IC} .

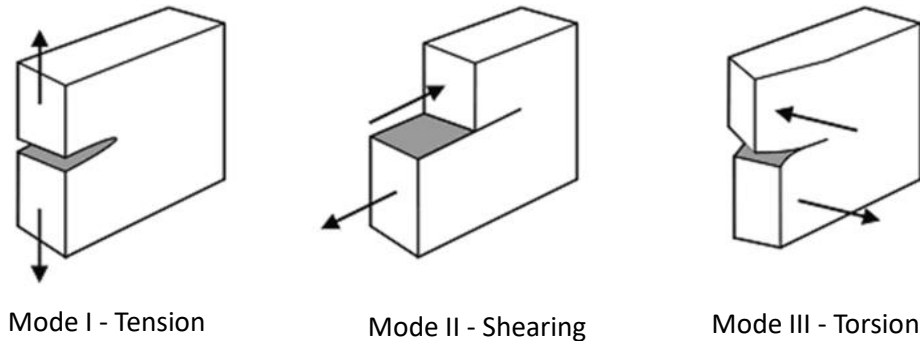


Figure 1.6 – The different independent modes of fracture. Adapted from Huda et al.⁴⁶

Griffith pioneered the field of fracture mechanics in the early 1920s, leading to the discovery of LEFM.⁴⁷ They demonstrated the relationship shown in Equation 1.2, where the product of the square root of the flaw size, \sqrt{a} , and the stress at fracture, σ_f , was almost constant. However, this relationship becomes problematic (with respect to linear elasticity theory) as the predicted stress (and hence strain) ahead of a crack tip could be infinite.^{48,49} Later, Irwin adopted a thermodynamic approach which utilised two energy terms: i) the elastic strain energy released when a crack grows, and ii) dissipating energy that includes some plastic dissipation and the surface energy.⁵⁰ Irwin's adaption was an improvement to Griffith's formula as calculations for both brittle and ductile materials were in good agreement with experimental data. Equation 1.3 illustrates Irwin's adaptation, where E represents the Young's modulus, γ is the surface energy, and G_p is the energy release related to plastic dissipation (and other dissipation sources) per unit area of crack growth, otherwise known as the strain energy release rate.

$$\sigma_f \sqrt{a} \approx C \quad \text{Equation 1.2}$$

$$\sigma_f \sqrt{a} = \sqrt{\frac{E(2\gamma + G_p)}{\pi}}$$

Equation 1.3

In 1957, Irwin soon realised a method for calculating the amount of energy available around the front of a crack with respect to asymptotic stresses and LEFM.⁴⁴ The “stress intensity factor”, K , could be related to Griffith’s energy terms with consideration of specimen geometry: furthermore, the thickness of test specimens plays an important role in the conditions at the tip of a crack. This gives rise to two sets of conditions (displayed in Equations 1.4 and 1.5) known as plane stress and plane strain that occur in thin and thicker components respectively, where Y is a correction factor (based on the specimen geometry), G_C is the critical energy release rate, and ν is Poisson’s ratio. Plane strain conditions are intrinsic to the material itself, providing a lower result than those of plane stress (illustrated in Fig. 1.7).⁴³ Fracture will occur under both conditions when K is higher K_C .

$$K = Y\sigma\sqrt{\pi a}$$

Equation 1.4

$$K_C = \begin{cases} \sqrt{EG_C} & \text{plane stress} \\ \frac{\sqrt{EG_C}}{1-\nu^2} & \text{plane strain} \end{cases}$$

Equation 1.5

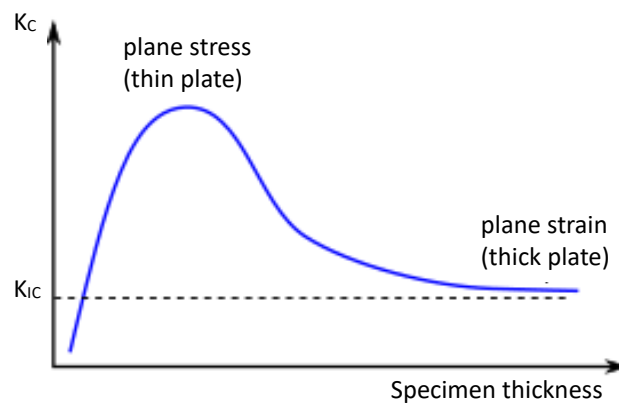


Figure 1.7 – Diagram illustrating the change in fracture toughness with increasing specimen thickness, giving rise to the plane stress and plane strain conditions. Adapted from Anderson.⁴³

Standard methods to evaluate the fracture toughness of ceramic materials include bar-shaped specimens that may undergo 3-point flexure, or the Charpy and Izod impact methods.^{15,51} The latter techniques can be used to determine the energy required on impact to onset fracture. Specimens of suitable thickness (and geometry) must be notched with sharp, reproducible cracks prior to applying a load. The goal is to induce reliable crack initiation sites that follows plane strain conditions in Mode I loading which leads to the evaluation of K_{IC} plane strain fracture toughness. Testing through three-point flexure require larger specimens than those used in compact tension, and the choice of test may depend on geometric constraints that arise from how materials are processed. There are other methods that are less plausible but are still widely used, involving indentation via diamond-based tools, e.g., VIF, at high loads to initiate crack propagation at the apices of indents.⁵²⁻⁵⁴ Indentation fracture toughness is utilised as it is easy to perform and requires far less volume of material. On one hand, some authors suggest that the evaluation of fracture toughness through indentation should be considered as an estimate as they do not produce consistent results.^{54,55} On the other hand the Palmqvist method was standardised by ISO in 2009, validated by work that involved evaluating the toughness of cemented carbides.^{56,57}

1.2 Composites and ceramic-based materials

A basic approach to improving a brittle material's resistance to fracture would be to integrate a secondary material into the host material. So-called ceramic-based composites can display enhanced toughness over monolithic analogues, provided the components positively interact with one another. A composite can be defined as a material that is comprised of two or more different constituents, with clear and definable interfaces throughout the material's microstructure.⁵⁸ Host materials are commonly referred to as the 'matrix' of the composite, whilst secondary materials are described as a 'filler', or reinforcement. A common example is concrete: a mixture of stone particulates encased in cement.⁵⁹ This composite is widely used as a structural material but does exhibit poor tensile performance in comparison to its compressive resistance (which is ten times higher), like ceramics. This brittleness is alleviated with the introduction of another component such as reinforcing bars referred to as "rebar" that can resist high tensile forces.⁵⁹ Rebar can be composed of several types of material dependent on the environment the reinforced concrete will be subjected to, and any cost considerations.

Predictions can be made on the behaviour of a composite material once a filler has been incorporated. The rule of mixtures illustrates that for a composite made from two materials some properties (e.g. Young's modulus, thermal conductivity, density) can be estimated during the preliminary stages of designing new materials.^{15,60,61} The property of a composite, X_c , can be related to the properties of the constituents, X_1 and X_2 , and the volume fractions of the host material and the filler, V_1 and V_2 (expressed as $1 - V_1$) respectively. This is illustrated in Equation 1.6.

$$X_c = V_1X_1 + (1 - V_1)X_2 \quad \textbf{Equation 1.6}$$

However, there are some drawbacks to this rule. Frequently, is derived using a model of a composite material which contains alternating stacks of each constituent throughout its thickness.^{61,62} Additionally, when deriving mechanical properties such as the elastic modulus it is common to derive the equation with a uniform application of stress across the volume of the composite.⁶¹ Predictions using this rule should be taken as an upper limit because most composite materials will contain small, defective regions that will reduce its maximum performance. Nowadays, more complex and intricate architectures for integrating secondary materials within ceramics are being explored and developed. Designing novel microstructures must require thoughtful consideration of the incorporating the reinforcement to maximise performance, which include: i) interactions with the host material, ii) homogeneity in dispersing the reinforcement, and iii) orientation of the secondary material throughout the matrix.^{63,64} Overlooking these factors can be detrimental to the in-service behaviour of composites and reduce their attractiveness towards application.

In the case of ceramic-based materials, reinforcement that demonstrates some plastic behaviour would be suitable for improving fracture characteristics and toughness. CMCs were successfully realised during the mid-1900s to overcome this issue whilst also providing an enhancement to thermal shock resistance in some materials.^{65,66} Yttria-stabilised zirconia was largely studied as it was found that doping zirconia with varying quantities of yttria induces geometrical changes in the crystalline structure.^{67,68} The material was found to generate an extrinsic toughening mechanism referred to as transformation toughening. Intrinsic toughening mechanisms are inherent to a material and occur in front of the propagating crack (Fig. 1.8). One example is the formation of plastic zones ahead of the crack tip if the material exhibits plasticity.⁶⁹ Another example is the refinement of grain size within a polycrystalline material, which subjects a crack to interact with more grain boundaries thereby increasing the energy necessary for fracture to occur. Extrinsic toughening mechanisms such as crack bridging and crack deflection are only onset if crack propagation has already begun.

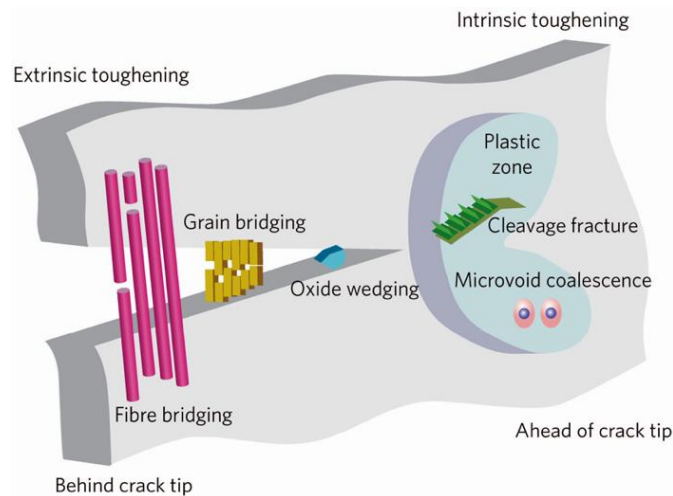


Figure 1.8 – A diagram of intrinsic and extrinsic toughening mechanisms that have been identified during crack propagation in front of the crack tip and in the wake of the crack. Taken from Ritchie.⁶⁹

Another design strategy to improve a ceramic's mechanical properties is to embed small particles or 2D-reinforcements within the ceramic matrix; this fabrication of concrete that was mentioned previously is one such process. Fibres and whiskers can provide a continuous reinforcement along large length scales which aids in: a) increasing the energy required to initiate crack propagation, and b) bridging cracks if propagation is progressing through the cross-section of a material.⁶⁹ One example of fibre-reinforced CMCs are SiC/SiC-whisker composites that are extensively used in aerospace applications due to their high temperature mechanical capabilities, oxidation resistance, and low density.^{66,70–72} Aside from ceramic reinforcement, both metals and polymers, and carbon-based materials have all been utilised as 1D/2D-fillers to provide different enhancements to the structural behaviour of ceramic-based materials in a wide variety of applications.^{73–76}

1.3 Natural materials

Throughout evolution, biological organisms have fabricated composite materials with a limited selection of elements which they gather from their surroundings. These naturally occurring composites are mainly identified as structural implements to provide strength and support to softer, internal tissues.^{77–80} In some cases, however, these materials will also possess other functional behaviour that is of importance to sustaining the organism's life. Wood is one example: a composite which is predominantly made from cellulose (an organic biopolymer) provides vital structural integrity to flora, but it is also responsible for the fluid transport from the roots of the organism to its leaves.⁸¹ This additional trait that wood exhibits arise due to an intricate architecture on various length scales and how each of the individual components are arranged.^{79,81} For researchers who design and fabricate engineering components, these natural materials provide a valuable insight into exploring and creating the next generation of high-performance composites. They will not only be made from constituents that individually display attractive characteristics and properties, but also exhibit an ordered microstructure that can be generated through some form of assembly process during its fabrication.

1.3.1 Nacre and structural hierarchy

Most fauna also produce complex, composite architectures: including bone, teeth, and shells.^{80,82} Nacre is a thin, iridescent layer that is found in species of mollusc shells.^{77,82–84} It is a natural composite that is primarily comprised of aragonite, a polymorph of calcium carbonate, but also contains a small percentage (~5 wt.%) of a chitin-based biopolymer. The components themselves are mechanically weak materials that are comprised of relatively low, molecular weight elements. However, nacre outperforms both constituents and displays exceptionally high mechanical properties which are greater than what the rule of mixture may predict for synthetic

composites.⁶⁰ This work was pioneered by Currey in the 1970s, who was also investigating the mechanical performance of biological systems which included hair and skin.^{83,85} Most notably, the fracture toughness greatly differs when monolithic aragonite ($K_{IC} = 1 \text{ MPam}^{1/2}$) is compared to nacre with varying hydration levels ($K_{IC} = 3.3 - 9 \text{ MPam}^{1/2}$).⁷⁷ Fig. 1.9 depicts the structural hierarchy of nacre on various length scales.

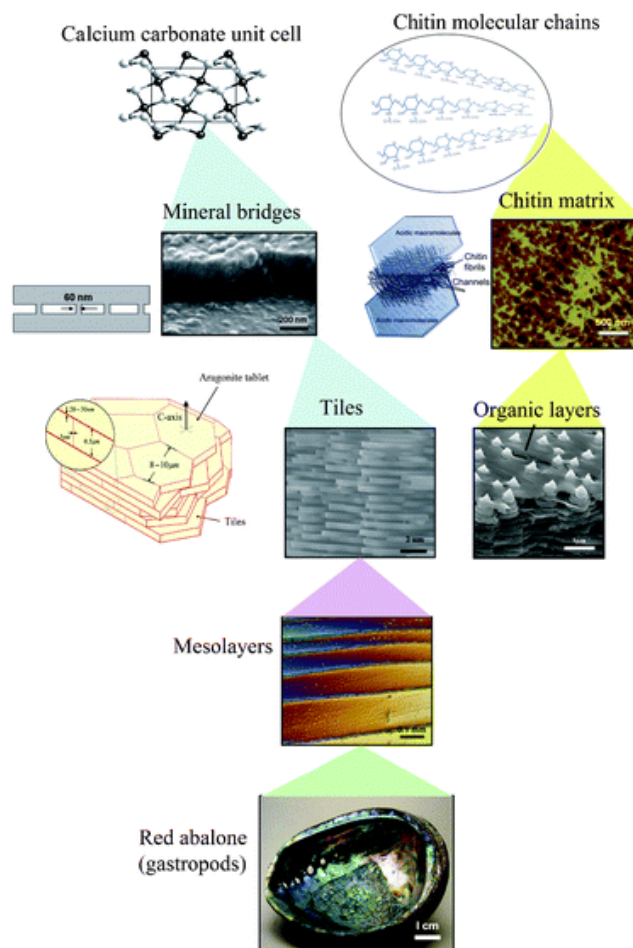


Figure 1.9 – Diagram of the structural hierarchy found in sheet nacre. It has been demonstrated from this work that there are 5 levels of hierarchy on various length scales. Taken from Bhushan and Sun.⁷⁷

Aragonite nanograins (3 – 10 nm) are surrounded by a thin layer organic polymer on the nanoscale, which are assembled into tablets (0.2 – 1 μm thickness, 2 – 10 μm width). These tablets are also separated by mineral bridges (50 nm in width) that are sandwiched within the polymeric material.^{77,86} There are two mineralisation types of nacre: columnar, and sheet. When stacked, the 3D architecture in sheet nacre can be considered as a “brick-and-mortar structure” which is created by virtue of the organism’s biomineralisation pathway. The mineral bridges act as nucleation points of tablet growth and depending on the species of mollusc is where two crystal formations arise.^{77,84} Generally, columnar nacre consists of tessellated columns of aragonite plates, whilst in sheet nacre (illustrated in the previous figure for a species of gastropod) aragonite tablets and their boundaries between neighbouring plates are randomly distributed which generates the brick-and-mortar appearance.⁷⁷

One may have realised that the exceptional traits that nacre displays is due to the well-ordered microstructure and small quantities of biological polymer to incur numerous extrinsic toughening mechanisms which aragonite does not exhibit. As nacre reaches its yielding point, sliding of stacked platelets occurs which greatly toughens the material through frictional forces that must be overcome.^{86,87} Several nano-asperities decorate the surface of aragonite tablets and significantly increase both the strength and toughness during the slip of tablets.^{77,87} The chitin-based polymer acts also as a ductile phase that is bonded between the nanograins and assembled tablets, enabling more efficient load-transfer between adjacent tablets when faced with compressive stress.⁸² Additionally, the polymeric filler also improves the resistance to crack propagation, dissipating energy released upon crack propagation which reduces the possibility of trans-granular fracture (failure through the aragonite tablets), and increases the likelihood of intergranular fracture along grain boundaries of neighbouring platelets.⁸⁶ Extrinsic toughening mechanisms that exist on the microscale such as crack deflection and pull-out are typically observed in fractographic studies of nacre.^{82,86} Furthermore, nanoscale toughening mechanisms have been classified that includes the rotation and sliding of aragonite nanograins and molecular level toughening due to the unfolding of chitin domains.⁸⁸

A large variety of nacre-like materials have been fabricated and studied to identify the toughening mechanisms which arise from processing complex architectures, and primarily enhance the mechanical performance when compared to monolithic analogues of host materials.^{77,89,90} Furthermore, a combination of high strength and stiffness is not easily achieved in the typical fabrication of synthetic composites. As a damage-tolerant material, nacre is a brilliant material to take inspiration from, and many researchers have already explored a variety of fabrication techniques for the manufacture of advanced, engineering composites with nacre-like architectures.^{89,91-}

94

1.3.2 Fabrication techniques towards bio-inspired materials

Currently there are a few promising routes which have been explored to assemble and arrange components. First, wet processing of raw materials has been a common practice to produce advanced composite materials.⁹⁵ This method for the molecular-level mixing of solid components within a solvent can create homogeneous dispersions of two or more materials (e.g., ceramic and metal particles). The functionalisation of surfaces for improving the mixing and wettability between the constituent materials is something that many researchers take advantage of.⁹⁴ However, one issue is that wet processing can become quite complicated, and many involve several steps which may require an adequate level of lab expertise. In addition, the use of hazardous solvents or precursor materials could be circumvented to encourage more environmentally friendly techniques to be utilised within industrial sectors.⁹⁶

Another route that has attracted attention is additive manufacturing that can be considered as methods assisted by CAD to assemble materials layer-by-layer.^{60,97-99} These are fabrication routes which include 3D-printing/robocasting, stereolithography, and techniques such as CVD and electrophoretic deposition. But there are also multiple drawbacks to these procedures which are difficult to overcome.^{60,97} This includes the cost of sophisticated, expensive machinery and potentially lengthy processing times.

Also, the issue of combining a high printing resolution (for nano-scaled architectural features) and an upscaled manufacturing process is prominent in many of the currently available techniques, e.g., stereolithography. Furthermore, there is also a limited array of materials available that can be processed with these routes.

A promising, yet cost-effective avenue to fabricating bulk materials has been identified with the potential for creating high-performance, nacre-like structures: freeze-casting.^{60,92,100–103} Freeze-casting (illustrated in Fig. 1.10), otherwise known as ice templating, involves the cooling of a solvent to create a solid, but porous, object from a suspension of particles. Casting is typically followed by freeze-drying, in which the frozen solvent is sublimed from solid to gas to expose the porous replica.^{104,105} The size, geometry and orientation of the porous architecture can be tailored by extrinsic parameters such as freezing rates, solvent, particle size, and morphology of the casting material, as well as the casting mould itself.^{106,107} This simple, but effective, technique has been extensively utilised for processing ceramics since Fukasawa *et al.* explored the creation of porous alumina ceramics, once freeze-dried structures have undergone a form of sintering.¹⁰⁸ Since, this has been extended for fabricating many other ceramics,¹⁰³ metals,¹⁰⁹ biopolymers,¹¹⁰ and also hybrid materials.^{111,112} A wide variety of applications have currently been unearthed such as filtration membranes,¹¹³ biomaterials,⁶⁰ and in the development of structural materials.^{89,97}

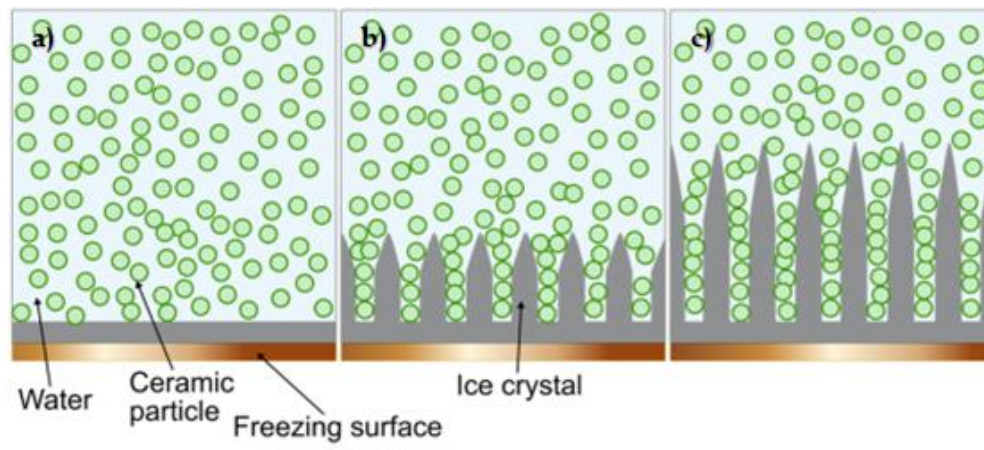


Figure 1.10 – A schematic of how the solidification front forms in unidirectional freezing at the bottom of a freeze-casting mould, generating aligned solvent crystals between the suspended solid particles. Adapted from Su et al.¹¹⁴

The generation of channels is produced by the cooling of solvent, causing nucleation and crystallisation of solvent molecules along the temperature gradient until the entire solvent volume has frozen.¹⁰⁷ From a thermodynamic perspective, the solidification front is governed intrinsically by the interfacial free energies of particle-ice interactions, particle-solvent interactions and ice-solvent interactions (Equation 1.7).¹¹⁵ In short, solid particles will be rejected from the solidification front if the free energy of the system ($\Delta\gamma_0$) is positive, and if ice front velocity is lower than the critical freezing front velocity. The most common solvent that is utilised is water, however organic solvent-based suspensions can also be prepared that will have an impact on the produced microstructure: the decision between using organic or water-based suspensions would ultimately depend on the desired porosity specifications.¹⁰³ Regarding the water-based processing of ceramic materials, long-range lamellae, i.e., thin layers of material, are generated along the solidification front during the growth of ice crystals.¹⁰³ Another factor impacting the architecture which is generated is the use of additional processing reagents including dispersants, cryo-protectors, and binding materials.^{105,116}

$$\Delta\gamma_0 = \gamma_{ps} - (\gamma_{pl} + \gamma_{sl}) > 0$$

Equation 1.7

In 2008, Ritchie *et al.* fabricated alumina-PMMA composites using freeze-casting as the first step in generating lamellar and nacre-like (with a further infiltration step) architectures, except the ceramic 'bricks' were one magnitude thicker ($5\ \mu\text{m}$) than the dimensions of aragonite tablets found in nacre, plus the volume proportion (80%) of the ceramic component is much lower.⁸⁹ Nevertheless, the composite outperformed a ceramic analogue fabricated using the same conditions, reaching a fracture toughness value almost double the monolithic material ($2.8\ \text{MPam}^{1/2}$ to $5.5\ \text{MPam}^{1/2}$) when tested through the SENB method. This was attributed to the extrinsic toughening mechanisms that were onset by virtue of the homogenous distribution of PMMA throughout the fine pores of the ceramic body, which were generated in the casting step. But some flexural strength was lost as a trade-off for incorporating such a large volume of PMMA (300 MPa to 210 MPa). Fig. 1.11 illustrates the brick-and-mortar architecture established in this work.

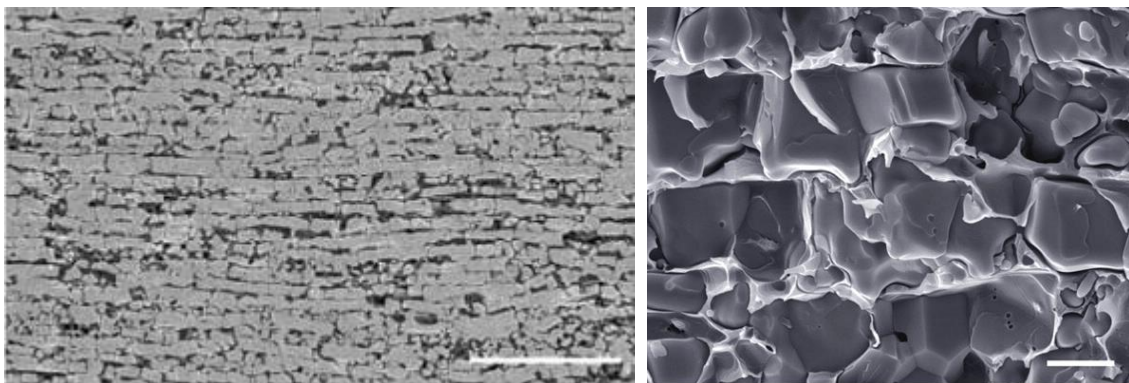


Figure 1.11 – SEM images of alumina/PMMA composites which demonstrate its similarities to the natural material nacre. Scale bars – left = $100\ \mu\text{m}$, right = $3\ \mu\text{m}$. Taken from Ritchie *et al.*⁸⁹

More recently, a novel ceramic-metal composite fabricated by Bouville *et al.* demonstrated the capability of producing a multifunctional, nacre-like material consisting of alumina platelets coated in iron oxide that were assembled using MASC followed by hot pressing as the densification step.⁹⁴ MASC is similar to freeze-casting as porous architecture is generated, but it does not rely on the solidification of solvent crystals – a magnetic field aligns material as it dries inside a porous mould. Thoughtful consideration of reactions between alumina and iron oxide at elevated temperatures lead to the formation of hercynite, an interphase which improved the wetting of the ceramic and metal interfaces. Toughening mechanisms that included crack deflection and pull-out were observed at the alumina surfaces, plus utilisation of iron as the ductile phase (reduced from iron oxide during heat treatment) gave rise to the nacre-like architecture, which similarly exhibited rising R-curve behaviour.⁹⁴ Both the flexure strength and SENB fracture toughness were comparable to some of the highest values reported in the literature for nacre-like materials (up to 400 MPa and 15 MPam^{1/2} respectively, depending on the vol.% of iron that is included).¹¹¹ Additionally, the composite exhibited noticeable magnetisation and improved induction heating, as well as a lower electrical resistance. The latter decreased from >300 M Ω to 119 k Ω to 2 Ω as the vol.% of iron changed from 4 % to 8.9 % to 12.4 %.⁹⁴ The change in functional properties with respect to the fraction of filler relates to percolation threshold theory.^{117,118} This statistical theory describes how a phase transition can occur due to the generation of a connected component. When considering composite materials, this concept is associated with the connectivity of components within the material - for example, in the metal-ceramic composite with 12.4 vol.% iron the electrical resistance greatly decreased due to a more continuous pathway of filler material being created through the microstructure of the composite. It is expected that there was little connectivity between the iron-based components in the 4 vol.% composite which did not alter the ceramic matrix's electrically-insulating nature.

1.4 Graphene-reinforced materials

1.4.1 Graphene and graphene-related materials

Since its isolation in 2004 from the University of Manchester, graphene has rapidly evolved as one of the most attractive components to implement within the development of novel materials.¹¹⁹ It can be considered as an allotrope of carbon as it is comprised of a flat, hexagonal arrangement of carbon atoms along one plane. The graphene motif can be considered as a 2D building block that forms other carbon allotropes with different morphologies (Fig. 1.12). It can be wrapped into fullerenes, rolled into nanotubes, and vertically stacked to form graphite.¹²⁰

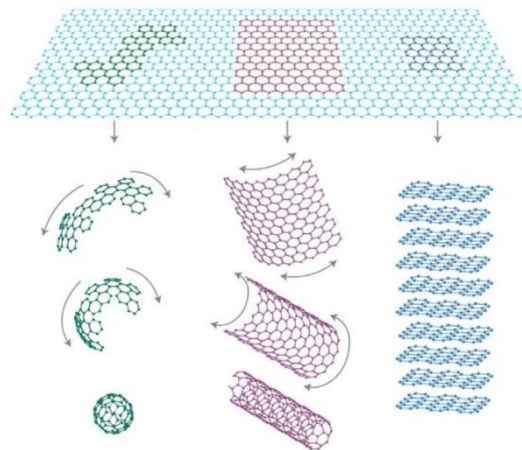


Figure 1.12 – Illustration of the graphene motif being utilised as a building block for other carbon-based allotropes. Taken from Geim and Novoselov.¹²⁰

In this honeycomb-like architecture, each atom is bonded to three nearest neighbours, whilst also contributing one electron into the valence band of the molecule – this valence band contacts the conduction band (which is of higher energy) and exhibits electrical behaviour akin to a semi-metal. Although, its unusually high electronic transport properties are best described by massless, relativistic particles.^{120,121} This

ability of particles (Fermions) to essentially travel unimpeded across relatively long distances also generates high in-plane thermal conductivity (beyond 5000 W(mK)^{-1})¹²² as particles are permitted to travel without any energy-loss interactions. In addition, graphene sheets are near-transparent in contrast to the black colour of graphite.¹²³

There is a mixture of top-down and bottom-up approaches to fabricating graphene and GRMs. A common route has been through exfoliation of bulk graphite, which may be as simple as applying adhesive tape to graphite and peeling away few-layer graphene sheets.¹¹⁹ More sophisticated techniques include the Hummer's method (and modified analogues),¹²⁴⁻¹²⁶ and routes involving chemical vapour deposition onto metallic substrates.¹²⁷⁻¹²⁹ Hummer's method was developed in 1958 and involves using strong acids to oxidise graphite, with later modifications improving the efficiency and quality of resulting material. The oxidised structure is then sonicated to disperse layers of GO, and further chemical or thermal reduction will form rGO.¹³⁰ The reduction stage removes most of the oxygen-containing functional groups and restores the electrical network which was lost upon oxidation. Structural changes are illustrated in Fig 1.13. Graphene itself is a planar molecule containing only sp^2 hybridised C=C bonds, whilst GO and rGO consist of a mixture of sp^2 and sp^3 character which is dependent on its level of oxidation.¹³¹ The materials can easily be distinguished from one another by a variety of characterisation techniques that include Raman spectroscopy, XRD, and XPS.^{132,133}

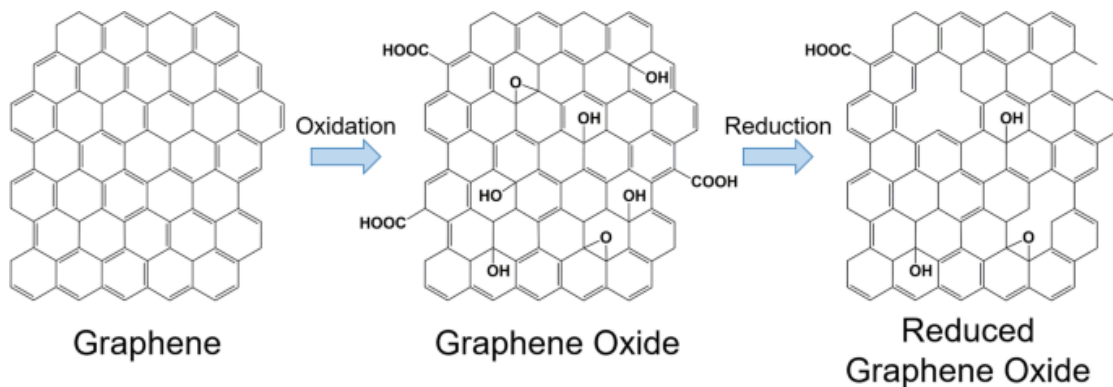


Figure 1.13 – Chemical structures of graphene, GO, and rGO. Taken from Lee and Park et al.¹³⁴

Functionalisation in this manner also provides the additional benefit of hydrophilicity which, compared to the hydrophobic nature of graphene sheets, improves its dispersibility in solvents and ease of processing.¹²⁵ As they are mechanically strong, flexible, and extremely lightweight, graphene-related materials have become increasingly used as a mechanical reinforcement in structural materials over the past two decades.¹³⁵ Furthermore, graphene’s electronic and thermal transport capabilities have improved the multifunctionality of materials as it has been shown to generate traits that include (but are not limited to) damage-sensing abilities,¹³⁶ and providing interference with electromagnetic radiation, i.e. EMI shielding.^{137,138} The unique combination of properties that graphene-reinforced composite materials can demonstrate enables them to be candidates towards several applications including energy production and storage, biomedical implants, and spacecraft technologies.

1.4.2 Graphene as fillers in ceramic-based materials

Over the past few years, there has been lots of engagement in the development of ceramic-graphene composites. The recent review by Ramirez *et al.* in 2021 showcases how this class of materials that has gained lots of traction, particularly since 2017

according to their work.¹³⁹ An earlier review published during 2017 shares the same thoughts and suggests that ceramic-graphene materials have large potential for structural and functional applications.¹⁴⁰ However, one of the main challenges that both reviews clearly describe is the distribution and orientation of graphene within composite materials. It has been mentioned that graphene sheets are hydrophobic and will agglomerate in a facile manner, so its dispersion into the host material must be critically considered. The interactions between graphene and the host are also key: bonds they will form during heat treatment are important in obtaining enhancements, particularly for the mechanical properties of ceramic-based materials.¹³⁹ Fig. 1.14 illustrates several of the design considerations that should be accounted for including the processing and sintering stages.

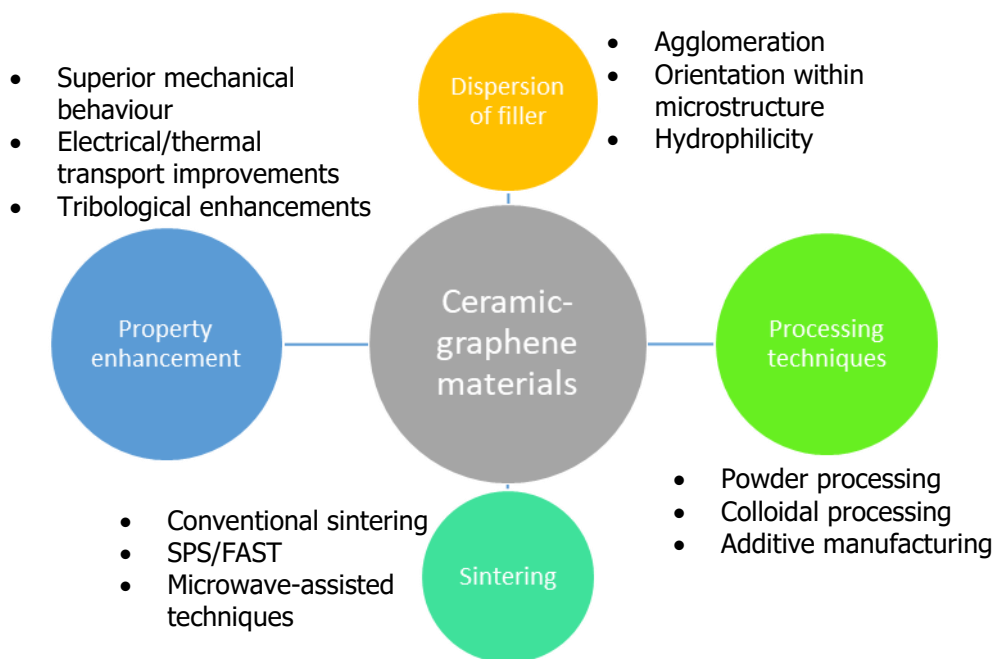


Figure 1.14 – Diagram of design considerations whilst undertaking the fabrication of ceramic-graphene materials.

1.4.2.1 Ceramic-graphene materials with random dispersion of filler

There are multiple research groups across the world who are currently engaged in fabricating ceramic-graphene composites that exhibit varied microstructural features and performance. A simple search in Scopus (shown in Fig. 1.15) using the keywords “ceramic AND graphene AND composite” generates 1466 results (from 2004 onwards), with a steady increase seen since 2009 which was the year that scientists at Manchester University received the Nobel Prize in Physics. Over 50+ documents have been published each year from 2014 and onwards, which figure has risen to over 150+ in the past few years with these studies predominantly being carried out in China, India, the United States, and Spain. However, this is most likely an under-approximation considering the utilisation of graphene-related materials which may not be mentioned, or perhaps are unconventionally named within the title, abstract, or keywords. The decrease in document submission between 2019 – 2023 can be attributed to the COVID-19 pandemic, however it is expected that this number will rapidly increase in the next few years like the trend observed beginning in 2010.

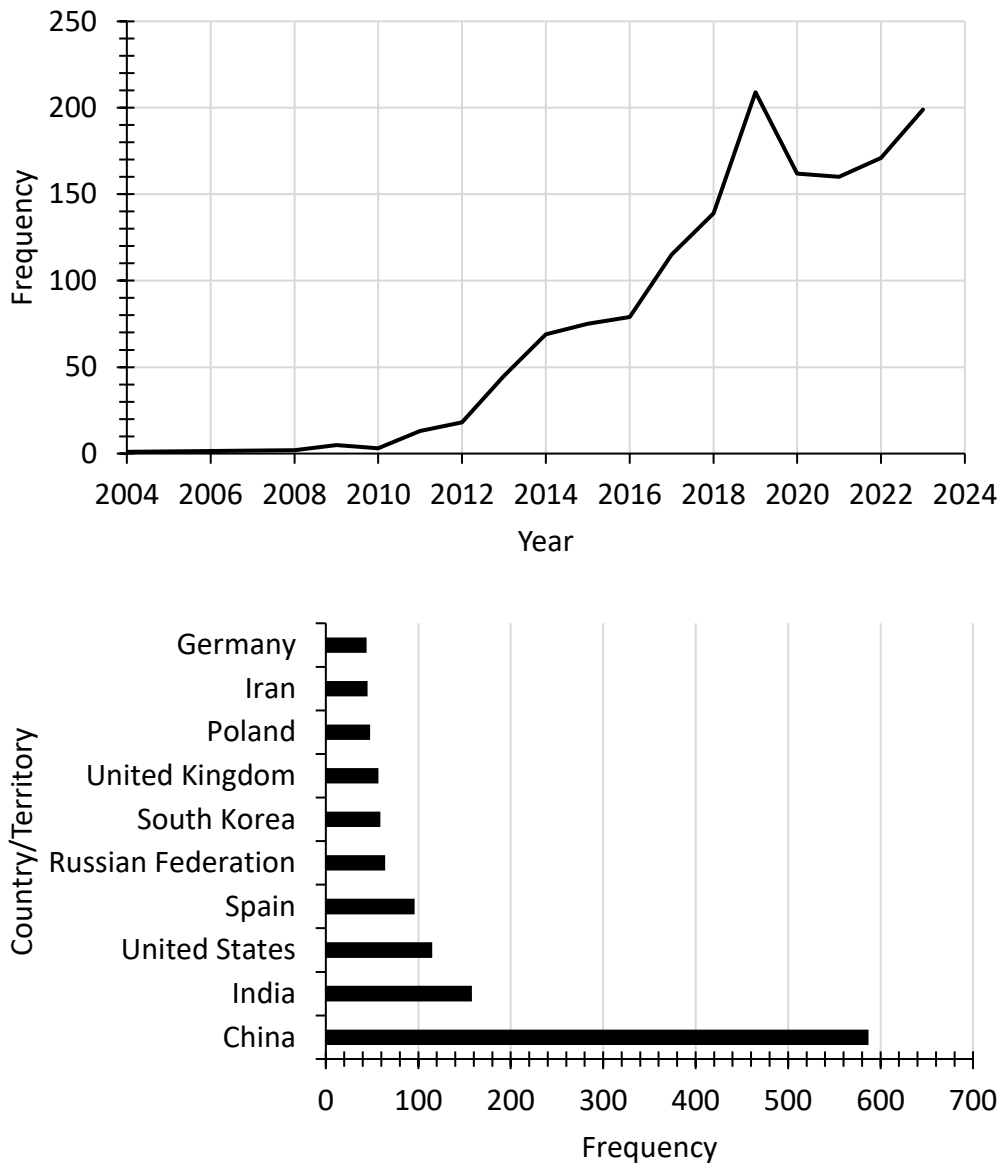


Figure 1.15 – Analysis of 1466 document results from the phrase “ceramic AND graphene AND composite” using the Scopus search bar (as of 10th Dec 2023). **Top)** frequency of documents published from 2004 – 2023. **Bottom)** frequency of documents published from the top ten different countries/territories.

Soon after the isolation of graphene collaborative work conducted in China fabricated composite materials by ball-milling alumina powder and graphite for different lengths, then observing the resultant mixture by TEM.¹⁴¹ The ratio of graphite to alumina was

5:95 by volume. TEM images illustrated that multiple-layer graphene sheets between 3 – 8 nm were exfoliated from the bulk graphite and distributed throughout the submicrometric alumina powder. After consolidation via SPS, the fracture surfaces of the composite materials exhibited a much finer microstructure than that of pure alumina and it was concluded that the addition of graphene sheets was impeding ceramic grain growth during the sintering cycle.¹⁴¹ Unfortunately, no physical or mechanical properties were characterised for the composites within this study.

Later in 2010, another group from China opted to utilise GO rather than graphene to reduce the extent of flake agglomeration in the final composite.¹⁴² Through wet processing techniques, and the use of a chemical reducing agent, they prepared hybrid alumina-rGO powders with 2 wt.% filler that were sintered with SPS at 1300 °C. They reached the same conclusion as the previously mentioned study which was noticeable grain growth suppression after addition of the reinforcement. This is shown in Fig. 1.16 and was attributed to the diffusion of alumina grains being hindered by well-dispersed nanosheets of graphene.¹⁴² Fracture toughness measurements were performed via the SENB method and showed an improvement of over 50 % (3.40 MPam^{1/2} to 5.21 MPam^{1/2}), onset by extrinsic toughening mechanisms that include pull-out and crack bridging. But in their conclusions, it was believed that optimisation of the composite's microstructure would yield a greater enhancement.¹⁴² This may come in an improvement in final density, as composite materials exhibited a relative density of only 96 %.

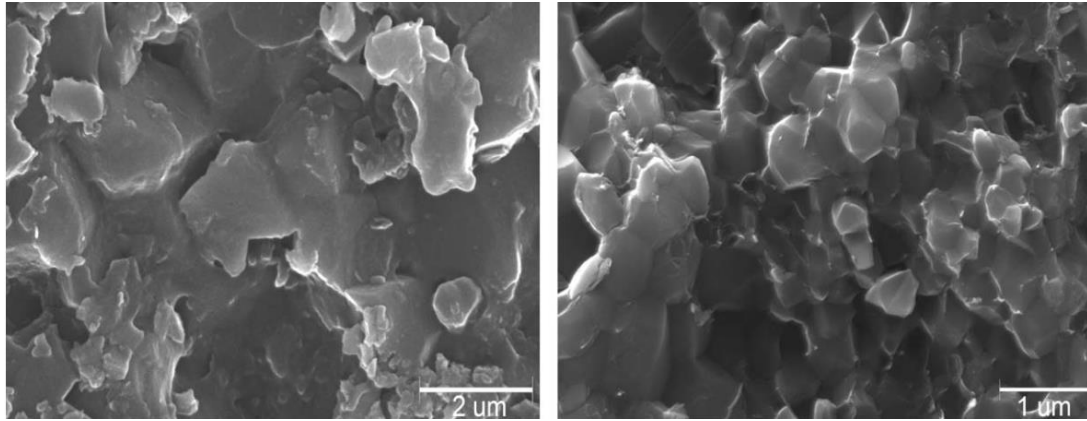


Figure 1.16 – SEM images illustrating the microstructures of alumina-based materials. **Left)** monolithic alumina. **Right)** alumina-rGO composite, which illustrates the refinement of alumina grains in the sintered composite sample. Adapted from Fan et al.¹⁴²

Also, work performed in 2013 within the UK demonstrated the incorporation of low volume fractions (up to 1.33 vol.%) of graphene filler within alumina, sintered through SPS at 1500/1550 °C.¹⁴³ However, the precursor material was graphene platelets rather than GO, which were procured from a manufacturer and characterised by SEM as part of the study. A 0.38 vol.% filler addition exhibited the highest fracture toughness (3.53 MPam^{1/2} to 4.49 MPam^{1/2}) and flexure strength (400 to 523 MPa) when tested through the SEVNB method.¹⁴³ However, a trade-off in Vickers microhardness is illustrated in the results upon increasing the graphene content. The composites were dense (above 99.5 %) and well-dispersed nanosheets of graphene were clearly visible, but they did visualise the existence of elongated pores at the interfaces between ceramic and graphene components (Fig. 1.17). The authors suggest this arises from poor interface bonding in some regions which induces variable shrinkage rates during the cooling section of sintering.¹⁴³ Furthermore, they believe that these pores are the origins of fracture and conclude that excessive graphene inclusion leads to weaker composites.

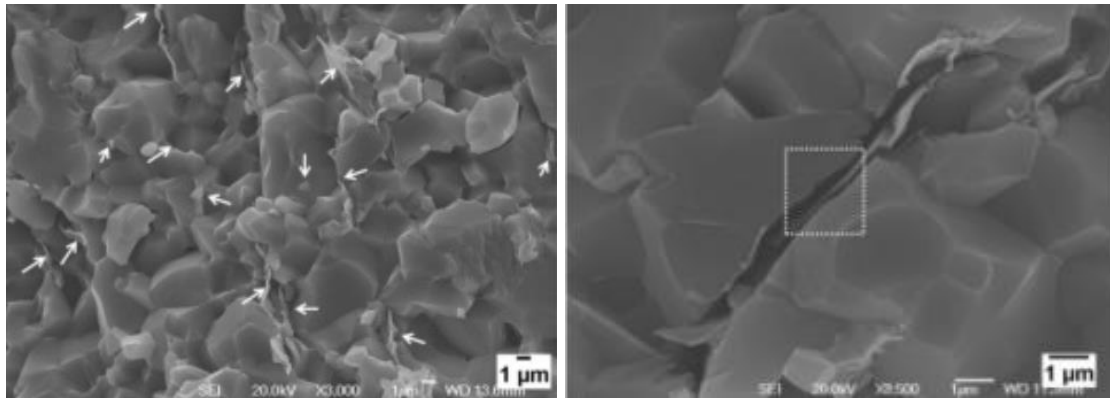


Figure 1.17 – SEM images depicting the microstructure of an alumina-graphene composite. **Left)** the well-dispersed nature of graphene nanosheets within the alumina matrix. **Right)** the existence of pores at the interfaces between ceramic grains and graphene nanosheets. Adapted from Jiang et al.¹⁴³

The addition of graphene fillers has also been applied to other structural ceramics. SiC has been reinforced with graphene nanosheets (up to 6 wt.%) in a similar fashion to Jiang *et al.* but sintered using hot-pressing equipment at 2100 °C.¹⁴⁴ The relative density of composites decreased upon increasing the fraction of reinforcement (from 99.9 % to 98.6 % with 4 wt.% addition), and it was also illustrated that the microstructure contained well-dispersed graphene platelets. The authors also state that the sintering step results in the oriented distribution of the filler which are predominantly aligned perpendicular to the plane of hot pressing. However, these were not all single platelets. Some of the reinforcement was overlapping in regions close to SiC/SiC grain boundaries, but also close to pores which were determined as origins of fracture during bending tests.¹⁴⁴

The authors also utilised two methods to determine fracture toughness: the SEVNB method, and an indentation method with a Vickers indenter. Their results shown that toughness increases as the fraction of reinforcement is raised, and that indentation fracture toughness value is slightly higher than obtained through SEVNB: 3.3 to 4.6

MPam^{1/2} for the indentation method, compared to 3.1 to 4.2 MPam^{1/2} for the SEVNB test.¹⁴⁴ The improvement was attributed to crack bridging and crack branching at the micro- and nanoscale, with limited crack deflection being observed on the nanoscale. It is thought that this observation relates to the small dimensions of the filler and the very brittle matrix.¹⁴⁴ Also, in some regions an unusual mechanism was detected – on the surface of overlapping platelets, cracks were spotted propagating perpendicular to the primary fracture surface (Fig. 1.18).¹⁴⁴ This feature was reported previously in work that fabricated Si₃N₄-graphene composites and is believed to be representative of graphene sheets that are wrapped and anchored around SiC grains – the resultant is a wall of graphene along the grain boundary, which arrests cracks and forces them to continue propagation in three dimensions through the material.¹⁴⁵ Although, an excess of graphene material, i.e., agglomerates, in some regions was believed to be the reason for early fracture in composites with 6 wt.% filler.

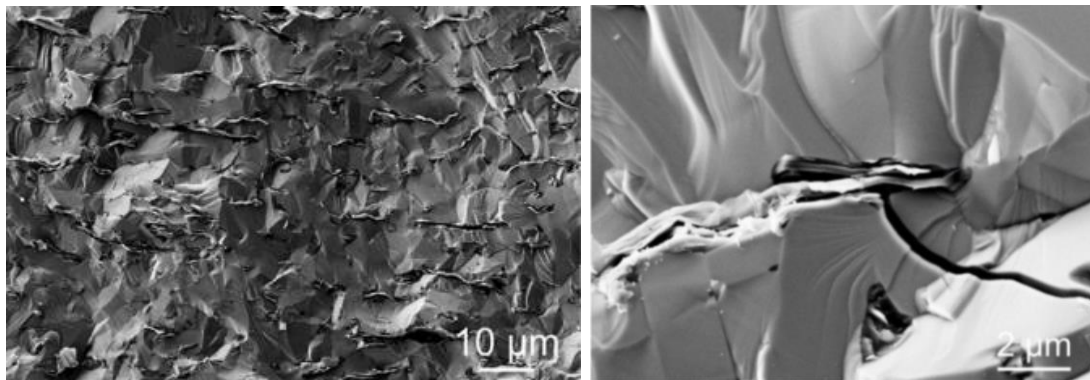


Figure 1.18 – Left) microstructure depicted in SiC/graphene composites processed using Spark Plasma Sintering. **Right)** fracture surface of a composite illustrating the occurrence of crack branching in three dimensions. Adapted from Sedlák et al.¹⁴⁴

1.4.2.2 Architectural design within ceramic-graphene materials

So far, a brief review has been given on various ceramic-graphene composites that incorporate the reinforcement in a random fashion during processing. Although, Sedláček *et al.* did realise a preferential alignment of 2D filler material when utilising SPS.¹⁴⁴ The next two examples will demonstrate structural arrangement of both ceramic and graphene-based components. The fabrication strategy developed by Sun *et al.* incorporates a well-dispersed and oriented reinforcement of GRM in the form of FLG into ceramic-based materials.¹³⁷ This unconventional approach utilised expandable graphite which is treated in a microwave oven to increase the interlayer spacing between sheets of graphene; this was followed by vacuum-assisted infiltration with a liquid ceramic precursor assisted by an organic, silane-based coupling agent. Sintering via SPS (at temperatures depending on the ceramic matrix) led to dense composite materials with highly-oriented inclusions of FLG, characterised by HRTEM and XPS. Several ceramic-graphene composites were fabricated during their studies including alumina-FLG (shown in Fig. 1.19), zirconia-FLG and amorphous silica-FLG.¹³⁷

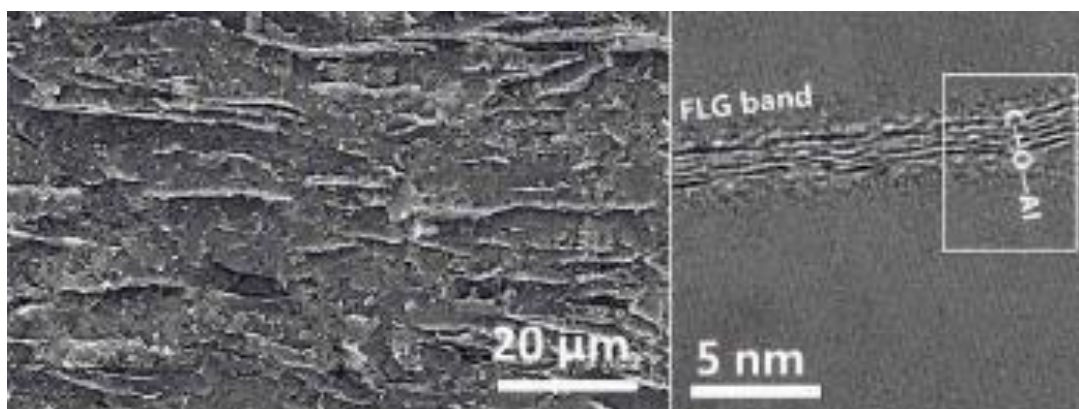


Figure 1.19 – Left) microstructure of alumina-FLG composite containing 5 vol.% of filler. **Right)** HRTEM image depicting the presence of FLG within the ceramic matrix. Adapted from Sun *et al.*¹³⁷

For the ceramic-FLG composites that have been mentioned, their investigation reports large improvements in the mechanical, tribological (wear-related), and functional properties such as EMI.¹³⁷ For alumina-FLG, flexural strength (through three-point flexure) is 32 % higher than monolithic samples, whilst the fracture toughness improved significantly by 240 % when measured through SEVNB methods. These relate to an efficient load transfer of stress between the ceramic matrix and graphene-like filler, and modified behaviour of stable crack propagation through numerous extrinsic toughening mechanisms that includes crack bridging, crack deflection, crack branching, and pull-out.¹³⁷ This study demonstrates that careful consideration of the microstructural arrangement within ceramic-graphene composites can vastly improve their mechanical properties.

Furthermore, Wang and Bi *et al.* explored the creation of nacre-like architecture through freeze-casting hybrid suspensions of GO and alumina material.⁹³ This is based on previously discussed work by Bouville *et al.*⁹⁴ In summary, a mortar was prepared by ball-milling GO with alumina nanoparticles in water (along with casting additives), then alumina platelets were added. GO was added from 0 – 1 wt.% in increments of 0.25 to fabricate nacre-like composites with various amounts of filler. The resultant slurry was ball-milled again for a shorter time and then subject to freeze-casting. Once dried pre-sintering at 1300 °C was carried out, followed by hot pressing at 1500 °C which produced the nacre-like microstructures shown in Fig. 1.20.⁹³ Highly-oriented rGO is distributed throughout the host alumina platelets that are also aligned from the casting step. Although, the addition of 1 wt.% did create severe misalignment of platelets, and several agglomerates of the graphene-like material was observed through SEM.⁹³

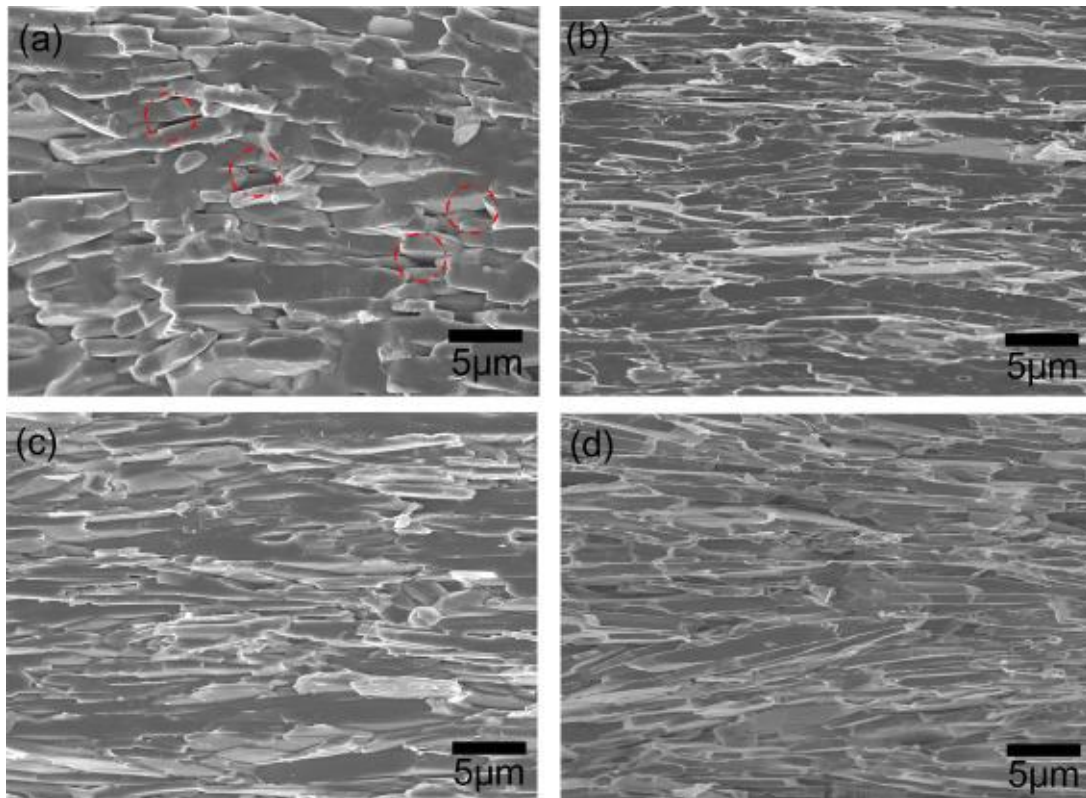


Figure 1.20 – Fracture surfaces of alumina-rGO composite with 0 – 0.75 wt.% addition of filler. The red circles indicate pores found in the monolithic material. Adapted from Wang and Bi et al.⁹³

The highest mechanical properties were found with an addition of 0.5 wt.% filler. At 0.75 wt.% addition, the density and properties began to diminish compared to other composites with lower rGO inclusions. The authors state that this is based on the number of defective regions of reinforcement that were observed, similar to work that has been discussed in the previous section.^{93,144} Density increased from 96 to <99 % with 0.5 wt.% addition, whilst flexure strength (in three-point flexure) and fracture toughness (through SENB) reached a maximum of 388 MPa and 7.75 MPam^{1/2} respectively – an increase of approximately 41 and 21 % compared to consolidated alumina platelets.⁹³ Like other studies, toughening mechanisms such as crack deflection, bridging, and branching were observed, alongside other microscopic phenomena that include the presence of mineral bridges and frictional sliding between

stacked platelets.⁹³ These toughening mechanisms are all observed in the fracture behaviour of nacre, although the length scale of the brick-and-mortar architecture (and hence the mechanisms occur on) is roughly one order of magnitude lower in the natural material.⁷⁷ This approach illustrates smart considerations when processing ceramic-graphene composites.

Chapter 2 Experimental procedure

2.1 Overview of processing strategy

An overview of the processing strategy is provided in Fig. 2.1. To summarise, the primary objective is to create ceramic scaffolds with directional porosity that can be infiltrated with a graphene precursor dispersed in an aqueous medium. This novel method showcases a combination of advanced processing techniques with an aim to produce bulk ceramic-graphene materials with an ordered microstructure. Unidirectional freeze-casting has the potential to generate aligned, porous architecture, so a colloidal suspension of the raw ceramic material is prepared prior to casting. This casting step is also considered as environmentally friendly, which is beneficial for promoting its usage over other processing routes towards ceramic-graphene materials that have been described previously in Chapter 1 (Section 1.4).

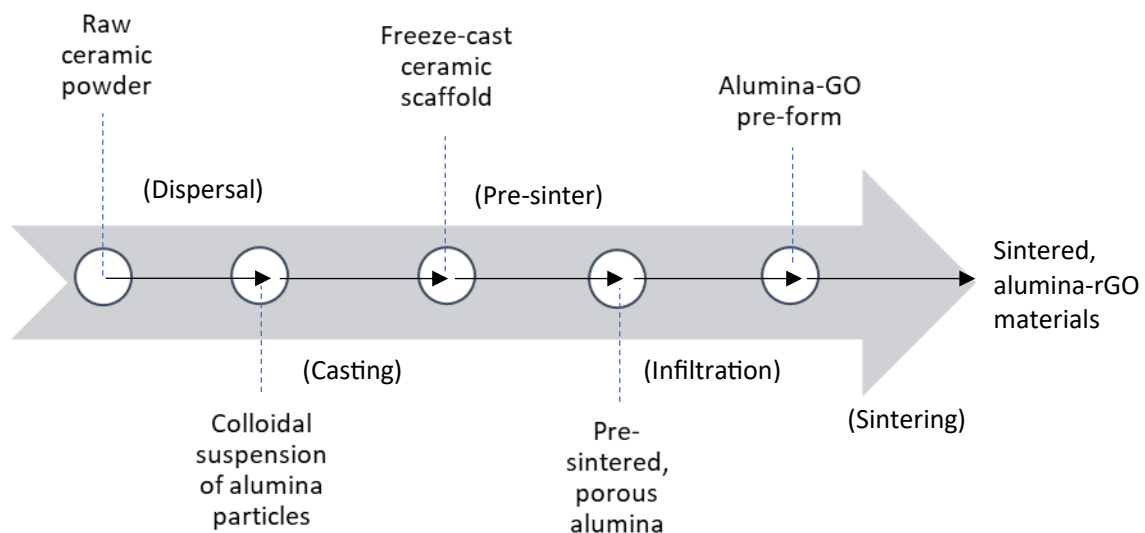


Figure 2.1 – Illustration of the processing strategy designed for creating alumina-graphene materials.

Recent work performed at Cardiff University demonstrated the potential for graphene-ceramic materials to be fabricated using a similar approach that involved freeze-casting scaffolds made from dilute, water-based suspensions of graphene precursor, then infiltrating this host with a ceramic suspension.¹⁴⁶ The proposed strategy herein involves the reverse, i.e., utilising a graphene precursor (GO) as the reinforcement to a freeze-cast ceramic matrix. Using GO as the filler material would circumvent the differences in hydrophilicity during the infiltration procedure and permit uptake into the open pores of freeze-cast material in a more facile step.

First, suspensions consisting of α -alumina powder (BA15-W white aluminium oxide, $d_{50} = 0.1 \mu\text{m}$, Baikowski, France), Grade III de-ionised water, 10 wt.% PVA solution, sucrose (>99 %, Merck, UK) and a dispersant were prepared utilising ultrasonication. The PVA solution was prepared from solid content (>95 %, Fisher Scientific, UK) dissolved in de-ionised water. The dispersant of choice was DOLAPIX CE64 (Zschimmer & Schwarz, Germany), a widely utilised dispersant for processing ceramic suspensions with high solid loadings.^{147–150} The chemical structure of its monomer is provided in Fig. 2.2.

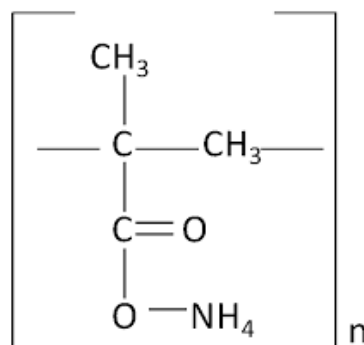


Figure 2.2 – Chemical structure of the dispersing agent DOLAPIX CE64.

After identifying suspensions of ceramic powder that were well-dispersed and possessed a unimodal distribution of individual grains, freeze-casting could commence. Ethanol ($\geq 99.5\%$, Honeywell, UK), and liquid nitrogen in two separate chambers were chosen as the refrigerant for the freeze-casting program. Cylindrical specimens of 30 mm diameter were freeze-cast and freeze-dried to generate large, porous ceramic scaffolds. Freeze-dried specimens were pre-sintered in a conventional furnace to remove the casting additives and provide structural integrity to the delicate ceramic structures before the introduction of further material.

Diluted, water-based suspensions from two graphene oxides (1 wt. % GO suspension in water, average particle size = $<10\ \mu\text{m}$, Graphenea, Spain; custom-made GO, Imperial College London, UK) were prepared via speed-mixing. Suspensions were degassed, then carefully introduced into the porous architecture using a vacuum chamber. Hybrid scaffolds were frozen after the infiltration step, then a second freeze-drying step was carried out to retain the porous architecture, which completed the fabrication of 30 mm alumina-GO pre-forms. The now dried alumina-GO materials undergo SPS to consolidate material and simultaneously onset the reduction of graphene oxide ($\text{GO} \rightarrow \text{rGO}$) within an inert atmosphere. 30 mm monolithic alumina was also prepared to compare the microstructural differences and (primarily) mechanical behaviour against alumina-rGO materials sintered with similar conditions. The following sections provide more comprehensive details about each separate stage of the processing route.

2.1.1 Preparation of ceramic suspensions

Ceramic suspensions were homogenised with an ultrasonic transducer (UIP 1000HD, Hielscher Ultrasonics GmbH, Germany) in combination with magnetic stirring at 600 rpm. After some quick trials, the transducer was chosen to be set at 70 % power during its operation. Ultrasonication is the process of transferring ultrasound energy through a fluid to induce cavitation – the rapid evolution, growth, and collapse of micrometre-sized bubbles.^{151,152} It has been demonstrated that raw materials can be dispersed from this shear-inducing process and is a viable method of breaking hard agglomerates in the fabrication stages of material synthesis and processing.^{153,154} Fig. 2.3 provides an illustration of the processing set-up.

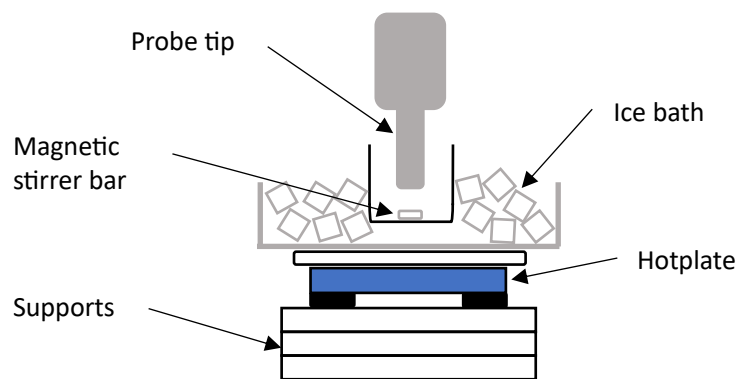


Figure 2.3 – Schematic of the ultrasonic apparatus used in dispersing ceramic-based suspensions.

First, de-ionised water was set to stir then the molecular dispersant, DOLAPIX CE 64 (0.5 wt.% wrt. ceramic loading), was added and left to mix for 5 minutes. This was based on literature work that incorporated this proportion to maintain a homogeneous dispersion of fine ceramic particles.^{104,155,156} Alumina powder was slowly added, then the remaining casting additives (10 wt.% PVA solution, 1.4 wt.% wrt. ceramic loading; sucrose, 4 wt.% wrt. water content) were weighed and placed into the stirring suspension of ceramic particles. These weight percentages were selected based on

prior literature.^{89,116,157} To finish, the resulting mixture was homogenised using ultrasonication for 5 minutes with a pause of 2 minutes halfway. Solid loadings of ceramic powder between 20 – 40 wt.% of the total solid mass were chosen based on literature work demonstrating that low-to-moderate solid loadings can generate highly porous specimens (>75 %).^{156,158} The temperature was constantly monitored using a temperature probe and external cooling was provided by an ice bath underneath the glass beaker. For reference, 90 g of 30 wt.% alumina suspension would contain approximately 60 g water, 27 g alumina powder, 0.135 g DOLAPIX CE 64, 0.378 g PVA solution, and 2.4 g sucrose.

2.1.2 Freeze-casting/-drying of ceramic materials

Custom-made, unidirectional freeze-casting apparatus (Fig. 2.4) was utilised to fabricate porous ceramic specimens. To begin with the temperature controller unit was connected to a band heater around the top of a copper rod and set with the parameters shown in Table 2.1, starting at Setpoint 1.

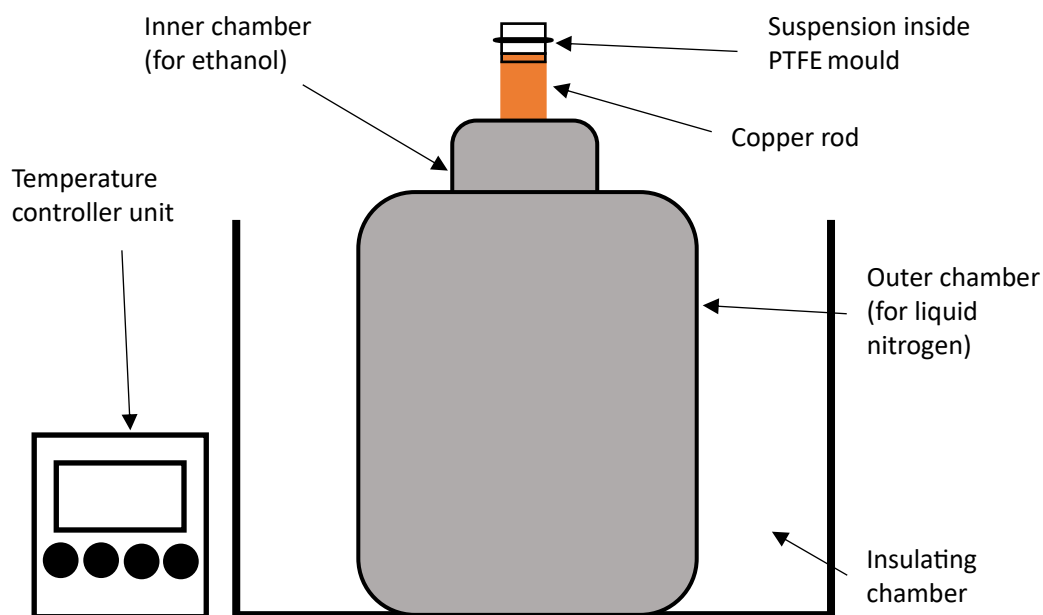


Figure 2.4 – Schematic of the custom freeze-casting set-up.

Table 2.1 – Table of parameters set for the freeze-casting procedure.

Setpoint 1, SP1 (°C)	Setpoint 2, SP2 (°C)	Cooling rate (°Cmin⁻¹)	Dwell at SP2 (min)
20	-170	5	60

These parameters were used in previous work at Cardiff University that utilised water-based freeze-casting which generated long-range porosity throughout specimens.¹⁴⁶ Other well-cited literature work has also utilised this freezing rate to control the growth of ice crystals and obtain a fine microstructure without sacrificing long-range order.^{104,159,160} Approximately 150 mL of ethanol was added to a stainless-steel chamber, covering about 2 cm of a 25 mm copper rod. 3 – 5 L of liquid nitrogen were added to an external steel chamber and constantly topped up. An insulating polystyrene box containing polystyrene beads housed the two chambers. The 30 mm casting mould comprised of 4 PTFE parts that made the walls, a copper plate to act as the thermal conductor, and rubber O-rings that held all the pieces together. In addition, each piece was thoroughly greased to contain material whilst resisting the expansion of water during freezing. After checking for any leaks, the program started. Fig. 2.5 provides a drawing of the PTFE mould cast via FDM that was designed by Mr Mohammad Arshad during a Research Opportunities Placement in 2017.

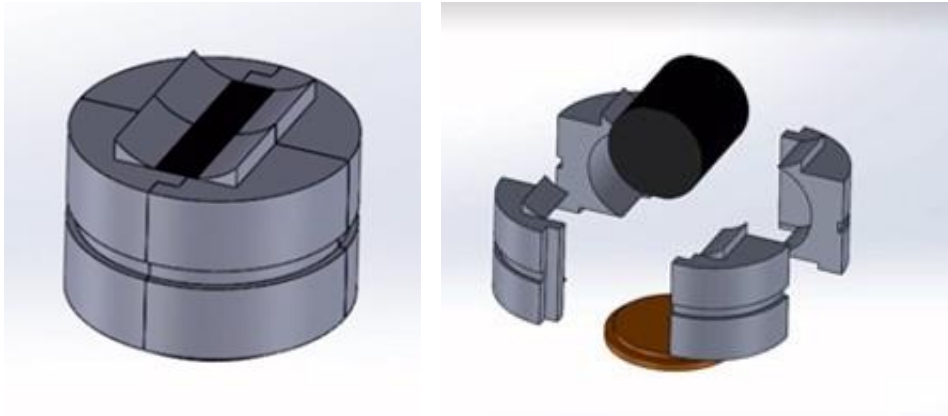


Figure 2.5 – Closed and expanded drawings of the PTFE mould, fabricated by fused deposition modelling, used in the freeze-casting process.

Once frozen, cast materials were subject to a drying treatment using a freeze-drier (Lablyo -85, Frozen in Time Ltd, UK) fitted with an 8-port flask manifold. Specimens were held inside glass flasks, attached to the manifold with a rubber cap whilst the compressor and vacuum pump were running, then left for 72 hours. Drying specimens in this manner retained the porous architecture that was created in the casting process without any internal deterioration. Scaffolds between 20 – 40 wt.% solid loading were fabricated, with 2 – 5 specimens being created for each formulation. Although only one specimen made from a 27.5 wt.% alumina suspension was successfully prepared.

2.1.3 Pre-sintering of ceramic materials

Pre-sintering of freeze-cast ceramic scaffolds was performed utilising a muffle furnace (1500 HTC, Carbolite Gero, UK), taking advantage of the programmable capabilities of this apparatus to create cycles with differing setpoints, heating rates and dwell times. This a critical step for ensuring casting additives utilised in the previous processing steps are eliminated and monolithic alumina remains. Fig. 2.6 illustrates the pre-sintering cycle to the highest dwell point of 900 °C for 30 mins at a rate of 5

$^{\circ}\text{Cmin}^{-1}$, with an additional dwell at 120 $^{\circ}\text{C}$ for 30 mins to ensure that no moisture remained. A dwell at 900 $^{\circ}\text{C}$ has been utilised like other literature work to provide some mechanical strength to the scaffolds (once the boundaries of ceramic particles begin to migrate together),^{161–163} whilst simultaneously losing some structural integrity provided by the casting additives.

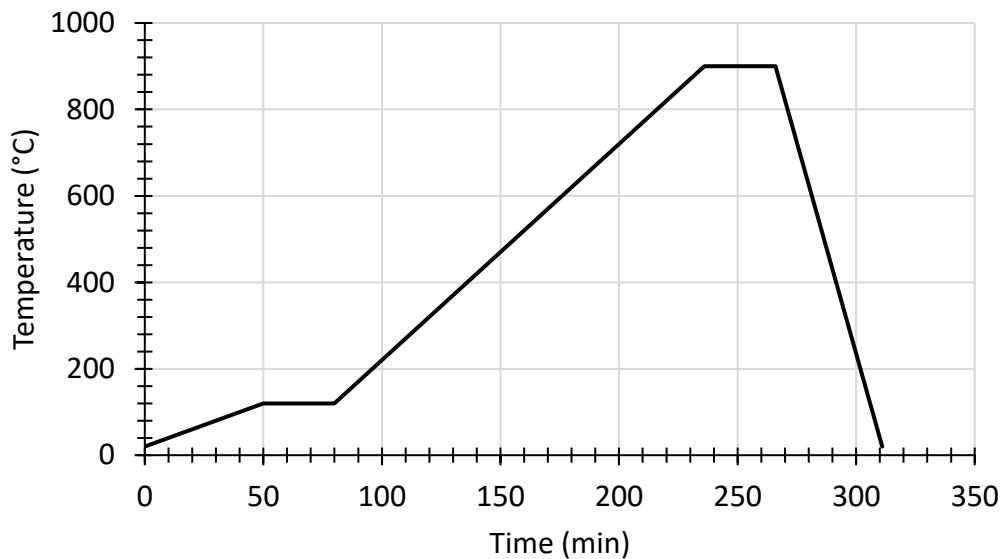


Figure 2.6 – Plot of the pre-sintering program for porous, ceramic scaffolds with remaining casting additives.

2.1.4 Infiltration of porous, ceramic materials with graphene oxide

Graphene oxide powder can be added to water to create a stable dispersion of the solid material; these are typically prepared by manufacturers between concentrations of 0.5 – 5 wt.%. Two batches of graphene oxide were investigated – a commercial suspension of 1 wt.% GO in de-ionised water, and a custom-made laboratory batch with unknown concentration. Both stock concentrations were validated by freezing aliquots of the material, following by freeze-drying to leave solid material behind;

weights were measured before and after this process to verify the solid content. This verification process was performed three times for each stock suspension. Once prepared, suspensions of either 0.025, 0.1, or 0.25 wt.% were then taken to a speed mixer (DAC 800.1 FVZ, Synergy Devices Ltd, UK) to homogenise the contents for 10 mins at 1800 rpm. These three concentrations were chosen to determine a suitable amount of GO that can infiltrate freeze-cast materials and generate continuous layers of reinforcement in sintered composites. If there is not enough of the reinforcing phase present, then continuity may not be achieved which would affect the electrical properties based on percolation theory; too much might form agglomerates in regions of the microstructure and lower the improvements in mechanical behaviour.

Vacuum-assisted infiltration of ceramic scaffolds was conducted utilising a vacuum degassing system (DS-26P, easycomposites, UK). Graphene oxide suspensions were degassed at -1 bar for 5 minutes, then pipetted over and around the 30 mm cylindrical specimens (held inside 35 mm polypropylene containers). The pressure was initially reduced to -0.9 bar for a few minutes to eliminate a substantial amount of air from the porous scaffolds. This first step was then repeated, but with lowering the pressure close to the apparatus' limit (-1 bar). Once bubbling visibly ceased (after 10 – 15 minutes), nominal pressure was restored, and the samples were taken out of the vacuum chamber and placed inside a freezer for at least 2 hours to solidify the water-based infiltrate. Frozen composite specimens were then freeze-dried for 72 hours to retain the internal microstructure generated through freeze-casting.

2.1.5 Spark Plasma Sintering of ceramic-based materials

Consolidation of ceramic-based materials was carried out using a spark plasma sintering system (HP D10-SD, FCT Systeme GmbH, Germany) with an accompanying chiller unit. Samples were contained within graphite die sets lined with graphite foil. Once the die was charged, it was pre-compacted using a cold press before adding a jacket of carbon felt for further insulation and transferring it to the SPS furnace.

Sintering took place under vacuum within an inert atmosphere of argon gas. Specimens were subjected to a pre-designed sintering program using the following parameters. DC pulse sequences of 10:5:12:2 or 1:0:1:0 (on/off/number of pulses/extra pause time) were utilised which may be described as pulsed, or continuous, sequences respectively. The temperatures used to sinter ceramic-based materials were between 1000 – 1500 °C that was held for either 1 or 5 minutes. This was monitored via an optical pyrometer focused through a 10 mm channel within the top punch of the graphite die roughly 5 mm away from the top of the sintering material. A pressure of 50 or 60 MPa was applied uniaxially at the start of the program before the heating segments had begun, plus the heating and cooling rates were set to 50 or 100 °Cmin⁻¹ with the preliminary program adopting natural cooling. Fig. 2.7 illustrates the apparatus itself and the graphitic components used for assembling 30 mm die sets.



Figure 2.7 – Left) photograph of SPS Type HP D10-SD and chiller unit. **Right)** graphitic components used to assemble 30 mm die sets.

2.2 Overview of characterisation techniques

To meet the primary objectives of this research, several characterisation techniques have been utilised (Fig. 2.8) at various stages of the processing strategy. As this work aims to create porous ceramic scaffolds that can be infiltrated with a water-based graphene precursor, characterisation of the host matrices' microstructural features is vital. Over recent years, researchers have promoted the utilisation of μ -computed tomography, a non-destructive imaging technique, to view porous characteristics of freeze-cast materials.^{106,164,165} This was the most powerful technique used in the investigation and focused on evaluating: i) the orientation and alignment of pores fabricated during casting, and ii) the homogeneity of these channel size (diameter).

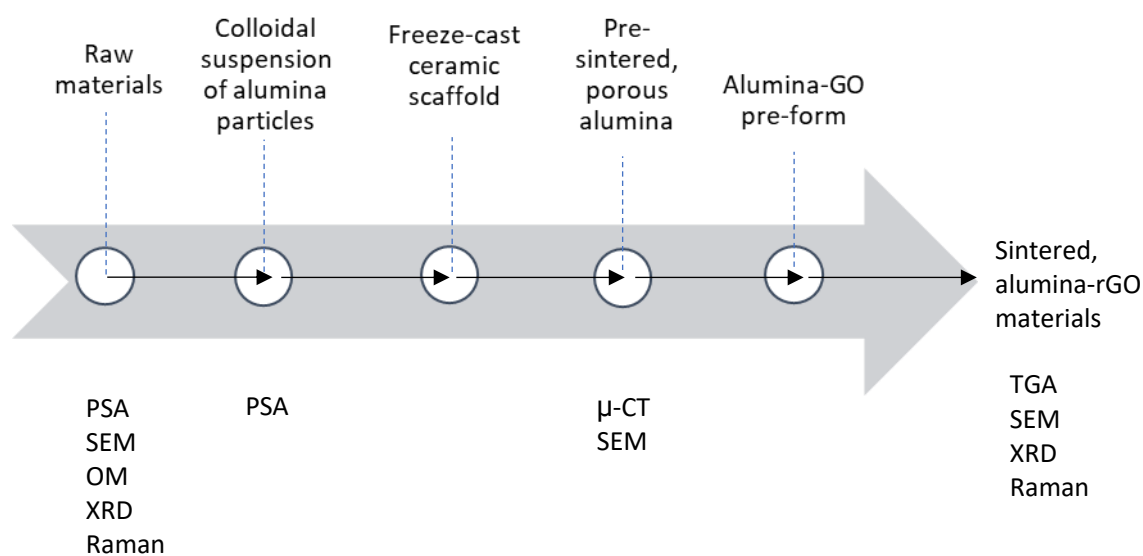


Figure 2.8 – Illustration of the characterisation techniques utilised at various stages of the processing strategy.

Once porous materials have been infiltrated with the graphene precursor, visualisation of its uptake into the core of the scaffold is paramount. In addition, quantification of the reinforcement is necessary to further determine the hybrid materials' physical

properties, such as specific density. After sintering, the main objectives are: i) evaluating the extent of GO reduction, and ii) visualisation of the material's microstructure and a comparison against pure ceramic material sintered using similar conditions. A description of the testing of material properties for monolithic ceramic and ceramic-graphene materials is provided in Section 2.3. Graphite (Duragraph 120, Erodex, UK) was utilised as a comparative material to GO during its characterisation.

2.2.1 Particle size analysis

The distribution of particle sizes of the as-received alumina powder and colloidal suspensions with varying ceramic content (that also include the dispersant) was determined using PSA. A particle size analyser (Mastersizer 3000, Malvern Panalytical, UK) fitted with a wet sample dispersion unit (Hydro EV, Malvern Panalytical, UK) was employed to evaluate the volume distribution. This was with measurements set to perform 6 scans each lasting 10 seconds within the range of 0.01 – 1000 μm . Displayed results are either the full set of measurements, or the average of the 6 scans.

2.2.2 Thermogravimetric analysis

The estimation of graphene-like reinforcement within alumina-graphene materials was evaluated using TGA. The latter used 5 specimens of composite material, acquiring 2 measurements for each specimen. A thermogravimetric analyser (TGA/SDTA851e, Mettler Toledo, UK) was utilised in combination with compatible software (STARe, Mettler Toledo, UK). 70 μL alumina crucibles were utilised to house samples, and masses of samples between 50 – 70 mg were weighed with a 5 decimal precision balance (AE200, Mettler Toledo, UK). In all cases, the heating program was set to reach 1000 $^{\circ}\text{C}$ (from ambient conditions) in air at a rate of 5 $^{\circ}\text{Cmin}^{-1}$.

2.2.3 Viscosity

Viscosity measurements of stock and dilute GO suspensions were recorded with a rheometer (MCR 92, Anton Paar, UK) in combination with compatible software (Rheocompass, Anton Paar, UK). The measuring head was fitted with a 50 mm measuring plate and a gap of 0.6 mm was utilised. Constant shear tests were carried out for 2 minutes at a shear rate of 50 s^{-1} , with data being recorded every 5 seconds. Deionised water was also measured as a reference material. The calculation of shear viscosities was automatically provided through the software with Equation 2.1, formulated from Newton's second law of thermodynamics.¹⁶⁶

$$\mu = \frac{F}{A\dot{\gamma}} \quad \text{Equation 2.1}$$

Where A is the area of the measuring plate, F is the applied force (experimentally calculated from the torque and measuring plate area), and $\dot{\gamma}$ is the rate of shear deformation.

2.2.4 Optical microscopy

Optical microscopy is based on the focusing of wavelengths of visible light through a system of lenses to create a magnified, visual image. In a simple, compound microscope, an objective lens (or a series of lenses) will focus light that is being reflected from an object, which is further magnified by an eye-piece lens.¹⁶⁷ This can be complimented by mounting a digital camera to observe the sample and collect images via a computer trough a set of diaphragms and collection lenses.^{167,168} It is thought that the first, practical binocular microscope was invented by J.L Riddell during the 1850s, yet it is believed that earlier usage of compound devices was apparent in the 17th Century.^{169,170}

Evaluation of as-received, graphene oxide flakes and the visualisation of Vickers indentations was performed using OM. GO suspensions were subject to dilution (<25 ppm) in a mixture of water and isopropanol, then deposited onto Si-SiO₂(300nm) wafers for observation. 125 flakes were viewed from each GO batch to identify the average flake size and form a frequency distribution. This was performed using an optical microscope (DMLM, Leica, UK) in conjunction with image capturing equipment and software (UI-1460LE-C-HQ, IDS GmbH, Germany – uEYE cockpit, IDS GmbH, Germany). Scale bars were produced with a microscope calibration ruler at various magnifications, and post-processing was performed using ImageJ software (National Institutes of Health, Bethesda, USA).

2.2.5 Scanning electron microscopy

SEM differs to OM as a beam of electrons are fired at a sample, producing a variety of detectable signals after the sub-atomic particles interact with (or just below) the surface topography and composition of a material.^{171,172} This process is performed within a vacuum to inhibit unwanted contamination from atoms and molecules in the atmosphere. The result is an image with resolution on the nanometre scale, with a large depth of field that generates 3D images, useful for understanding the morphology of a sample.¹⁷² The working principle is that electrons are fired toward an anode from a source towards a collimator, which then passes through a series of condenser lenses to further focus the beam. Scans are carried out in a “raster pattern” by virtue of scanning coils that are present in the set-up,¹⁷¹ referring to scanning in parallel lines from side to side, or top to bottom, in a rapid manner. The various interactions that may occur due to electron irradiation at a sample’s surface is shown in Fig. 2.9.

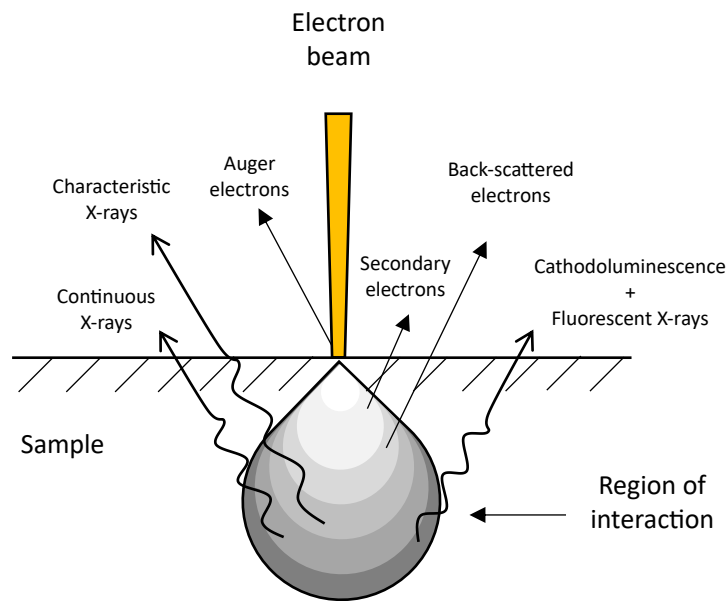


Figure 2.9 – Diagram of the possible interactions that can occur after electrons penetrate the surface composition of a sample.

The most common types of detectors are SE and BSE detectors that are positioned on the side of the chamber, or in-line with the electron gun, respectively. SE detectors (first conceived by Everhart and Thornley) collect low-energy (~ 50 eV) electrons after they are involved in inelastic scattering processes a few nanometres below the surface of a sample.^{172,173} SE detectors typically come as standard with SEM equipment, with most apparatus integrating a combination of detector types.

SEM was employed for determining the particle size of as-received and dispersed alumina powder, measuring the pore size and lamellae thickness of freeze-cast materials, and for performing fractographic analysis on monolithic alumina and alumina-graphene specimens. 200 grains were evaluated to determine the average grain size of materials and form a frequency distribution after sintering. This was conducted using a field-emission scanning electron microscope (Crossbeam 1540XB, Carl-Zeiss, UK) and corresponding software (SmartSEM® V5.05 XB, Carl-Zeiss, UK).

The electron beam was set to operate at either 5 or 10 kV. Some specimens were sputtered with a conductive layer of Au/Pd alloy to combat the extent of surface charging, which is referenced in the caption for any related figures. Micrographs were analysed using ImageJ software.

2.2.6 Raman spectroscopy

Raman spectroscopy operates based on the absorption and emission of visible light to measure the vibrational energy modes of molecules within a sample. This technique was first developed by Raman and Krishnan in 1928, after observing a scattering effect as light passed through organic liquids which followed earlier predictions of this phenomena.^{174,175} During absorption, the electromagnetic field that accompanies photons interacts with the electron density of a molecule, creating an excited molecular state after overcoming an energy gap.¹⁷⁶ However, after emission from the “virtual state” the associated energy of the photon has shifted up or down (Stokes and Anti-Stokes scattering). This less intense, Raman signal is an inelastic scattering process that arises due to a transfer of energy between the molecules of the sample and the scattered photons.¹⁷⁶ In brief, the process begins by an illuminating a sample with monochromatic, visible light which causes interactions between the incident beam of photons and excitations (such as molecular vibrations, or phonons) within the sample. A change in energy occurs which can be measured and related to molecular changes of structures found within molecules.¹⁷⁶ This energy transfer is illustrated in Fig. 2.10 and the necessary conditions for each scattering event are indicated.

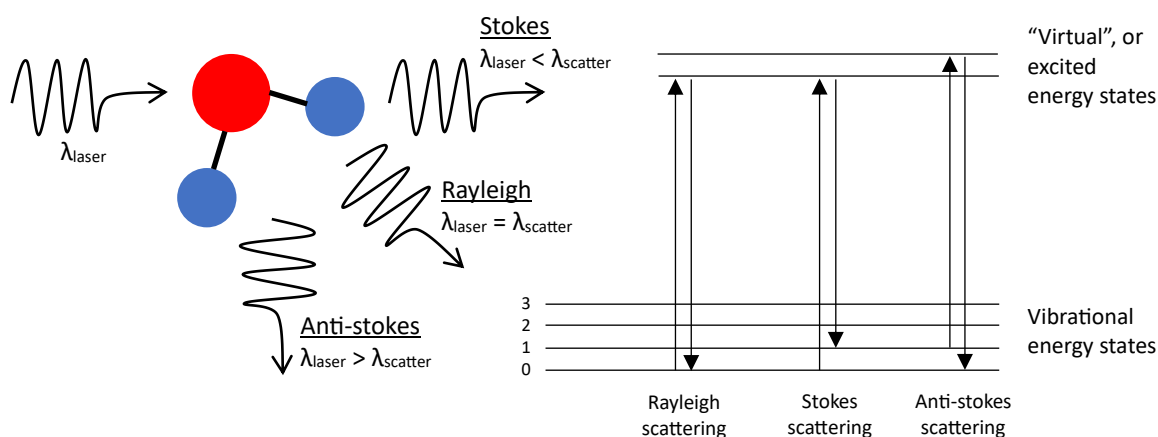


Figure 2.10 – Left) illustration of scattering processes. **Right)** Jablonski energy level diagram for the associated changes in vibrational energy.

To compare the nature of graphene-related materials, and to identify changes after the sintering stage, a Raman spectrometer (LabRAM HR Evolution, HORIBA, UK) with compatible software (LabSpec 6, HORIBA, UK) was employed. A laser of wavelength 532 nm and a spot size of 1 μm was utilised to obtain scans after 2 accumulations, each lasting for 5 minutes, or 10 in the case of graphite and composites including reduced graphene oxide. The chosen region of interest was between wavenumbers of 1000 and 2000 cm^{-1} . This is because previous studies have demonstrated that graphene-related materials can be distinguished from one another by identifying the positions and intensities of the D and G signals.¹⁷⁷ These two signals are commonly found close to 1350 and 1600 cm^{-1} respectively, which is shown in Fig. 2.11.

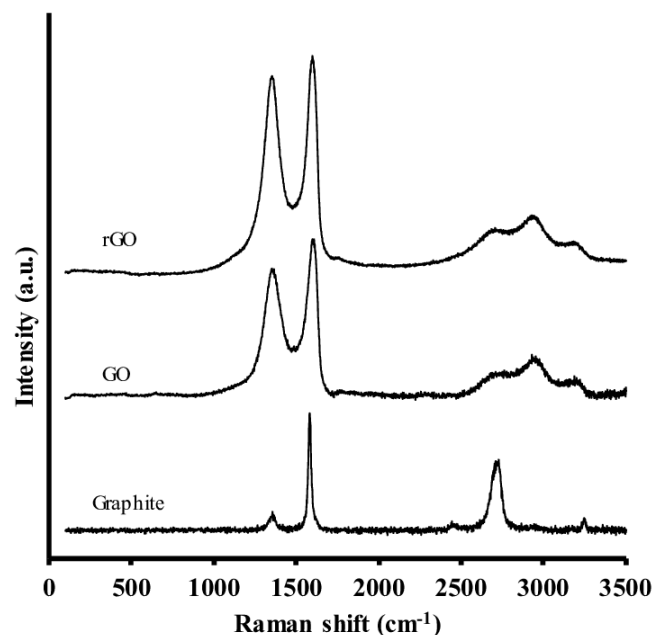


Figure 2.11 – Typical Raman spectra obtained for graphene-related materials between 0 and 3500 cm^{-1} . Adapted from Álvarez and López-Ramón et al.¹³¹

2.2.7 X-ray diffraction

The process of XRD involves electrons within the material interacting with electromagnetic radiation in the form of X-rays at various, but specific, angles and directions.^{178,179} To summarise, a beam of X-rays is fired at a sample to create a diffraction pattern, otherwise known as a “reflection”, through the scattering of incident X-rays. The recorded 2-D data of angles and intensities can be translated into a 3-D map of electron density, and ultimately this diffraction pattern relates to the position of atoms in a crystal.¹⁷⁸ This technique is also excellent for determining unit cell parameters, i.e., the angles and lengths that provide the simplest building block for crystal lattice identification.¹⁷⁸

Bragg diffraction is a special condition in which the wavelength of radiation is comparable to that of the spacing between lattice planes (1-10s of angstroms). An outcome is generated only if the encountered scattering is coherent and elastic: thus the intended properties of scattered X-rays are that they are constructive and in-phase, and that they do not transfer energy to the crystal's electronic structure during the scattering process.¹⁷⁹ Sharp, intense peaks are formed in the diffraction pattern that are associated with the intense incident X-rays that are collected after interacting with the crystalline matter. A mathematical relationship known as Bragg's law (Equation 2.2) was formulated and is widely utilised for estimating the spacing between atomic planes.¹⁷⁹

$$n\lambda = 2d\sin(\theta) \quad \text{Equation 2.2}$$

Where n is the diffraction order (typically 1 as it is illustrating the repetition of diffraction), λ is the X-ray wavelength, d is the spacing between crystallographic planes, and θ is the scattering angle. Fig. 2.12 illustrates the phenomenon of coherent, elastic scattering.

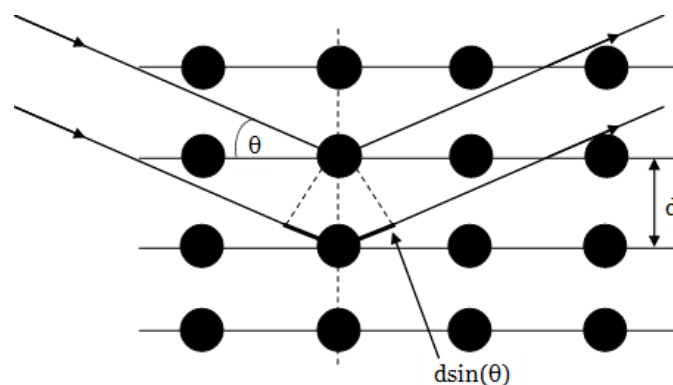


Figure 2.12 – Illustration of Bragg diffraction. Note that the second X-ray “wave” follows a path that includes an extra distance of $2d\sin\theta$.

Diffraction patterns were obtained using an X-ray diffractometer (D5000, Siemens, UK) in conjunction with post-processing software (DIFFRAC Plus XRD commander, Bruker, UK – X’Pert Highscore Plus, Malvern, UK). References provided with the measured data were supplied by the International Centre for Diffraction Data (ICDD) database. Cu (K_{α}) was utilised as the X-ray source, with samples being placed on top of (or inside) 3D printed polylactic acid (PLA) holders. All scans were performed between 2θ values of 5 – 80 and in increments of 0.02, with a scan speed of 0.8.

2.2.8 μ -computed tomography

μ -CT is a non-destructive imaging technique that combines X-ray scanning and powerful computational software to develop 3D projections of objects.^{180,181} This imaging method stems from computed tomography (established and patented in the late 1970s) that creates 2D projections: not long after during the early 1980s, public evidence from a physicist working at Ford Motor Company (L. Feldkamp) demonstrated the capability of fully reconstructing 3D images.¹⁸¹ The working principle of CT is based on the attenuation of X-ray radiation as it passes through an object. Equation 2.3 illustrates that whilst an X-ray passes through a solid, e.g., bone, the intensity of the radiation at distance x (I_x) will be affected by the solid object and the initial source of energy.¹⁸² Meanwhile, x is the distance from the radiation source and μ is the linear attenuation coefficient.

$$I_x = I_0 e^{-\mu x} \quad \text{Equation 2.3}$$

A detector is placed a distance away from an X-ray source, with the object that is to be scanned positioned between the two.¹⁸² Traditional CT equipment (known as fan-beam CT) combine a beam collimator with a 1D detection source to produce cross-sectional images of the object, whilst some apparatus discards the collimator and integrates a scintillator which is positioned in front of a charge-coupled device camera

to convert the detected X-ray signals into visible light.¹⁸² This alternative method is referred to as cone-beam CT.¹⁸¹ In both cases, either the object or the X-ray source and detector is rotated to acquire several scans from different angles, which are then computationally rendered into a 3D model.

This work was supported by the National Research Facility for Lab X-ray CT (NXCT) through EPSRC grant EP/T02593X/1. An overview scan of an alumina scaffold was evaluated using a modified μ -CT scanner (225 kVp Nikon/Xtek HMX system, Nikon Metrology, UK). The parameters of the X-ray source and detectors were a peak voltage of 160 kV, a maximum power was 17.5 W, and an exposure time of 250 milliseconds. This formed a voxel resolution of 4.52 μ m. Additionally, a 6 x 6 mm section close to the freezing surface was also evaluated using an X-ray microscope CT scanner (160 kVp Zeiss Xradia Versa 510 system, Carl Zeiss, Germany). Parameters were a peak voltage of 110 kV, a maximum power of 10 W, and an exposure time of 10 seconds, forming a 688 nm voxel resolution. Post-processing of scans was performed using ImageJ and open source 3D Slicer (<http://www.slicer.org>) to obtain 3D reconstructions and 2D cross-sectional images.¹⁸³

2.3 Testing of material properties

2.3.1 Specimen preparation

During the fabrication of materials, processing and sintering techniques can introduce unwanted defects against their surfaces. For example, the use of SPS involves encasing the sample in graphitic foil, which in some cases, causes carbon diffusion within the surface during consolidation.¹⁸⁴ Furthermore, surfaces may be rough: this roughness can induce regions of stress which may cause unprecedented failure during service. Therefore, prior to evaluating their mechanical or functional behaviour, it is critical that specimens are prepared in a way that: i) is reproducible, ii) forms flat, planar surfaces, and iii) does not introduce more defects along its surface.

30 mm disc-shaped specimens were subject to grinding, polishing, and sectioning before any mechanical, thermal, or electrical testing. Grinding and polishing was performed using an automatic grinder-polisher unit (Ecomet™ 30 Semi-Auto, Buehler, UK) allowing up to 4 samples to be treated at once. Polishing was carried out manually on individual samples in a three-step manner. Specimens for determination of flexure strength and functional behaviour were ground to 1200-grit finish, whereas specimens for micromechanical testing (hardness, indentation toughness) were polished to a mirror finish (to 1 μm). A summary of each grinding/polishing step is given in Table 2.2. Cutting was performed with precision cutting/grinding equipment (Accutom-100, Struers, UK) accompanied with a diamond-bonded cut-off wheel (MOD13, Struers, UK). Parameters included a rotation speed (of the cut-off wheel) of 2750 rpm, and a feed rate of 0.010 mmmin^{-1} .

Table 2.2 – Table of grinding and polishing steps taken to prepare ceramic-based materials for various mechanical tests – it should be noted that a different surface was utilised for each successive polishing step.

Step no.	1	2	3	4	5	6
Treatment	Grinding	Grinding	Grinding	Polish	Polish	Polish
Surface	MD-Piano (Struers), 120	MD-Piano, 500	MD-Piano, 1200	MD-Largo (Struers), 9- μ m diamond fluid	MD-Largo, 3- μ m diamond paste	MD-Largo, 1- μ m diamond paste
Applied force (N)	35	20	20	-	-	-
Lubricant	Water	Water	Water	IPA	IPA	IPA
Time	Until planar	5-10 minutes	<5 minutes	<2 minutes	<2 minutes	<2 minutes

Flexure testing

+ physical properties

Indentation



2.3.2 Densities of fabricated materials

2.3.2.1 Bulk density

Bulk densities of freeze-cast scaffolds (prior to pre-sintering) were calculated by obtaining: i) the mass of the specimen with a 3 decimal precision balance (Explorer EX423, Ohaus, Switzerland), and ii) the volume, utilising a digital calliper accurate to ± 0.03 mm for measuring the diameter and height of cylindrical, freeze-cast materials. The reported volume was calculated based on an average of 1 height and 4 diameter measurements.

2.3.2.2 Density through Archimedes' principle

Densities of sintered materials were determined from Archimedes' principle, utilising a 4 decimal precision balance (LA-310s, Sartorius, Germany) fitted with a density determination kit (YDK-01, Sartorius, Germany). Samples were labelled with a felt pen before weighing, and the glass beaker filled with deionised water. The method began with boiling the samples in water for 2 hours and measuring their mass in water, before placing them in a drying furnace at 120 °C for between 2 hours to determine their dry weight in air. The temperature of the water was monitored using a temperature probe. The density of bulk alumina at 100 % theoretical density was taken as 3.99 gcm^{-3} , whilst the density of rGO (possessing a high level of reduction) was taken as 1.90 gcm^{-3} .¹⁸⁵ These were both used to approximate the theoretical density of alumina-rGO composites through the rule of mixtures. The aim was to collect five measurements to generate an average and standard deviation, from which the relative density and remaining porosity were determined (Equations 2.4 – 2.6).¹⁸⁶ However, results obtained for monolithic alumina sintered at 1000 and 1400 °C are representative of only three and two measurements respectively.

$$\rho_{sample} = \frac{m_1 \cdot \rho_{water}}{m_2} \quad \text{Equation 2.4}$$

$$Relative\ density = \frac{Density\ of\ sample}{Density\ at\ theoretical\ density} (\times 100) \quad \text{Equation 2.5}$$

$$Porosity = 100 - RD, \% \quad \text{Equation 2.6}$$

2.3.3 Vickers hardness

Hardness measurements of sintered materials was carried out using a universal hardness testing machine (NOVA 360, InnovaTest, UK) fitted with a Vickers indenter between loads of 0.5 – 10 kg for 10 seconds. Small pieces of material were embedded within epoxy resin using a laboratory mounting press (Primopress, Struers, UK) prior to carrying out any measurements. Indentations made using 1 kg-force followed ASTM E384-17. Indentations were created at least 0.1 mm apart from each other to avoid the deformation created by other testing regions and images were collected via optical microscopy to manually measure the diameters of the indentations. Equation 2.7 was utilised to convert the measured diameters of indentations into hardness values, based on the force that is applied and the angle between opposite faces of the diamond tool.¹⁸⁷ Equation 2.8 was used to convert Vickers hardness values into GPa.

$$Vickers\ hardness, H_V = \frac{2F \frac{\sin(136^\circ)}{2}}{d^2} = 1.854 \frac{F}{d^2} \quad \text{Equation 2.7}$$

$$H_V(GPa) = H_V \times 0.00981 \quad \text{Equation 2.8}$$

2.3.4 Fracture toughness

Fracture toughness of sintered materials was determined using the VIF method, with the same equipment using for determining microhardness. Indentations were made on polished cross-sections of specimens between loads of 1 – 30 kg for 10 seconds to induce the propagation of cracks that could be observed and measured. The measured lengths were then applied to the formulas developed by Palmqvist and Anstis to calculate the fracture toughness (Equations 2.9 and 2.10 respectively).^{57,188} 3 – 5 indentations were performed, and the developed cracks were investigated using SEM.

$$W_K \approx K_{IC} = 0.0028\sqrt{H} \cdot \sqrt{\frac{P}{L}} \quad \text{Equation 2.9}$$

Where H is the hardness in GPa, P is the indentation load in N, and L corresponds to the sum of the length of the propagated cracks in m.

$$K_{IC} = 0.016\left(\frac{E}{H}\right)^{\frac{1}{2}} \cdot \sqrt{\frac{P}{c^{\frac{3}{2}}}} \quad \text{Equation 2.10}$$

Where E is the Young's modulus in GPa, H is the hardness in GPa, P is the indentation load in MN, and c is the sum of the propagating cracks plus half of the diagonal width in m. An illustration is provided in Fig. 2.13 to display the lengths that were measured.

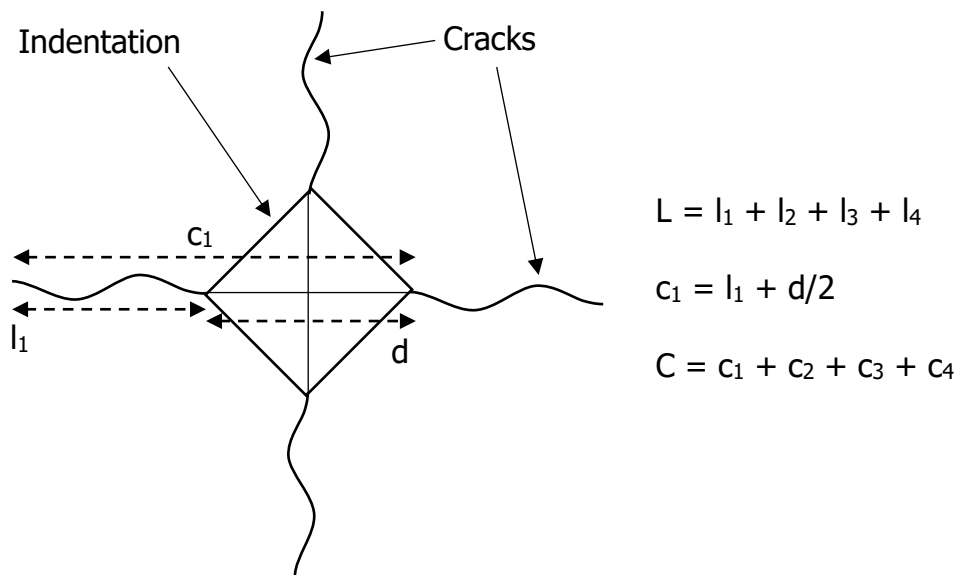


Figure 2.13 – Diagram illustrating the lengths to be measured for evaluating the indentation fracture toughness caused by a Vickers indenter.

After the investigation of fracture toughness, surfaces were re-polished to a 3 μm finish for approximately 15 minutes to identify the type of crack that has propagated. Two types of cracking patterns form in hard materials, i.e., ceramics, which are referred to as Palmqvist or radial-median which is illustrated in Fig. 2.14. The former is representative of deformation patterns that do not connect with the propagated cracks, whilst the latter is representative of a pattern that is connected to the cracks.¹⁸⁹ Radial-median cracks are also characterised by a large crack that forms underneath the surface of the indentation.

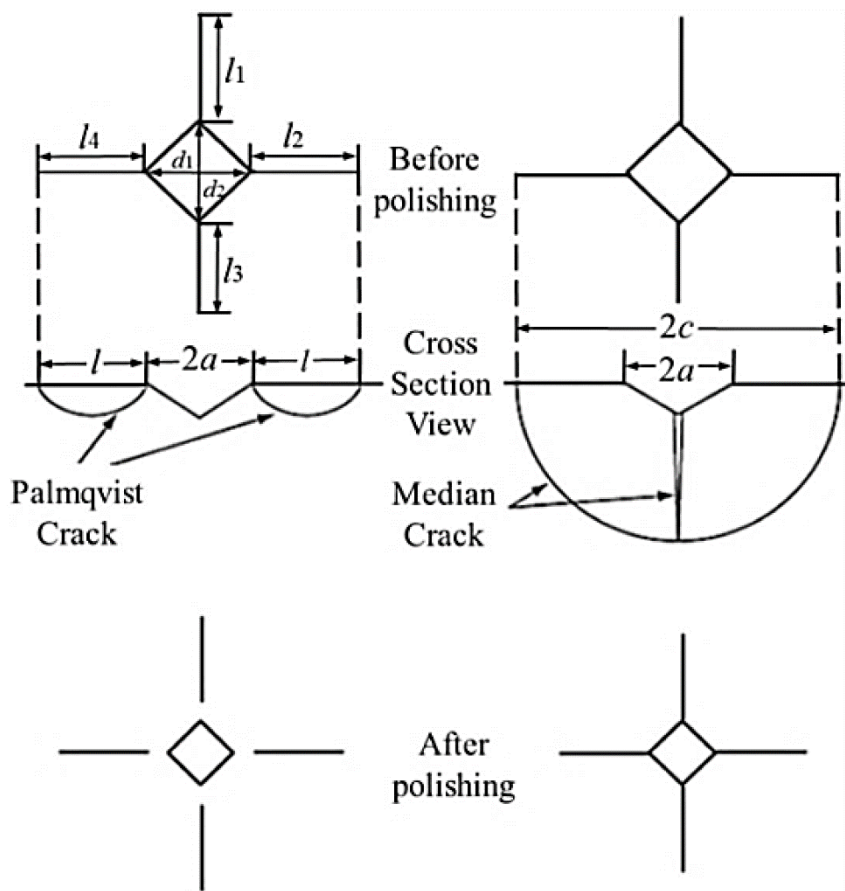


Figure 2.14 – Illustration of two common types of cracking patterns seen in hard materials after indentation. Taken from Žmak et al.¹⁹⁰

2.3.5 Flexural strength

Flexural strength of sintered materials was calculated with a 4-point bending moment in a universal testing machine (AllroundLine Z050, Zwick-Roell, UK). ASTM C1161 was followed. The top and bottom spans of the contacting rollers were 10 and 20 mm, respectively, and a crosshead speed of 0.1 mmmin^{-1} was used. Specimens were approximately $22 \times 2 \times 2 \text{ mm}$ (with lengths up to 30 mm), and post-experiment their fracture surfaces were investigated using SEM. Four specimens of alumina were tested alongside three specimens of the composite material – although this is not a reliable sample size it is thought that the obtained values are still representative of any

mechanical changes. Time constraints (due to COVID-19) and issues with equipment restricted the further fabrication of specimens. The flexure strength, σ_f , was calculated with Equation 2.11 by determining: i) the bending moment about the neutral axis, M , ii) the distance to the neutral axis, y , and iii) the second moment of area about the neutral axis, I . These three components can be determined using Equations 2.12 – 2.14 using the force measured at the yield point, F_{break} , the top and bottom spans of the rollers (S_T and S_B) and the thickness and width of bar-shaped specimens (d and b respectively).

$$\sigma_f = \frac{My}{I} \quad \text{Equation 2.11}$$

$$M = \frac{(S_B - S_T)F_{break}}{4} \quad \text{Equation 2.12}$$

$$y = \frac{d}{2} \quad \text{Equation 2.13}$$

$$I = \frac{bd^3}{12} \quad \text{Equation 2.14}$$

2.3.6 Electrical conductivity

In-plane electrical resistivity of sintered materials was determined at ambient conditions with 2-probe resistance measurements on bar-shaped specimens that were approximately 12 x 2.7 x 1.8 mm. Two specimens were cut from a disc-shaped alumina-graphene composite to evaluate the connectivity of infiltrated graphene networks: one from the core, and one closer to the perimeter of the disc. Silver paste was applied to the end faces of bars, then the resistance was measured whilst one contact was stationary, and the other positioned at points along the other face. 12 measurements were taken to create an average of the electrical resistivity, ρ , from Equation 2.15.

$$\rho = \frac{RA}{l} \quad \text{Equation 2.15}$$

Where R is the measured resistance in Ω , A is calculated cross-section of the specimen in cm^2 , and l is the length in cm between the contact probes. This was then converted into electrical conductivity using the inversely proportional relationship show in Equation 2.16.

$$\sigma = \frac{1}{\rho} \quad \text{Equation 2.16}$$

2.3.7 Thermal conductivity

This work was conducted at the Carbon and Science Institute (INCAR-CSIC, Oviedo, Spain). Thermal diffusivity of sintered materials was measured between 25 – 750 °C in 100 mLmin⁻¹ of argon flow using a laser flash analyser (LFA Microflash apparatus, NETZSCH, UK). Square-shaped specimens were prepared that were approximately 10 x 10 x 2 mm to measure the out-of-plane thermal transport properties, and graphite suspension (GRAPHIT 33, Kontakt Chemie, Germany) was sprayed onto the faces of monolithic alumina as they were white/ivory in colour. The relationship between temperature and specific heat capacity was evaluated with a calorimeter (Calvet C80, Setaram, Spain) equipped with stainless steel crucibles. Measurements were carried out between 25 – 155 °C at a rate of 0.2 °Cmin⁻¹ with 2 hours of stabilisation at the initial and final temperatures, then data was extrapolated up to 750 °C. Data analysis was carried out with compatible software (Calisto, Setaram, Spain). The thermal conductivity, k , was then calculated from Equation 2.17.

$$k = \alpha \rho c_p \quad \text{Equation 2.17}$$

Where c_p is the specific heat capacity in J(gK)⁻¹, α is thermal diffusivity in cm²s⁻¹, and ρ is the density in gcm⁻³. The latter was determined using the method described in Section 2.3.2.2.

Chapter 3 Fabrication of large alumina scaffolds with directional porosity and the consolidation of alumina

During this Chapter an investigation into the fabrication of freeze-cast alumina scaffolds, and consolidation of ceramic materials are given. The preparation of large, freeze-cast alumina scaffolds between 20 – 40 wt.% ceramic loading is presented. One of the primary objectives is to create large ceramic scaffolds with pores that are aligned along one direction, therefore exploring the internal microstructure with respect to pore homogeneity and orientation is crucial during their evaluation. An appreciation of the porous architecture is also gained through μ -CT. Combined with pore diameter and lamellae thickness results from scanning electron microscopy, an argument is provided in the concluding remarks for porous scaffolds that are best suited for the following infiltration step. The final section involves Spark Plasma Sintering monolithic alumina specimens in which an optimal sintering temperature was determined, and the microstructure of a sintered, freeze-cast scaffold was interpreted.

3.1 Optimising internal architecture of large, freeze-cast alumina scaffolds

This section aims to demonstrate the results in upscaling the creation of porous materials with an appropriate internal structure that could mimic nacre and provide insight such that larger specimens may be fabricated in the future. Chapter 1 (Section 1.3.2) discussed previous work that fabricated composite materials using freeze-casting, which has the potential to create well-ordered and intricate microstructures inspired by the structures of natural materials, e.g., nacre. However, one was

processed with a different technique (MASC),⁹⁴ and another utilised a 15 mm diameter freeze-casting mould which is relatively small.⁸⁹ The target in this study is to fabricate larger freeze-cast materials (30 mm diameter, 35 mm height) that possess layers (lamellae) of material close to that of nacre, i.e., $\sim 0.6 \mu\text{m}$ thickness. To achieve the smallest lamellae thickness whilst still maintaining enough mass for larger-scale mechanical testing, optimisation of the solid loading of alumina suspensions has been carried out by freeze-casting specimens within a cylindrical mould. Therefore, several suspensions with varying solids content between 20 – 40 wt.% were prepared to identify an optimal loading for ceramic scaffolds that will serve as the final composite material's matrix. After further processing (including sintering), the final composite must have a minimum thickness of 2 – 3 mm so that larger scale testing can be performed – this is indicated in Figure 3.1 which illustrates the intended processing route. Fabricating larger specimens would also expand the potential applications of the final composite materials.

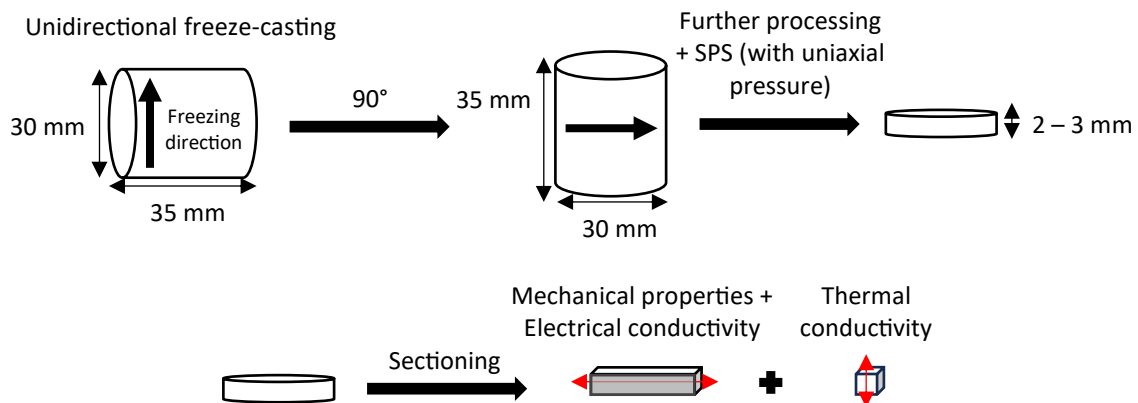


Figure 3.1 – Diagram of the developed processing route towards ceramic-graphene materials. The orientation of mechanical and functional testing on sectioned specimens is also illustrated. The grey face indicates where Vickers indentations would be created for measuring the hardness and fracture toughness. Red lines indicate the direction in which the electrical/thermal behaviour was measured.

3.1.1 Preparation of alumina suspensions

The objective in the casting stage was to freeze-cast a range of large alumina scaffolds with solid loadings between 20 – 40 wt.% to select the optimal loadings for subsequent GO infiltration. It was previously mentioned that these water-based formulations were chosen based on previous literature reports and contains alumina, DOLAPIX CE64 (a dispersing agent), PVA, and sucrose.^{105,116,157} Details on their addition with respect to either the ceramic powder or water can be found in Chapter 2, Section 2.1.1. However, before their preparation characterisation of the selected alumina powder was carried out to confirm such its composition and morphology.

3.1.1.1 Selection and characterisation of raw alumina

It seemed appropriate to select a starting material consisting of sub-micrometric particles as the aim is to mimic the thin layers observed in the structure of nacre. Thus, the layers of material made during freeze-casting would consist of these small particles. The review by Deville describes that small grain sizes are key to fabricating freeze-cast materials with fine and intricate architectures, i.e., >100 μm pore sizes.¹⁰³ BA15-W alumina powder (described in Chapter 2, Section 2.1) was selected due to its composition of 100 % α -phase and possession of a sub-micrometric grain size. Prior to any fabrication, it was critical that the starting material was characterised. Therefore, a study on BA15-W was conducted to validate the size of individual particles and to confirm that there are no other phases present. The as-received alumina powder was accompanied by a certificate of analysis from the manufacturer's R&D department, specific to the batch it was taken from. Details of the particle size distribution were provided, along with trace elements (detected using ICP-OES) that are shown in Table 3.1. According to dry laser diffraction analysis the d_{50} of alumina is 47.8 μm , whereas wet analysis gave a far smaller d_{50} of 0.12 μm .

Table 3.1 – List of trace elements and their concentrations found in BA15-W (provided by the manufacturer).

Element	Concentration (ppm)
Ca	6.9
Cr	<1.0
Fe	5.1
K	14.6
Mg	1.0
Na	10.8
Si	6.9

SEM analysis performed on the α -alumina powder is displayed in Fig. 3.2. It was realised that the as-received powder are spherical agglomerates of alumina between 15 – 150 μm in diameter. Their morphological appearance is consistent with a spray-drying process that the manufacturer utilised to create spherical agglomerates from a fine powder. These spherical agglomerates are comprised of finer, sub-micrometric particles that are approximately $0.13 \pm 0.01 \mu\text{m}$ in size, visualised after some processing: this involved 1 minute of ultrasonic processing, followed by freezing and drying to isolate individual particles. The particle size distribution (Fig. 3.3) is also consistent with the manufacturer’s data and the results obtained from SEM; the sizes of the ceramic agglomerates lie between 15 and 144 μm , and the d_{50} value was found to be 51.8 μm . These results illustrate that, prior to casting, as-received agglomerates had to broke down to disperse the individual ceramic grains.

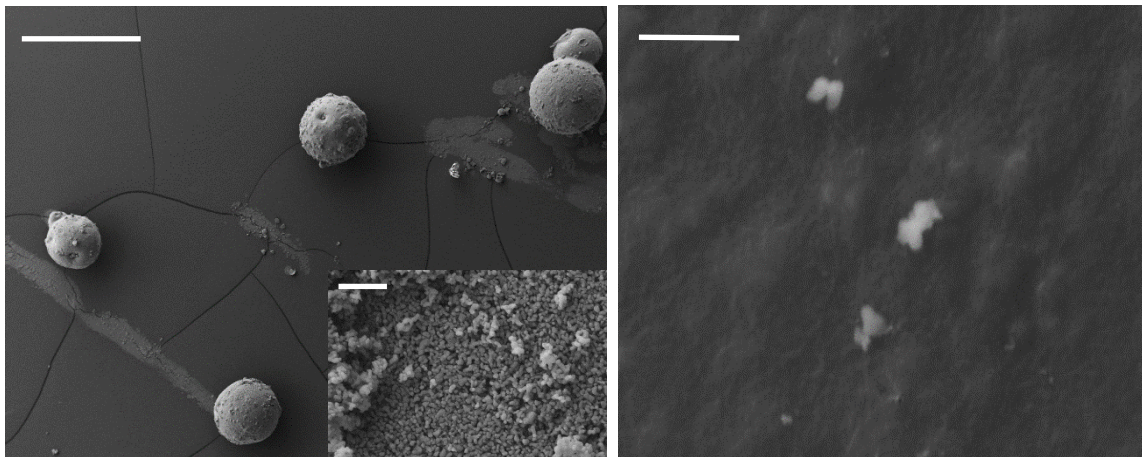


Figure 3.2 – Left) SEM image of as-received BA15-W alumina. Scale bar = 50 μm . Inset – higher magnification at the surface of an agglomerate. Scale bar = 1 μm . **Right)** SEM of individual grains after ultrasonic dispersion. Scale bar = 500 nm.

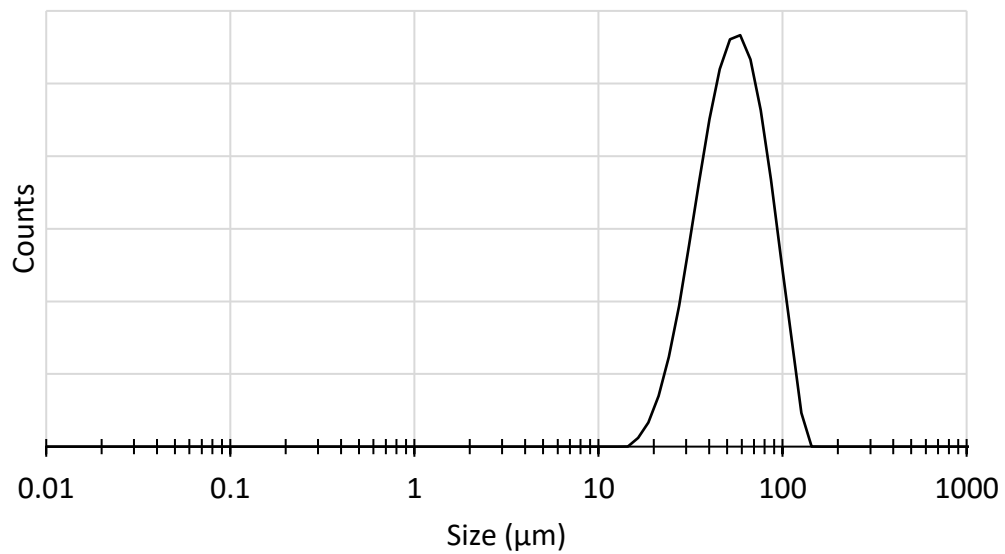


Figure 3.3 – Particle size distribution of as-received BA15-W alumina powder.

The XRD pattern shown in Fig. 3.4 confirms the presence of α -phase alumina compared against a provided reference, with major peaks at 2θ values of 25.44, 35.08, 37.70, 43.19, 52.50, 57.39, 61.09, 66.45, 68.12, and 76.83. There are three very small peaks (41.64, 59.65, 74.33) that are also accounted for in the reference for α -alumina which are lost slightly within the background signal. It could be argued that these belong to another phase of alumina, however, there are no other prominent peaks that suggest the presence of different alumina phases (γ , κ , δ).¹⁹¹ The weak, noisy region between 5 – 18 values of 2θ can be attributed to the specimen holders that were made from 3D-printed polylactic acid.^{192,193} It can therefore be concluded that this diffraction pattern is representative solely of the α -phase.

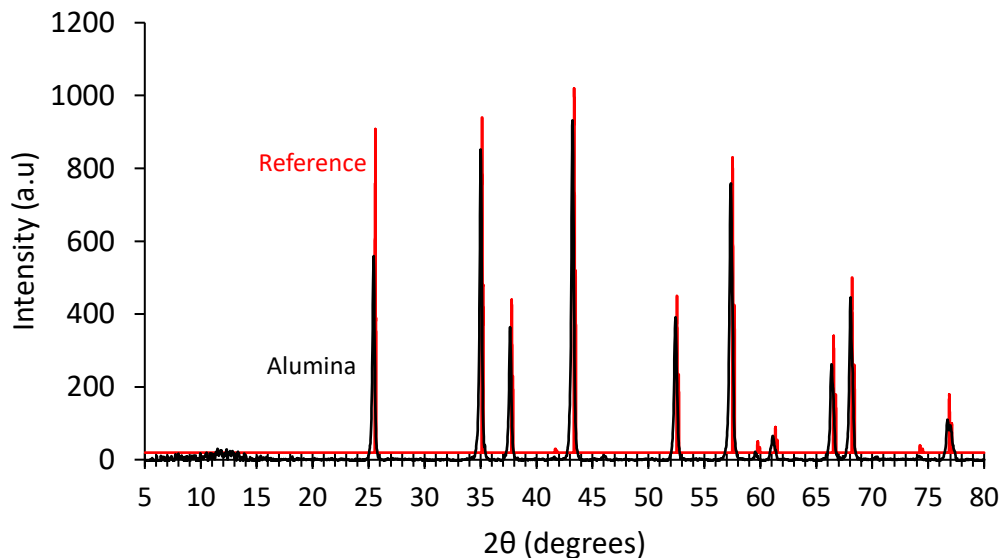


Figure 3.4 – X-ray diffraction pattern of as-received BA15-W alumina powder with ICDD reference 00-005-0712 for comparison.

3.1.1.2 Verification of the dispersion of starting alumina powder

This sub-section provides verification that the spherical agglomerates of BA15-W alumina powder are dispersed during ultrasonication. This was carried out for ceramic suspensions of 20, 30, and 40 wt.%. To determine an optimal time for sonication, a preliminary test was carried with a suspension of alumina containing a ceramic loading of 30 wt.% and sonication periods up to 10 minutes. During this investigation the suspensions of alumina also contained the dispersant (DOLAPIX CE64) at 0.5 wt.% with respect to the ceramic loading but did not possess the remaining casting additives (PVA and sucrose). Fig. 3.5 illustrates that a period of 2 minutes is sufficient time to produce a suspension of individual, sub-micrometric particles. However, 5 minutes of sonication produces a slightly narrower distribution. After 5 minutes, the temperature had increased from 17.7 to 35.2 °C. This result is akin to the distribution obtained for 10 minutes of sonication, but this amount of time may have a negative effect as the overall temperature of the suspension rose higher (from 17.8 to 43.1 °C) during this extended period. A report on the effects of sonication states that a rise in temperature can improve the dispersion of agglomerates,¹⁹⁴ and large increases may have unexpected outcomes such as water evaporation. Therefore, direct ultrasonication for a period of 5 minutes was carried forward to process suspensions containing varying ceramic content. Particles are found to be smaller than 1 μm, with corresponding d_{50} values of 0.1 μm for all tested suspensions. This agrees with the manufacturer's data for wet analysis of BA15-W alumina and provides evidence towards the dispersal of agglomerates into individual particles of alumina.

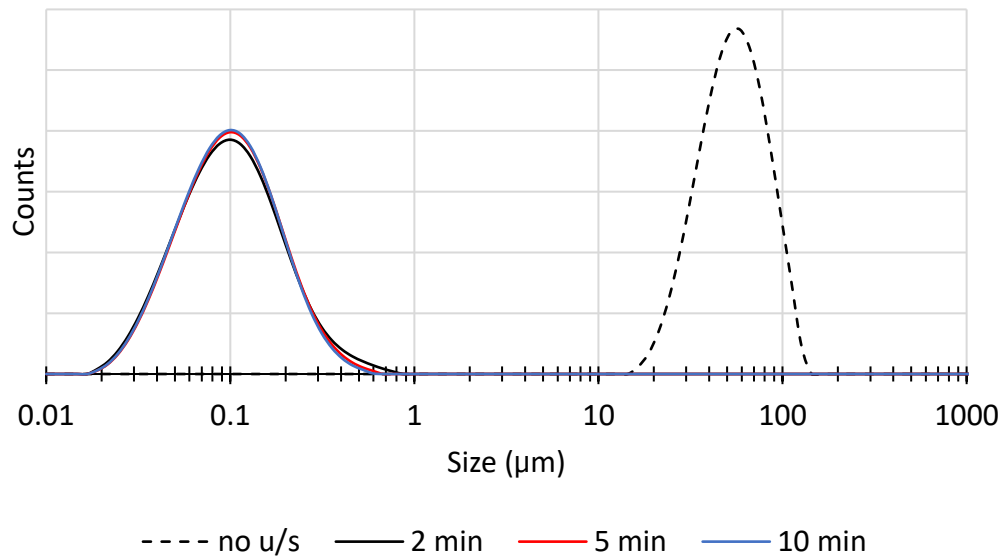


Figure 3.5 – Particle size distribution of a 30 wt.% BA15-W suspension processed with various periods of direct ultrasonication. The dashed line represents the size distribution of the raw alumina powder without any sonication.

Additional suspensions with ceramic loadings of 20 and 40 wt.% were then investigated to confirm that the dispersal of agglomerates is similar across the ceramic loading range that has been selected. The particle size distributions shown in Fig. 3.6 illustrate a vast decrease from the size of agglomerates into individual grains after 5 minutes of ultrasonication in all three suspensions. The three size distributions are similar in their appearance which suggests that alumina suspensions with various solid loadings between 20 – 40 wt.% only contain sub-micrometric particles (with 0.1 μm average) after they undergo ultrasonication.

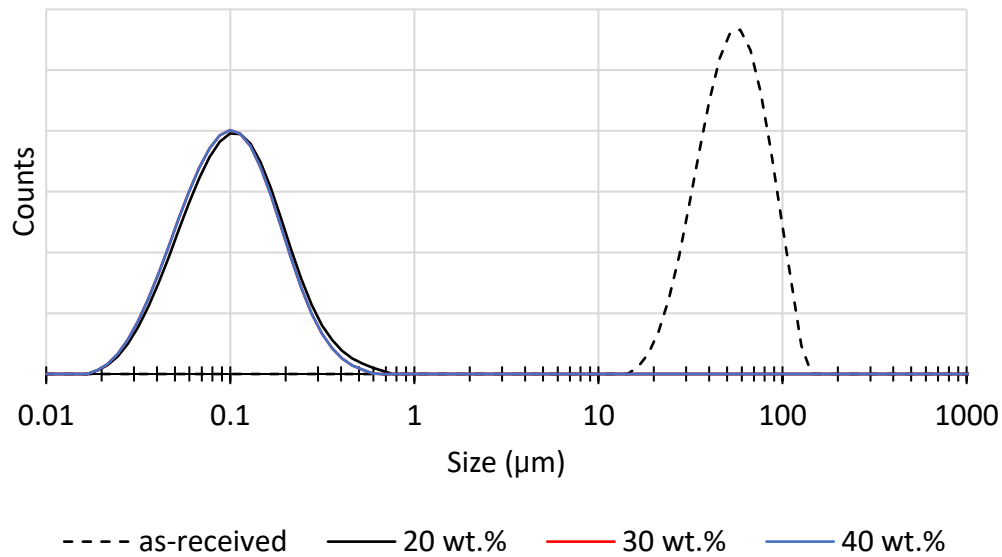


Figure 3.6 – Particle size distributions of BA15-W suspensions with various ceramic loadings after processing with direct ultrasonication for 5 minutes. The dashed line represents the size distribution of the raw alumina powder.

Fig. 3.7 illustrates separate results for a 30 wt.% suspension that possesses no dispersant, i.e., DOLAPIX CE64, in which particles with varying degrees of size can be observed. Ceramic agglomerates are broken down to a lesser degree ($d_{50} = 9.9 \mu\text{m}$), and the individual, sub-micrometric grains do not stay separated. This is evident by the changes in the particle size distribution which illustrates six measurements taken successively (10 seconds apart). This demonstrates the fact that the low concentration of dispersant molecules is supporting the stabilisation of sub-micrometric alumina grains in all three solid loadings that were tested. This is vital for the freeze-casting of fine architectures and maintaining a suspension that will not settle during the casting period.

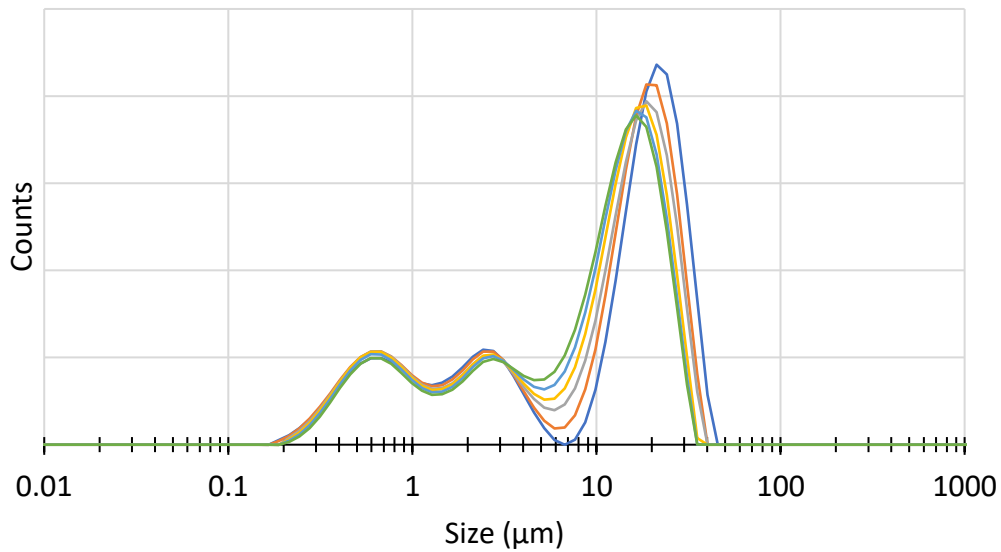


Figure 3.7 – Particle size distribution of a 30 wt.% alumina suspension without the addition of dispersant after processing with direct ultrasonication for 5 minutes. The 6 scans are not processed to illustrate changes to the particle sizes over time, beginning with the result in blue.

3.1.2 Processing ceramic scaffolds through unidirectional freeze-casting

3.1.2.1 Appearance and densities of freeze-cast alumina scaffolds

After the verification of agglomerate breakdown, unidirectional freeze-casting of alumina suspensions between ceramic loadings of 20 – 40 wt.% was carried out. All three casting additives (DOLAPIX CE64, PVA, and sucrose) are present in the ceramic suspensions. PVA solutions have been found to increase the viscosity of casting suspensions at small concentrations and improve the mechanical strength of freeze-cast materials.¹¹⁶ Sucrose has two functions which are: i) modifying the crystallisation process as the liquid volume freezes, and ii) improving the surface topology of the

lamellae of freeze-cast materials.¹⁰⁵ After freeze-drying, cast materials were approximately 30 mm in diameter and 35 mm in height with variations from scaffold to scaffold. One can visually ascertain that there are channels running in parallel with the faces of the cylindrical bodies, produced via the custom-made mould that was illustrated in Chapter 2, Section 2.1.2. The following images illustrate examples of the scaffolds fabricated scaffolds between the chosen solid loading range. Fig. 3.8 exhibits a 30 mm freeze-cast scaffold produced from a suspension containing 25 wt.% ceramic loading, showcasing its large size and the quality of fabrication. On the other hand, Fig. 3.8 illustrates that as the solid loading increased to 35 wt.% ceramic content and above, the quality of freeze-cast materials diminished slightly. Many of the cylindrical scaffolds became contorted in their shape with the sides of the scaffolds appearing concaved.



Figure 3.8 – Photographs of alumina scaffolds after freeze-drying. **Left)** comparison of a 25 wt.% alumina scaffold with a 2 pence coin. **Middle)** view of surface that is exposed from mould. **Right)** view of surface that contacts the copper bottom inside the mould.

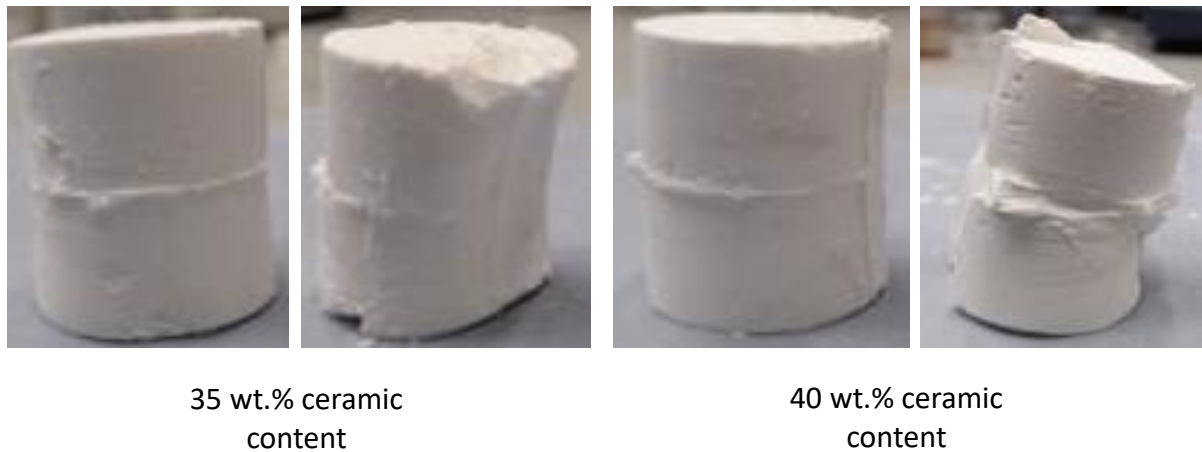


Figure 3.9 – Photographs illustrating inconsistencies in the geometries of some of the ceramic scaffolds cast from moderate ceramic loadings.

3.1.2.2 Effect of pre-sintering alumina scaffolds

Pre-sintering is the process of heating a specimen to a temperature below its typical sintering temperature and is commonly used to improve an object’s mechanical properties so that it may undergo further processing.¹⁹⁵ This occurs because of the partial coalescence of neighbouring grains by virtue of neck formation between the particles. In freeze-cast objects, additives that include binders and dispersants may also exist which can be released from their porous structure. In their current state, the freeze-cast materials may be referred to as “green bodies” which was mentioned in Chapter 1, Section 1.1.1. They are very fragile and susceptible to damage,^{18,104,196} so it is vital that these delicate structures are handled with care to avoid their collapse by mishandling them. The organics (sucrose, PVA, DOLAPIX CE64) added in their preparation are unwanted in the final, sintered materials because they would leave carbon residue within their internal microstructure if they remained. They become volatile at high temperatures and can be removed in a facile manner. This is demonstrated in Fig. 3.10 by a change in mass after pre-sintering alumina scaffolds at 900 °C for 30 mins. Once pre-sintering was carried out, alumina scaffolds lose a small portion of their weight (approximately 1 g) due to the removal of the additives.

The amount of sucrose is similar in each formulation as it is with respect to the mass of water, however there is small increases (<100 mg) in the amount of PVA and DOLAPIX CE64 utilised in the suspension preparation. Although, these small changes are not reflected in the calculated mass after pre-sintering.

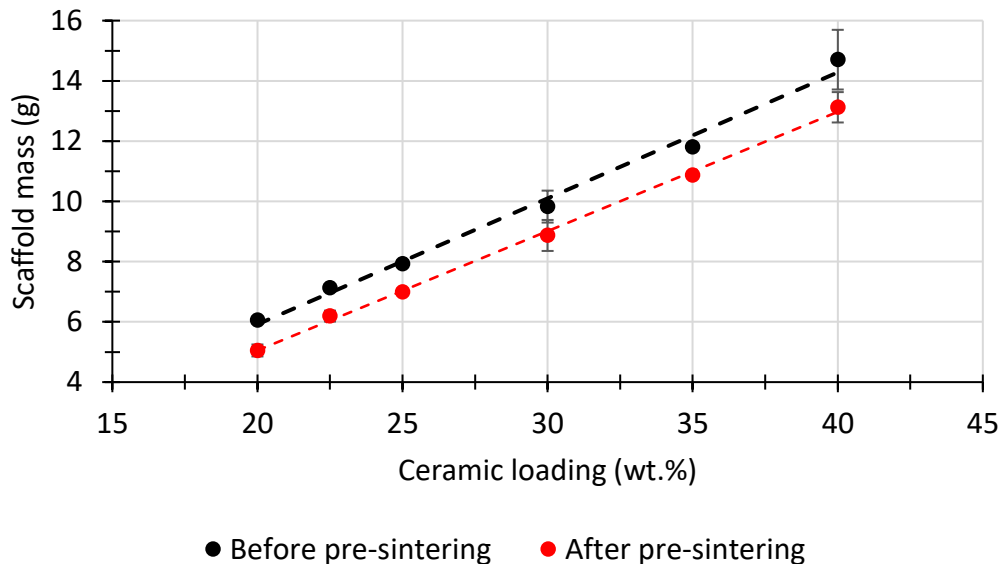


Figure 3.10 – Masses of freeze-cast alumina scaffolds before and after pre-sintering at 900 °C for 30 mins in air for a range of ceramic loadings. It should be noted that the result at 27.5 wt.% ceramic loading is indicative of only one specimen.

Fig. 3.11 shows the apparent densities and porosities that were calculated using specimens' geometric volume before and after pre-sintering. Freeze-cast materials created from 20 – 40 wt.% solid loadings of alumina possess very low bulk densities. This ranges between 0.25 – 0.59 gcm⁻³ before pre-sintering and decreases slightly to between 0.21 – 0.51 gcm⁻³ after the pre-sintering treatment. This also increases linearly with increasing ceramic content. The calculated porosities are substantial, reaching >85 % for all solid loadings and >90 % above 35 wt.% after pre-sintering. This is commonly seen in the literature for freeze-cast materials fabricated from low solid loadings which is well presented in the review by Deville.¹⁰³ The standard

deviation is more prominent at higher ceramic loadings, which correlates with the less consistent casting that was illustrated in Fig. 3.9.

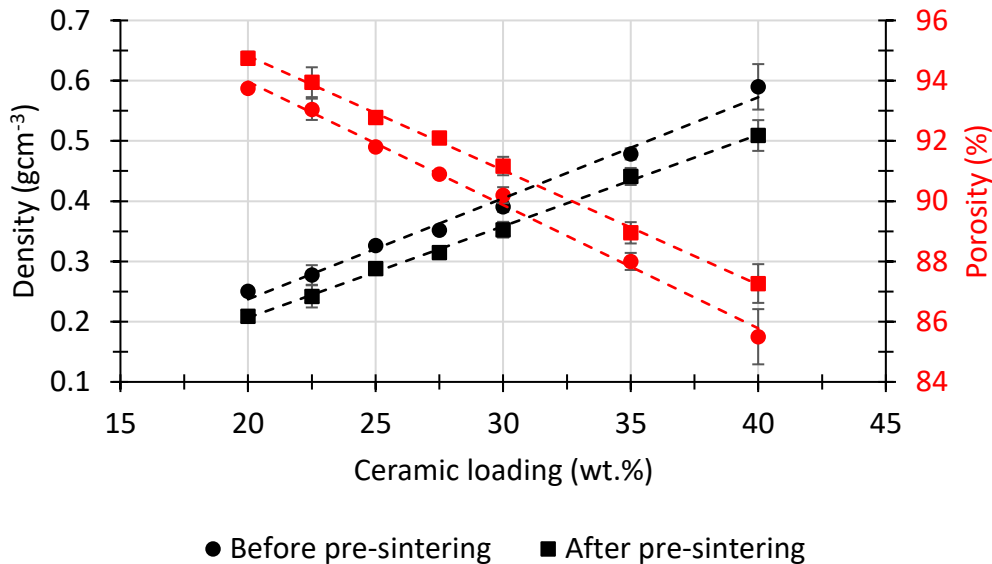


Figure 3.11 – Calculated densities and porosities of freeze-cast alumina cast alumina for a range of ceramic loadings.

3.1.3 Understanding internal architecture of large freeze-cast materials

Prior to infiltration with a filler material, understanding the ceramic scaffolds' internal microstructure with respect to the size and morphology of the host's architecture is advantageous. Understanding the pore geometry is one of the main focuses, however, their orientation and homogeneity throughout a large volume (30 mm diameter) is also a key aspect of this study. The use of μ -CT is highly beneficial due to its non-destructive nature, and some instrumentation have the capacity to image large entities, e.g., up to 300 mm inside the equipment utilised in this work. Although μ -CT was carried out, this technique is moderately time-consuming and expensive, and it would not have been feasible to investigate every freeze-cast structure that was

fabricated. Therefore, some scaffolds were cut and sectioned so that the pore size and lamellae thickness could be evaluated by SEM from the central core of each scaffold. This was conducted first to determine a suitable solid loading to focus on. As this fabrication strategy aims to process bulk composite materials, with the components themselves arranged in a particular fashion, identifying any defects in the long-range ordering of the host material will assist in future design considerations. Defects may include differences in the lamellae (wall) thickness and pore spacing of the architecture generated in the casting stage.

3.1.3.1 Architectural features of freeze-cast structures

Fig. 3.12 shows SEM images of pre-sintered, porous architecture that remained after the casting-drying process. Labels of freezing direction (FD), pressing direction (PD), and cross section (CS) have been designated to the three planes of freeze-cast pre-forms which will be utilised throughout the remainder of this document. The height of the scaffold was defined as PD as these materials will be uniaxially compressed during later SPS cycles. Scaffolds are predominantly comprised of long, thin lamellae in the freezing direction separated by pores in which ice crystals were sublimated from (during the drying process). The long-range, lamellar appearance of the solid walls is a result of using water as a solvent and a controlled freezing rate.^{103,104,197} A few ceramic bridges connecting the internal walls of the scaffold across the cross sectional plane. In addition, some randomly aligned ceramic domains can be identified which are typically seen in other ceramic structures processed through water-based, unidirectional freeze-casting.^{104,106}

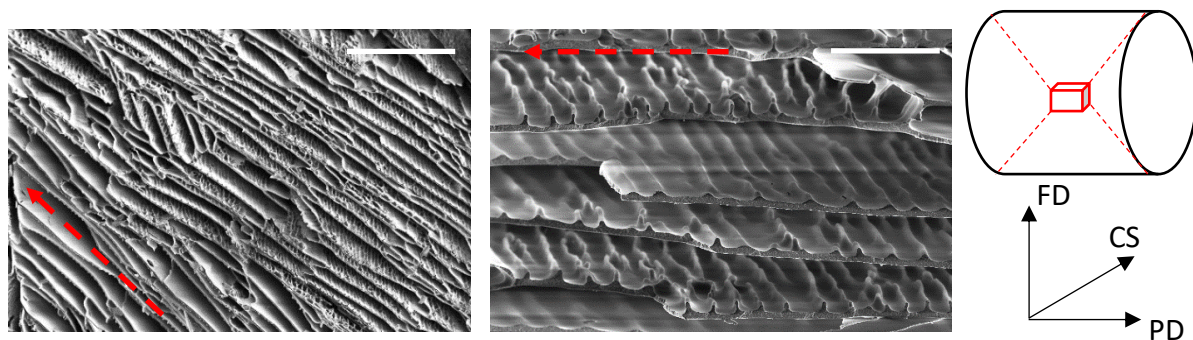


Figure 3.12 – SEM images of freeze-cast architecture produced from a 25 wt.% alumina suspension. **Left)** low magnification image through the CS axis. Scale bar = 500 μm . **Middle)** high magnification image that exhibits the surface roughness of ceramic lamellae. Scale bar = 100 μm . Red, dashed lines represent FD. **Right)** diagram representing the three planes that were defined.

SEM images were utilised to estimate the average pore size and lamellae thickness in freeze-cast materials. Fig. 3.13 displays how the two properties were measured and Fig. 3.14 illustrates the size distribution of lamellae thicknesses in scaffolds fabricated with different ceramic contents. For scaffolds created from 25, 35, and 40 wt.% ceramic loadings, it was determined that: i) there is no major difference in the average pore diameter upon increasing the ceramic content (41 μm to 37 μm), and ii) simultaneously, the average thickness of lamellae rises significantly (5 μm to 15 μm). The pore size is roughly similar as this is predominantly affected by the freezing rate which was identical for each scaffold that was studied (5 $^{\circ}\text{Cmin}^{-1}$).^{91,103} The increase in lamellae thickness is noted in other work and correlates with the increase in solid loading of ceramic material causing the growth of thicker walls during particle rejection from the solidification front.⁹¹ The increase in average lamellae thickness with increasing ceramic loading can be clearly seen and the distribution of lamellae thicknesses also broadens. As scaffolds fabricated from 25 wt.% suspensions possess a narrower distribution of thinner lamellae thicknesses the focus of the following $\mu\text{-CT}$ characterisation utilises one scaffold made with this formulation.

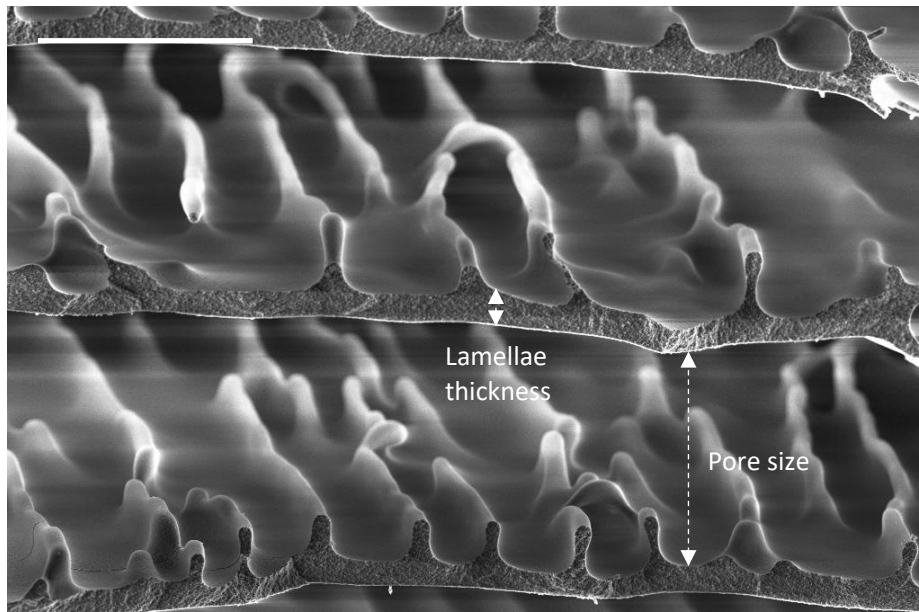


Figure 3.13 – SEM image of a freeze-cast scaffold illustrating how the pore size and lamellae thickness was measured. Scale bar = 50 μm . This was conducted for 25, 35, and 40 wt.% alumina scaffolds.

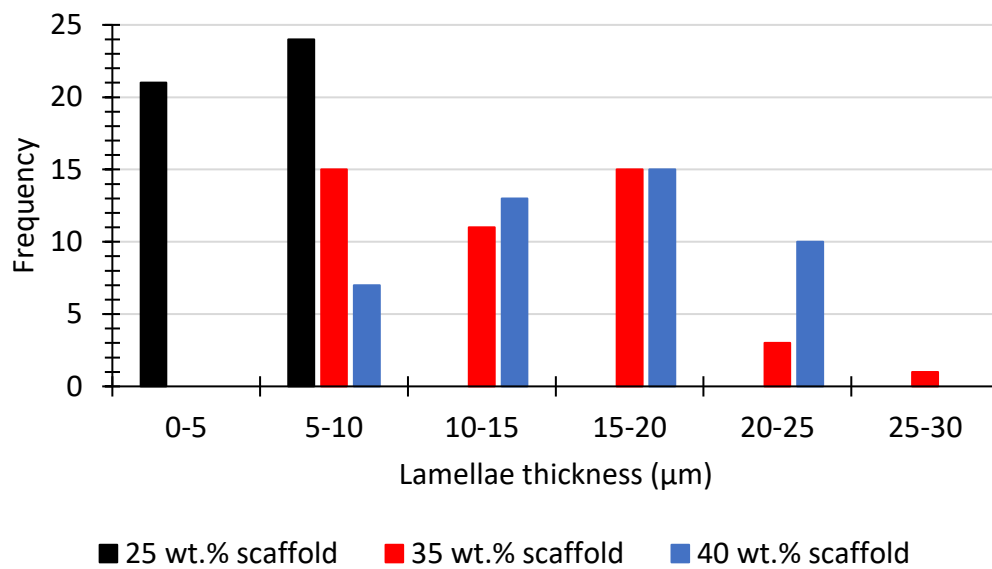


Figure 3.14 – Frequency distribution of the lamellae thicknesses within the core region of some porous, alumina scaffolds.

3.1.3.2 Visualisation through μ -computed tomography

It was possible to visualise an entire, 30 mm freeze-cast scaffold using μ -CT (Fig. 3.15e and 3.15f), however the voxel resolution ($4.52 \mu\text{m}$) was partially sacrificed.

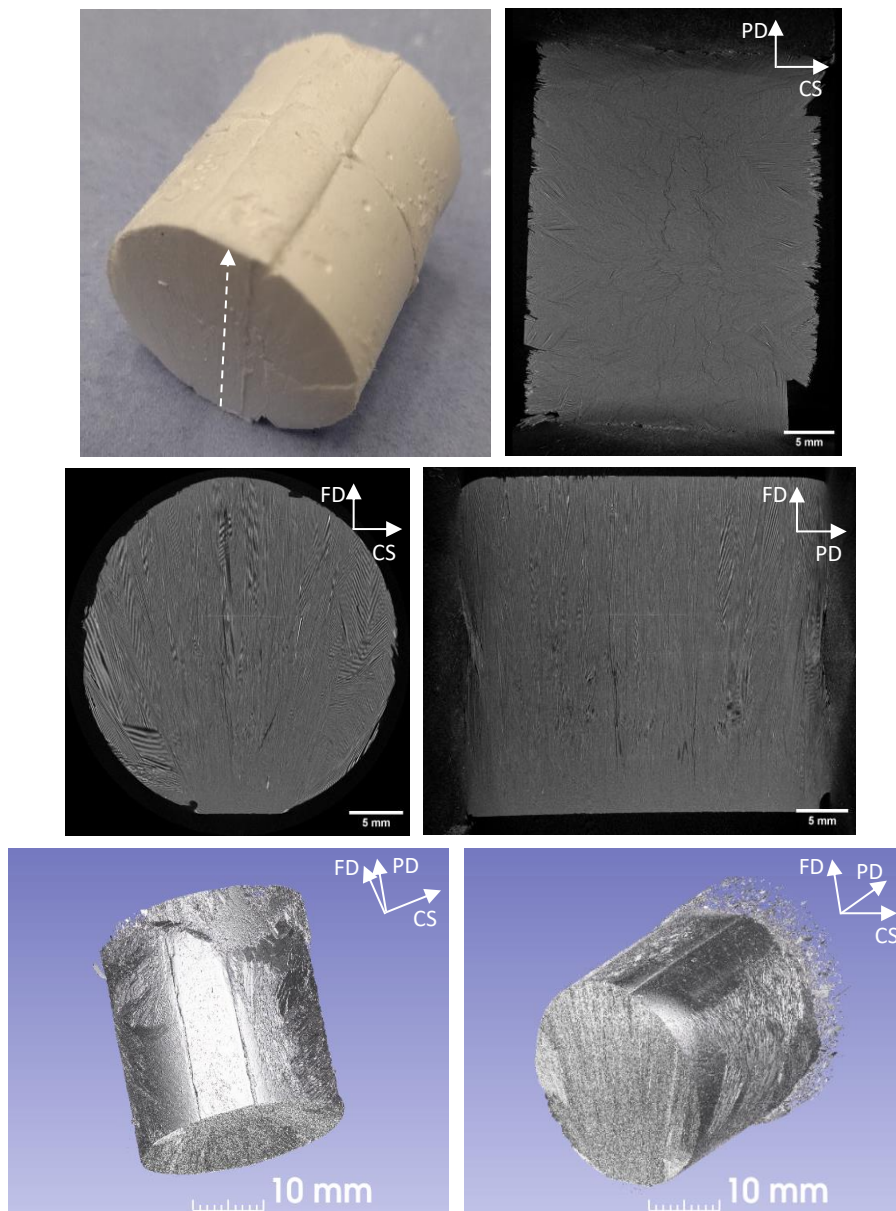


Figure 3.15 – **a)** photograph of a 25 wt. % alumina scaffold. **b), c)** and **d)** cross-sectional μ -CT images of the alumina scaffold along various planes. **e)** and **f)** μ -CT 3D reconstructions of the alumina scaffold. The dashed white line in **a)** represents the direction of freezing.

In the cylindrical structure, alumina lamellae are oriented along the FD axis which can be easily identified in Fig. 3.15c and 3.15d. The regular patterning of the lamellae in this fashion is indicative of unidirectional freeze-casting, and it has been stated previously that numerous channels (both the pores and solid walls) possess a lamellar appearance due to water-based processing. Randomly aligned domains that were observed in the previous sub-section can also be visualised across the entirety of the cylindrical entity (seen in Fig. 3.15b). However, there is a fan-like appearance to the ceramic lamellae following the FD axis: towards the sides of the freeze-cast material, there is deviation from the freezing direction (as much as 30°). It must also be highlighted that there is a section of the scaffold that does not appear to be porous unlike the rest of the freeze-cast pre-form which is displayed in Fig 3.16 from our results.

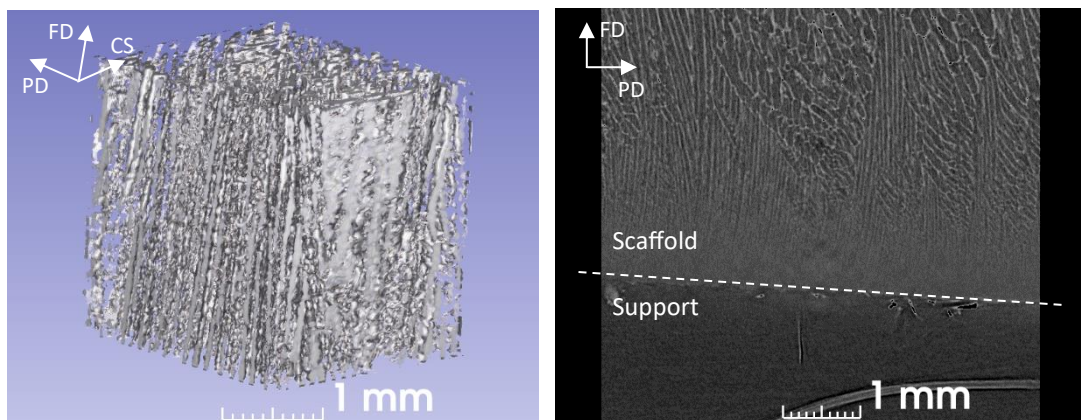


Figure 3.16 – Left) 3D reconstruction of the core region of the alumina scaffold. **Right)** high-resolution, cross-sectional image illustrating the dense, solid region that exists in freeze-cast materials.

This region of material is located at the “bottom” of scaffolds (along PD) which contacts the freezing surface during the casting procedure. This would signify a rapid solidification front which entraps the ceramic particles, as opposed to rejecting them from the freezing front.^{91,103} Therefore, particles do not congregate between the growing ice crystals and solid walls that follow FD will not be generated. Authors have identified this initial boundary layer (or zone) previously in computational and

experimental studies.^{159,198,199} The dense region is a result of the build-up of particles during the formation of the solidification front which, over time, forms a steady state to generate homogenous ice crystals.

3.2 Exploring the consolidation of alumina via Spark Plasma Sintering

It was mentioned in Chapter 1 (Section 1.1.2) that several factors can affect the extent of consolidation of ceramic materials: this includes (but is not limited to) temperature, particle size, dwelling time, heating/cooling rates, and the atmosphere it takes place within (i.e., reducing, oxidising, inert environments). In the case of SPS the influence of applying uniaxial pressure must also be considered. From studies in a previous PhD project performed at Cardiff University which consolidated smaller alumina specimens (of 20 mm diameter), a sintering procedure for SPS was trialled with BA15-W alumina powder to identify its potential for creating dense, 30 mm specimens. Once a procedure was found that consistently generated unbroken alumina materials, the influence of sintering temperature on the density and grain size was investigated. The consolidation of a freeze-cast scaffold was also carried out early in the experimental investigations using the trial conditions to understand if alignment of ceramic material can be achieved without a filler material and how the processing has affected the microstructure.

3.2.1 Optimising the consolidation parameters of as-received alumina

3.2.1.1 Preliminary sintering conditions

The first set of sintering conditions were as follows: a sintering temperature of 1300 °C, an applied pressure of 60 MPa, a dwell time of 1 minute, a heating rate of 100 °Cmin⁻¹, and a natural cooling step. The DC pulse sequence was set as 10-5-12-2. It was previously stated that these conditions were used first based on a PhD project previously conducted at Cardiff University. Fig. 3.17 shows SEM images of a fracture

surface and the appearance of a fine, sub-micrometric grain size. However, the alumina specimens obtained with these conditions had broken into multiple pieces during the consolidation process: this is likely attributed to the low thermal shock resistance of alumina. As the material cools, if there are fluctuations in the temperature throughout the specimen, this can impose internal stresses which could lead to cracking.^{200,201} Three main complications were realised using the aforementioned conditions: i) alumina materials were not fully dense, reaching a maximum value of 3.93 gcm^{-3} (98.5 % T.D), ii) specimens were prematurely fracturing during the sintering process, and iii) the chosen pressure (60 MPa) was causing the graphite tooling to prematurely break now and again.

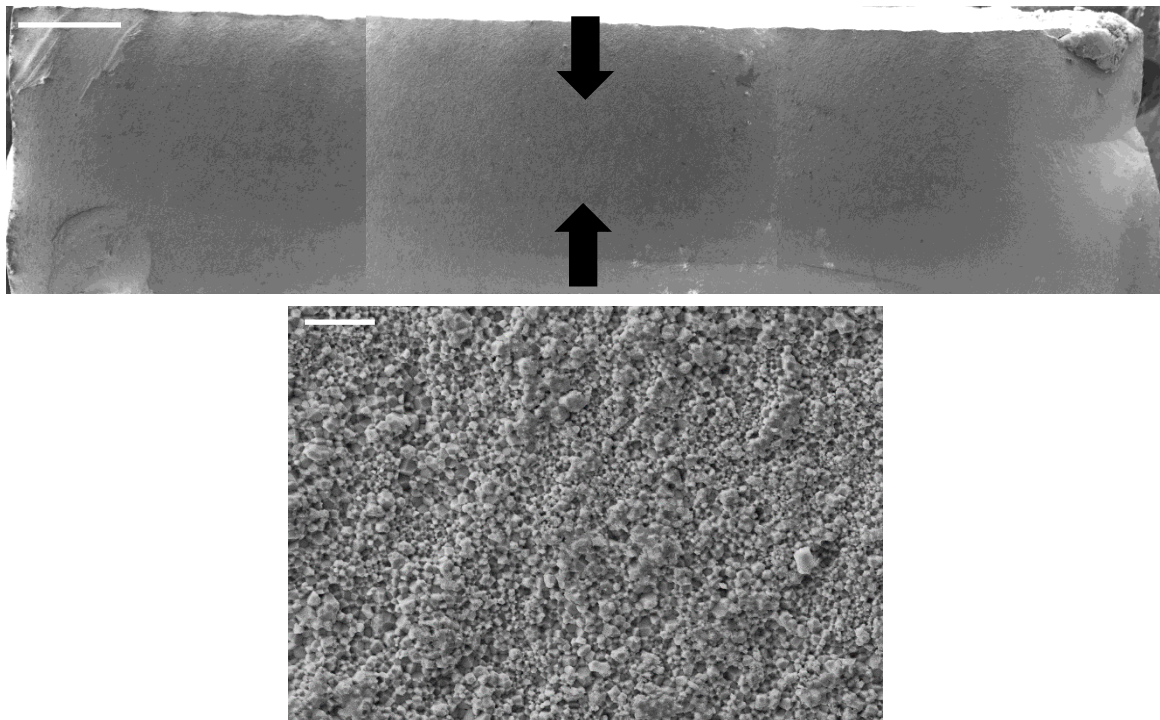


Figure 3.17 – SEM images of alumina sintered using SPS from as-received powder at 1300 °C, 60 MPa, $100 \text{ }^\circ\text{Cmin}^{-1}$ heating rate, natural cooling, a 1 min dwell. **Top)** overall fracture surface. Scale bar = 1 mm. Black arrows represent the direction of pressing. **Bottom)** high magnification image. Scale bar = 10 μm .

To alleviate the issues that were experienced with the preliminary conditions, the sintering procedure was re-evaluated. First, the pressure was dropped from 60 to 50 MPa – a compressive strength test demonstrated that the manufactured, 30 mm graphite punches could not withstand a maximum force of more than 45.4 kN (~ 64 MPa). Secondly, the dwell time was extended from 1 to 5 minutes as the prior specimens were not fully dense ($< 99\%$ T.D). Furthermore, to improve the homogeneity of the temperature throughout the core region of 30 mm specimens the heating and cooling rate were set to $50\text{ }^{\circ}\text{Cmin}^{-1}$, and the DC pulse sequence was altered from 10-5-12-2 (pulsed) to 1-0-1-0 (continuous). This change of parameters to slower and milder conditions resulted in the production of unbroken, 30 mm specimens fabricated from as-received BA15-W powder (Fig. 3.18). Using approximately 6.5 g of material, a sample of ~ 2.2 mm thickness is obtained. The average density based on 5 specimens was determined to be 3.96 gcm^{-3} (99.2 % T.D) which can be considered as fully dense.



Figure 3.18 – Photographs illustrating the comparison between sintered alumina specimens. **Left)** preliminary sintering conditions. **Right)** modified conditions using a continuous DC pulse sequence, lower pressure, and lower heating/cooling rates. Scale bar = 10 mm.

3.2.1.2 Influence of sintering temperature

Once monolithic alumina was fabricated more consistently through continuous DC sequencing, optimisation of the sintering temperature was carried out to evaluate the density and grain growth of alumina specimens. The selected temperature range was between 1000 – 1400 °C in increments of 100 °C. It was mentioned in Chapter 1 (Section 1.1.2) that fully dense alumina had been consolidated with small amounts of dopant at a temperature of 1150 °C,³⁵ however a study by Shen *et al.* illustrated the potential for monolithic alumina with a grain size of 0.4 µm to be consolidated through SPS to near theoretical density (>99 % T.D) at and beyond temperatures of 1250 °C with fast heating rates.²⁰² The investigation by Santanach *et al.* on the consolidation of non-doped alumina powder (5 µm aggregates consisting of 0.14 µm particles) demonstrated that increasing the temperature over 1300 °C has little effect on the density of the fabricated ceramics except for changes in the growth of grains.²⁰³

Table 3.2 illustrates that BA15-W alumina powder densifies to near theoretical density at and above a sintering temperature 1300 °C. The remaining parameters were as follows: a pressure of 50 MPa, heating and cooling rates of 50 °Cmin⁻¹, a dwell time of 5 minutes, and a continuous pulse sequence (1-0-1-0). The trend of increasing density with rising sintering temperature is noticeable and is detected in other literature studies that have consolidated alumina powders with various starting grain sizes.²⁰²⁻²⁰⁴ However, the result at 1200 °C appears to be inconsistent considering that the density is marginally lower than that of specimens sintered at 1000 °C. Fig. 3.19 illustrates these results with respect to the sintered specimens' porosity and it is clearly visible that the calculated porosity of alumina consolidated at 1200 °C (average porosity of 3.3 %) is unexpected. The standard deviation is no more than 0.07 % in all five results which signifies there was little difference between measurements.

Table 3.2 – Table of density measurements for alumina specimens sintered with increasing temperature.

Sintering temperature (°C)	Density (gcm ⁻³)	Relative density (%)
1000	3.87	97.0
1100	3.93	98.5
1200	3.86	96.7
1300	3.96	99.2
1400	3.97	99.5

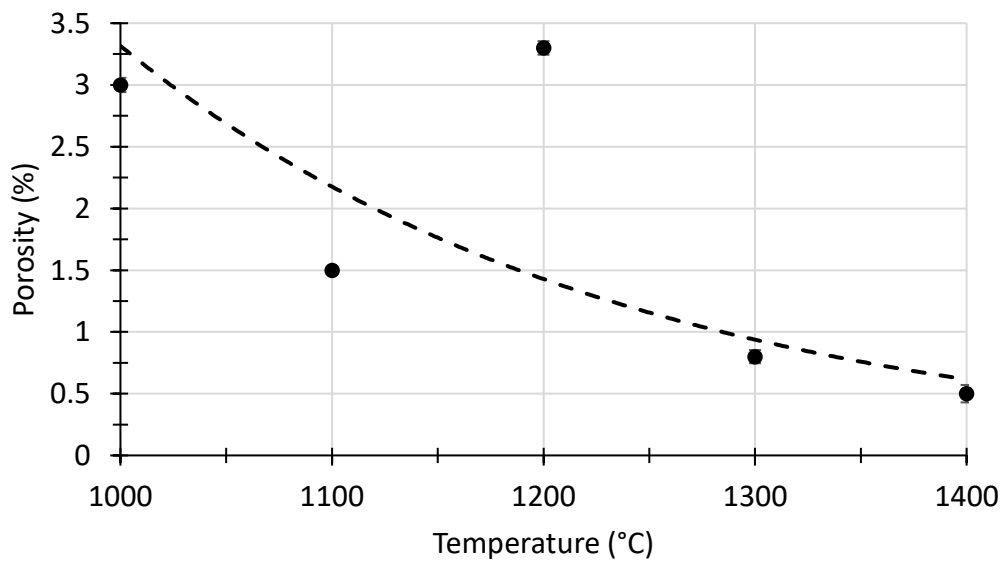


Figure 3.19 – Plot of calculated porosities for alumina specimens sintered with SPS at different temperatures.

To support the density results, analysis of the piston speed with respect to temperature up to the dwelling segment is presented in Fig. 3.20, providing more insight into the consolidation process. The data shows that in all alumina specimens the consolidation process begins at 900 °C. Also, it is evident that for alumina sintered at 1000 and 1100 °C there is less compaction than specimens sintered at 1200 °C and above because the piston speed does not reach maximum curvature before the dwelling segment. However, the data for specimens sintered at 1200 °C suggests that their consolidation has not progressed as far as those sintered at 1300 or 1400 °C because the piston speed is still in decline once the dwell point is reached. The piston speed in the latter two results reaches a value close to zero before the dwell commences, suggesting that the densification of alumina has completed. This does correlate with the calculated porosity results from the density data, except for the material sintered at 1200 °C which would be expected to possess a higher density than what has been measured.

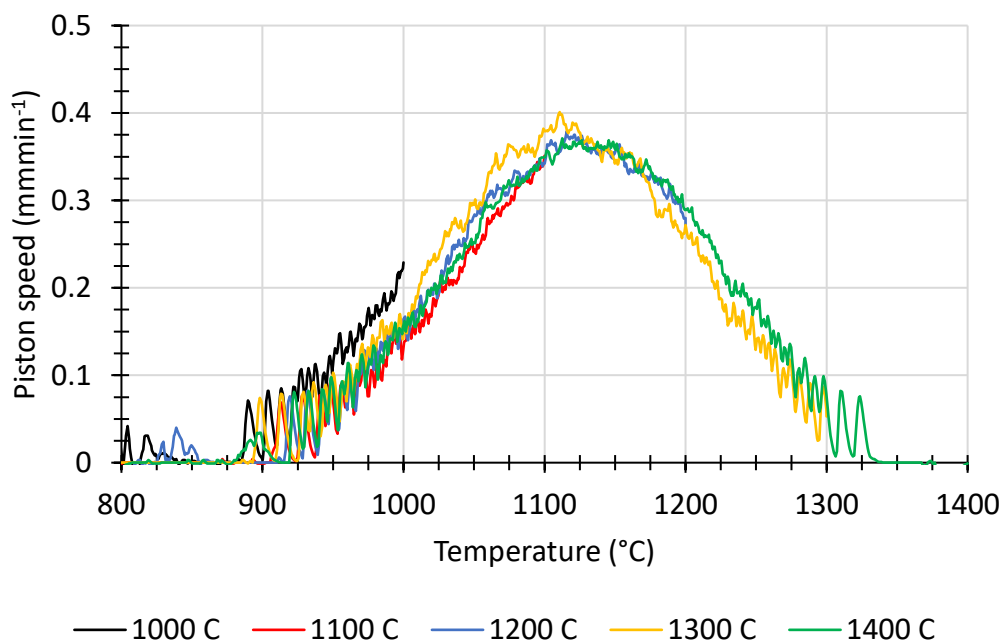


Figure 3.20 – Plot of piston speed versus temperature up to the dwell from the SPS programs used for alumina specimens sintered with increasing temperature. The remaining conditions were 50 MPa, 50 Cmin⁻¹ heating/cooling rates, 5 min dwell.

Further data was gathered by SEM from fractured surfaces of alumina specimens and temperatures of 1200, 1300, and 1400 °C to provide a visual comparison of their microstructure that can be paired against the porosity results. Fig. 3.21 illustrates the internal microstructures of alumina materials between 1200 – 1400 °C. Here, it is apparent that the ceramic grains within monolithic alumina have grown with increasing temperature. In addition, there are fewer observable pores with increasing temperature. The microstructure of the specimen sintered at 1200 °C is fine with limited grain growth, but porous in many regions with multiple grains that are not bound together. The measured grain size of the material sintered at 1300 °C are higher than those observed in the microstructure of alumina sintered with the preliminary sintering conditions, but this material possess a density closer to its theoretical value (3.96 gcm^{-3} compared to 3.93 gcm^{-3}) which is more favourable.

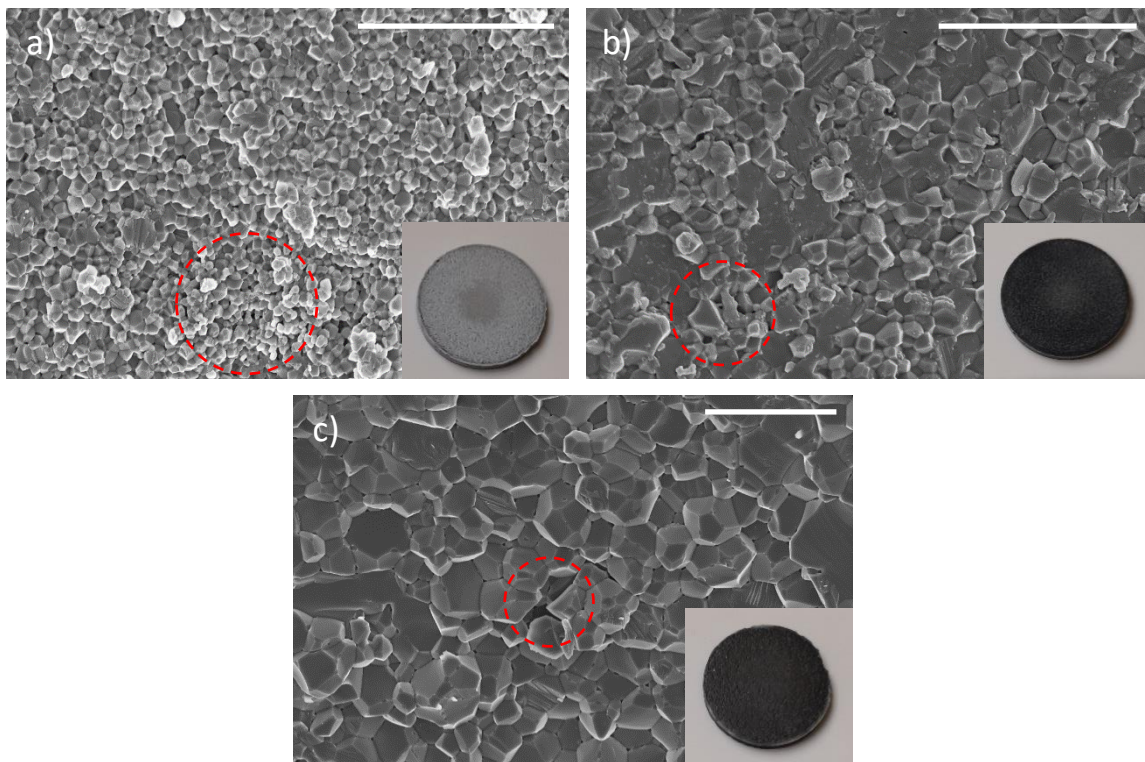


Figure 3.21 – SEM images of alumina specimens sintered from as-received powder at various temperatures. **a)** 1200 °C. **b)** 1300 °C. **c)** 1400 °C. Scale bars = 5 μm . Insets illustrate the visual appearance of 30 mm specimens. The dashed, red circles highlight some porous regions found in the microstructure.

Figure 3.22 illustrates the frequency distribution of measured grain sizes from alumina specimens sintered at 1200 – 1400 °C. There is a visible difference in the distribution of grain sizes as sintering temperature increases. Consolidation at 1200 °C produces an average grain size of $0.4 \pm 0.2 \mu\text{m}$: measured grains were under $1 \mu\text{m}$ (after starting from $0.13 \mu\text{m}$), however the prior SEM analysis illustrated large porous regions in these specimens. A sintering temperature of 1300 °C resulted in a grain size of $1.0 \pm 0.5 \mu\text{m}$, with this increasing further to $1.7 \pm 0.8 \mu\text{m}$ at a temperature of 1400 °C. Monolithic alumina sintered at 1300 and 1400 °C was fully dense ($>99\%$ T.D), but grain growth rises significantly (up to $4 \mu\text{m}$) for specimens consolidated at 1400 °C. The distribution of grain sizes is broader in alumina sintered at 1300 °C and above, but there remaining porosity is slightly lower.

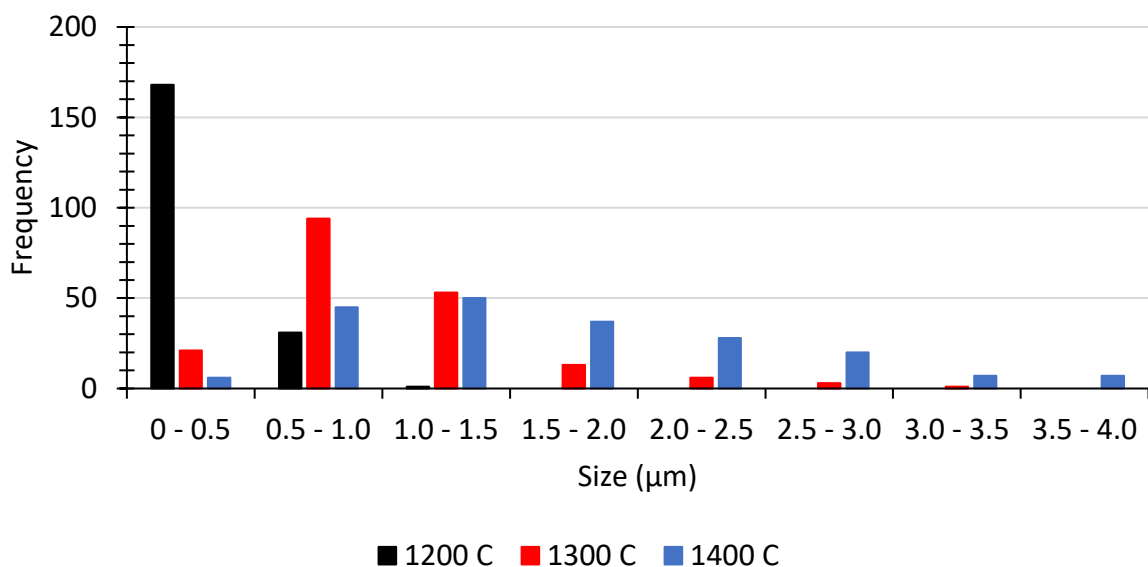


Figure 3.22 – Measured grain sizes from the microstructures of alumina specimens sintered with increasing temperature via SPS.

An X-ray diffraction pattern (Fig. 3.23) was obtained to clarify the retention of monolithic α -alumina, and to observe any possible contamination from the graphitic tools used during the sintering process. The pattern is akin to that obtained from the as-received powder; however, it could be acknowledged that the signal at 29.28 value

of 2θ could be some form of foreign matter. After verifying the signals for graphite,²⁰⁵ or aluminium-containing species,²⁰⁶ it was deduced that this may belong to a minute amount of $\text{Al}_4\text{O}_4\text{C}$.^{207,208} This compound could have been generated from a high temperature reaction between the sub-micrometric alumina powder and the graphite tooling that surrounds it.²⁰⁶ Nevertheless, it is currently difficult to comment on whether this species is present or not without further chemical characterisation.

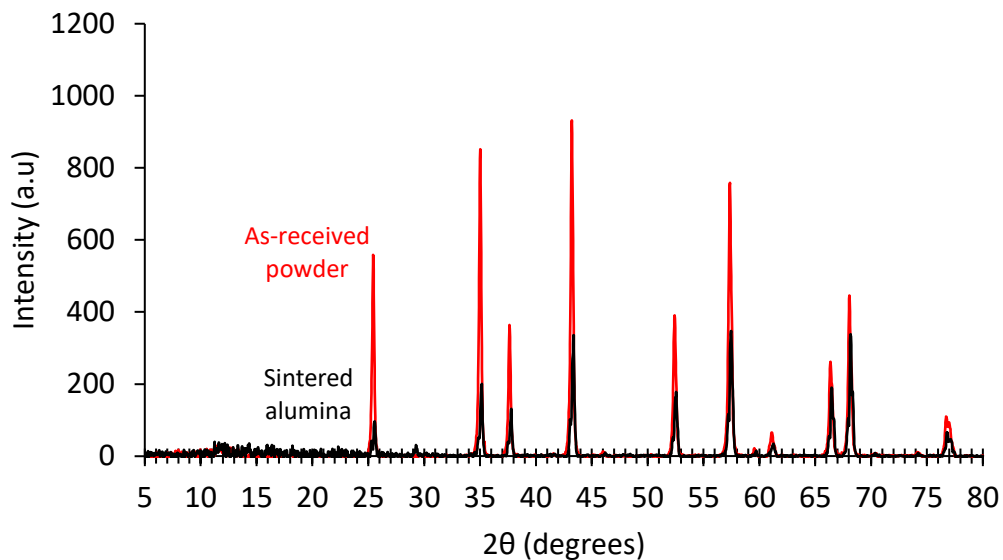


Figure 3.23 – X-ray diffraction pattern of BA15-W alumina sintered at 1300 °C with as-received BA15-W powder for comparison.

3.2.2 Consequences of sintering freeze-cast, alumina scaffolds

Considering that the aim is to fabricate a layered composite material, it was worthwhile consolidating a freeze-cast specimen prior to reinforcement with a filler material. This was to investigate if layers of ceramic material could be observed along the freezing direction using the aid of uniaxial pressure from SPS and without the presence of a reinforcement phase. An understanding on the differences between sintering as-received alumina and processing the powder (through sonication) may also be

accounted for. It must be noted that the scaffold that was utilised was comprised from a 27.5 wt.% alumina suspension. Fig. 3.24 illustrates the fracture surface and resulting microstructure of the freeze-cast scaffold.

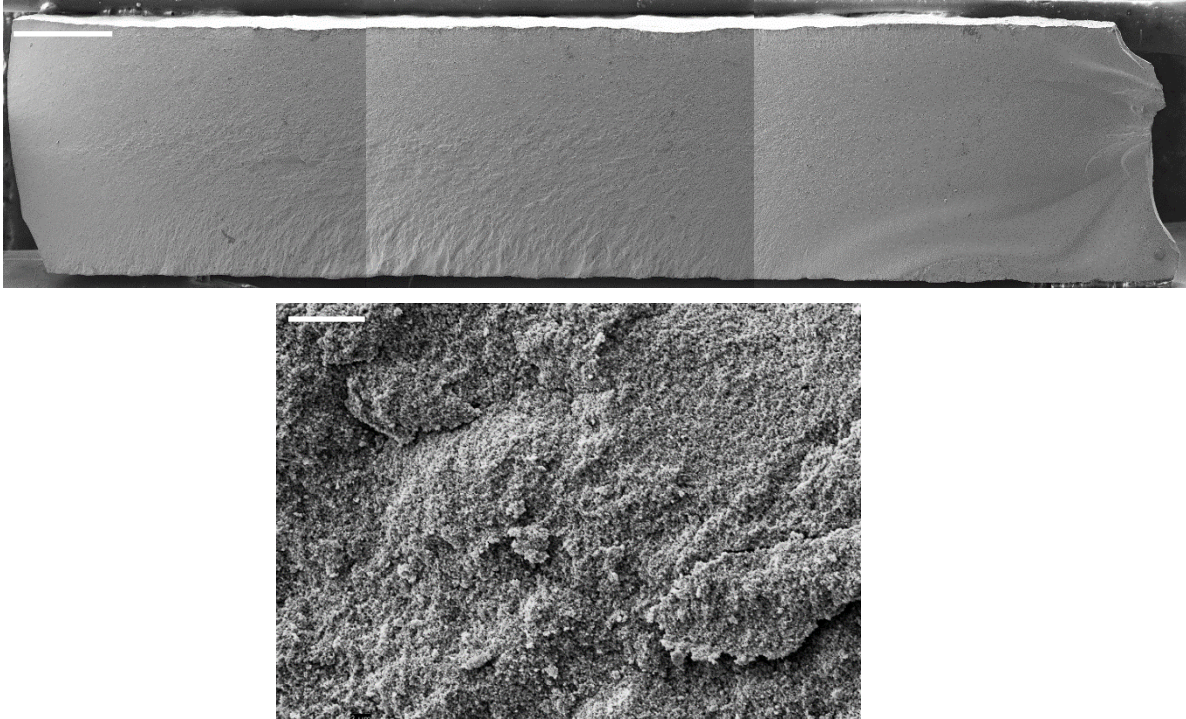


Figure 3.24 – SEM images of a freeze-cast alumina scaffold cast from a 27.5 wt.% suspension sintered using SPS at 1300 °C, 60 MPa, 100 °Cmin⁻¹ heating rate, natural cooling, and 1 min dwell. **Top)** overall fracture surface. Scale bar = 1 mm. **Bottom)** high magnification image. Scale bar = 5 μm.

This scaffold was fabricated during the preliminary stages of the experimental work, so the sintering conditions were those used in Section 4.2.1.1. To clarify, these were a sintering temperature of 1300 °C, 60 MPa pressure, a heating rate of 100 °Cmin⁻¹ and natural cooling, a dwell time of 1 minute, and a pulsed DC sequence (10-5-12-2). For the purposes of this study, it was not vital that the conditions were not optimised. Visually, there is little difference in the fracture surface when compared to that of the as-received powder sintered using the same sintering procedure (shown in Fig. 3.16) with no significant evidence to suggest any alignment of layers across the FD axis. It

could be argued that the core region of the specimen possesses a slightly different appearance, but the ceramic lamellae created whilst casting were not preserved. The grain size appears to be slightly lower with far lesser connectivity between grains, although the density of this sample was 3.93 gcm^{-3} (98.5 % T.D) which is akin to that of the specimen sintered from the as-received powder.

3.3 Discussion

3.3.1 On the fabrication of freeze-cast alumina with directionally-aligned architecture

The casting mould shown in Chapter 2 (Section 2.1.2) used to freeze-cast the alumina suspensions was made from PTFE components and the design was originally created through FDM 3D-printing. It was used to solidify the ice in an orientation perpendicular to the cylindrical faces and is comprised of 4 parts for its easy separation without any potential detriment to the frozen specimen. It has been stressed that the orientation of pores plays a very important role in the considerations during the design of graphene-reinforced composites. One of the objectives of this work is to generate materials with directionally aligned material that will eventually be consolidated into layers via SPS after rotation of cylindrical materials by 90°. If the specimen was directionally frozen from one face to the other in the typical fashion, then vertically aligned channels would be generated. Subsequently, whilst under an applied load during SPS these channels would be destroyed, and the layering of material would be redundant.

However, this alternative casting orientation caused a fan-like appearance along the FD axis. Recent computational work by Ilegbusi *et al.* involved constructing a valid model to predict the average pore size of freeze-cast chitosan-alginate structures which were fabricated with respect to various geometrical parameters of the mould.²⁰⁹ This investigation included different mould wall diameters and found that this can affect the homogeneity of pore sizes because different temperature gradients will exist. The differences in the prototype mould's wall thickness at various heights may have influenced the temperature distribution across the solidification front which resulted in poorer alignment of material across the CS axis. Commonly, the mould walls are fabricated from non-conductive material such as PTFE, but a study by Gil-

Duran *et al.* shown the materials that the mould walls are fabricated from play an important role in the solvent crystallisation because of their thermal properties.¹⁰⁶ They cast large (40 mm diameter, 50 mm height) ceramic scaffolds of 30 wt.% solid loading and found that using mould walls with a low thermal conductance (rubber) creates a far more uniform lamellar structure as opposed to aluminium walls which possess a far greater thermal conductivity. Thus, the homogeneity of the porous architecture that forms during the casting process is not only indicative of the chosen freezing rate, but factors that include the mould's composition, thickness, and its thermal properties.^{12,14} It could be suggested that utilising a different material (as opposed to copper) as the contact surface with lower thermal conductivity may reduce the size of the initial boundary layer which was illustrated in Fig. 3.16.

The global microstructure of a large alumina scaffold was successfully visualised through μ -CT which displayed the creation of long-range lamellae predominantly oriented along the direction of freezing. Although, the resolution with the chosen working parameters was not able to detect the presence of small asperities that were roughly 5 – 15 μm in diameter along the ceramic lamellae (illustrated in Fig. 3.12). This surface roughness was located on one of the faces of the ceramic walls and is believed to be related to the addition of sucrose before casting.^{89,105,210} Munch *et al.* reported that the addition of 4 wt.% sucrose into suspensions of alumina generated a microscopic roughness along the cast lamellae.¹⁰⁵ The visualisation of these intricate casting features demonstrates that the μ -CT analysis alone was not sufficient enough to provide an understanding of all the architectural features that large freeze-cast materials possess. Furthermore, the length scale at which the microstructural features exist on in freeze-cast materials from this investigation is one order of magnitude higher when compared to the architecture of the material nacre (displayed in Chapter 1, Section 1.3.1). For context, the average thickness of ceramic lamellae that have been created were 5 to 15 μm from 25 and 40 wt.% suspensions respectively, whilst the mineral tablets in nacre are approximately 0.6 μm thick – this is a difference of one order of magnitude, the same which is reported by Munch *et al.*⁸⁹ The review by Deville *et al.* describes that, based on extrapolated data, lamellae thicknesses can be

created as low as 1 μm when controlling the formulation and freezing rate,²¹¹ yet this is still double that of nacre's mineral component. An earlier review by Corni *et al.* discusses the variety of fabrication routes towards the creation of nacre-like materials yet they state that the use of freeze-casting is one of the most promising routes to develop bulk nacre-like materials and mimic its mechanical performance.²¹²

3.3.2 Selection of optimal solid loading of freeze-cast alumina for further processing

The microstructural analysis that was primarily conducted through SEM demonstrates that scaffolds fabricated with higher ceramic contents form larger and less homogeneous lamellae thicknesses, with a distribution between 10 and 30 μm : this would result in a final composite's architecture that is far less homogeneous. In contrast, thinner ceramic walls (throughout the same volume) would generate far more interfaces if a secondary material is introduced within the pores. Considering that one of the aims is to produce bulk composite materials with a layered microstructure inspired by nacre it would be ideal to select host matrices with consistent, long-range ordering. Therefore, the data indicates that the most suitable materials to carry forward for subsequent infiltration would be 25 wt.% alumina scaffolds because they exhibit a narrow distribution of smaller lamellae below 10 μm . The number of potential interfacial sites (in a chosen area) would be greater if a composite is made with a scaffold cast from 25 wt.% (5 μm average lamellae) when compared to 40 wt.% (15 μm average lamellae) because the alumina walls would be far thinner when consolidated using SPS. It is true that scaffolds produced below 25 wt.% were not investigated. They may have generated a finer microstructure with a lower wall thickness, however their final mass (<6.5 g, from Section 3.1.2.2) is quite low and would not have created sintered specimens that are thick enough for mechanical testing. More specifically, bar-shaped specimens with a thickness that is above 2 mm are commonly utilised in flexural strength testing.

3.3.3 Consolidation of alumina through Spark Plasma Sintering

It was found that the densification of BA15-W powder through SPS is limited below temperatures of 1200 °C. Specimens sintered at 1200 °C exhibit little grain growth: however, the presence of pores was observed in Fig. 3.21 and led to alumina specimens that were not dense (<99 % T.D). The sintering (piston speed) data and density calculations are comparable between specimens sintered at 1300 and 1400 °C, yet the extent of grain growth in specimens sintered at 1400 °C grows to micron-sized grains predominantly 1 – 4 µm in size (with an average of 1.7 ± 0.8 µm). However, the grain size distribution was narrower in specimens sintered at 1300 °C which produced an average of 1.0 ± 0.5 µm. This matches the findings by Santanach *et al.* that were mentioned at the beginning of Section 3.2.1.2 who found little difference in the densities of monolithic alumina specimens when sintering above temperatures of 1300 °C.²⁰³

A smaller grain size would be advantageous with regards to the ceramic's mechanical properties.²¹³ Larger grains are more prone to intragranular fracture which refers to the propagation of cracks through the grains, as opposed to intergranular fracture which describes the propagation of cracks along the boundaries of neighbouring grains.²¹⁴ The work of fracture increases if a crack must propagate around the sides of neighbouring ceramic grains, so materials that exhibit a smaller grain size are likely to possess greater mechanical behaviour including fracture toughness.²¹³ A mixture of both modes is exhibited in the SEM images shown in Fig. 3.21 with intergranular fracture occurring less frequently in specimens consolidated at 1400 °C. Therefore, a sintering temperature of 1300 °C was selected as the optimal temperature (in conjunction with the remaining parameters) to be used for consolidating composite materials.

With regards to the internal microstructure of the freeze-cast scaffold, there was little difference in comparison to specimens consolidated from the as-received powder.

Using the same sintering conditions, grain growth was slightly suppressed within the freeze-cast scaffold. This is likely to be related to the dispersal of the individual grains during ultrasonic processing. Their densities were also the same (98.5 % T.D) which provided further evidence for altering the sintering conditions to a longer, milder procedure. Also, without the use of any filler materials, individual ceramic layers aligned with the FD axis could not be distinguished after the sintering process – neighbouring lamellae that were compacted together during the pressing segment would have coalesced without the presence of a secondary material between them.

3.4 Concluding remarks

In summary, this chapter involved the preparation and casting of freeze-cast alumina scaffolds with directional porosity from a variety of ceramic loadings. Scaffolds with consistent ordering of the solid and porous features were then selected to use in further studies. Studies were also conducted on the consolidation of BA15-W alumina through SPS to define a procedure that would create unbroken, 30 mm specimens. The influence of sintering temperature on the density of as-received alumina was also investigated. It was found that the optimal scaffolds to focus on in the fabrication of ceramic-graphene composites were those cast from 25 wt.% alumina suspensions. This was because they possessed thin, ceramic lamellae (5 μm average) throughout the bulk of their structure and consisted of a mass akin to that of materials sintered from as-received powder (~ 6.5 g). Scaffolds formed from suspensions with a higher ceramic content were less consistent in their cylindrical geometry and generated less homogeneous and thicker lamellae.

Regarding the SPS of alumina from BA15-W powder, sintering conditions of 1300 $^{\circ}\text{C}$, 50 MPa pressure, 50 $^{\circ}\text{Cmin}^{-1}$, and 5 minutes dwell was selected as the optimal choice from the work that cycles that were investigated. The aim of the sintering experiments was to generate dense, unbroken 30 mm specimens and the formerly mentioned conditions produced alumina that was dense (99.2 % T.D) with observable grain growth from 0.13 to 1.0 μm . Faster, harsher conditions that included 60 MPa pressure, a heating rate of 100 $^{\circ}\text{Cmin}^{-1}$, and 1 minute of dwell produced specimens that broke during the sintering process and possessed a lower density. A separate study with a consolidated freeze-cast specimen demonstrated that, without the presence of any filler material, these materials exhibited little alterations from those materials produced from the as-received powder. Although, this was carried out with the preliminary sintering procedure which is not entirely representative of the optimal choice of conditions.

Chapter 4 Infiltration of alumina scaffolds using graphene oxide suspensions and their consolidation by Spark Plasma Sintering

In this chapter, an investigation into the uptake of water-based suspensions of GO inside the pores of freeze-cast alumina materials was carried out. Vacuum-assisted infiltration was carried out on scaffolds with, and without, the dense region of freeze-cast scaffolds that was identified in the previous chapter. This was to, eventually, identify ceramic-graphene pre-forms with well-dispersed reinforcement that was also homogeneously arranged throughout the microstructure. GO was selected as the infiltrate material to avoid the utilisation of hydrophobic graphene-like materials. This is advantageous in this processing route as quantities of the solid material may be mixed solely with water to form a suspension of readily dispersible material. Additionally, the use of organic solvents is avoided which is beneficial in developing environmentally-friendly processing strategies. The first section identifies a suitable concentration of GO to provide continuous, well-dispersed inclusions of GRM. The use of two different GOs into porous ceramics was also evaluated after some of their physicochemical features were characterised. Namely, the two water-based suspensions were as follows.

- i) Graphenea, 1 wt.% GO suspension in water

- ii) Imperial College London, custom-made GO suspension

The custom-made GO was previously prepared at Imperial College London through a modified Hummer's method by chemical exfoliation of 300 – 500 μm flakes of natural graphite powder, but no data was provided on the quality of the material: thus, physicochemical characterisation is imperative. Once alumina-GO pre-forms were obtained, they were consolidated through SPS, under similar conditions to those used for the as-received alumina – primarily, the aim was to consistently reproduce dense specimens to compare against the monolithic alumina specimens fabricated in the previous Chapter (Section 3.2.1.2). Density measurements and data from the sintering cycles provide information towards the extent of their consolidation, whilst fracture surfaces were investigated using SEM to identify the microstructural arrangement of both the ceramic and GRM components.

4.1 Optimisation of the concentration of GO suspensions

A suitable concentration of GO had to be identified such that the infiltration within porous alumina materials processed by freeze casting (Chapter 3, Section 3.1.2) generated a continuous and well-dispersed layers of reinforcement after sintering by SPS. Three concentrations were tested using the commercial GO suspension: namely, these are 0.025, 0.1, and 0.25 wt.% which were all diluted from the stock concentration (1 wt.%). The composite materials were named with the notation of $\text{XAl}_2\text{O}_3:\text{YGO}$, where X represents the solid loading of the suspensions used in freeze-casting, and Y refers to the concentration of the GO suspension. Figure 4.1 displays the microstructures of alumina-rGO materials obtained after SPS sintering using a temperature of 1300 $^\circ\text{C}$ – however, the dwell time and heating/cooling rates differ for each specimen as they were fabricated during preliminary work.

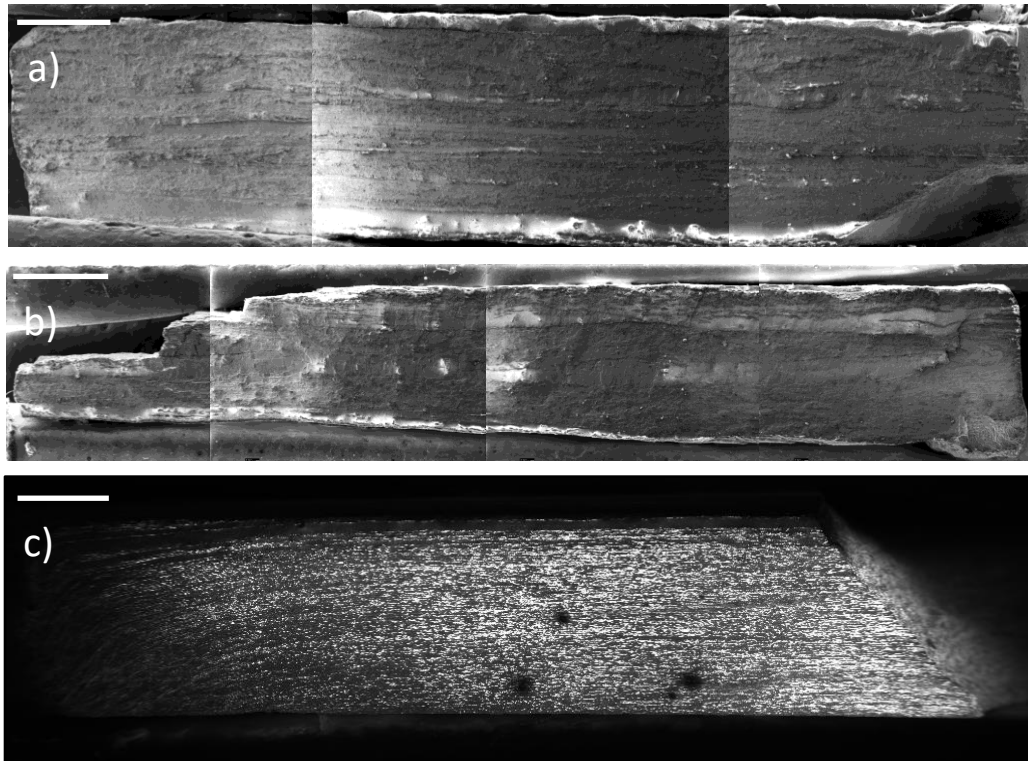


Figure 4.1 – SEM images of rGO-reinforced alumina composites sintered at 1300 °C that were fabricated by drop casting and vacuum-assisted infiltration of alumina scaffolds with different water-based GO suspensions. **a)** $22.5\text{Al}_2\text{O}_3:0.025\text{GO}$, **b)** $25\text{Al}_2\text{O}_3:0.1\text{GO}$, **c)** $25\text{Al}_2\text{O}_3:0.25\text{GO}$. Scale bars = 1 mm. The images shown in Fig. 4.1a and 4.1b were taken with secondary electron signals, whilst Fig. 4.1c was captured with in-line, back-scattered electrons.

Regardless of the sintering conditions, the results show the possibility to successfully infiltrate (and sinter) porous alumina scaffolds made from low solid loadings (22.5, 25 wt.%). All three sintered composites were 30 mm in diameter, roughly 2.2 mm in thickness, and close to 6.5 g in weight. This matches the weight and dimensions of specimens sintered from the as-received powder in Chapter 3 (Section 3.2.1). The presence of highly-oriented filler material is visible perpendicular to the direction of pressing during the sintering procedure. Although, the two materials that had been infiltrated with 0.025 and 0.1 wt.% of GO (Fig. 4.1a and 4.1b respectively) exhibit large regions of the microstructure that are void of any continuity of reinforcement.

These areas that are solely composed of the alumina matrix were found to be as large as 220 μm which is 10 % of the overall thickness. On the other hand, the composite material displayed in Fig. 4.1c exhibits a well-dispersed reinforcement across its cross-section which led to the decision to use 0.25 wt.% suspensions of GO. As such, the remainder of this Chapter demonstrates the fabrication of materials shown in the latter image, which is based on the infiltration of 0.25 wt.% GO suspensions within porous alumina scaffolds.

4.2 Physicochemical features of graphene oxides

Prior to utilisation, the flake size and degree of order of the two GOs used were characterised. The former was conducted after dilution and careful deposition that was described in the methods (Section 2.2.4), whilst the latter was carried out using X-ray diffraction (section 2.2.6) and Raman spectroscopy (Section 2.2.7). XRD also evaluated the lattice spacing of GRMs rather than the phase of the material that was assessed in Chapter 3, Section 3.1.1.1. This is important analysis to conduct as the quality and chemical composition of GO flakes could vastly differ. Furthermore, understanding the size of the flakes is critical – if the flakes are very large in comparison to the pore sizes of the ceramic scaffolds, this may have an impact on the success of infiltration. For clarity's sake, the commercially-available GO will be denoted as "GO_{supplier}", whilst the suspension provided by Imperial College London will be referred to as "GO_{custom}".

Dispersed flakes of GO_{supplier} were observed (Fig. 4.2) using OM and found to have an average size of $8 \pm 2 \mu\text{m}$. Some of the single-layer flakes can be seen crumpling over themselves after deposition, exhibiting their extremely thin and flexible nature. In some regions, agglomerates of multi-layer GO were also identified (inset of Fig. 4.2) by virtue of a stark change in optical contrast – these do not contribute to the determined flake size. The frequency distribution illustrates that most of the individual flakes are below $10 \mu\text{m}$, which is valid according to the manufacturer's data.

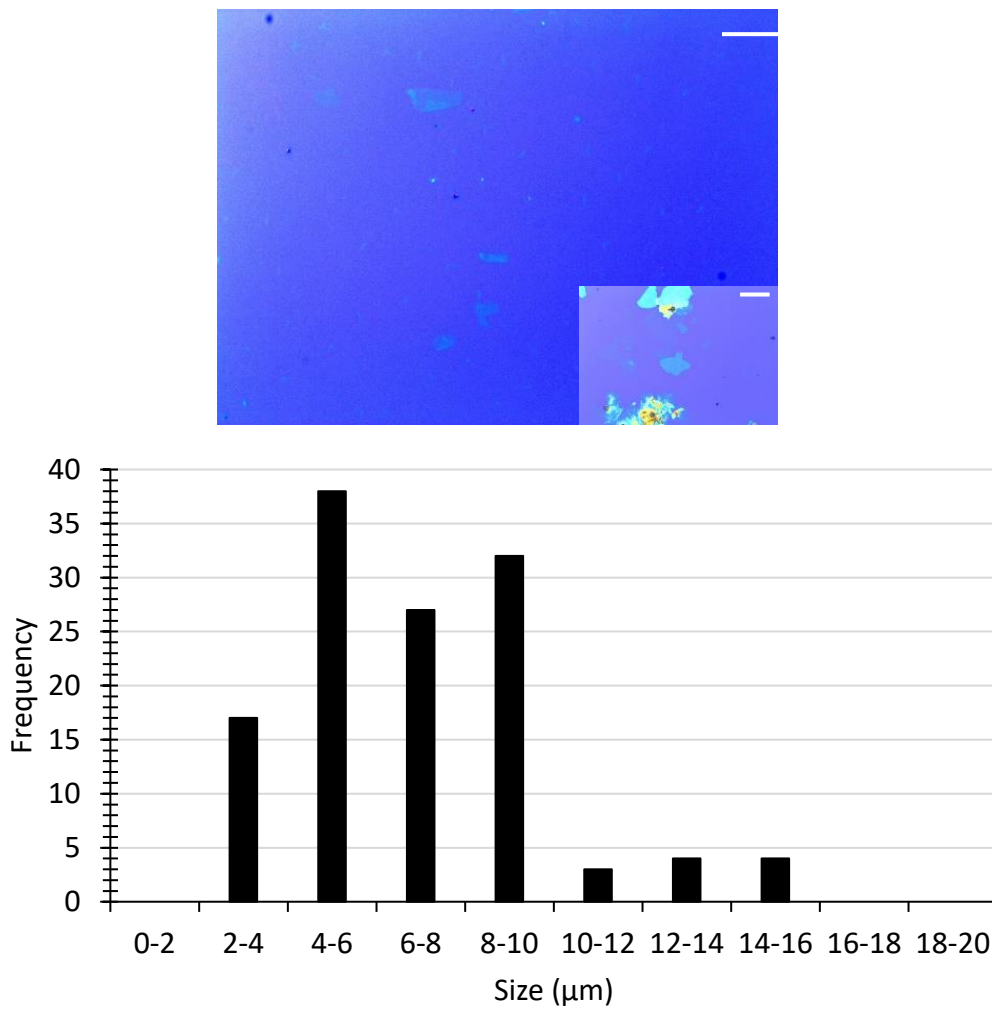


Figure 4.2 – Top) OM image of deposited flakes of GO_{supplier} on Si-SiO₂(300 nm). Scale bar = 20 μm. Inset illustrates GO agglomerates. Scale bar = 20 μm. **Bottom)** frequency distribution for the size of GO_{supplier} flakes.

The custom-made suspension was previously fabricated at Imperial College London, but there was no previous characterisation to validate our findings. The collected results show a clear difference in the lateral size of GO_{custom} as flakes are much larger than GO_{supplier} , with an average size of $22 \pm 9 \mu\text{m}$. Multiple optical images are provided in Fig. 4.3 illustrating their larger size over GO_{supplier} . The distribution of flake sizes is also far broader with some flakes found to be as large as $50 \mu\text{m}$ in diameter, but no flakes were found to be less than $5 \mu\text{m}$.

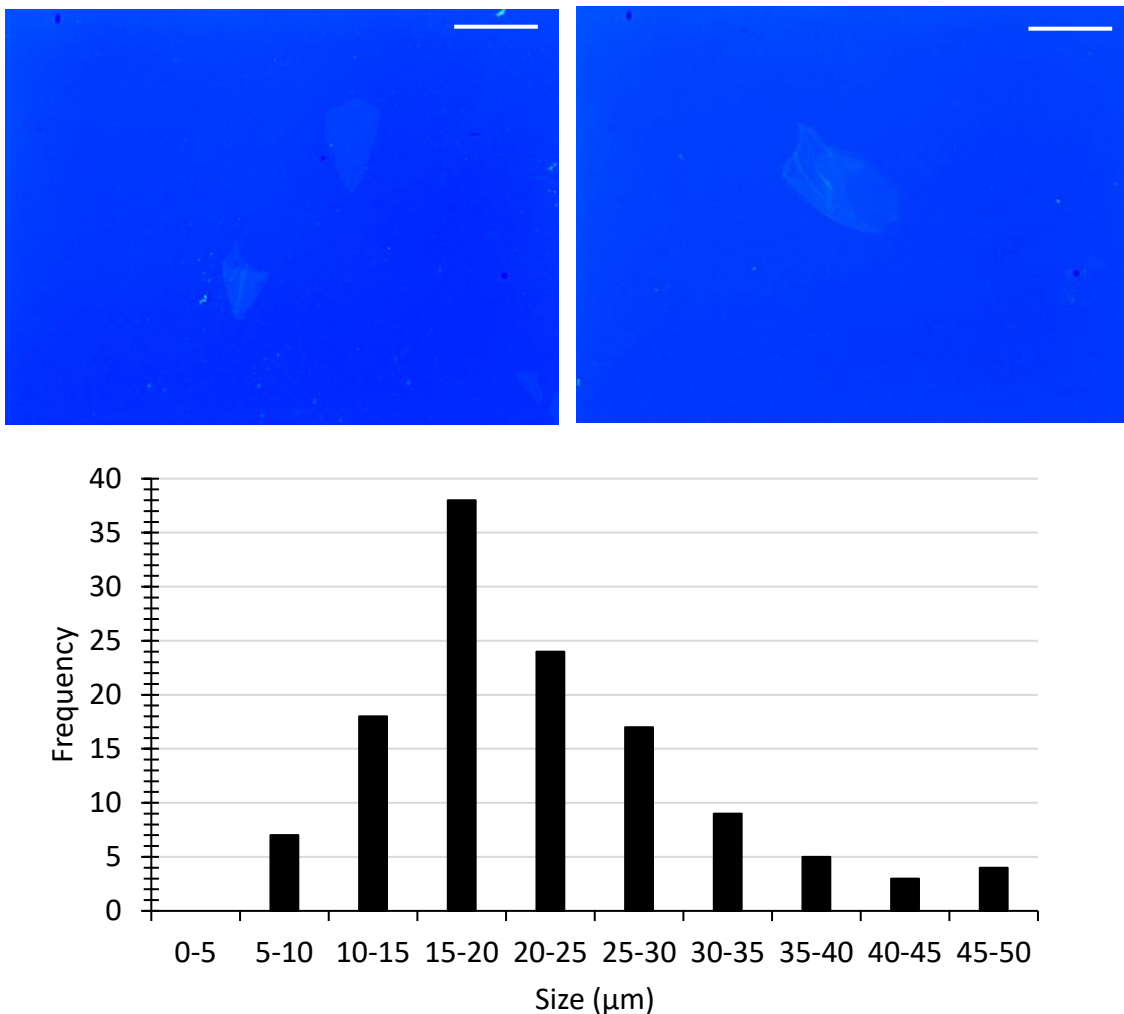


Figure 4.3 – Top) OM images of dispersed flakes of GO_{custom} . Scale bars = $20 \mu\text{m}$. **Bottom)** frequency distribution for the size of GO_{custom} flakes.

The data provided by Raman spectroscopy (Fig. 4.4) demonstrates a clear difference in GO with respect to graphite however no major difference between the two GO batches can be identified. Graphite was used as a comparison because its structure closely resembles that of GO, without intercalation of oxygen-containing functional groups. Both GO samples show two main peaks situated at 1350 and 1596 cm^{-1} that correspond to the D and G bands respectively, although it is true that another broad peak centred close to 2700 cm^{-1} exists which was illustrated in the methods (Section 2.2.6).^{215–217}

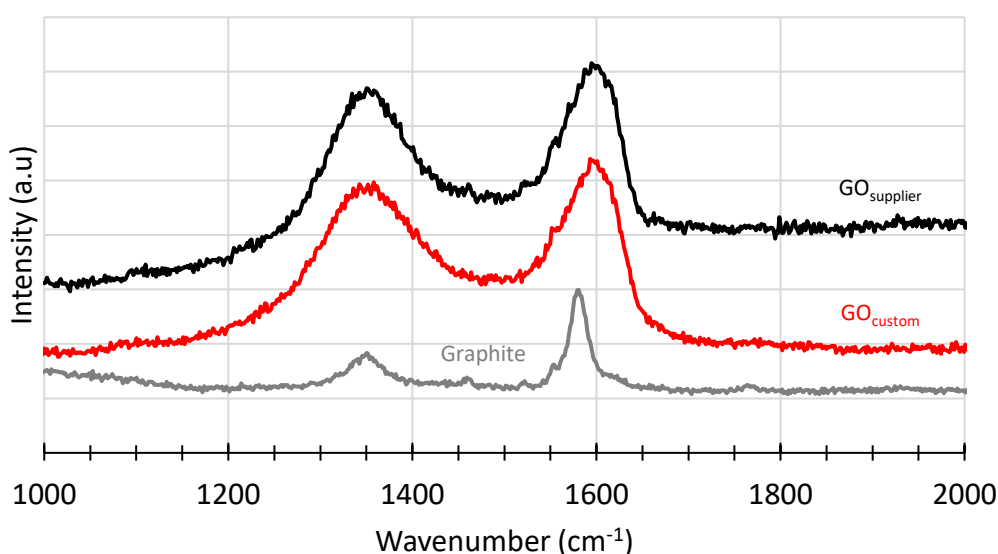


Figure 4.4 – Raman spectra of $\text{GO}_{\text{supplier}}$, $\text{GO}_{\text{custom}}$ and graphite.

In GRMs, the D band is derived from a disorder-induced mode and this is far less intense in graphite than the G signal which are located at 1350 and 1581 cm^{-1} , respectively.²¹⁸ The intense G peak arises due to the symmetry elements present in graphite which forms a major E_{2g} optical symmetry mode.²¹⁹ This can be further linked to a strong presence of sp^2 hybridisation within the hexagonal lattice structure of graphite, in comparison to the mixed sp^2 and sp^3 character found in GO.^{220,221} The ratio between the peak intensities (D/G ratio) can signify the extent of disorder, with more ordered GRMs possessing lower D/G ratios.²¹⁹ When compared to graphite that

possessed a D/G ratio of 0.61, GO exhibits a much higher D/G ratio of 0.94, which can be attributed to a material with far more disorder;²²² GO contains a number of oxygen-containing functional groups (epoxides, hydroxyls, carboxyls) which disrupts its long-range crystallinity, particularly when compared to graphite. The Raman spectrum obtained for GO_{custom} is very similar to that of GO_{supplier}, but it may be argued there are some subtle differences. It is difficult to observe, but the peak positions of both D and G signals have shifted by no more than 5 cm⁻¹. Plus, the intensity between the two peaks, i.e., the D/G ratio, has also dropped slightly from 0.94 to 0.91.

The collected X-ray diffraction pattern is characteristic of GO – one major peak at a 2 θ value of 10.48. Compared to graphite, which produces an intense, line-like peak at a scattering angle of 26.24, the d-spacing of GO is much larger (0.84 nm compared to 0.34 nm). There is a stark contrast between the patterns of GO and graphite which is clearly displayed in Fig. 4.5, much like the Raman data that was acquired. This is a similar result to previous reports, with the change arising due to the partial expansion of graphitic layers during the exfoliation process.^{223,224} After an oxidative process, carbon sheets in GO will possess a variety of oxygen-containing functional groups decorating the axial positions of tetrahedrally-bound carbon. Considering the inclusion of oxygen moieties is not consistent at every carbon atom, there will be some variation in the d-spacing across sheets of material,²²⁵ creating the broader signal, i.e., there is signal broadening due to steric effects. The smaller peaks at higher scattering angles (42.54, 44.54, 53.82, and 77.38) are related to smaller, crystallographic domains that are not aligned with the path of the oncoming radiation.

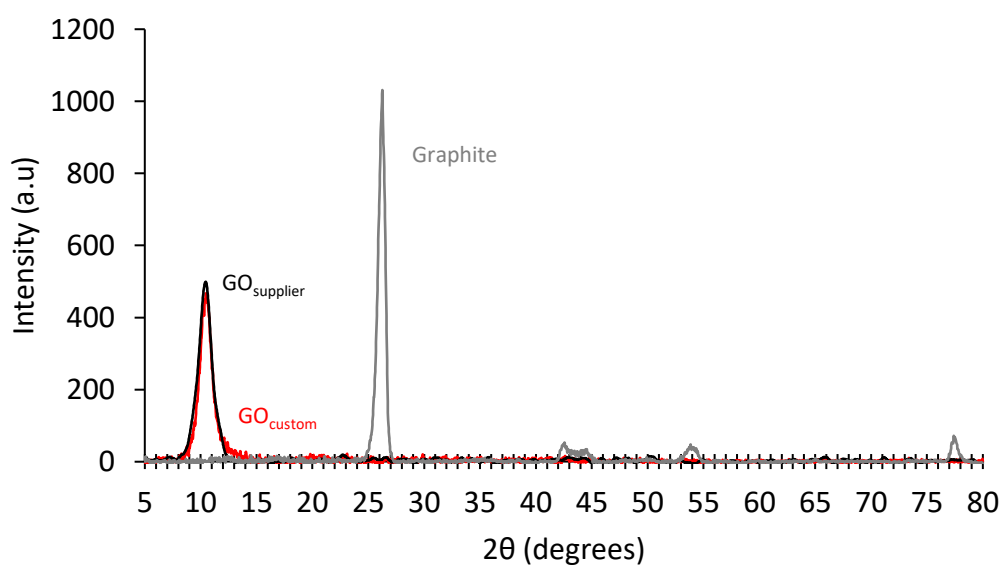


Figure 4.5 – XRD pattern of $\text{GO}_{\text{supplier}}$, $\text{GO}_{\text{custom}}$ and graphite.

The XRD pattern of $\text{GO}_{\text{custom}}$ closely resembles the pattern obtained for $\text{GO}_{\text{supplier}}$. The custom-made GO produces a signal that matches $\text{GO}_{\text{supplier}}$, with respect to both the intensity and peak position (10.48). The two signals have a similarly broad nature, provided in the previous Raman spectrum. It is clear from these simple analytical techniques that the physicochemical features of procured GOs can vary. This is predominantly in the size distribution of GO flakes; however minor changes could be revealed using diffraction techniques or spectroscopic characterisation.

4.3 Infiltrating porous ceramic materials with water-based suspensions of graphene oxide

Previous studies have identified the capacity of pre-sintered, porous ceramics to be infiltrated with filler materials, including metals through melt infiltration,^{226,227} and ceramics through the infiltration of polymer-derived constituents.²²⁸ Ceramic particles have also been deposited within porous materials via slurry impregnation, often under reduced pressure inside a vacuum.^{229–231} One example involves the impregnation of reticulated ZrO₂ scaffolds with a less concentrated slurry of ZrO₂ particles to alter the morphology of internal pores – before infiltration, the pores are triangular in geometry, with failure of these materials initiating at their sharp corners.²²⁹ However, after infiltration the apices had become denser and rounder, providing an enhancement to the mechanical strength. Yet, there is little evidence towards approaches that deliver GRMs into the pores of a material. In 2014, Dhawan *et al.* demonstrated the feasibility of drop-casting suspensions of rGO onto vertically aligned MWCNTs, i.e., a MWCNT forest, as-described by the authors.²³² This resulted in a sandwich-panel composite structure, with rGO acting as the face sheets after its deposition. Drop-casting was also utilised in recent work by Schütt *et al.* to deposit exfoliated graphene along the walls of a ceramic (zinc oxide) scaffold.²³³

Therefore, two approaches for infiltration were selected: first, drop-casting was trialled to visually comprehend the effectiveness of infiltration in various regions of the porous ceramics. This method is quite trivial and does not require any prior lab experience. The second technique requires more involvement and utilised a pressure chamber to encourage greater uptake of solid material into the pores of the ceramic scaffolds. It was illustrated in Fig. 4.1 that infiltration of porous ceramics with GO suspensions can lead to well-dispersed and continuous reinforcement. This was seen when utilising suspensions of 0.25 wt.% as opposed to lower concentrations of 0.025 and 0.1 wt.%. Therefore, this section describes the processing strategy to deposit GO from a water-

based suspension with a concentration of 0.25 wt.% within 30 mm, porous cylindrical alumina matrices.

4.3.1 Preparation of graphene oxide suspensions

Prior to their use, the weight percentage of the stock GO suspensions were validated after freezing and freeze-drying small aliquots of the liquids to isolate the solid material. This was critical to verify, especially for the custom-made suspension considering its stock concentration is unknown. It was determined (from three aliquots) that the solid material in GO_{custom} is 0.36 ± 0.01 wt.%, which was far lower than the concentration of GO_{supplier} ; this was found to be 1.06 ± 0.04 wt.% which is in close agreement to the manufacturers value of 1 wt.%. Furthermore, the viscosities of stock and diluted GO suspensions of 0.25 wt.% were measured at a constant shear rate to evaluate their viscosity during flow, which may affect the infiltration process. The measurements in Fig. 4.6 illustrates a clear decrease in viscosity with decreasing GO concentration in both batches.

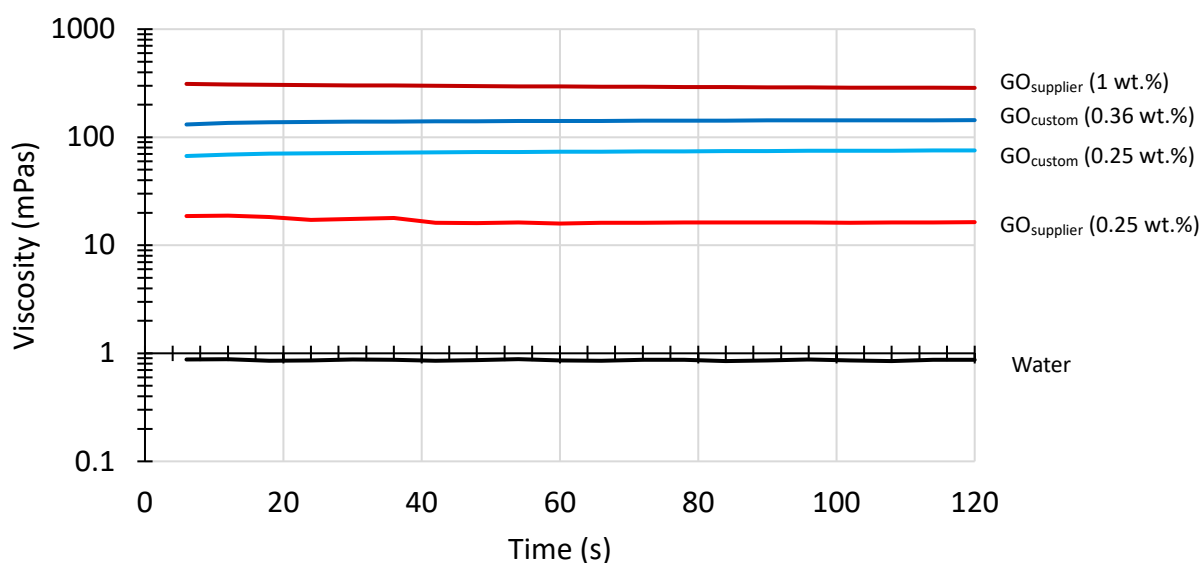


Figure 4.6 – Viscosity measurements provided for various suspensions of graphene oxide and water for comparison at a shear rate of 50 s^{-1} .

The stock solutions of GO exhibit viscosities of 286 and 144 mPas (after 120 seconds), for GO_{supplier} and GO_{custom} respectively. These values decrease to 75 and 16 mPas after the stock solutions are diluted to 0.25 wt.%. For reference, the viscosity of the dilute suspension containing GO_{supplier} (8 μm) resembles that of low-weight aqueous glycols,^{234,235} whilst the value obtained from dilute GO_{custom} (22 μm) is comparable to cooking oils.^{236,237} The difference in viscosity can be attributed to the size of GO flakes present in each batch. Larger flakes would possess a greater surface area, and therefore, would be more likely to interact with each other (whilst in suspension) when compared with smaller flakes.²³⁸ This would reduce the extent of flow and subsequently increase the viscoelastic behaviour. What can be suggested is that the data illustrates GO suspensions containing larger flake sizes possess higher viscosities than those with smaller flakes; the difference may play a role during the infiltration of ceramic scaffolds that exhibit pores on the microscale.

4.3.2 Optimisation of the infiltration method for depositing graphene oxides within porous ceramics

In the first instance, simple drop-casting was utilised to verify that this processing route could be realised. This strategy was intended to allow for the uptake of GO suspensions within the pores of freeze-cast scaffolds to provide an effective dispersion of GRMs throughout a ceramic matrix. This was performed on porous alumina cast from both low and moderate solid loadings (22.5 and 40 wt.%) to identify its applicability on a range of freeze-cast materials with varying degrees of porosity. To clarify, freeze-cast materials have been pre-sintered at 900 °C for 30 minutes (illustrated in Chapter 3, Section 3.1.2.2) prior to these studies. Figure 4.7 demonstrates the viability to drop-cast GO suspensions within the porous ceramic materials (followed by freezing and drying). One can visually ascertain a grey-brown appearance to the outside of scaffolds post-infiltration: upon examination of the internal core (in the xy plane), this off-white appearance is also visible. The trials through drop-casting provides visual evidence that GO has been deposited on the perimeter and inside the core of the freeze-cast material.



Figure 4.7 – Images of a 40 wt.% alumina scaffold that has been drop-cast with a 0.025 wt.% suspension of $\text{GO}_{\text{supplier}}$. **Left)** infiltrated scaffold. **Right)** core section of the specimen that illustrates the deposition of $\text{GO}_{\text{supplier}}$ through FD axis.

A GO "skin" also formed along the top face of the scaffold due to an excess of solid flakes agglomerating on the surface of the ceramic material during the freezing period. This is an unwanted feature and could be carefully extracted with tweezers. The 40 wt.% alumina scaffold was not perfectly cylindrical which was illustrated in the previous Chapter (Section 3.1.2.1). Once the infiltration route was realised as a possible technique to disperse GO flakes throughout porous freeze-cast materials cast from low to moderate solid loadings, the primary method of infiltration was investigated: vacuum-assisted infiltration. The reasoning for focussing on 25 wt.% scaffolds as the host material primarily was because they exhibit a mass close to 6.5 g which will produce sintered materials with a thickness close to 2.2 mm (as seen in Chapter 3, Section 3.2.1) and possess well-ordered ceramic walls in comparison to those made from higher solid loadings. The intention for using this method was to allow for the permeation of GO flakes throughout the entirety of porous alumina bodies with the assistance of reduced pressure. The following tests involved the use of suspensions containing 0.25 wt.% of either GO_{supplier} or GO_{custom}. Fig. 4.8 depicts the first experiment using vacuum-assisted infiltration.

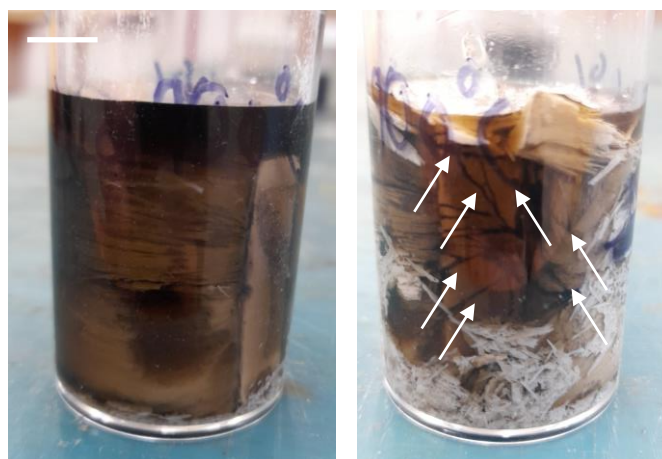


Figure 4.8 – Unsuccessful test of an alumina scaffold infiltrated with a 0.25 wt.% $\text{GO}_{\text{supplier}}$ suspension using vacuum-assisted infiltration. **Left)** before the infiltration procedure. Scale bar = 10 mm. **Right)** scaffold destroyed after the infiltration process. Larger cracks are highlighted with thin, white arrows.

As the pressure was lowered to -1 bar, bubbles were observed evacuating from the sides of the scaffold which was promising. Unfortunately, when the pressure was lowered during a period of approximately 2 minutes, it was visible that the ceramic scaffold was destroyed during the latter stage of infiltration. Note the severe cracking throughout the scaffold and debris that has formed around the sides of the scaffold in the container. A steadier decrease in pressure over a period of 10 minutes was performed in subsequent tests, leading to successful infiltration without collapse of the delicate ceramic material. Thus, for any following experimentation the pressure was lowered to -1 bar in a far steadier decline whilst infiltrating scaffolds with $\text{GO}_{\text{supplier}}$ and $\text{GO}_{\text{custom}}$.

The subsequent images show the extent of infiltration within two, pre-sintered 25 wt.% alumina scaffolds using 0.25 wt.% suspensions of $\text{GO}_{\text{supplier}}$. The first scaffold was left whole, whilst the second underwent removal of a dense region of material that was identified through μ -CT in Chapter 3 (Section 3.1.3.2). It is clearly visible that the whole scaffold has a large section of the porous alumina body (through the core)

has not been infiltrated with the water-based suspension: however, the process does deposit GO inside the perimeter of the scaffold. Comparison against a sectioned scaffold that is displayed in Fig. 4.9 (with the dense region removed) depicts a much more homogeneous deposition of the filler material. Once the dense section was extracted, the water-based suspension was able to permeate towards the core.

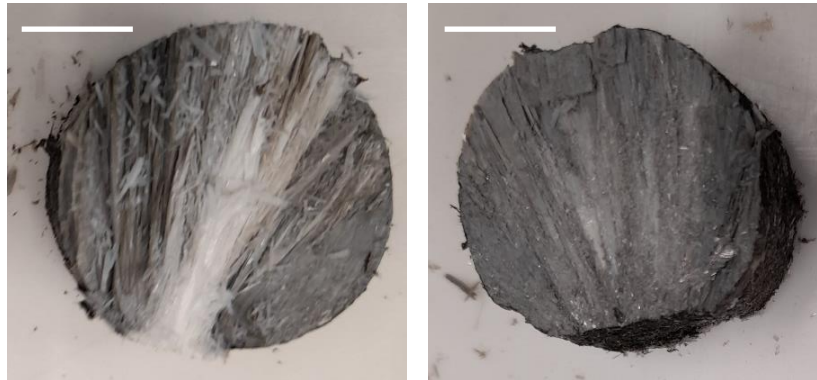


Figure 4.9 – Images of 25 wt.% alumina scaffolds vacuum-infiltrated with a 0.25 wt.% $\text{GO}_{\text{supplier}}$ suspension. **Left)** a whole scaffold with no physical changes. **Right)** a scaffold with which the dense region of material has been removed. Scale bars = 10 mm.

After cutting open scaffolds infiltrated with $\text{GO}_{\text{custom}}$, a result akin to that of $\text{GO}_{\text{supplier}}$ is visible. Fig. 4.10 depicts that the perimeter of the cylindrical ceramic body has been penetrated by the water-based infiltrate. However, there was still a limited amount of GO flakes that had reached the core of the whole scaffold, since the homogeneity of the pores was compromised at the “bottom” of the freeze-cast alumina. After removal of this section of the scaffold, there was much more homogeneous deposition of $\text{GO}_{\text{custom}}$ within the core. Although, some white streaks are still visible which may suggest there are some internal regions that have not been successfully infiltrated by the water-based suspension of GO flakes.

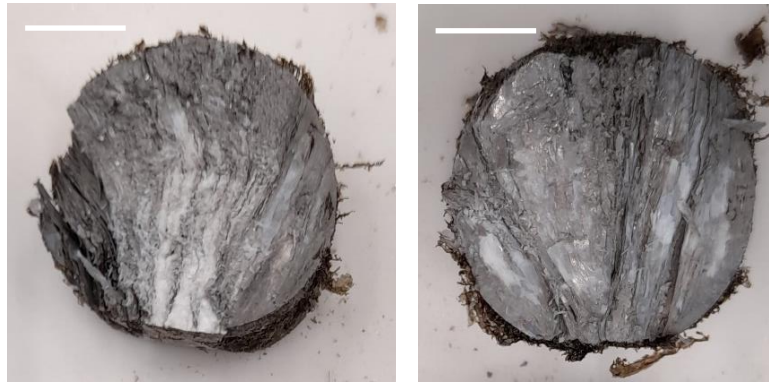


Figure 4.10 – Images of 25 wt.% alumina scaffolds vacuum-infiltrated with a 0.25 wt.% $\text{GO}_{\text{custom}}$ suspension. **Left)** a whole scaffold. **Right)** a scaffold with the dense region of material has been removed. Scale bars = 10 mm.

Comparing the visual homogeneity of sectioned scaffolds of $25\text{Al}_2\text{O}_3:0.25\text{GO}_{\text{supplier}}$ and $25\text{Al}_2\text{O}_3:0.25\text{GO}_{\text{custom}}$, GO deposition throughout the host alumina is slightly better when utilising $\text{GO}_{\text{supplier}}$. This difference in the extent of infiltration is likely due to the difference in flake sizes ($8\ \mu\text{m}$ compared to $22\ \mu\text{m}$ averages in $\text{GO}_{\text{supplier}}$ and $\text{GO}_{\text{custom}}$ respectively), combined with the increase in viscosity with increasing flake size. What this investigation illustrates is that smaller GO flakes are more susceptible to permeation into the pores of freeze-cast scaffolds formed from 25 wt.% alumina suspensions. Due to the time constraints imposed by COVID-19, it was not possible to sinter specimens of $25\text{Al}_2\text{O}_3:0.25\text{GO}_{\text{custom}}$. Therefore, the following section describes the sintering of materials infiltrated with 0.25 wt.% suspensions of $\text{GO}_{\text{supplier}}$.

4.4 Consolidation of alumina-GO pre-forms through Spark Plasma Sintering

This section outlines the sintering results of alumina-GO specimens that consistently produced unbroken disc-shaped specimens, alongside some comparisons to monolithic alumina sintered with the same conditions. This is with regards to the composite specimen referred to as $25\text{Al}_2\text{O}_3:0.25\text{GO}$ that was infiltrated with $\text{GO}_{\text{supplier}}$, i.e., the suspension which contained smaller flake sizes. The results gathered from the composite material are compared alongside monolithic alumina fabricated from as-received powder with the same sintering conditions.

4.4.1 Sintering and density of alumina-rGO materials

After freezing and drying GO-infiltrated alumina scaffolds, sintering was the final step in this processing route that has been illustrated herein. This was performed using SPS with two primary objectives in mind: i) take advantage of the simultaneous application of pressure to consolidate large, freeze-cast cylindrical specimens whilst preserving the internal layered structure, and ii) onset the thermal reduction of GO to create rGO, forming graphene-like material throughout the composite's microstructure. This sintering technique also has the added benefit of vastly reducing the consolidation time of alumina-based materials, which is commonly a few hours during conventional sintering to obtain high densities (depending on the starting powder size).^{29,190,239} First, 30 mm green bodies of alumina-GO required placement inside graphitic moulds for SPS consolidation. The skin of GO material surrounding the composite was removed before fitting cylindrical specimens within partially-assembled moulds. This process was somewhat time-consuming, but necessary to avoid any potential defective regions around the sides of the specimens post-sintering. The task was performed carefully as to not disrupt or destroy the delicate, lightweight material. Cold pressing of the top (and bottom) die followed its insertion within the mould to

contain the entire specimen. Fig. 4.11 demonstrates how free-standing, alumina-GO materials were (carefully) inserted into graphitic die sets to undergo Spark Plasma Sintering.

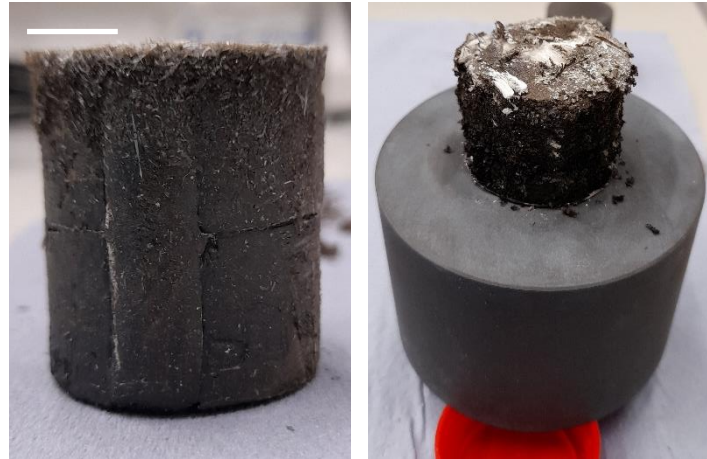


Figure 4.11 – Photographs of alumina-GO material prior to the SPS consolidation. **Left)** free-standing scaffold after the freezing and drying process that followed infiltration. Scale bar = 10 mm. **Right)** fitting the composite entity within a 30 mm graphite mould for the SPS procedure.

Chapter 3 (Section 3.2.1.1) involved obtaining sintering conditions that could consistently generate unbroken, 30 mm specimens of monolithic alumina that were fully dense (<99 % T.D). This was after identifying multiple issues with sintering the as-received alumina powder whilst using the preliminary sintering conditions. As a reminder these were a sintering temperature of 1300 °C, a pressure of 60 MPa, a heating rate of 100 °Cmin⁻¹, a natural cooling step, and a dwell time of 1 minute. Optimal alumina-GO bodies (25Al₂O₃:0.25GO) were subject to the sintering conditions that produced unbroken and dense alumina specimens which were a sintering temperature of 1300 °C, a pressure of 50 MPa, a heating rate of 50 °Cmin⁻¹ (followed by a cooling rate of 50 °Cmin⁻¹), and a dwell time of 5 minutes. Piston speed data was gathered after sintering a composite specimen to compare against that of monolithic alumina sintered with the same conditions. The plot shown in Fig. 4.12 illustrates a change in the densification process that commences in monolithic alumina around 900

°C, with consolidation of the composite initiating slightly before at a temperature of approximately 850 °C.

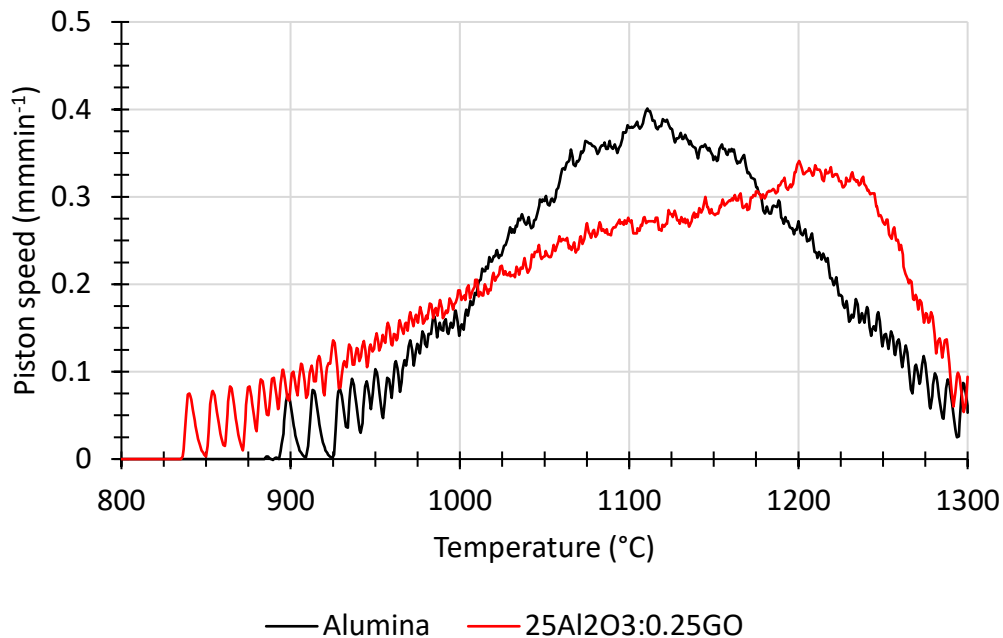


Figure 4.12 – Plot of piston speed versus temperature up to the dwell from the SPS programs used for alumina and 25Al₂O₃:0.25GO specimens sintered with 1300 °C, 50 MPa, 50 °Cmin⁻¹ heating/cooling rates, 5 min dwell.

Consolidation in both materials up to the dwell point ceases at a similar point which is a sign that the composite may possess a theoretical density close to that of monolithic alumina (99.2 % T.D). The curvature of the piston speed peak is slightly broader, which may provide some evidence towards greater consolidation under the same sintering parameters: an explanation could stem from the higher thermal conductivity of the graphene-like material throughout the alumina matrix; in particular, during the transformation from GO to rGO.²⁴⁰ This would provide more effective heating within the ceramic material, which relies on non-conductive sintering (in monolithic ceramic specimens).

The composite's microstructure which, after heat-treatment under vacuum in an inert atmosphere, is expected to contain rGO like other studies that have thermally reduced GO materials through SPS.^{93,241–243} To determine the amount of carbon-based material, i.e., rGO, that was incorporated within the sintered composites, an investigation through TGA was conducted after grinding samples. This would eventually lead to calculating the density of alumina-rGO composites. Fig. 4.13 depicts that after increasing the temperature (in air) alumina-based composites lose a very small portion of their mass.

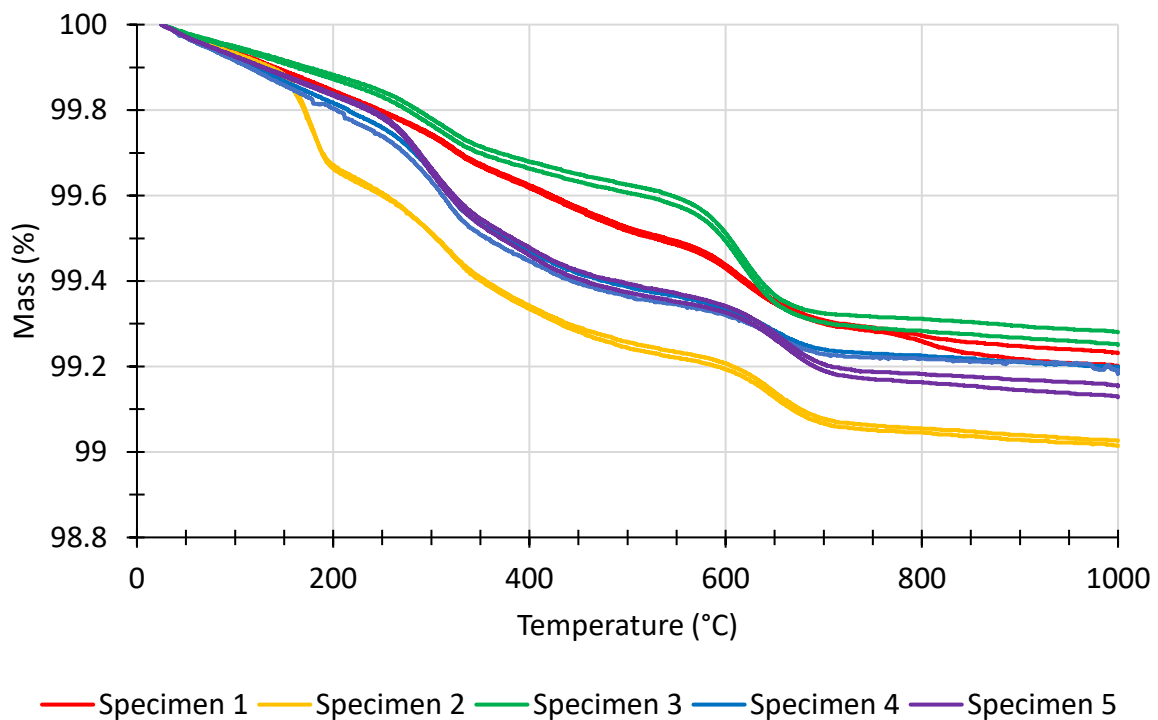


Figure 4.13 – Plot of TGA curves to determine carbon content within $25\text{Al}_2\text{O}_3:0.25\text{GO}$ composites.

An average loss of approximately 0.8 wt.% (1.7 vol.%) of the total weight was found. With this value, the sample referred to as $25\text{Al}_2\text{O}_3:0.25\text{GO}$ will be simplified to “alumina-0.8rGO” during the remainder of this document. This weight loss is associated with the combustion of carbon-related content, primarily between the temperature range of 450 – 650 °C.^{244,245} Although, mass loss begins at 200 °C (due

to remaining oxygen-containing functionality),^{246,247} until a temperature of approximately 700 °C which is consistent with previous work by Lavin-Lopez *et al.* that performed a similar procedure.²⁴⁷ There is a slight drop around 170 °C during the measurements taken for Specimen 2, but it is thought that this is related to the combustion of fatty acid compounds rather combustion relating to graphene-like material,²⁴⁸ i.e., in this instance, human contamination.

After estimating the carbon content, the relative density of alumina-0.8rGO could be approximated to compare against monolithic alumina. As the composite materials contain an average of 0.8 wt.% rGO, the volume percentage (1.7 vol.%) was calculated that could be utilised to evaluate their density. Using the rule mixtures (which is based on isotropic composite materials), the average theoretical density of composite materials was determined to be 3.95 gcm⁻³. This is lower than monolithic alumina (as shown in Table 4.1), due to the addition of a filler material with a lower density. However, the relative density of the composite specimens is partially higher (99.5 % T.D), with alumina-0.8rGO composites averaging a density of 3.93 gcm⁻³. This increase in density is also seen in work by Jiang *et al.* who also sintered alumina-rGO materials;¹⁴³ furthermore, work by Zhou *et al.* presented similar values (close to theoretical density) for 1 wt.% addition of GO to alumina-based materials.²⁴³

Table 4.1 – Densities of alumina and alumina-rGO materials sintered using SPS at 1300 °C. The theoretical density is provided (in red).

Material	Density (gcm⁻³)	Relative density (%)
Alumina	3.96 (3.99)	99.2
Alumina-0.8rGO	3.93 (3.95)	99.5

4.4.2 Microstructural evaluation of alumina-rGO composites

As mentioned previously in Section 4.1, the disc-shaped specimens based on 25 wt.% alumina suspensions were similar in weight and thickness (6.5 g and 2.2 mm respectively) to those sintered from the raw powder. The SEM images provided in Fig. 4.14 illustrate the obtained microstructure of alumina-0.8rGO on various length scales.

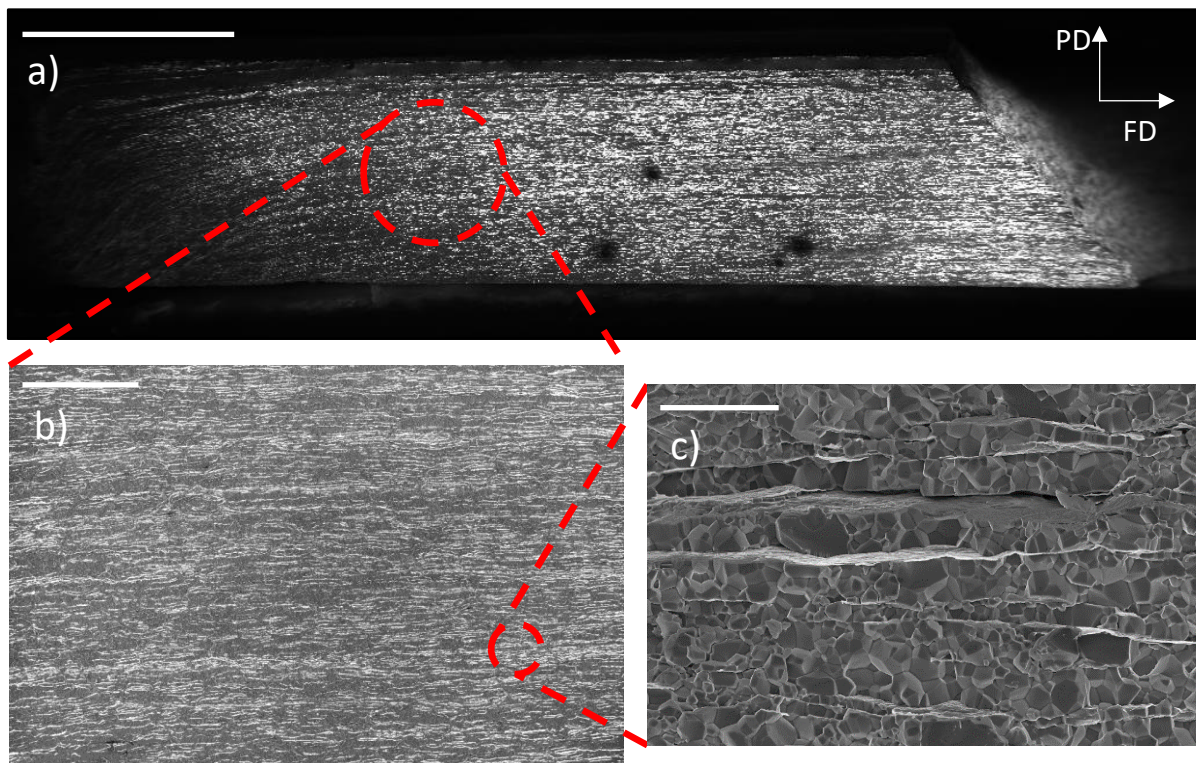


Figure 4.14 – SEM images of the microstructure of alumina-0.8rGO at various length scales **a)** 38x magnification. Scale bar = 1 mm. **b)** 200x magnification. Scale bar = 200 μm . **c)** 5000x magnification. Scale bar = 10 μm .

Upon close inspection, the dispersion of rGO is moderately homogeneous throughout the PD axis of the sintered material which is predominantly visible as regions of continuous ribbon-like material. Although, the flakes themselves are not monolayers, but rather stacks of few- or multiple-layer rGO which is visible in several regions of the composite's microstructure. With the aid of higher magnification images, one can

realise that the ceramic walls are separated by layers of graphene-like material. During SPS, the applied pressure has collapsed the once tubular pores (of $\sim 40 \mu\text{m}$) into thin channels that contain the graphene-like reinforcement. The walls of the host matrix are between $0.5 - 7 \mu\text{m}$, with an average thickness of $2.7 \mu\text{m}$: prior to sintering, the lamellae thickness was up to $10 \mu\text{m}$ in 25 wt.% scaffolds. The average alumina grain size was evaluated to be $0.7 \pm 0.4 \mu\text{m}$ for alumina-0.8rGO, whereas the average of monolithic alumina is slightly larger ($1.0 \pm 0.5 \mu\text{m}$). Fig. 4.15 demonstrates the difference in the size of alumina grains that are present in the bulk of the composite compared to its monolithic counterpart.

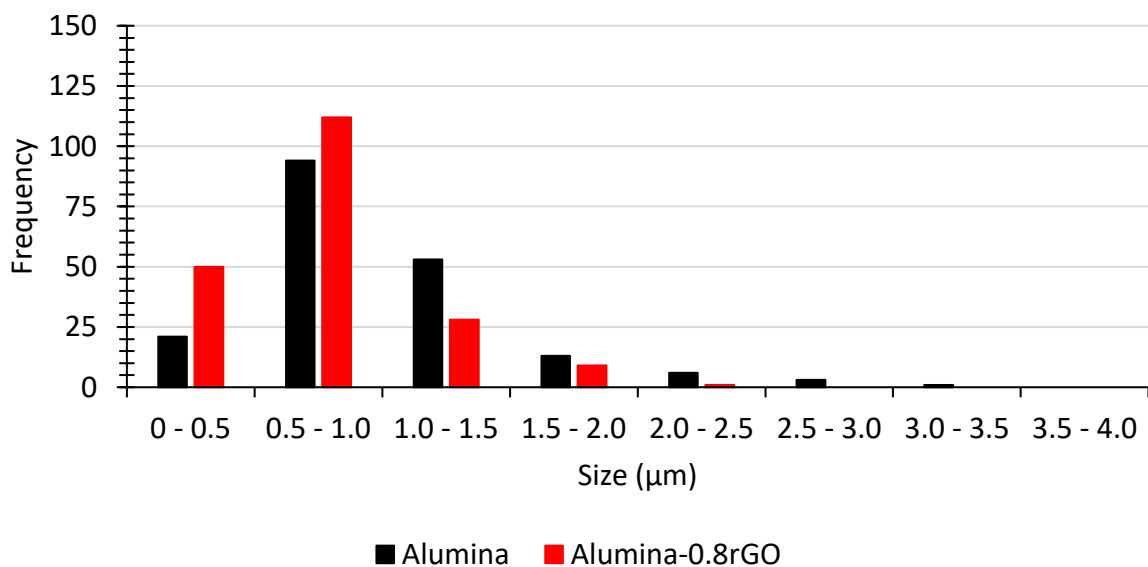


Figure 4.15 – Measured grain sizes from the microstructures of alumina-based materials sintered at $1300 \text{ }^\circ\text{C}$ via Spark Plasma Sintering.

Measured grains within the composite material were found to be below $2.5 \mu\text{m}$, compared to the higher value of $3.5 \mu\text{m}$ for monolithic alumina. The difference in grain sizes between monolithic and reinforced alumina suggests that the incorporation of GO influences grain growth within the ceramic matrix during its consolidation. These changes can be associated to the graphene-like reinforcement which is impeding the growth in the ceramic grains by creating several barriers throughout the cross-section.

Thus, the number of nearest neighbouring grains is reduced. This limitation in grain growth has been noted in other graphene-reinforced ceramics sintered with similar sintering equipment.^{143,241,249,250} The obtained microstructure possesses many similarities to the alumina-FLG composite fabricated by Sun *et al.* that was illustrated in Chapter 1, Section 1.4.2.2.¹³⁷ The microstructure consisted of highly-oriented layers of expanded graphite (5 vol.%) sandwiched ceramic walls that are similar thickness as those observed in alumina-0.8rGO (0.5 – 7 μm). Although, they processed the material in a reverse-like manner, intercalating an expanded graphite network with liquid ceramic precursor and an organic coupling agent. The microstructure of alumina-0.8rGO is also a close match to the rGO-reinforced alumina composite processed by Zhou, Qiu, Wang, and Fang *et al.*²⁴³ They introduced 1 – 4 wt.% of reinforcing material through ball-milling GO and alumina powder with ethanol as a lubricant, however their alignment of rGO with 1 wt.% addition is far less homogeneous when compared to the FD axis of alumina-0.8rGO. The comparisons to the referenced literature demonstrate that it is possible to create similar microstructures of alumina-based composites with graphene-like reinforcement through this water-based, environmentally friendly process.

Characterisation through Raman spectroscopy and XRD was also carried out on rGO-reinforced materials to compare to their monolithic counterparts. The Raman spectrum obtained from alumina-rGO composites shown in Fig. 4.16 possesses some evidence that illustrate a change to the graphene-like reinforcement after heat-treatment, i.e., sintering. Although, the low intensity of the composite's spectrum arises due to the difference in laser spot size when compared to the thickness of rGO inclusions (single-layers, or multiple-layer agglomerates) within the material. The spot size is much larger than these reinforcements, therefore it was difficult to obtain a well-resolved spectrum unless more time-consuming methods such as Raman mapping are utilised.

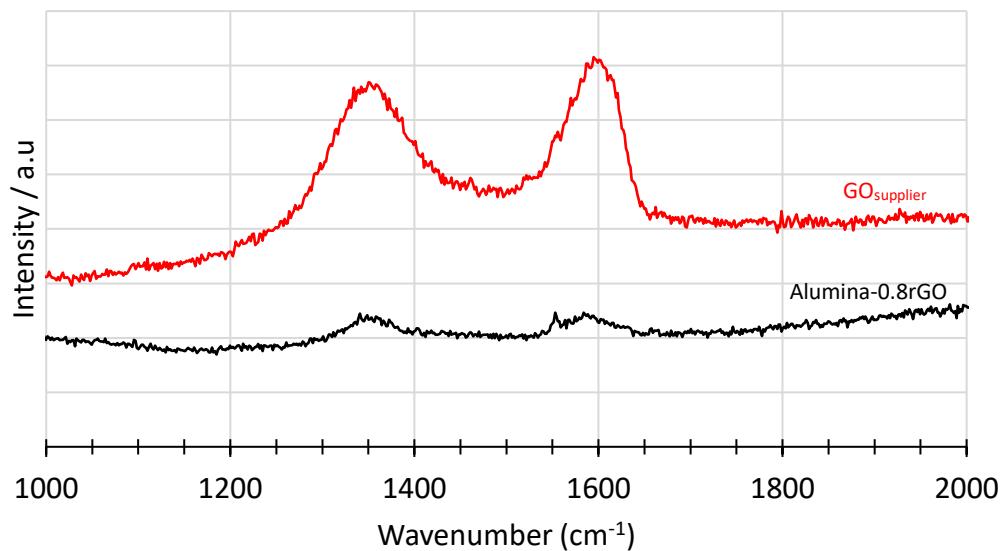


Figure 4.16 – Raman spectrum of alumina-0.8rGO material sintered at 1300 °C and GO_{supplier} for comparison.

Nevertheless, some information can be extracted. The peak position of the G signal has blue-shifted slightly (from 1596 to 1584 cm⁻¹), relating to the conversion of GO to a more graphitic-like compound with sp² hybridisation.^{219,223,251} This was illustrated in Section 4.1.1 where the spectrum of graphite is compared to GO_{supplier}. There is little change to the D/G ratio of the reinforcement found in alumina-0.8rGO (0.98 compared to 0.94). Also, a small shoulder has appeared in the G peak at 1553 cm⁻¹: some

researchers point out that this is related to stacking of disordered material which has retained some of its oxygen content after the reduction stage.^{215,252} This was realised through Gaussian curve fitting between 1500 – 1550 cm^{-1} , with the signal being labelled as the D_3 peak. This could be associated to the multiple-layer stacks of rGO noticed in previous SEM images.

The diffraction pattern shown in Fig. 4.17 is a close match to that of sintered alumina, except for the broad region relating to the PLA holder used to house the solid sample. Although, there is no clear evidence of the reduction of GO to rGO in this data, which was expected to produce a signal between 2θ values of 23 – 26 (as found in other studies involving the production of rGO).^{222,253,254} This broad peak would also coincide with one of the alumina peaks, situated at 25.44. What this pattern demonstrates is that rGO has no major effect on the crystalline structure of the α -alumina matrix. The signal at a value of 29.38 remains, evaluated as a negligible amount of an alumina-containing species (suggested as $\text{Al}_4\text{O}_4\text{C}$) within Chapter 3 (Section 3.2.1.2). This may have formed from a high-temperature reaction between the alumina matrix and the graphene-like reinforcement and/or the graphitic tooling.

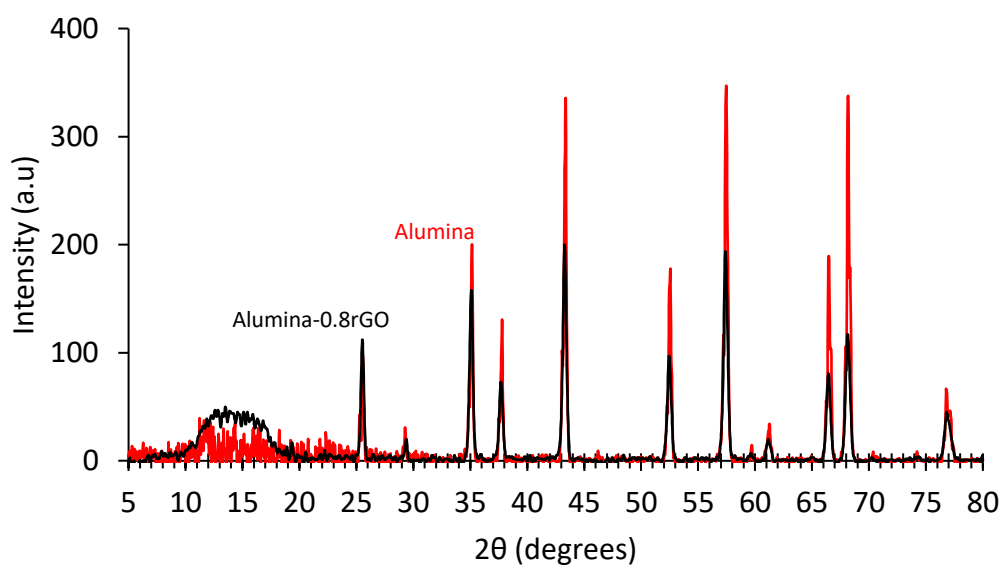


Figure 4.17 – X-ray diffraction pattern of alumina-0.8rGO sintered at 1300 °C and BA15-W alumina for comparison.

4.5 Discussion

4.5.1 Characterisation of GO batches

According to the evaluation of physicochemical features of two GOs, the primary difference between the manufacturer and custom-made batch was the average flake size and their size distribution. The batch procured through an international supplier exhibited a narrow distribution of flake sizes between 2 – 16 μm , whilst that of the custom-made suspension was far broader across 5 – 50 μm . This can be directly related to the manufacturing process itself which may have utilised different flake sizes of pristine graphene. Imperial College London utilised graphite powder with a flake size between 300 – 500 μm , so it is likely that the manufacturer (Graphenea) uses a smaller flake size. Although, there is one feature of the flakes which was not evaluated during the characterisation of GO which is the thickness of single-layer flakes. The assessment may be conducted through height mapping from atomic force microscopy measurements, which is illustrated in literature studies who have characterised graphene-like materials in this manner.^{119,217,243,255}

Furthermore, additional characterisation would be needed to provide more comprehensive evidence for the quality of these GOs; with regards to their extent of oxygen content and the functional groups that are present. The Raman spectra of both GOs were very similar, but the ratio of D/G signals was slightly lower in $\text{GO}_{\text{custom}}$ and could relate to less disorder in its structure, i.e., lower variation in oxygen functionalisation. It could also be argued that the diffraction pattern caused by $\text{GO}_{\text{custom}}$ is slightly sharper. This may confirm a more ordered structure with less variation in its oxygen moieties, which is the same suggestion from the Raman data. Further data should be acquired by using XPS to assess the carbon/oxygen ratios of the two GO batches and determine the percentage of oxygen in each batch which can provide further analysis on the extent of disorder.^{217,222,224} Simultaneously,

quantitative evidence of the various functional groups can be acquired by assessing the binding energy of the C_{1s} orbital.^{217,222}

4.5.2 Infiltration process and extent of GO deposition

It was realised that the water-based infiltration of freeze-cast materials can be a viable route to create structural ordering of two components. This was primarily demonstrated for the vacuum-assisted infiltration of porous alumina freeze-cast from low solid loadings (22.5, 25 wt.%), although it also illustrated that drop-casting could be performed on scaffolds cast from moderate solid loadings, i.e., 40 wt.%. However, the effectiveness of the secondary material's dispersion will predominantly depend on its size. This strategy could also be a possible method to incorporating other types of material (metals, other ceramics) into the ceramic scaffolds to form other ceramic-based composites. If dispersibility is an issue, then a dispersant may be added which would need to be removed prior to sintering. In these studies, the "size selectivity" is based on the pore diameter created during casting process and the dimensions of the infiltrate, i.e., the flake size of GO, being deposited within the channels of the scaffold. The viscosity of 0.25 wt.% GO_{supplier} and GO_{custom} varied, which may have also influenced the behaviour of suspensions during their uptake inside pores because the custom-made batch contained larger flakes and exhibited a higher viscosity. It was found that scaffolds infiltrated with larger flakes still contained some areas (within the core) that did not visually show any GO deposition. This was through a difference in colour, where regions were still white as opposed to possessing a grey-brown appearance.

Although, a different problem may have played a role in the extent of infiltration with larger flake sizes which is the potential blockage of pores. In Chapter 3, Section 3.1.3.1 the internal pores of 25 wt.% alumina scaffolds were found to be approximately 41 μm , and when compared to the distribution of flake sizes in GO_{custom} (5 – 50 μm) it is easy to see that a problem may occur. It relates to the size selectivity of the infiltration

process. Once a flake above 41 μm reaches a small, tubular channel that it is being forced through (under reduced pressure), it can become clogged and may impede further deposition of solid material along that specific pore. This effect has been noted in other work such as the infiltration of suspended particles into the pores of zeolitic columns,²⁵⁶ and the permeability of sand and gravel particulates into concrete.^{257,258}

After sintering materials infiltrated with $\text{GO}_{\text{supplier}}$, it was shown that the extent of filler dispersion is good throughout the (roughly) 2 mm specimens of alumina-0.8rGO, but after a thorough study of several regions of the core sections, some areas were observed which do not visually possess any reinforcement – this area of material within the microstructure is on a length scale of approximately 100 μm which is illustrated in Fig. 4.18. This is a similar finding, although on a slightly smaller scale, to the preliminary study (shown in Section 4.1) which investigated the infiltration of varying concentrations of GO. In turn this may adversely affect the behaviour of the composite, but this does impose the idea of future work to extend the period which scaffolds remain under vacuum during the infiltration process (from 15 to 30 or 60 minutes). This could allow solid material to reach pores of the alumina scaffold that may not have encountered the GO suspension.

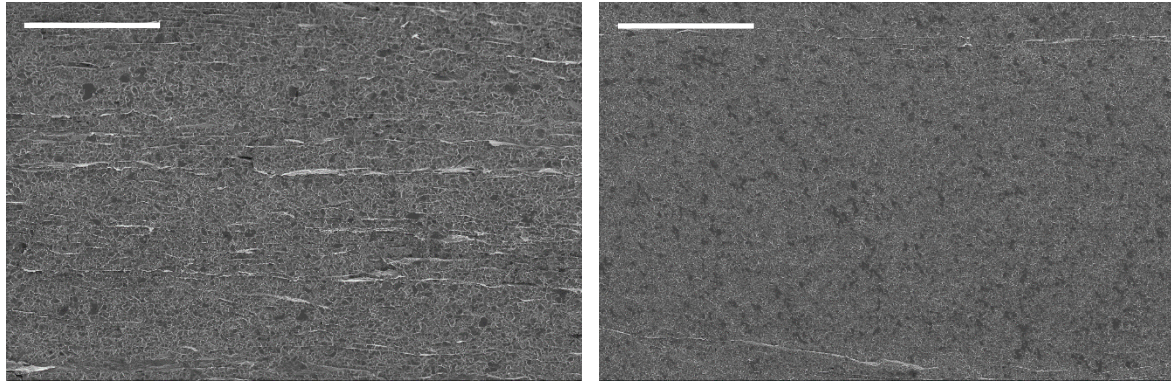


Figure 4.18 – SEM images of two sections of an alumina-0.8rGO composite sintered at 1300 °C, 50 MPa, 50 °Cmin⁻¹ heating/cooling rates, 5 min dwell. **Left)** a typical homogenous region of the composites. **Right)** inhomogeneity of the arranged rGO reinforcement within the core of the specimen. Scale bars = 50 µm.

4.5.3 Evidence for rGO in ceramic-based composites

The characterisation that was conducted provided little evidence towards the addition of rGO into the alumina matrix, or its extent of thermal reduction during SPS. The obtained Raman spectrum possessed a very low intensity because the laser spot size was much larger than the size of the rGO inclusions when measuring through the FD-PD plane, therefore it was difficult to obtain a well-resolved spectrum unless more time-consuming methods such as Raman mapping are utilised. A spectrum with far higher intensity would have produced a more reliable D/G ratio which may have been evaluated. However, this would not have assessed the reduction process of GO to rGO through SPS. XPS could be utilised to determine the change in oxygen content (mentioned previously in 4.5.1) and provide a C/O ratio, which has been shown in previous works by Yan *et al.* who studied the thermal transformation process with a number of characterisation methods.²⁵⁹ In addition, the XRD pattern did not provide any conclusive evidence on the formation of rGO in alumina-based composites – although, this is a similar result to the pattern obtained in the investigations of alumina-graphene materials (sintered with field-assisted sintering techniques) by

Rivero-Antúnez *et al.* and Zhou *et al.* Both of their results indicate that the alumina structure is not affected by the presence of graphene-like materials, hence no peak is formed in their diffraction patterns.^{243,260}

4.6 Concluding remarks

In summary, the infiltration of porous alumina materials with water-based suspensions of GO, and the subsequent consolidation of alumina-GO entities to generate alumina-rGO composites were shown. Prior to their use, the physiochemical of two graphene oxides were characterised with the main difference being the size distribution of flake sizes; the custom-made GO suspension was far broader than the batch manufactured by an international supplier (22 μm average, compared to 8 μm). The infiltration of porous, freeze-cast alumina was shown to be a promising avenue to create reinforced alumina with a homogeneous dispersion of GO. Results demonstrated that the infiltration of smaller GO flakes creates a more consistent dispersion throughout the porous host material due to the size-selective nature of the procedure. Although, this novel strategy is far from optimised and would require further experimentation.

After consolidation through SPS, highly-oriented GRM (rGO) was found to be distributed in a ribbon-like fashion throughout the cross-section of composite specimens; however, large regions of microstructure were found to be void of the filler material after infiltration with suspensions of 0.025 and 0.1 wt.% GO. Alumina scaffolds cast from suspensions of 25 wt.% solid loading infiltrated with 0.25 wt.% suspensions of GO were found to contain 0.8 wt.% of rGO after sintering. Regions that comprised solely of the alumina matrix were also found after infiltration with this concentration of GO, but they were smaller by a factor of approximately 2. A refinement of the grain size was also determined when compared to a monolithic counterpart. XRD analysis showed that the addition of rGO did not affect the structure of alumina. On the other hand, more conclusive evidence is required to obtain a better understanding on the extent of thermal reduction of GO (through SPS) in the composite materials.

Chapter 5 Mechanical and functional properties of alumina-based materials

This Chapter illustrates the measurements of mechanical and functional properties of alumina-based materials that were described in the previous Chapters to evaluate their potential applications. Two materials were tested: monolithic alumina, and alumina-0.8rGO that possesses highly-oriented GRM. Both these materials were identified as fully-dense materials (<99 % T.D) when sintered with the following conditions: 1300 °C, 50 MPa applied pressure, heating/cooling rates of 50 °Cmin⁻¹, and a dwell time of 5 minutes. The obtained values are also compared to results gathered from literature which produced alumina-GRM composites. Ultimately, the aim of this testing was to identify the mechanical and physical influences of a small proportion of GRM that was distributed in a specific fashion within the host material. The disc-shaped samples were ground and cut to produce square- or bar-shaped specimens that are illustrated in Fig. 5.1. The orientation of the testing procedures is also highlighted – to clarify the mechanical testing, 4-point flexure tests were carried out on sectioned bars and Vickers indentations were created along the PD-FD plane afterwards.

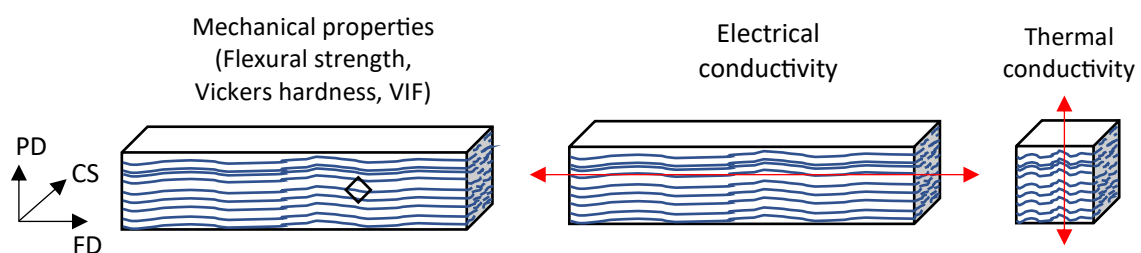


Figure 5.1 – Illustration of the specimens produced from disc-shaped, sintered materials to produce square- and bar-shaped specimens for mechanical and functional testing.

5.1 Mechanical properties

Three mechanical properties were investigated in this section: namely, the hardness, flexural strength, and fracture toughness. Hardness values were calculated at different loadings to probe both the bulk hardness and the localised microhardness around the filler material within alumina-0.8rGO. The fracture toughness was determined using the VIF method, then the possibility of extrinsic toughening mechanisms was investigated through SEM (provided in the discussion section). 4-point flexure tests were carried out on bar-shaped specimens to provide an indication on the influence of highly-oriented rGO. In all testing scenarios monolithic alumina sintered through SPS with the same conditions (1300 °C, 50 MPa, 50 °Cmin⁻¹ heating/cooling rates, 5 minute dwell) is used as a comparison.

5.1.1 Vickers hardness

Indentation tests were carried out along the FD axis (shown in Fig. 5.1) of specimens to determine both the bulk hardness and microhardness. A separate test along the CS plane was also performed to evaluate the nature of the dispersion of rGO throughout the alumina matrix on the microhardness. Fig. 5.2a and 5.2b display optical microscopy images of cross sections of polished surfaces for monolithic alumina and alumina-0.8rGO, whilst Fig. 5.2c and 5.2d show Vickers indentations produced from a 2 kg load. There were no major defects detected along the surfaces except for a few minor scratches that are predominantly visible on the composite material. While monolithic alumina shows a homogeneous surface, the presence of rGO reinforcement is noticeable (from left to right) along the FD axis of the composite.

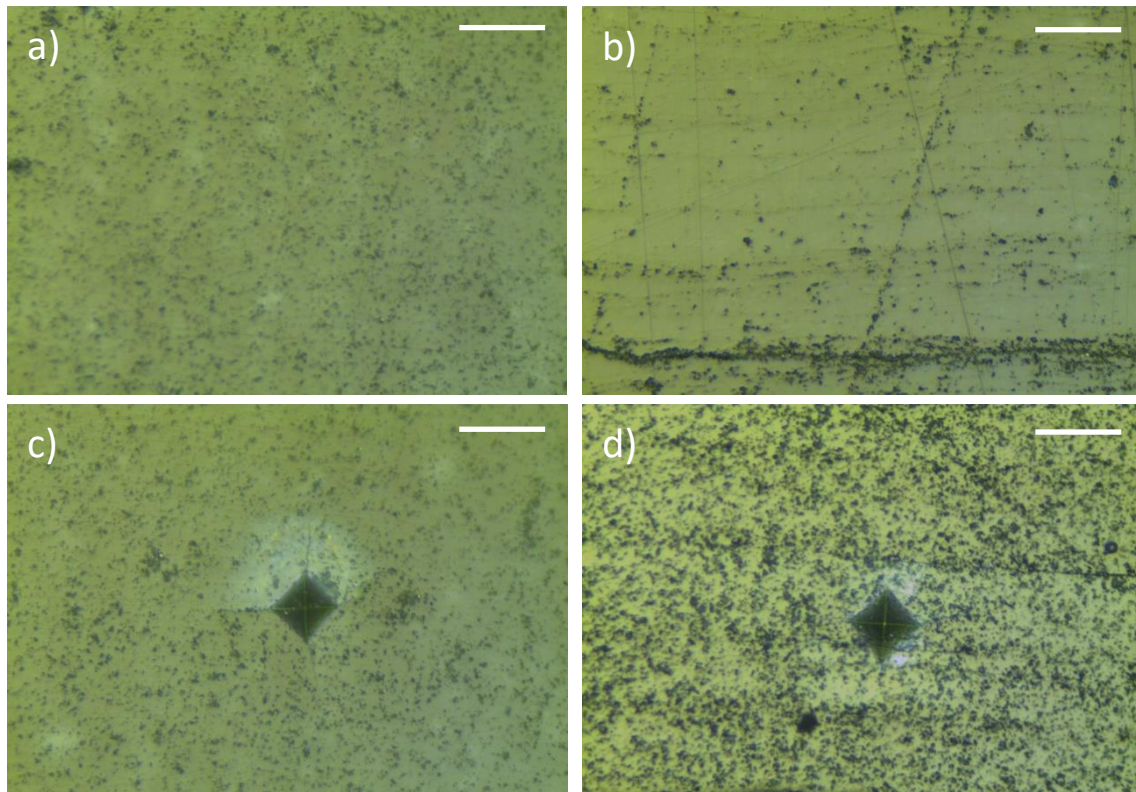


Figure 5.2 – Optical micrographs of the FD-PD plane of alumina-based materials polished to a 1 μm finish, and Vickers indentations created using a 2 kg load. **a)** monolithic alumina. **b)** alumina-0.8rGO. **c)** monolithic alumina after indentation. **d)** alumina-0.8rGO after indentation. Scale bars = 50 μm .

Figure 5.3 illustrates the microhardness values at indentation loads between 0.5 – 10 kg. Following the methods for determining hardness described in Chapter 2 (Section 2.3.3), monolithic alumina reaches a hardness of 21.89 GPa. After reinforcement with a low proportion (<1 wt.%) of rGO, hardness decreases to 20.16 GPa. This change is relatively small (a 5% reduction), demonstrating that the composite material retains a high measure of hardness. At higher loads beyond 1 kg the bulk hardness is measured, which was found to be lower in both materials falling to 20.27 and 17.17 GPa respectively (at 10 kg loading). This illustrates a loading dependence on the obtained hardness values in these two materials: this relationship is referred to as the indentation size effect and is commonly seen in other literature data.^{261–264}

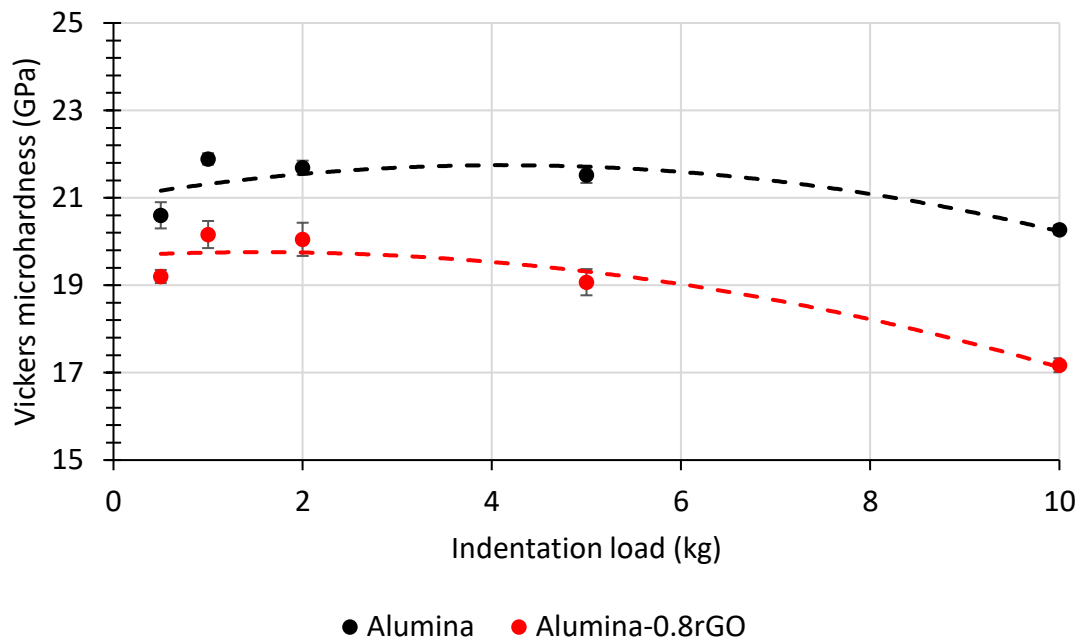


Figure 5.3 – Calculated hardness values at various loads for alumina-based materials sintered at 1300 °C, 50 MPa, 50 °Cmin⁻¹ heating/cooling rates, 5 min dwell.

A separate study was performed at the lowest applied load (0.5 kg) to understand if the dispersion of rGO was different along the FD-PD and PD-CS planes of the composite. Fig. 5.4 illustrates the two planes and exhibits no major evidence to suggest any inhomogeneity as the layered reinforcement appears to be consistent along both directions. Fig. 5.5 supports this claim as the plot of microhardness measured along both planes displays there was no significant difference in hardness between the FD-PD and PD-CS planes. Furthermore, indentations created in regions through the reinforcement of rGO provide similar results to those that were performed on areas that appeared to be free of them – although, rGO may lie just below the surface.

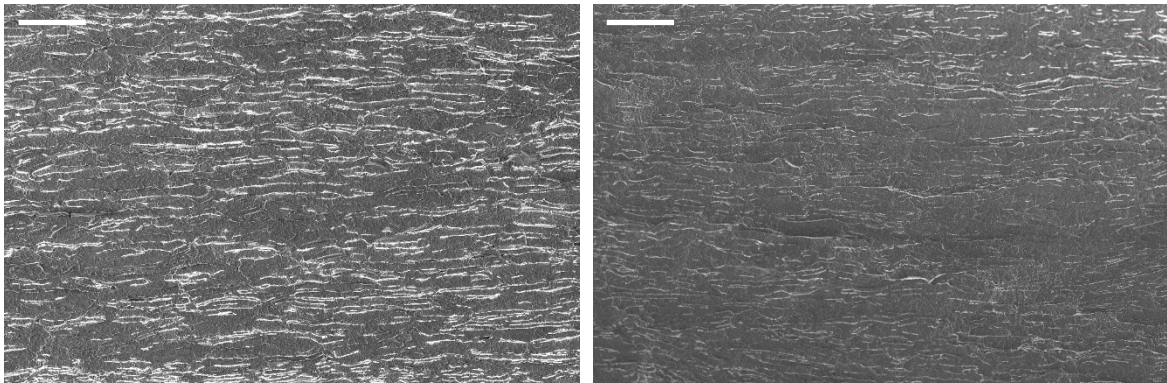


Figure 5.4 – SEM images of alumina-0.8rGO across two different planes to illustrate the homogeneity in rGO reinforcement. **Left)** FD-PD plane. **Right)** PD-CS. Scale bars = 50 μm .

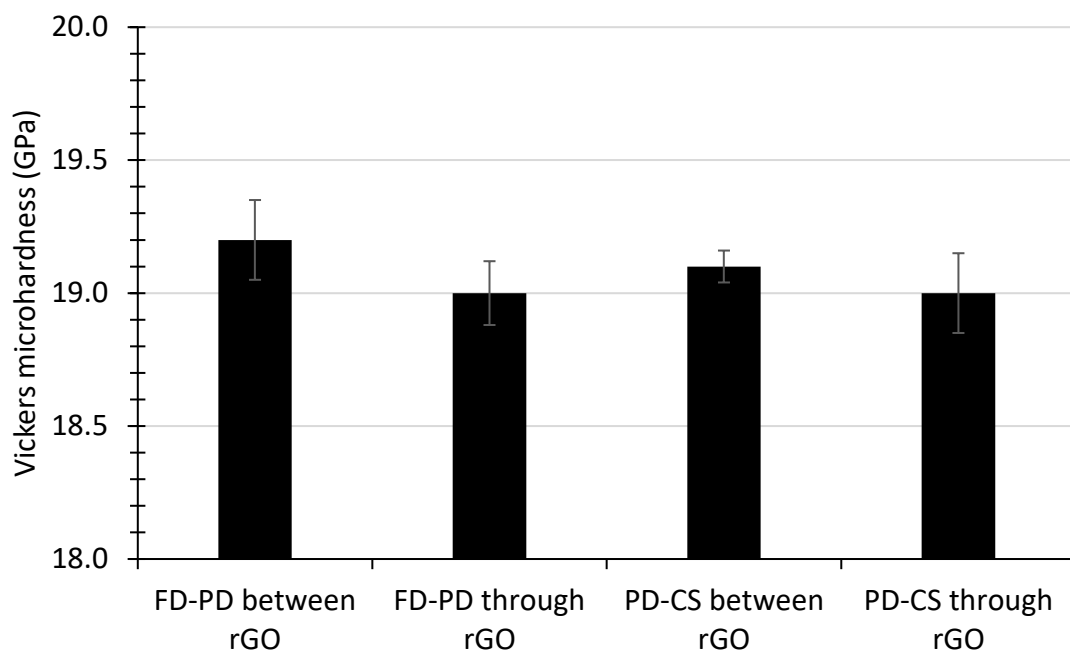


Figure 5.5 – Microhardness values of alumina-0.8rGO (at 0.5 kg load) through two different orientations, representing regions that were indented between or through visible areas of rGO.

5.1.2 Flexural strength

The flexural strength of alumina-based materials was investigated through 4-point bending tests using the method explained in Chapter 2 (Section 2.3.5). This was conducted in combination with microscopy studies to understand the influence of highly-oriented rGO layers within the composite material. Table 6.1 displays the calculated results for monolithic alumina and alumina-0.8rGO, indicating that the composite specimens were 20 % stronger during 4-point flexure.

Table 5.1 – Flexural strength values for alumina-based materials sintered at 1300 °C, 50 MPa, 50 °Cmin⁻¹ heating/cooling rates, 5 min dwell.

Material	Flexural strength (MPa)	Standard deviation (MPa)
Alumina	262	± 35
Alumina-0.8rGO	314	± 32

The SEM images of fracture surfaces in Fig. 5.6 show the microstructures of monolithic and rGO-reinforced alumina (Fig. 5.6a and 5.6b respectively) specimens and a clear difference in their fracture surfaces is visible. In monolithic alumina the fracture surface is smooth and homogeneous, whilst the surface of alumina-0.8rGO clearly show a layered microstructure where areas of rGO material, i.e., white stripes extending across the FD axis, appear to have been pulled out from the ceramic matrix. Fig. 5.6c and 5.6d demonstrate a step-like morphology on the microscale of the composite, arising from fracture through the layers of ceramic and graphene-like components. The presence of slightly agglomerated rGO material can also be observed in the microstructure of alumina-0.8rGO, e.g., in the middle of Fig. 5.6b.

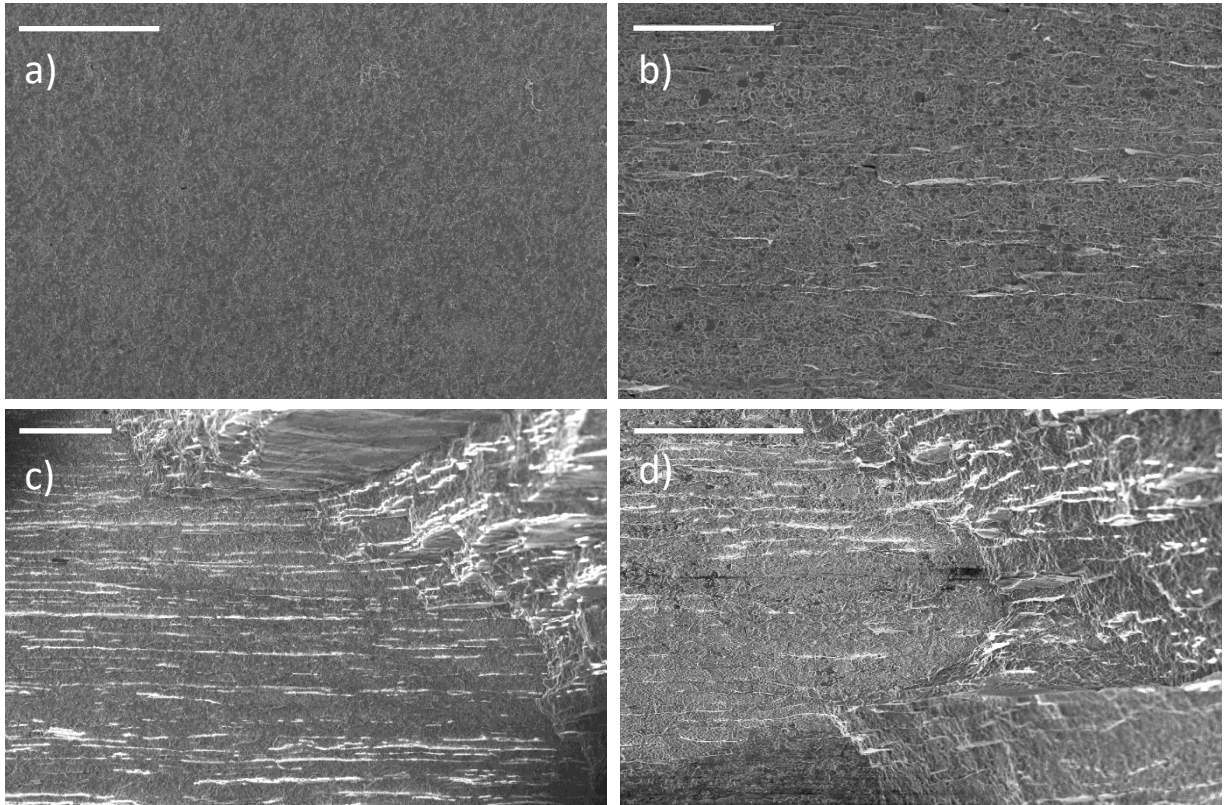


Figure 5.6 – SEM images of the <99 % T.D fracture surfaces illustrating the differences in their microstructures. **a)** monolithic alumina. **b)** alumina-0.8rGO. **c)** and **d)** step-like morphology of alumina-0.8rGO after failure. Scale bars = 50 μm .

5.1.3 Indentation fracture toughness

The Vickers indentation fracture method was chosen to analyse the toughness of the composite material and comparing it with the monolithic one. Testing was conducted following the methods reported in Chapter 2 (Section 2.3.4) between indentation loads of 1 – 30 kg. Two different equations – the Palmqvist and Anstis formulae – were utilised to evaluate fracture toughness. SEM images displayed in Fig. 5.7 show the indentations created in monolithic and rGO-reinforced alumina at the highest load of 30 kg.

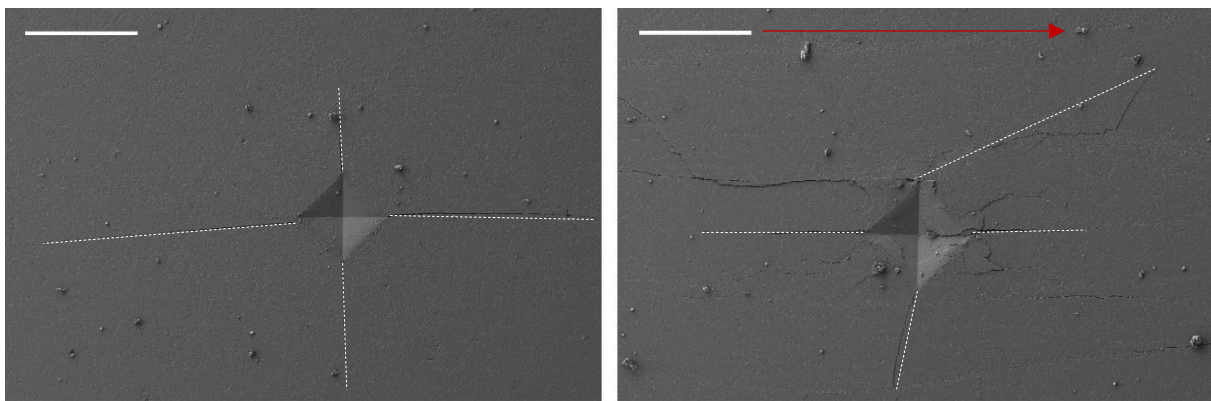


Figure 5.7 – SEM images of Vickers indentation patterns at a load of 30 kg on alumina and alumina-0.8rGO cross sections. **Left)** monolithic alumina. **Right)** alumina-0.8rGO. Scale bars = 200 μm . The red arrow indicates the FD axis. The dashed white lines illustrate which cracks were taken into consideration and measured to calculate the fracture toughness.

The cracks emanating from the apices of Vickers indentations made in monolithic alumina were quite linear which is representative of brittle failure in materials. In contrast, the cracking pattern in alumina-0.8rGO was far more complicated, with a multitude of cracks propagating from both the apices and the sides of the indentations. The indentation itself was also slightly larger due to the decrease in microhardness that was determined in the previous section. Furthermore, cracks appeared to be

slightly shorter (than those in monolithic alumina), whilst several of them have been deflected from the PD axis towards the FD axis. This can be attributed to rGO that has been incorporated throughout the host alumina that has created interfaces for cracks to propagate along. The complex cracking pattern can make it difficult to identify which cracks should be utilised when determining the fracture toughness – the annotations in Fig. 5.7 provide an indication on which cracks should be used, and which ones that were avoided. In some instances, cracks were not produced on the apices of indentations and in these cases the crack length was taken as zero. Fig. 5.8 illustrates the fracture toughness values obtained from the VIF method following the Palmqvist and Anstis formulae. The plot of results shows that the alumina-0.8rGO possesses a higher fracture toughness than its monolithic counterpart at all tested loads. However, the indentation size effect has caused varying values of toughness (akin to the hardness values).²⁶⁵ When both formulae are applied to the composite material, the results are in good agreement with each other: however, evaluating monolithic alumina with the Palmqvist equation generated higher results than those from the Anstis equation.

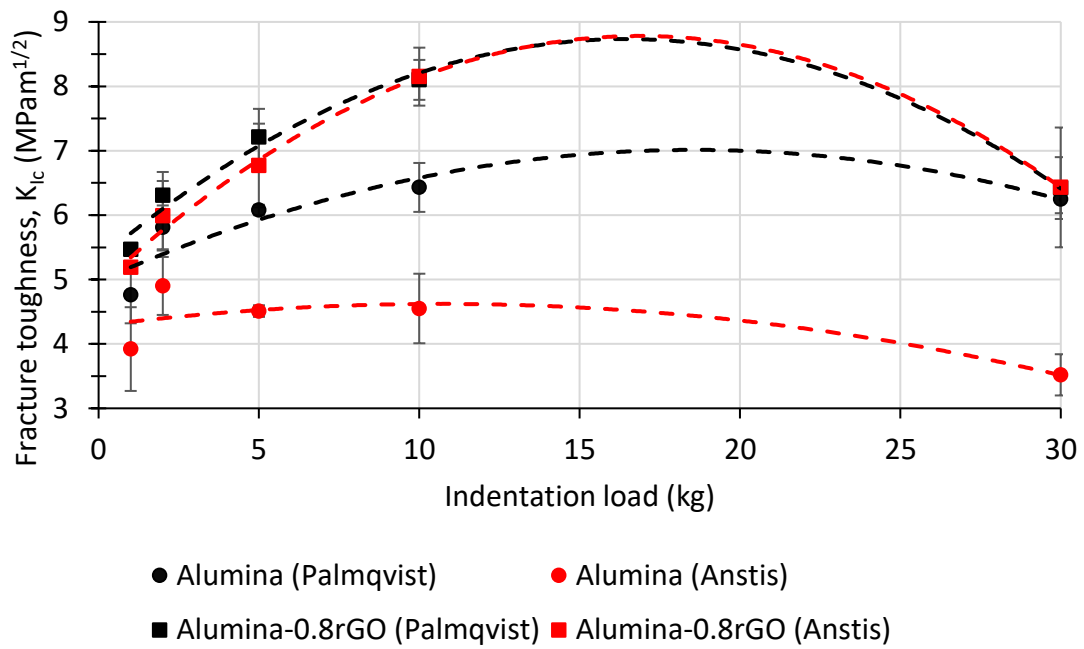


Figure 5.8 – Calculated VIF values at various indentation loads using the Palmqvist and Anstis formulae for alumina-based materials sintered at 1300 °C, 50 MPa, 50 °Cmin⁻¹ heating/cooling rates, 5 min dwell.

5.2 Functional behaviour

In Chapter 1 (Section 1.4.1) the attractive properties of graphene and GRMs were discussed regarding their integration within composite materials. This included their incorporation to alter other functional properties, including their thermal and electrical behaviour. The capability of electrical or thermal transport will be directly affected by the homogeneity, orientation, and the extent of agglomeration of the reinforcement material.¹³⁹ Moreover, the connectivity of GRMs within the matrix will influence electrical transport. The following segment illustrates the thermal and electrical behaviour for alumina-based materials.

5.2.1 Thermal conductivity

The thermal conductivity was measured through the thickness of square-shaped specimens, such that the out-of-plane conductivity was measured along the PD axis. One composite specimen was also fabricated using a sintering temperature at 1500 °C with the goal of measuring a difference based on the extent of rGO reduction. The disc-shaped specimen broke during SPS which is why further mechanical testing was not conducted – fortunately a square-shaped specimen could be recovered and prepared to measure its thermal properties. The thermal conductivity results were obtained through the method described in Chapter 2 (Section 2.3.7) and calculated after identifying the relationship between temperature and specific heat capacity for each material (illustrated in Table 5.2) that were derived from calorimetry testing.

Table 5.2 – Calculated specific heat capacity relationships for alumina-based materials.

Material	Measured relationship
Alumina	$C_p = 0.0015T + 0.7257$
Alumina-0.8rGO@1300	$C_p = 0.0014T + 0.7109$
Alumina-0.8rGO@1500	$C_p = 0.0016T + 0.6951$

Fig. 5.9 displays the thermal conductivities of the three tested materials. The trend illustrated by monolithic alumina is a decrease in thermal conductivity with increasing temperature. Unexpectedly, the addition of highly-oriented rGO throughout the alumina matrix has reduced the out-of-plane thermal conductivity across the chosen temperature range. However, the trend shown by alumina-0.8rGO sintered at 1300 °C appears to be somewhat linear in its appearance as the measurement temperature rises. At 25 °C, the conductivity of monolithic alumina is 39.6 W(mK)^{-1} , dropping to 9.5 W(mK)^{-1} after the incorporation of highly-oriented rGO when the composite is sintered at the same temperature. At high temperatures (750 °C), these values decrease to 20.3 and 7.3 W(mK)^{-1} for the monolithic and composite material respectively. When alumina-0.8rGO is sintered at 1500 °C, the results are higher than that of the same material sintered at a lower temperature; a value of 26.2 W(mK)^{-1} was determined at 25 °C which drops to 12.6 W(mK)^{-1} at 750 °C.

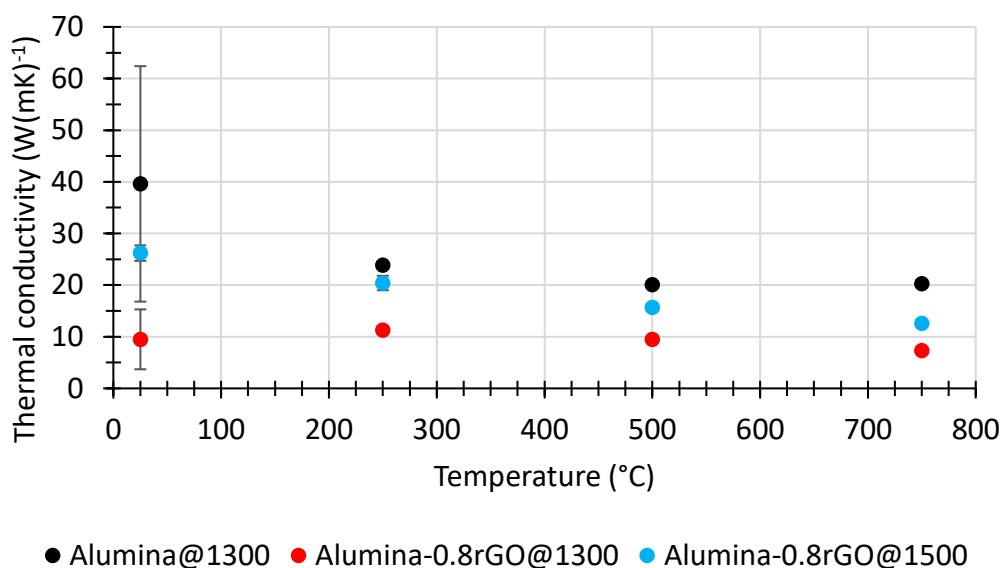


Figure 5.9 – Plot of the out-of-plane thermal conductivity at increasing temperatures for alumina-based materials.

5.2.2 Electrical conductivity

It was expected that during the SPS process the GO is thermally reduced and be transformed into rGo which is an electrically conductive material. The electrical resistivity was measured (to determine the conductivity) following the method described in Chapter 2 (Section 2.3.6) with the aim of providing evidence if the alumina-based composites: i) become conductive after the addition of highly-oriented rGO at the defined mass fraction (0.8 wt.%), and ii) possess an interconnecting network of rGO throughout the whole specimen that is above the percolation threshold. Two regions of the disc-shaped specimens obtained from SPS were probed: namely, the core and perimeter of composite materials. Fig. 5.10 displays the orientation that bar-shaped specimens were cut from to measure the in-plane electrical resistivity along the FD axis of material.



Figure 5.10 – Illustration of the orientation that 2-probe resistivity measurements were conducted along. The dashed lines represent the electric field lines that would be generated due to electrical transport.

Table 5.3 displays the electrical resistivities (and conductivities) from two sections of the disc-shaped composite. As an electrically insulating material, alumina exhibits a very high resistance and therefore possesses significantly limited conductivity. However, after the addition of a small fraction of rGO, there was a stark difference which has increased the electrical conductivity by at least six orders of magnitude when compared to the monolithic material. Although, the conductivity of the core and perimeter were considerably different: the specimen cut from the perimeter demonstrated a conductivity that was two orders of magnitude higher than the core, rising from 1.3×10^{-4} (0.00013) to 6.9×10^{-2} (0.069) Scm^{-1} . This difference can be related to the SEM images shown in the discussion of the previous Chapter (Section 4.5.2) which illustrated sections of the core that did not possess any filler material.

Table 5.3 – Table of in-plane electrical resistivities and conductivities at ambient conditions for alumina-based materials sintered at 1300 °C, 50 MPa, 50 °Cmin⁻¹, 5 min dwell. Literature data for monolithic alumina from Centeno et al. is included for comparison.

Specimen	Electrical resistivity (Ωcm)	Electrical conductivity (Scm^{-1})
Alumina ²⁴¹	1×10^9	1×10^{-9}
Alumina-0.8rGO (core)	7.7×10^3	1.3×10^{-4}
Alumina-0.8rGO (perimeter)	15	6.9×10^{-2}

5.3 Discussion

5.3.1 Mechanical behaviour

The microhardness measurements for monolithic alumina agree with other dense, fine-grained alumina ($<0.6 \mu\text{m}$) which have been sintered using field-assisted techniques.^{266,267} However, the mentioned literature does apply much higher pressures beyond 70 MPa,²⁶⁷ or slightly higher temperatures of 1350 °C.²⁶⁶ The decrease of 9 % microhardness (at 1 kg loading) in alumina-0.8rGO suggests a lesser ability to resist plastic deformation compared to its monolithic analogue. This small reduction is indicative of adding a low amount of reinforcement that is more compliant than the ceramic grains that surrounds it.^{143,266} Regardless of the refinement in the grain size from 1 to 0.7 μm (demonstrated in Chapter 4, Section 4.4.2) in monolithic and rGO-reinforced alumina respectively, the results suggest that the addition of the soft graphene-like material is the dominant factor in the drop of the hardness values. The similar values obtained from testing the microhardness of alumina-0.8rGO in two different planes is most likely attributed to well distributed layers of rGO throughout the host alumina along both the FD and CS axes.

The value obtained for the flexural strength of monolithic alumina (262 MPa) appears to be quite low considering that one author state values as high 490 MPa,²⁶⁸ but it is generally observed to be between 280 - 400 MPa depending on the processing conditions that are utilised.^{143,241,269} This is a broad range of values, however flexural strength results can drastically differ depending on the type of test fixture utilised. It was briefly mentioned in Chapter 1 (Section 1.1.3.1) that the four-point flexure method may be preferred as it provides a more uniform stress concentration across the volume of test specimens, which typically results in lower reported values than those calculated from three-point flexure. For example, Centeno *et al.* sintered at higher temperatures of 1500 °C, 80 MPa pressure, and a shorter holding time of 1

minute and they report that the flexural strength (through three-point flexure) of dense monolithic alumina with a grain size of up to 4 μm reached 350 MPa.²⁴¹ Liu and Wang *et al.* sintered alumina platelets through hot-pressing to a density of 96 % T.D at 1300 °C, 30 MPa, and a two hour dwell and determined its strength (through three-point flexure) to be 326 MPa.²⁶⁸ Unfortunately, they did not provide a grain size for their fabricated microstructure. Boniecki *et al.* fabricated dense (99 % T.D) alumina with a grain size of 0.8 μm through cold pressing and conventional sintering using 1350 °C and a one hour dwell.²⁶⁹ Testing (through four-point flexure) on thirty samples produced an average flexure strength of 277 MPa which is a close match to the value determined from this study. It has been proposed that large differences in flexural strength may arise from the porosity fraction,²⁷⁰ although the alumina-based materials that have been fabricated herein are fully dense (<99 % T.D). Work by Rowthu *et al.* produced alumina with remaining porosity (of 7 %) and a grain size of approximately 0.3 μm after cold pressing and sintering at 1300 °C inside a conventional furnace with one hour dwell.²⁷⁰ Their flexure strength values (through four-point flexure) ranged between 260 – 490 MPa from at least ten samples, with most of the samples sintered at the stated conditions lying closer to the middle of the specified range. The grain size is far lower than what was shown in this work which could correlate with their far higher flexure strength values although the porosity fraction is far higher. However, this is contradictory to what the authors suggest which is that the total porosity is a key microstructural property that will affect flexural strength (as opposed to the grain size).²⁷⁰

Nevertheless, the trend of increasing flexure strength is consistent with previous studies that produced alumina-based materials with small amounts of GRM.^{93,137,143,241,271} Centeno *et al.* demonstrated that incorporating 0.22 wt.% of rGO within alumina can lead to a flexure strength of approximately 610 MPa – this is an increase of roughly 74 % over monolithic alumina.²⁴¹ The alumina-FLG composite containing 5 vol.% reinforcement that was fabricated by Sun *et al.* demonstrates a 32 % increase in its flexural strength when compared to its monolithic counterpart (424 to 560 MPa).¹³⁷ They state that the SPS conditions were a temperature of 1400 °C

and 40 MPa but they did not provide a dwell time. Unexpectedly, the addition of 0.5 vol.% rGO in the study by Lee *et al.* demonstrated no major change to the flexural strength, but integration of expanded graphite raised the flexural strength from 330 to 424 MPa, i.e., an improvement of 28 % over alumina.²⁷² The materials were cold pressed then consolidated with conventional sintering using 1700 °C and three hours of dwell. The enhancements in these studies are thought to be related to the interfaces between ceramic and reinforcing components which can impede the motion of fracture.²⁷² Some agglomerates of multiple layers of rGO appear to be visible within the microstructure of alumina-0.8rGO shown in Fig. 5.6b which may contribute towards the small increase (20 %) in strength from 262 to 314 MPa.^{93,143,241} Limitations in the improvement of flexural strength can be caused by agglomerates of GRMs forming defects within the composite microstructure which may serve as origin points for crack initiation.^{93,144} This suggests that the incorporation of highly-oriented, multi-layer agglomerates of rGO may only improve the flexure strength by a small proportion. Otherwise, the findings conform with the results obtained by other groups that show an improvement after the integration of GRMs into alumina.^{143,241}

The results obtained for the fracture toughness varied when applying the Palmqvist and Anstis formulae, which is the same result demonstrated by Fabijanić *et al.* who studied several formulae that showed varying results for the fracture toughness of cemented carbides.¹⁸⁹ Their study also illustrates that identification of the type of crack can provide evidence towards an appropriate selection of formula in relation to the variation of fracture toughness values. Radial-median cracks (shown in Chapter 2, Section 2.3.4) can be characterised by cracks that connect to the deformation pattern after polishing the surface. This type of cracking pattern formed in the Vickers indentations that are shown in the optical micrographs of Fig 5.11 for both alumina-based materials in patterns made at 30 kg; deformation patterns created at the lower loads were also checked and found to display the same cracking pattern. These radial-median cracks provide evidence to promote the use of the Anstis equation as opposed to the Palmqvist equation for both alumina-based materials based on the referenced literature.¹⁸⁹ Some groups that have worked with ceramic-based materials propose

that results at loads <10 kg are more valid in hard materials.^{189,190,260,273–275} Thus, this suggests that the values of fracture toughness are more likely to be those calculated from loading at 30 kg so it can be thought that the values of 3.52 MPam^{1/2} for monolithic alumina and 6.43 MPam^{1/2} for alumina-0.8rGO are the most representative.

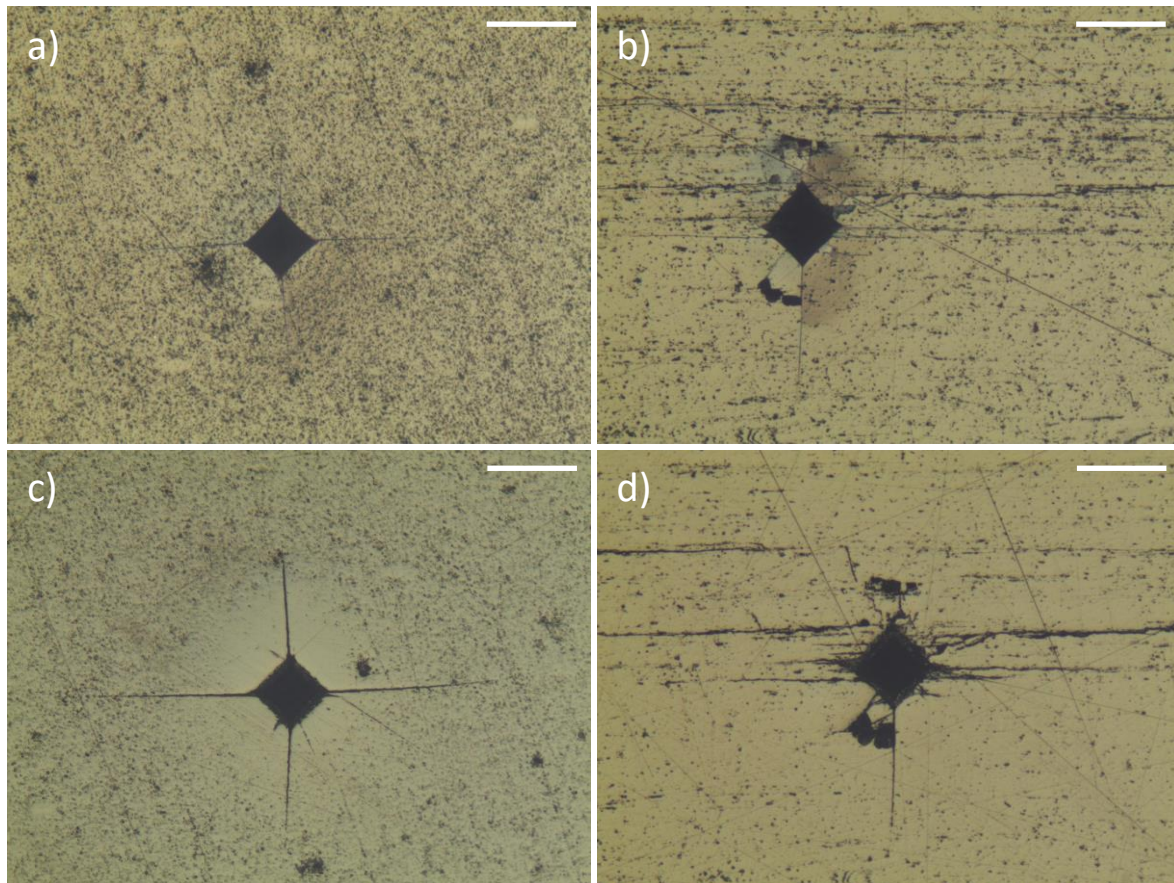


Figure 5.11 – Optical micrographs of material surfaces before and after polishing which illustrate the radial-medial cracks produced from Vickers indentations (made at 30 kg). **a)** monolithic alumina before polishing, **b)** alumina-0.8rGO before polishing. **c)** monolithic alumina after polishing. **d)** alumina-0.8rGO after polishing. Scale bars = 200 μm.

With these values in mind, an increase of approximately 80 % is seen after the addition of highly-oriented rGO at both 10 and 30 kg loadings. Some previous authors suggest an increase after the addition of similar proportions of GRMs into ceramic-based composites.^{266,274} Several studies also suggest a dependence on the fraction of

graphene-like materials that are incorporated within ceramic matrices,^{143,241} which can sometimes lead to a diminished toughness.^{93,276} Although, it is difficult to compare the absolute values as many studies utilise notched beam methods which are considered more appropriate (over indentation techniques). Otherwise, percentage increases close to those reported herein are seen in studies by Ahmad *et al.* (73 %, with 50 nm graphene sheets) and Kim *et al.* (75 % with 150 μm , electrochemically-expanded graphene flakes).^{272,277}

The improvement in fracture toughness and flexural strength for the composite can be attributed to extrinsic toughening mechanisms (exhibited in Fig. 5.12) that have been introduced due to the addition of rGO within the alumina matrix. Many of these mechanisms are reported in prior research on ceramic-GRM composites and have been referenced where necessary. It was previously illustrated that the deformation patterns from Vickers indentations displayed deflected cracks predominantly along the FD-axis. This deflection can be related to the layer-by-layer fashion in which rGO is distributed through the alumina matrix, promoting propagation along the interfaces between the host and filler materials (as shown in Fig 5.12a).^{137,241,266,278} Subsequently, this generated a more torturous cracking pathway throughout the microstructure compared to the monolithic material and increases the work of fracture. In addition, debonding between the two components can be observed (in Fig. 5.12b and 5.12c) along cracks in several regions that the rGO inclusions are located, which would require further energy to disrupt the frictional force that would be generated.²⁷⁹ This also leads to the crack bridging of the flexible rGO inclusions and improves the material's toughness by plastically deforming.^{93,137,241,266,278} Furthermore, crack branching is also evident (in Fig. 5.12c), raising the work of fracture because propagating cracks are redirected.^{93,266}

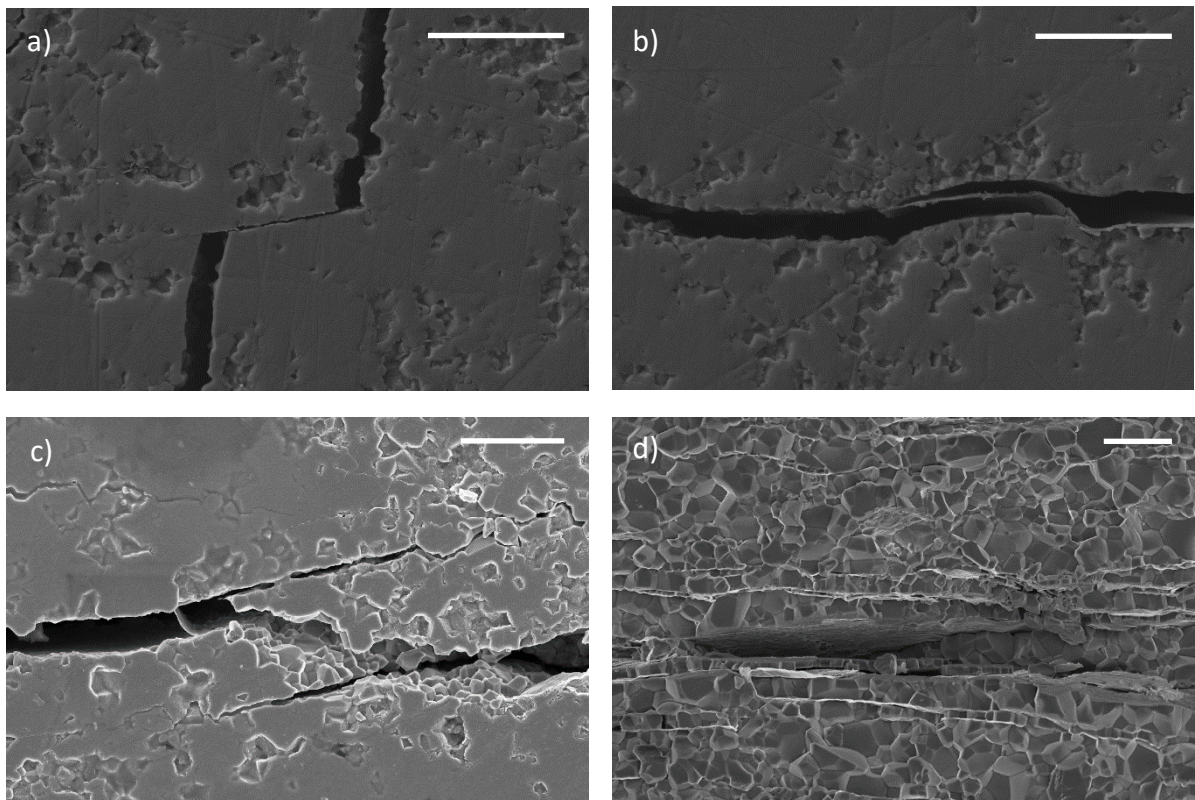


Figure 5.12 – High magnification SEM images of alumina-0.8rGO after Vickers indentation and flexure strength testing. **a)** crack deflection, **b)** crack bridging and rGO debonding, **c)** crack branching and intergranular fracture, **d)** pull-out of matrix and reinforcement. Scale bars = 5 μm . Higher contrast thresholds were set in **c)** and **d)** so that exposed ceramic grains were in view.

The pull-out of both ceramic and highly-oriented rGO components was visible in fracture surfaces after 4-point flexure tests (in Fig. 5.12d) which contributes as a toughening mechanism towards the improvement in mechanical behaviour.^{93,243,266,278} This mechanism plays a role in the step-like fracture appearance which was previously exhibited in this Chapter. Friction between the crack faces absorbs some energy and hence increases the toughness; higher contact area between the two would promote a higher degree of toughening.^{137,243,266,278,280} The wavy appearance of many of the rGO inclusions would also increase the frictional forces required to initiate the pull out of materials.¹³⁷ The presence of both intergranular fracture and intragranular modes

are present in the fracture surfaces of the composite material similar to that of monolithic alumina shown in Chapter 3, Section 3.2.1.2. Cracks in Fig. 5.12c can be seen predominantly propagating along the boundaries of neighbouring grains rather than propagating through the grains themselves. This would also increase the work of fracture and contribute to the improvement in toughness.²⁶⁶

5.3.2 Electrical and thermal transport

The reduction in the out-of-plane thermal conductivity is unexpected given that the thermal properties of single-layer graphene is extremely high. Although, the proportion of rGO that has been introduced into the ceramic matrix is quite low (0.8 wt.%), leading to suggest that another factor may be in effect. Evidence in the literature work by Tuan *et al.* suggests that the grain size of the host matrix plays an important role in thermal conductivity.²⁴⁹ This grain size dependence is due to thermal boundary resistance (often referred to as Kapitza resistance) of neighbouring grains; as the number of grain boundaries increases within a given material, the number of interfaces that must be overcome increases.^{276,281–283} This leads to greater carrier scattering of phonons within the crystal structure lattice which disrupts the transport capabilities and decreases its thermal conductivity. In the previous Chapter (Section 4.4.2), the grain size of monolithic and rGO-reinforced alumina was found to be 1.0 to 0.7 μm respectively. Also, the composite material sintered at 1500 °C possessed a grain size of 0.9 μm . As the grain size of monolithic alumina is higher than those of the composite materials this would correlate with less interfacial resistance, and therefore a higher thermal conductivity value. One may presume that the in-plane conductivity of alumina would increase after the addition of rGO, however literature work by Çelik *et al.* demonstrates that this behaviour is only seen at temperatures above 600 °C for graphene-like additions between 5 – 15 vol.%.²⁸⁴

Comparing the obtained values to work that has been previously performed, a similar decrease in alumina-GRM materials is noted when measuring the out-of-plane thermal

conductivity.^{276,284} Rutkowski *et al.* fabricated dense, alumina-based composites that were reinforced with multilayer graphene platelets and consolidated through SPS at 1550 °C. They demonstrate that conductivity decreases from 31.6 to 27.1 W(mK)⁻¹ (measured at 25 °C) when increasing the wt.% of 4 nm thickness graphene from 0 to 1.²⁸⁴ It is true that the composite with 0.8 wt.% rGO that was fabricated from this study does exhibit agglomeration of rGO in regions of its microstructure. Unfortunately, the Rutkowski and co. do not provide SEM images of their material that contains 1 wt.% reinforcement so it cannot be clarified whether agglomerates exist. The value of 31.6 W(mK)⁻¹ decreased as the mass fraction increased (to 19.7 W(mK)⁻¹ with 10 wt.% addition) which they suggest is based on the poorer orientation of graphene material when compared SEM images of a composite that possess 2 wt.% reinforcement. Altering the thickness of graphene did not produce a significant change to the out-of-plane measurement.

Their conductivity value is akin to obtained by Tuan *et al.* (27 W(mK)⁻¹ at 25 °C).²⁴⁹ Çelik *et al.* also demonstrated that an addition of 3 vol.% graphene nanoplatelets (with an average diameter of 400 nm) decreased the thermal conductivity from approximately 34 to 28 W(mK)⁻¹.²⁷⁶ This a similar result to the study by Rutkowski and co., but this group incorporated a marginally higher proportion of graphene. Although, the authors changed the sintering temperature based on the vol.% of reinforcement that has been included within the alumina matrix, stating this is to exhibit the highest densification possible. It remains unclear why result for the composite material obtained at 25 °C (9.5 W(mK)⁻¹) is very low. It may be difficult to compare absolute out-of-plane values against the mentioned literature because they utilise various sintering conditions that produce different grain sizes (in the host material) starting from their respective raw materials. Nevertheless, the evidence shows that the incorporation of GRMs into an alumina matrix will influence the out-of-plane thermal conductivity because of a grain size refinement. Furthermore, this suggest that the extent of thermal reduction on rGO (by raising the sintering temperature) does not appear to be a dominant factor in altering the conductivity value.

It was also determined that alumina-0.8rGO was electrically active: although, the value obtained of the core and perimeter of disc-shaped specimens was different. It was also mentioned that the measurements of the perimeter section were found to be in the range of 10^{-2} Scm^{-1} . The value obtained for the perimeter section is of notable importance as the material possesses eligibility for preparation through EDM; this method of machining requires an electrical conductivity value in the stated order of magnitude.²⁸⁵ This provides an alternative method to machining the ceramic-based composites which would not be possible without the inclusion of rGO. However, this higher conductivity was only found in the perimeter specimens. This provides evidence that the percolation network throughout the perimeter section is more connected, suggesting that the deposition of GO (during infiltration) has not fully permeated the core of freeze-cast specimens.

The resistivity for the perimeter section of alumina-0.8rGO ($15 \text{ } \Omega\text{cm}$) is eight orders of magnitude lower than monolithic alumina and is the same result as the in-plane resistivity calculated by Centeno *et al.*²⁴¹ They sintered ball-milled, alumina-GO powders through SPS. However, their alumina-rGO specimens contained smaller mass fractions of graphene (0.22 wt.%) that was mentioned in the discussion of flexural strength. This does suggest that their lower amount of reinforcement was better dispersed throughout the alumina matrix. Regarding other studies on alumina-rGO materials, conductivity values differ significantly. For example, nacre-like composites investigated by Li *et al.* demonstrated an electrical conductivity two order of magnitude higher (6.3 Scm^{-1}) than the perimeter section of our specimens.²⁸⁶ The microstructure of their nacre-like material is comparable to the one produced herein, containing layer upon layer of alternating alumina and graphene-like components: however, they state the utilisation a chemical reduction step (with hydrazine hydrate) to partially deoxygenate GO. Moreover, they do not provide any details on the fraction of reinforcement that was incorporated within the host matrix. This makes it tough to relate the reported high conductivity to any microstructural component except for the highly-oriented stacking of rGO.²⁸⁶ Work by Hong *et al.* on alumina-rGO shows a lower value of conductivity whilst introducing a similar amount of filler material (1 wt.%,

compared to 0.8 wt.%).²⁷⁴ The conductivity was determined to be $7 \times 10^{-3} \text{ Scm}^{-1}$ which is one order of magnitude lower than the perimeter section of alumina-0.8rGO. Their processing steps also incorporate chemical reduction to transform GO (like the previously mentioned study), but they utilise molecular-level mixing by sonication as opposed to more intricate processing.²⁷⁴ This avenue did create well-distributed GRM, but a highly-oriented microstructure was not characterised. The plot in Fig. 5.13 displays more in-plane conductivity values for alumina-graphene materials compared to the mass fraction of reinforcement, illustrating that the composite fabricated in this work generated an appreciable result.

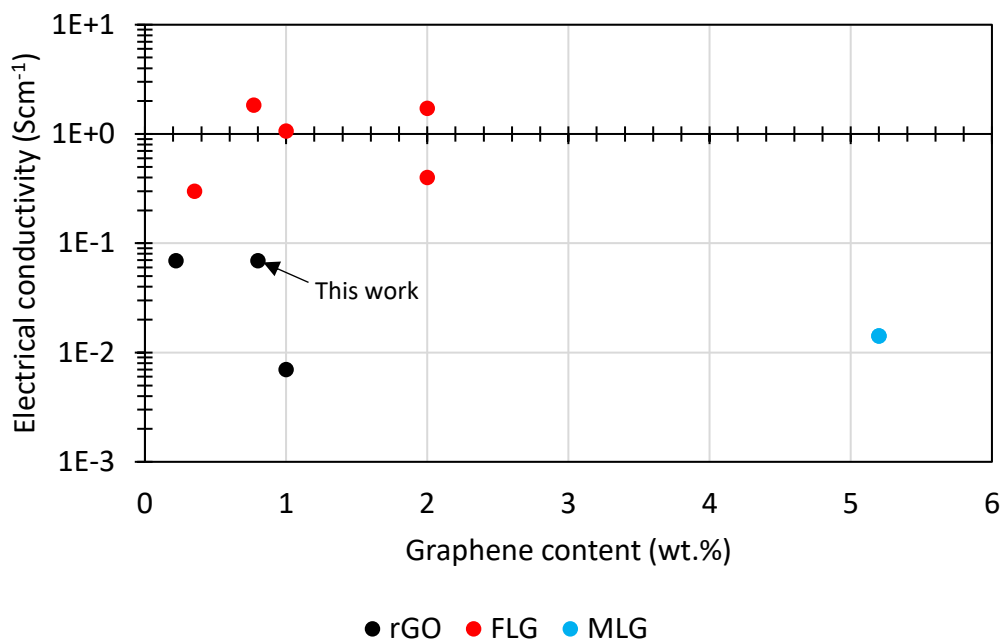


Figure 5.13 – Plot of electrical conductivities compared to the mass fraction found in the literature for alumina-GRM materials.^{241,274,276,287–292} Note that this has not considered sintering temperature for rGO-reinforced materials.

5.4 Concluding remarks

In conclusion, the results show that the addition of small amounts of highly-oriented rGO into the microstructure of alumina will alter the mechanical capabilities, and the electrical and thermal transport behaviour in specific directions. In comparison to monolithic alumina, the microhardness of alumina-0.8rGO decreased slightly by 9 % (at 1 kg loading), whilst the bulk hardness was reduced by 18 % (at 10 kg loading). The flexural strength measured through 4-point bending increased by 20 %. Most notably, the fracture toughness increases by 80 % (at 10 and 30 kg loadings) which was determined using the VIF method and applying the Anstis formula. The enhancements were attributed to extrinsic toughening mechanisms (crack deflection, bridging and branching, and pull-out) that were generated because of rGO addition.

With regards to functional behaviour, composite materials possess a lower out-of-plane thermal conductivity between a temperature range of 25 – 750 °C, attributed to a refinement in the grain size. This is not regarded as a negative influence in this instance as this may prove useful in thermal shielding applications. Also, the electrical behaviour was altered from insulating (in alumina), to conducting in varying degrees (in alumina-0.8rGO). In the core sections of disc-shaped composites, conductivity increases by six orders of magnitude (from $1 \times 10^{-9} \text{ Scm}^{-1}$), whereas this increases further by eight orders of magnitude (to $6.9 \times 10^{-2} \text{ Scm}^{-1}$) in perimeter sections. This does demonstrate a difference in the homogeneity (and connectivity) of the graphene-like reinforcement in specimens of alumina-0.8rGO. Nevertheless, this may prove beneficial towards smart, low-voltage applications such as structural health monitoring in multi-material devices, or electrical signalling components.

Chapter 6 Potential applications of alumina-rGO composites

This Chapter identifies possible applications of the composite material created during this investigation. The ideas are based on the mechanical and functional properties illustrated previously with the material in question (alumina-0.8rGO) that is stronger, tougher, and electrically active in comparison to a monolithic counterpart. Small reductions in the hardness and thermal conductivity were also measured. Although, the geometry of the ceramic-based composites made from the processing route and the timescale in which they are produced are both large factors that affects their potential applicability when compared to well-established industrial practices. With regards to the simple geometry fabricated through SPS, more complex components such as gears and turbine blades have been consolidated over recent years with different materials (from powder).^{293,294} However, the fabrication route towards the composites described herein is restricted based on the freeze-casting process: fabricating large and complex geometries that contains homogeneous pore sizes (and wall thicknesses) requires significant understanding and development of the casting method.¹⁵⁸ Machining ceramics into small, complex shapes can be challenging due to their brittleness.²⁹⁵ Therefore, the listed applications are predominantly based on the disc-shaped geometry that was produced.

6.1 Ring-shaped components

One application is the production of ceramic-based bearings and seal rings.²⁹⁶⁻²⁹⁹ The former supports a moving part whilst carrying a load, and the latter is used in fastenings to block the leakage of gases or liquids. Predominantly, they see usage in high-temperature scenarios such as during the operation of furnaces and refineries in which commonly used steel materials may fail. This is due to their lower resistance to

physical and chemical attack.²⁹⁸ Further high-performance applications may include their usage in helicopter rotors and X-ray tubes which are prone to sustaining substantial physical and chemical attack, respectively. A simple, flat seal ring (of 30 mm diameter) could be fashioned from the disc-shaped composite by creating an inner bore with a diamond-based drill tip that must be of similar diameter to that of the screw. The hole can then be ground to the desired finish using appropriate diamond-based tools. The production of bearings possessing inner or outer teeth, i.e., gear-shaped components, might be more challenging from our composite material because of the simple geometry created during freeze-casting.

These ceramic-based components are typically comprised of silicon carbide (SiC), Si₃N₄ or ZrO₂; however, all three are more expensive raw materials than alumina. Alumina-rGO components could be effective as an alternative because the measured fracture toughness rivals that of monolithic ZrO₂ (4 – 8 MPam^{1/2}),³⁰⁰ and it also possess a hardness close to that of Si₃N₄, which can be between 16 – 20 GPa depending on its sintering conditions and particle size.^{263,301,302} Although, the thermal conductivity of SiC (with sintering aids) is higher than our composite which may prove significant in the resistance to thermal shock and failure at high temperature.^{303,304} Additionally, the low density of the composite material (3.95 gcm⁻³) would make it a lightweight alternative to common steels which are typically twice as dense.³⁰⁵ However, the tribological properties such as the rate of wear and coefficient of friction have not been investigated which would be appropriate to understand in these scenarios. It has been proposed by Sun *et al.* that alumina-graphene materials can display extremely low coefficients of friction due to the presence of lubricating tribofilms generated by GRMs.¹³⁷ For utilisation in X-ray tubes, further testing on their irradiation by electrons and X-rays would also be needed.

6.2 Blade-like tools

Disc-shaped specimens of the composite could be also fashioned into the tips of blade-like implements such as small culinary knives or straight cut-off knives. They would primarily serve as a cheaper alternative to expensive, ZrO₂-based analogues which outperform stainless steel components based on their far greater hardness and resistance to corrosion. The combination of these two properties give rise to longer-lasting blades that would require less frequent sharpening, but the sharpening process would require specialised equipment for ceramic-based materials. The composite material exhibits a higher hardness (~17 GPa at 30 kg loading), although the moderately low flexural strength (of 314 MPa) may limit its applicability to softer materials to prevent chipping of the cutting edge.

The production of turbine blade geometries with ceramic-based components when compared to metals can provide benefits that include weight reduction and operating temperature capabilities.³⁰⁶ However, the proposed casting technique would require significant evaluation. Work by NASA illustrated the potential to develop turbine blades from raw powders by freeze-casting (including alumina), although the underlying principles of the casting technique was not well established at the time of this study.³⁰⁷ Little characterisation was performed in their investigation, so the extent of material (and pore) homogeneity of these blade-like components is unclear within this report. The casting of complex geometries would require analysis on the thermal gradients at different sections of the mould and the mould composition akin to the studies shown in Gil-Duran *et al.*¹⁰⁶ Engagement in freeze-casting these geometries would be valuable towards the progression of fabricating ceramic-based turbine blades (and other complex shapes) using alternative processing routes.

6.3 Heat-shielding

Considering the composite material possesses a lower thermal conductivity, it could be possible to utilise them in thermal protection systems to resist heat absorption. This may be to insulate thermally-sensitive structures, or to protect an operator from being burnt. However, it must be stated that oxide-based ceramics (except thoria, ThO_2) are not suitable for usage in ultra-high temperature applications ($<2000\text{ }^\circ\text{C}$) such as rocket nozzles for the re-entry spacecraft because of their respectively low melting points compared to carbides, borides, and nitrides.^{308,309} Suitable high temperature applications may include protection for small electronics and motors, components in fuel injectors and exhaust nozzles, and barrel shrouds on firearms. The lightweight nature of the composite material would also be beneficial in these scenarios as many of these objects are manufactured from steels that possess a much greater density.

6.4 Electrical signalling

One application that could take advantage of the composite material's electrical conductivity is the fabrication of signalling components in electrical circuits. Ideally, they would be integrated into low current scenarios as the resistivity of the composite is relatively high, i.e., $15\ \Omega\text{m}$ within the perimeter section, which is comparable to sea water.³¹⁰ Potential components may include power resistors (to convert large electrical signals to thermal energy) or fixed capacitors. Using alumina-0.8rGO within the listed components would be advantageous over metallic-based conductors due to greater stability in high temperatures. It may be suggested that brushes found in electrical motors would be a suitable application. These components transfer electricity between the stator and rotating shaft (commutator) within motors experience frictional forces during their service.^{311,312} They are commonly comprised of graphitic material but may include additions of materials such as copper or molybdenum disulfide to improve the

tribological properties by the generation of thin, solid lubricants called tribofilms.^{312,313} However, they do require a low resistance to operate effectively, e.g., within a range $>1 \Omega$ for a copper-graphite brush,³¹⁴ therefore utilising alumina-0.8rGO may not be practical.

6.5 Structural health monitoring in layered components

Based on its electrically active nature, it may be possible to utilise alumina-0.8rGO to sense damage through ET. This concept is classed as NDE which has received little attention in the field of ceramic materials but is an active area of interest in polymer-graphene materials.³¹⁵ NDE is critical to monitor the structural integrity of objects during their lifecycle without causing further damage to an object.^{316,317} If conducted correctly, defective regions of objects will produce a measurable change in the electrical resistance after the application of voltage.³¹⁵ The conductive, ceramic-based layer that is bonded within a component that may experience cracking or wear can monitor its structural integrity and aid in deciding when maintenance is necessary. During the former, an increase in the measured electrical resistance would suggest that the continuous electrical network has been disrupted by failure within the composite's structure, i.e., crack propagation, material pull-out. In the latter, if wear progresses through a component, this may be monitored by evaluating its electrical resistivity along the length in which the composite is present.

Limitations may arise based on the bonding of alumina-0.8rGO to other materials. Ideally, this would be compatible with materials that undergo a lower sintering temperature than alumina to not compromise the microstructure of the composite. One example using solely alumina-based materials could be to include the composite layer that has been sandwiched between two monolithic regions of alumina – this layered material could be fabricated by adding alumina powder above and below an alumina-GO scaffold prior to sintering through SPS. However, improvement of the dispersion within the core of the composite would be necessary as the in-plane

electrical conductivity of core and perimeter sections of the disc-shaped specimens did show a difference in the order of two magnitudes.

Conclusions

This thesis described an investigation into the fabrication of alumina-rGO materials using advanced processing techniques to generate an ordered microstructure, with the goal of obtaining superior mechanical performance. The included studies provide insight into freeze-casting large, cylindrical entities to generate a highly oriented porous architecture which is aligned with the faces of the cylinder. This was beneficial in generating a layered composite microstructure (after Spark Plasma Sintering) and extends the knowledge base in upscaling this casting approach towards the creation of bigger prototype materials. The developed processing strategy also offers another route for creating dense, rGO-reinforced ceramics in an environmentally friendly manner when compared to those that utilise toxic solvents. The main conclusions from processing and testing the composite materials are listed below.

- Highly porous, cylindrical alumina scaffolds were produced through freeze-casting suspensions of sub-micrometric ceramic particles. These were cast between low-to-moderate ceramic loadings of 20 – 40 wt.%. 25 wt.% scaffolds was identified as the optimum based on the homogeneous size of the alumina channels, plus the target weight of sintered materials (6.5 g). Scaffolds made from higher solid loadings also exhibited more inconsistent casting.
- The water-based infiltration of porous alumina scaffolds was found to be a size-selective approach to integrate graphene-like materials. Both drop casting and vacuum-assisted infiltration may be utilised to infiltrate scaffolds cast from low or moderate solid loadings. After preliminary infiltration (and sintering), the utilisation of 0.25 wt.% GO suspensions was deemed suitable in creating continuous layering of the reinforcing material.

- Once sintered through SPS, specimens of composite material (made from 25 wt.% alumina scaffolds) possess ceramic layers between a thickness of 0.5 - 7 μm separated by well-dispersed rGO reinforcement material along the material's cross-section. After infiltration with a 0.25 wt.% GO suspension, the proportion of rGO within the alumina matrix was determined by TGA to be roughly 0.8 wt.%. The incorporation of rGO layers also invoked a refinement in the grain size of alumina (from 1 to 0.7 μm).
- When compared to monolithic alumina, the hardness of alumina-0.8rGO (at 1 kg loading) decreased slightly by 9 %, whilst the flexural strength and fracture toughness increased by 20 and 80 % respectively. The thermal conductivity decreased between 25 – 750 $^{\circ}\text{C}$, whilst the electrical conductivity increased by at least six orders of magnitude, and up to eight orders of magnitude in perimeter sections of disc-shaped specimens.
- Potential applications from the disc-shaped specimens may include sealing rings and washers, blade tips for small cutting tools, and electrical signalling components such as power resistors or fixed capacitors. However, further applicability is hindered by the inability to fabricate complex geometries through freeze-casting, and processing time considerations which are both major factors in cost-effective industrial fabrication.

Future work

There are several, further experimental studies that can be carried out with regards to the alumina-rGO materials that were explored. Some inhomogeneity in the porous architecture was observed in the cylindrical scaffolds that were freeze-cast using the prototype mould. Whilst this demonstrated the potential of casting cylindrical bodies with microstructure aligned with the faces of cylinder, it may be preferable to fabricate square-based geometries. This would overcome the observed problem of aligning outer pores with the freezing direction because the thermal gradient would be more homogeneous along the PD-CS plane. Of course, this would also require square-shaped, graphite die sets during the sintering procedure. The investigation into freeze-casting complex geometries, which was briefly discussed in Chapter 6 (Section 6.2), could also be studied. This would further progress the knowledge in this field, however, this would require thorough understanding of the different thermal gradients that would likely arise due to differences in a mould's dimensions and the freezing rate that is applied.

Additionally, it may be thought that increasing the amount of graphene would give rise to materials with enhanced mechanical and functional performance, yet, on the contrary the reverse is true because GRMs exhibit extreme properties in single layers. A more in-depth study on the concentration of GO suspensions to incorporate well-dispersed reinforcement during the infiltration process could identify a lower concentration that still retains the continuity found when using 0.25 wt.% GO. More sintering parameters could also be investigated – for example, reducing the holding time for unbroken specimens could further inhibit ceramic grain growth whilst maintaining near theoretical density. The same is true for altering the heating and cooling rates, which was not investigated with a continuous pulse sequence. The effect of sintering temperature on the composite materials was only utilised to provide insight on the extent of rGO reduction through thermal conductivity measurements.

Also, only a small batch of alumina-rGO materials was fabricated, with a limited number of specimens being available for testing, e.g., in 4-point flexure tests. It is true that this is not a large enough sample size to provide a reliable result on the flexural strength, but the provided data still suggests an improvement. An increase in the number of fabricated specimens would also allow for fracture toughness testing through more reliable methods to be performed, i.e., notched beam techniques. R-curve testing would also be beneficial to perform to provide further insight into the extrinsic toughening. Further testing of functional behaviour including wear properties including the rate of wear and coefficient of friction, and the electromagnetic shielding capabilities would be extremely useful to study. The latter has been recognised as a very promising application for use in various sectors to mitigate the interference that electronics experience from unwanted electromagnetic fields such as radio- and microwaves.¹³⁹ This additional testing may have been accomplished if it were not for time constraints imposed by the COVID-19 pandemic.

It was mentioned in Chapter 4 (Section 4.5.2) that this processing route can offer the possibility to fabricate alternative composite materials, provided that the filler material is hydrophilic like GO. If not, alternative infiltration solvents such as alcohols could be utilised, but this would compromise the solely water-based strategy. It is thought that the generation of an ordered microstructure with multiple interfaces can have profound effects on the behaviour of materials with secondary components.³¹⁸ This may primarily involve the use of other ceramics or metal components: specific examples for infiltrating alumina could involve a suspension of metal particles such as iron or nickel, or ceramics including iron oxide or magnesia. The incorporation of metals would be useful to create composites with improved ductility and generate magnetic capabilities that would only further their applicability.³¹⁹ On the one hand, an advantage is that they may be more facile to process in comparison to GRMs. On the other hand, it is easy to suggest numerous different reinforcements, however their integration must consider factors like: i) the sintering temperature of both components, which for the mentioned metals through SPS, are slightly lower than alumina,^{320,321} and ii) potential mismatches in thermal expansion or shrinking.³¹⁸ Many

of the emerging possibilities towards creating new composite materials that exhibit multifunctional behaviour are still in their early stages of development but show considerable potential.

References

- 1 V. V. Vikulin, I. Yu. Kelina, A. S. Shatalin and L. N. Rusanova, *Refractories and Industrial Ceramics*, 2004, **45**, 383–386.
- 2 J. M. Schoenung, in *Encyclopedia of Materials: Science and Technology*, Elsevier, 2001, pp. 8921–8926.
- 3 D. P. Kaur, S. Raj and M. Bhandari, in *Advanced Ceramics for Versatile Interdisciplinary Applications*, Elsevier, 2022, pp. 15–39.
- 4 J. C. Williams and E. A. Starke, *Acta Mater*, 2003, **51**, 5775–5799.
- 5 M. Hashmi, *Comprehensive materials processing*, Newnes, 2014.
- 6 R. Asthana, A. Kumar and N. Dahotre, *Materials processing and manufacturing science*, Elsevier, 2006.
- 7 M. A. Meyers and K. K. Chawla, *Mechanical Behavior of Materials*, Cambridge University Press, 2008.
- 8 A. M. Donoghue, N. Frisch and D. Olney, *J Occup Environ Med*, 2014, **56**, S12–S17.
- 9 M. Herrmann, in *Handbook of Advanced Ceramics*, Elsevier, 2013, pp. 301–328.
- 10 N. K. Vail, L. D. Swain, W. C. Fox, T. B. Aufdlemorte, G. Lee and J. W. Barlow, *Mater Des*, 1999, **20**, 123–132.
- 11 K. L. Murty and I. Charit, *Journal of Nuclear Materials*, 2008, **383**, 189–195.
- 12 S. K. Srivastava, G. K. Gupta, T. C. Joshi, A. Pandey, D. Muchhala, V. Shrivastava, P. Singh, D. P. Mondal, R. Kumar and S. Ranjan, in *Advanced Ceramics for Versatile Interdisciplinary Applications*, Elsevier, 2022, pp. 1–14.
- 13 M. Steen, *International Materials Reviews*, 1999, **44**, 165–216.
- 14 J. B. Wachtman, W. R. Cannon and M. J. Matthewson, *Mechanical Properties of Ceramics*, Wiley, 2009.
- 15 W. D. Callister Jr, *Materials science and engineering an introduction*, John Wiley & Sons, 2007.
- 16 D. P. H. Hasselman, *Materials Science and Engineering*, 1985, **71**, 251–264.
- 17 R. Danzer, T. Lube, P. Supancic and R. Damani, *Adv Eng Mater*, 2008, **10**, 275–298.
- 18 M. Trunec and K. Maca, in *Advanced Ceramics for Dentistry*, Elsevier Inc., 2014, pp. 123–150.
- 19 T. Pereira, J. V Kennedy and J. Potgieter, *Procedia Manuf*, 2019, **30**, 11–18.
- 20 S. E. Ghiasian, P. Jaiswal, R. Rai and K. Lewis, in *Volume 2A: 44th Design Automation Conference*, American Society of Mechanical Engineers, 2018.
- 21 J. A. Pask, *Journal of Materials Engineering*, 1989, **11**, 267–274.
- 22 S. J. Kang, *Sintering*, Elsevier, 2005.
- 23 R. M. German, in *Sintering of Advanced Materials*, Elsevier, 2010, pp. 3–32.
- 24 A. M. Okoro, S. S. Lephuthing, S. R. Oke, O. E. Falodun, M. A. Awotunde and P. A. Olubambi, *JOM*, 2019, **71**, 567–584.
- 25 E. Wheat, M. Vlasea, J. Hinebaugh and C. Metcalfe, *Mater Des*, 2018, **156**, 167–183.

- 26 R. M. German, in *Encyclopedia of Materials: Science and Technology*, Elsevier, 2001, pp. 8641–8643.
- 27 B. C. Carter and G. M. Norton, *Ceramic Materials*, Springer New York, New York, NY, 2007.
- 28 S. Kang, *Sintering: densification, grain growth and microstructure*, Elsevier, 2004.
- 29 S. Lamouri, M. Hamidouche, N. Bouaouadja, H. Belhouchet, V. Garnier, G. Fantozzi and J. F. Trelkat, *Boletín de la Sociedad Española de Cerámica y Vidrio*, 2017, **56**, 47–54.
- 30 S.-H. Chae, Y.-W. Kim, I.-H. Song, H.-D. Kim and M. Narisawa, *J Eur Ceram Soc*, 2009, **29**, 2867–2872.
- 31 O. Guillon, J. Gonzalez-Julian, B. Dargatz, T. Kessel, G. Schierning, J. Räthel and M. Herrmann, *Adv Eng Mater*, 2014, **16**, 830–849.
- 32 M. Omori, *Materials Science and Engineering A*, 2000, **287**, 183–188.
- 33 Y. H. Ji, Z. H. Ge, Z. Li and J. Feng, *J Alloys Compd*, 2016, **680**, 273–277.
- 34 J. I. Tani and H. Kido, *Physica B Condens Matter*, 2005, **364**, 218–224.
- 35 S. H. Risbud, C. H. Shan and R. A. Holl, *J Mater Res*, 1995, **10**, 237–239.
- 36 O. Guillon, Springer, Berlin, Heidelberg, 2012, pp. 195–213.
- 37 K. L. Watson, *Foundation Science for Engineers*, Macmillan Education UK, London, 1998.
- 38 R. E. Smallman and A. H. W. Ngan, *Modern Physical Metallurgy*, Elsevier, 2014.
- 39 F. Wredenbergh and P. L. Larsson, *Wear*, 2009, **266**, 76–83.
- 40 P. Groth, *Entwicklungsgeschichte der mineralogischen Wissenschaften*, J. Springer, 1926.
- 41 R. Morrell, *Palmqvist Toughness for Hard and Brittle Materials*, 1997.
- 42 J. Fischer, B. Stawarczyk and C. H. F. Hämmerle, *J Dent*, 2008, **36**, 316–321.
- 43 T. L. Anderson, *CRC Press*, 2017, **76**, 1255–1269.
- 44 G. R. Irwin, *J Appl Mech*, 1957, **24**, 361–364.
- 45 R. W. Steinbrech, in *Fracture Mechanics of Ceramics*, Springer US, Boston, MA, 1992, pp. 187–208.
- 46 Z. Huda, R. Bulpett and K. Y. Lee, *Design Against Fracture and Failure*, 2010.
- 47 A. A. Griffith, *Philosophical Transactions of the Royal Society of London. Series A, Containing Papers of a Mathematical or Physical Character*, 1921, **221**, 163–198.
- 48 S. Lenci, *Int J Fract*, 2001, **108**, 275–290.
- 49 M. Liu, Y. Gan, D. A. H. Hanaor, B. Liu and C. Chen, *Eng Fract Mech*, 2015, **149**, 134–143.
- 50 S. Ya. Yarema, *Materials Science*, 1996, **31**, 617–623.
- 51 A. F. Bower, *Applied mechanics of solids*, CRC press, 2009.
- 52 J. B. Quinn and G. D. Quinn, *J Mater Sci*, 1997, **32**, 4331–4346.
- 53 K. M. Liang, G. Orange and G. Fantozzi, *J Mater Sci*, 1990, **25**, 207–214.
- 54 J. J. Kruzic, D. K. Kim, K. J. Koester and R. O. Ritchie, *J Mech Behav Biomed Mater*, 2009, **2**, 384–395.
- 55 G. D. Quinn and R. C. Bradt, *Journal of the American Ceramic Society*, 2007, **90**, 673–680.
- 56 B. Roebuck and E. G. Bennett, *Hard metal toughness tests*, 2005.

- 57 B. Roebuck, E. G. Bennett, L. Lay and R. Morrell, *Palmqvist Toughness for Hard and Brittle Materials*, 2008.
- 58 V. M. Karbhari, *Durability of composites for civil structural applications*, Woodhead Publishing Limited, 2007.
- 59 C. R. Gagg, *Eng Fail Anal*, 2014, **40**, 114–140.
- 60 U. G. K. Wegst, H. Bai, E. Saiz, A. P. Tomsia and R. O. Ritchie, *Nat Mater*, 2015, **14**, 23–36.
- 61 P. K. Mallick, *Fiber-Reinforced Composites*, CRC Press, 2007.
- 62 J. W. Martin, *Choice Reviews Online*, 2002, **39**, 39-6443-39-6443.
- 63 R. M. Jones, in *Mechanics of Composite Materials*, CRC Press, 2018, pp. 367–466.
- 64 G. Ramirez, *Journal of Structural Engineering*, 1999, **125**, 1082–1082.
- 65 L. Zoli, A. Vinci, L. Silvestroni, D. Sciti, M. Reece and S. Grasso, *Mater Des*, 2017, **130**, 1–7.
- 66 R. Naslain, *Compos Sci Technol*, 2004, **64**, 155–170.
- 67 H. G. Scott, *J Mater Sci*, 1975, **10**, 1527–1535.
- 68 P. Duwez, F. H. Brown and F. Odell, *J Electrochem Soc*, 1951, **98**, 356.
- 69 R. O. Ritchie, *Nat Mater*, 2011, **10**, 817–822.
- 70 C. A. Nannetti, A. Ortona, D. A. de Pinto and B. Riccardi, *Journal of the American Ceramic Society*, 2004, **87**, 1205–1209.
- 71 R. T. Bhatt and J. D. Kiser, *J Eur Ceram Soc*, 2021, **41**, 6196–6206.
- 72 R. T. Bhatt, F. Sola-Lopez, M. C. Halbig and M. H. Jaskowiak, *J Eur Ceram Soc*, 2022, **42**, 3383–3394.
- 73 N. Travitzky, *Advances in Applied Ceramics*, 2012, **111**, 286–300.
- 74 W. J. E. M. Habraken, J. G. C. Wolke and J. A. Jansen, *Adv Drug Deliv Rev*, 2007, **59**, 234–248.
- 75 E. K. Akdogan, M. Allahverdi and A. Safari, *IEEE Trans Ultrason Ferroelectr Freq Control*, 2005, **52**, 746–775.
- 76 T. Rodriguez-Suarez, J. F. Bartolomé and J. S. Moya, *J Eur Ceram Soc*, 2012, **32**, 3887–3898.
- 77 J. Sun and B. Bhushan, *RSC Adv*, 2012, **2**, 7617–7632.
- 78 P. Y. Chen, A. Y. M. Lin, Y. S. Lin, Y. Seki, A. G. Stokes, J. Peyras, E. A. Olefsky, M. A. Meyers and J. McKittrick, *J Mech Behav Biomed Mater*, 2008, **1**, 208–226.
- 79 P. Fratzl and R. Weinkamer, *Prog Mater Sci*, 2007, **52**, 1263–1334.
- 80 J. Vincent, *Structural biomaterials*, Princeton University Press, 2012.
- 81 M. H. Ramage, H. Burridge, M. Busse-Wicher, G. Fereday, T. Reynolds, D. U. Shah, G. Wu, L. Yu, P. Fleming, D. Densley-Tingley, J. Allwood, P. Dupree, P. F. Linden and O. Scherman, *Renewable and Sustainable Energy Reviews*, 2017, **68**, 333–359.
- 82 A. P. Jackson, J. F. Vincent and R. M. Turner, *Proc R Soc Lond B Biol Sci*, 1988, **234**, 415–440.
- 83 J. D. Currey and J. D. Taylor, *J Zool*, 1974, **173**, 395–406.
- 84 M. Rousseau, E. Lopez, P. Stempflé, M. Brendlé, L. Franke, A. Guette, R. Naslain and X. Bourrat, *Biomaterials*, 2005, **26**, 6254–6262.
- 85 J. D. Currey, *Proceedings of the Royal Society of London - Biological Sciences*, 1977, **196**, 443–463.
- 86 H. Kakisawa and T. Sumitomo, *Sci Technol Adv Mater*, 2011, **12**, 064710.

- 87 R. Z. Wang, Z. Suo, A. G. Evans, N. Yao and I. A. Aksay, *J Mater Res*, 2001, **16**, 2485–2493.
- 88 T. Sumitomo, H. Kakisawa, Y. Owaki and Y. Kagawa, *J Mater Res*, 2008, **23**, 3213–3221.
- 89 E. Munch, M. E. Launey, D. H. Alsem, E. Saiz, A. P. Tomsia and R. O. Ritchie, *Science (1979)*, 2008, **322**, 1516–1520.
- 90 I. Corni, T. J. Harvey, J. A. Wharton, K. R. Stokes, F. C. Walsh and R. J. K. Wood, *Bioinspir Biomim*, 2012, **7**.
- 91 S. Deville, E. Saiz, R. K. Nalla and A. P. Tomsia, *Science (1979)*, 2006, **311**, 515–518.
- 92 F. Bouville, *J Mater Res*, 2020, **35**, 1076–1094.
- 93 L. Wang, J. Bi, W. Wang, Y. Chen, R. Liu and X. Sun, *Ceram Int*, 2019, **45**, 8081–8086.
- 94 E. Poloni, F. Bouville, C. H. Dreimol, T. P. Niebel, T. Weber, A. R. Biedermann, A. M. Hirt and A. R. Studart, *Sci Rep*, 2021, **11**, 1621.
- 95 R. F. Gibson, *Compos Struct*, 2010, **92**, 2793–2810.
- 96 V. Dhand, G. Mittal, K. Y. Rhee, S. J. Park and D. Hui, *Compos B Eng*, 2015, **73**, 166–180.
- 97 F. Libonati and M. J. Buehler, *Adv Eng Mater*, 2017, **19**.
- 98 A. R. Studart, *Chem Soc Rev*, 2016, **45**, 359–376.
- 99 A. Velasco-Hogan, J. Xu and M. A. Meyers, *Advanced Materials*, 2018, **30**.
- 100 C. Huang and Q. Cheng, *Compos Sci Technol*, 2017, **150**, 141–166.
- 101 K. Evers, S. Falco, N. Grobert and R. I. Todd, *J Eur Ceram Soc*, 2020, **40**, 417–426.
- 102 G. Shao, D. A. H. Hanaor, X. Shen and A. Gurlo, *Advanced Materials*, 2020, **32**, 1907176.
- 103 S. Deville, *Adv Eng Mater*, 2008, **10**, 155–169.
- 104 S. Deville, E. Saiz and A. P. Tomsia, *Acta Mater*, 2007, **55**, 1965–1974.
- 105 E. Munch, E. Saiz, A. P. Tomsia and S. Deville, *Journal of the American Ceramic Society*, 2009, **92**, 1534–1539.
- 106 S. Gil-Duran, D. Arola and E. A. Ossa, *JOM*, 2020, **72**, 1477–1486.
- 107 W. L. Li, K. Lu and J. Y. Walz, *International Materials Reviews*, 2012, **57**, 37–60.
- 108 T. Fukasawa, M. Ando, T. Ohji and S. Kanzaki, *Journal of the American Ceramic Society*, 2001, **84**, 230–232.
- 109 A. Röthlisberger, S. Häberli, F. Krogh, H. Galinski, D. C. Dunand and R. Spolenak, *Sci Rep*, 2019, **9**, 1–9.
- 110 R. Dash, Y. Li and A. J. Ragauskas, *Carbohydr Polym*, 2012, **88**, 789–792.
- 111 J. Huang, W. S. Rubink, H. Lide, T. W. Scharf, R. Banerjee and M. Minary-Jolandan, *Adv Eng Mater*, 2019, **21**, 1801103.
- 112 H. Hudelja, T. Konegger, B. Wicklein, J. Čretnik, F. Akhtar and A. Kocjan, *Open Ceramics*, DOI:10.1016/j.oceram.2021.100069.
- 113 Y. Liu, W. Zhu, K. Guan, C. Peng and J. Wu, *Ceram Int*, 2018, **44**, 11901–11904.
- 114 F. Su, J. Mok and J. McKittrick, *Ceramics*, 2019, **2**, 161–179.
- 115 I. Nelson and S. E. Naleway, *Journal of Materials Research and Technology*, 2019, **8**, 2372–2385.

- 116 K. Lebreton, J. M. Rodríguez-Parra, R. Moreno and M. I. Nieto, *Advances in Applied Ceramics*, 2015, **114**, 296–302.
- 117 A. A. Saberi, *Phys Rep*, 2015, **578**, 1–32.
- 118 S. Kirkpatrick, *Rev Mod Phys*, 1973, **45**, 574–588.
- 119 K. S. Novoselov, A. K. Geim, S. V. Morozov, D. Jiang, Y. Zhang, S. V. Dubonos, I. V. Grigorieva and A. A. Firsov, *Science (1979)*, 2004, **306**, 666–669.
- 120 A. K. Geim and K. S. Novoselov, *Nat Mater*, 2007, **6**, 183–191.
- 121 Z. Li, L. Chen, S. Meng, L. Guo, J. Huang, Y. Liu, W. Wang and X. Chen, *Phys Rev B Condens Matter Mater Phys*, DOI:10.1103/PhysRevB.91.094429.
- 122 A. A. Balandin, S. Ghosh, W. Bao, I. Calizo, D. Teweldebrhan, F. Miao and C. N. Lau, *Nano Lett*, 2008, **8**, 902–907.
- 123 S. E. Zhu, S. Yuan and G. C. A. M. Janssen, *EPL*, 2014, **108**, 17007.
- 124 W. S. Hummers and R. E. Offeman, *J Am Chem Soc*, 1958, **80**, 1339–1339.
- 125 D. V. Kosynkin, A. L. Higginbotham, A. Sinitskii, J. R. Lomeda, A. Dimiev, B. K. Price and J. M. Tour, *Nature*, 2009, **458**, 872–876.
- 126 D. C. Marcano, D. V. Kosynkin, J. M. Berlin, A. Sinitskii, Z. Sun, A. Slesarev, L. B. Alemany, W. Lu and J. M. Tour, *ACS Nano*, 2010, **4**, 4806–4814.
- 127 P. R. Somani, S. P. Somani and M. Umeno, *Chem Phys Lett*, 2006, **430**, 56–59.
- 128 A. Reina, X. Jia, J. Ho, D. Nezich, H. Son, V. Bulovic, M. S. Dresselhaus and K. Jing, *Nano Lett*, 2009, **9**, 30–35.
- 129 H. Ren, M. Tang, B. Guan, K. Wang, J. Yang, F. Wang, M. Wang, J. Shan, Z. Chen, D. Wei, H. Peng and Z. Liu, *Advanced Materials*, DOI:10.1002/ADMA.201702590.
- 130 S. Pei and H.-M. Cheng, *Carbon N Y*, 2012, **50**, 3210–3228.
- 131 M. Ruidíaz-Martínez, M. A. Álvarez, M. V. López-Ramón, G. Cruz-Quesada, J. Rivera-Utrilla and M. Sánchez-Polo, *Catalysts*, 2020, **10**, 520.
- 132 W. Gao, *Graphene Oxide: Reduction Recipes, Spectroscopy, and Applications*, 2015, 61–95.
- 133 Y. Zhu, S. Murali, W. Cai, X. Li, J. W. Suk, J. R. Potts and R. S. Ruoff, *Advanced Materials*, 2010, **22**, 5226–5226.
- 134 N. Bellier, P. Baipaywad, N. Ryu, J. Y. Lee and H. Park, *Biomater Res*, 2022, **26**, 65.
- 135 D. G. Papageorgiou, I. A. Kinloch and R. J. Young, *Prog Mater Sci*, 2017, **90**, 75–127.
- 136 E. D’Elia, S. Barg, N. Ni, V. G. Rocha and E. Saiz, *Advanced Materials*, 2015, **27**, 4788–4794.
- 137 C. Sun, Y. Huang, Qiang Shen, W. Wang, W. Pan, P. Zong, L. Yang, Y. Xing and C. Wan, *Sci Adv*, DOI:10.1126/sciadv.abb1338.
- 138 Y. Huang, K. Yasuda, C. W.-A. A. M. & Interfaces and undefined 2020, *ACS Publications*, 2020, **12**, 34.
- 139 C. Ramírez, M. Belmonte, P. Miranzo and M. I. Osendi, *Materials*, 2021, **14**, 2071.
- 140 K. Markandan, J. K. Chin and M. T. T. Tan, *J Mater Res*, 2017, **32**, 84–106.
- 141 T. He, J. Li, L. Wang, J. Zhu and W. Jiang, *Mater Trans*, 2009, **50**, 749–751.
- 142 K. Wang, Y. Wang, Z. Fan, J. Yan and T. Wei, *Mater Res Bull*, 2011, **46**, 315–318.
- 143 J. Liu, H. Yan and K. Jiang, *Ceram Int*, 2013, **39**, 6215–6221.

- 144 R. Sedlák, A. Kovalčíková, V. Girman, E. Múdra, P. Rutkowski, A. Dubiel and J. Dusza, *J Eur Ceram Soc*, 2017, **37**, 4307–4314.
- 145 L. S. Walker, V. R. Marotto, M. A. Rafiee, N. Koratkar and E. L. Corral, *ACS Nano*, 2011, **5**, 3182–3190.
- 146 G. Menendez, T. Kynaston, I. J. Villar-Garcia, M. Gao, S. L. Evans and V. G. Rocha, *J Eur Ceram Soc*, 2022, **42**, 6574–6582.
- 147 E. Feilden, C. Ferraro, Q. Zhang, E. García-Tuñón, E. D’Elia, F. Giuliani, L. Vandeperre and E. Saiz, *Sci Rep*, 2017, **7**, 1–9.
- 148 M. Vukšić, I. Žmak, L. Čurković and A. Kocjan, *Open Ceramics*, 2021, **5**, 100076.
- 149 S. Gaydardzhiev and P. Ay, in *Journal of Materials Science*, 2006, vol. 41, pp. 5257–5262.
- 150 S. P. Rao, S. S. Tripathy and A. M. Raichur, *Colloids Surf A Physicochem Eng Asp*, 2007, **302**, 553–558.
- 151 M. Sivakumar, S. Y. Tang and K. W. Tan, in *Ultrasonics Sonochemistry*, Elsevier B.V., 2014, vol. 21, pp. 2069–2083.
- 152 C. N. Cheaburu-Yilmaz, H. Y. Karasulu and O. Yilmaz, in *Polymeric Nanomaterials in Nanotherapeutics*, Elsevier, 2018, pp. 437–468.
- 153 V. A. Hackley and M. R. Wiesner, *CEINT, National Institute of Standards and Technology*, 2010, 1–10.
- 154 I. Kaur, L. J. Ellis, I. Romer, R. Tantra, M. Carriere, S. Allard, M. Mayne-L’hermite, C. Minelli, W. Unger, A. Potthoff, S. Rades and E. Valsami-Jones, *Journal of Visualized Experiments*, 2017, **2017**, 56074.
- 155 E. Munch, J. Franco, S. Deville, P. Hunger, E. Saiz and A. P. Tomsia, *JOM*, 2008, **60**, 54–58.
- 156 S. Deville, P. Miranda, E. Saiz and A. P. Tomsia, in *Proceedings of the International Conference on Manufacturing Science and Engineering*, 2006, vol. 2006.
- 157 S. Algharaibeh, A. J. Ireland and B. Su, *J Eur Ceram Soc*, 2019, **39**, 514–521.
- 158 G. Shao, D. A. H. Hanaor, X. Shen and A. Gurlo, *Advanced Materials*, 2020, **32**.
- 159 S. Deville, E. Maire, A. Lasalle, A. Bogner, C. Gauthier, J. Leloup and C. Guizard, *Journal of the American Ceramic Society*, 2009, **92**, 2489–2496.
- 160 S. Deville, E. Saiz, R. K. Nalla and A. P. Tomsia, *Science (1979)*, 2006, **311**, 515–518.
- 161 E. Johansson, O. Lidström, J. Johansson, O. Lyckfeldt and E. Adolfsson, *Materials*, 2017, **10**, 138.
- 162 F. Golestani-fard, M. Mazaheri, M. Aminzare and T. Ebadzadeh, *J Eur Ceram Soc*, 2011, **31**, 2593–2599.
- 163 K. Miao, L. Liu, J. Cao, R. He, S. Li, L. Wu, Z. Lu and D. Li, *J Mater Sci Technol*, 2023, **159**, 184–193.
- 164 H. Lee, T.-S. Jang, J. Song, H.-E. Kim and H.-D. Jung, *Materials*, 2017, **10**, 367.
- 165 P. J. Lloreda-Jurado, S. K. Wilke, K. Scotti, A. Paúl-Escolano, D. C. Dunand and R. Sepúlveda, *J Mater Res*, 2020, **35**, 2587–2596.
- 166 J. Mewis and N. J. Wagner, *Colloidal Suspension Rheology*, Cambridge University Press, 2011.
- 167 K. Uluç, G. C. Kujoth and M. K. Başkaya, *Neurosurg Focus*, 2009, **27**, E4.

- 168 M. W. Davidson and M. Abramowitz, in *Encyclopedia of Imaging Science and Technology*, John Wiley & Sons, Inc., Hoboken, NJ, USA, 2002.
- 169 A. Van Helden, *Transactions of the American Philosophical Society*, 1977, **67**, 1.
- 170 J. L. Riddell, *J Cell Sci*, 1854, **s1-2**, 18–24.
- 171 Y. Zhu and H. Inada, in *Encyclopedia of Nanotechnology*, Springer Netherlands, Dordrecht, 2012, pp. 2273–2280.
- 172 J. Goldstein, D. Newbury, J. Michael and N. Ritchie, *Scanning electron microscopy and X-ray microanalysis*, 2017.
- 173 T. E. Everhart and R. F. M. Thornley, *J Sci Instrum*, 1960, **37**, 246–248.
- 174 A. Smekal, *Naturwissenschaften*, 1923, **11**, 873–875.
- 175 C. V. Raman and K. S. Krishnan, *Nature*, 1928, **121**, 501–502.
- 176 E. Smith and G. Dent, *Modern Raman Spectroscopy – A Practical Approach*, Wiley, 2004.
- 177 S. Perumbilavil, P. Sankar, T. Priya Rose and R. Philip, *Appl Phys Lett*, , DOI:10.1063/1.4928124.
- 178 Dr. A. K. Singh, *Advanced X-ray Techniques in Research and Industry*, IOS Press, 2005.
- 179 W. H. Bragg and W. L. Bragg, *Proceedings of the Royal Society of London. Series A, Containing Papers of a Mathematical and Physical Character*, 1913, **88**, 428–438.
- 180 M. Stauber and R. Müller, in *Methods in Molecular Biology*, Humana Press, 2008, vol. 455, pp. 273–292.
- 181 L. A. Feldkamp, L. C. Davis and J. W. Kress, *Journal of the Optical Society of America A*, 1984, **1**, 612.
- 182 J. D. Boerckel, D. E. Mason, A. M. McDermott and E. Alsberg, *Stem Cell Res Ther*, 2014, **5**, 144.
- 183 A. Fedorov, R. Beichel, J. Kalpathy-Cramer, J. Finet, J.-C. Fillion-Robin, S. Pujol, C. Bauer, D. Jennings, F. Fennessy, M. Sonka, J. Buatti, S. Aylward, J. V. Miller, S. Pieper and R. Kikinis, *Magn Reson Imaging*, 2012, **30**, 1323–1341.
- 184 B. B. Bokhonov, A. V. Ukhina, D. V. Dudina, A. G. Anisimov, V. I. Mali and I. S. Batraev, *RSC Adv*, 2015, **5**, 80228–80237.
- 185 L. Torrisi, M. Cutroneo, A. Torrisi and L. Silipigni, *Physica Status Solidi (A) Applications and Materials Science*, 2022, **219**, 2100628.
- 186 Archimedes, *The Works of Archimedes*, Cambridge University Press, 2009.
- 187 R. L. Smith and G. E. Sandly, *Proceedings of the Institution of Mechanical Engineers*, 1922, **102**, 623–641.
- 188 G. R. Anstis, P. Chantikul, B. R. Lawn and D. B. Marshall, *Journal of the American Ceramic Society*, 1981, **64**, 533–538.
- 189 T. Aleksandrov Fabijanić, D. Ćorić, M. Šnajdar Musa and M. Sakoman, *Metals (Basel)*, 2017, **7**, 143.
- 190 I. Žmak, D. Ćorić, V. Mandić and L. Ćurković, *Materials*, 2019, **13**, 122.
- 191 F. Hu, X. Wu, Y. Wang and X. Lai, *RSC Adv*, 2015, **5**, 54053–54058.
- 192 J. O. Akindoyo, N. A. A. binti Husney, N. H. Ismail and M. Mariatti, *Polymers and Polymer Composites*, 2021, **29**, 992–1002.
- 193 M. Zorah, I. R. Mustapa, N. Daud, J. H. Nahida, N. A. S. Sudin, A. A. Majhool and E. Mahmoudi, *Journal of Advanced Research in Fluid Mechanics and Thermal Sciences*, 2020, **70**, 97–111.

- 194 F. Ali, L. Reinert, J. M. Levêque, L. Duclaux, F. Muller, S. Saeed and S. S. Shah, *Ultrason Sonochem*, 2014, **21**, 1002–1009.
- 195 J. P. Annaraj, N. Bose and N. R. J. Hynes, 2019, p. 070027.
- 196 R. Wang, Y. Li, Y. Tian and Z. Li, *Dig J Nanomater Biostruct*, 2020, **15**, 253–259.
- 197 H. Schoof, J. Apel, I. Heschel and G. Rau, *J Biomed Mater Res*, 2001, **58**, 352–357.
- 198 K. M. Pawelec, A. Husmann, S. M. Best and R. E. Cameron, *J Mater Sci*, 2015, **50**, 7537–7543.
- 199 S. S. L. Peppin, M. G. Worster and J. S. Wettlaufer, *Proceedings of the Royal Society A: Mathematical, Physical and Engineering Sciences*, 2007, **463**, 723–733.
- 200 R. W. Davidge, in *Concise Encyclopedia of Advanced Ceramic Materials*, Elsevier, 1991, pp. 478–481.
- 201 D. Sherman and D. Schlumm, *Scr Mater*, 2000, **42**, 819–825.
- 202 Z. Shen, M. Johnsson, Z. Zhao and M. Nygren, *Journal of the American Ceramic Society*, 2002, **85**, 1921–1927.
- 203 J. G. Santanach, A. Weibel, C. Estourns, Q. Yang, C. Laurent and A. Peigney, *Acta Mater*, 2011, **59**, 1400–1408.
- 204 Y. Aman, V. Garnier and E. Djurado, *Journal of the American Ceramic Society*, 2011, **94**, 2825–2833.
- 205 Z. Q. Li, C. J. Lu, Z. P. Xia, Y. Zhou and Z. Luo, *Carbon N Y*, 2007, **45**, 1686–1695.
- 206 J.-M. Lihmann, *J Eur Ceram Soc*, 2008, **28**, 633–642.
- 207 Y. Sun, Y. Chen, C. Ding, G. Yang, Y. Ma and C. Wang, *Sci Rep*, 2013, **3**, 1749.
- 208 P. Jiang, J. Sun, W. Xue, J. Chen, R. Vasant Kumar and Y. Li, *Solid State Sci*, 2015, **46**, 33–36.
- 209 A. Rouhollahi, O. Ilegbusi, S. Florczyk, K. Xu and H. Foroosh, *Ann Biomed Eng*, 2020, **48**, 1090–1102.
- 210 S. Deville, *Materials*, 2010, **3**, 1913–1927.
- 211 Q. Cheng, C. Huang and A. P. Tomsia, *Advanced Materials*, DOI:10.1002/adma.201703155.
- 212 I. Corni, T. J. Harvey, J. A. Wharton, K. R. Stokes, F. C. Walsh and R. J. K. Wood, *Bioinspir Biomim*, 2012, **7**, 031001.
- 213 J. Seidel, N. Claussen and J. Rödel, *J Eur Ceram Soc*, 1995, **15**, 395–404.
- 214 K. R. Kambale, A. Mahajan and S. P. Butee, *Metal Powder Report*, 2019, **74**, 130–136.
- 215 S. Claramunt, A. Varea, D. López-Díaz, M. M. Velázquez, A. Cornet and A. Cirera, *The Journal of Physical Chemistry C*, 2015, **119**, 10123–10129.
- 216 R. Muzyka, S. Drewniak, T. Pustelny, M. Chrubasik and G. Gryglewicz, *Materials*, 2018, **11**, 1050.
- 217 D. A. Jasim, N. Lozano and K. Kostarelos, *2d Mater*, 2016, **3**, 014006.
- 218 F. Tuinstra and J. L. Koenig, *J Chem Phys*, 1970, **53**, 1126–1130.
- 219 S. Reich and C. Thomsen, *Philosophical Transactions of the Royal Society of London. Series A: Mathematical, Physical and Engineering Sciences*, 2004, **362**, 2271–2288.

- 220 A. C. Ferrari, J. C. Meyer, V. Scardaci, C. Casiraghi, M. Lazzeri, F. Mauri, S. Piscanec, D. Jiang, K. S. Novoselov, S. Roth and A. K. Geim, *Phys Rev Lett*, 2006, **97**, 187401.
- 221 S. Ma, Y. Si, F. Wang, L. Su, C. Xia, J. Yao, H. Chen and X. Liu, *Sci Rep*, 2017, **7**, 2588.
- 222 L. Stobinski, B. Lesiak, A. Malolepszy, M. Mazurkiewicz, B. Mierzwa, J. Zemek, P. Jiricek and I. Bieloshapka, *J Electron Spectros Relat Phenomena*, 2014, **195**, 145–154.
- 223 S. N. Alam, N. Sharma and L. Kumar, *Graphene*, 2017, **06**, 1–18.
- 224 H.-H. Huang, K. K. H. De Silva, G. R. A. Kumara and M. Yoshimura, *Sci Rep*, 2018, **8**, 6849.
- 225 H. K. Jeong, M. H. Jin, K. P. So, S. C. Lim and Y. H. Lee, *J Phys D Appl Phys*, 2009, **42**, 065418.
- 226 W. B. Hillig, *Journal of the American Ceramic Society*, 1988, **71**, C-96-C-99.
- 227 P. E. de Jongh and T. M. Eggenhuisen, *Advanced Materials*, 2013, **25**, 6672–6690.
- 228 O. T. Picot, V. G. Rocha, C. Ferraro, N. Ni, E. D’Elia, S. Meille, J. Chevalier, T. Saunders, T. Peijs, M. J. Reece and E. Saiz, *Nat Commun*, 2017, **8**, 14425.
- 229 I.-K. Jun, Y.-M. Kong, S.-H. Lee, H.-E. Kim, H.-W. Kim and K. C. Goretta, *Journal of the American Ceramic Society*, 2006, **89**, 2317–2319.
- 230 U. F. Vogt, M. Gorbar, P. Dimopoulos-Eggenschwiler, A. Broenstrup, G. Wagner and P. Colombo, *J Eur Ceram Soc*, 2010, **30**, 3005–3011.
- 231 S. Rannabauer, G.-M. Söffker, M. Scheunemann, U. Betke and M. Scheffler, *Adv Eng Mater*, 2017, **19**, 1700211.
- 232 A. P. Singh, M. Mishra, D. P. Hashim, T. N. Narayanan, M. G. Hahm, P. Kumar, J. Dwivedi, G. Kedawat, A. Gupta, B. P. Singh, A. Chandra, R. Vajtai, S. K. Dhawan, P. M. Ajayan and B. K. Gupta, *Carbon N Y*, 2015, **85**, 79–88.
- 233 C. Arndt, M. Hauck, I. Wacker, B. Zeller-Plumhoff, F. Rasch, M. Taale, A. S. Nia, X. Feng, R. Adelung, R. R. Schröder, F. Schütt and C. Selhuber-Unkel, *Nano Lett*, 2021, **21**, 3690–3697.
- 234 T. Sun and A. S. Teja, *J Chem Eng Data*, 2004, **49**, 1311–1317.
- 235 P. Gonzalez-Tello, F. Camacho and G. Blazquez, *J Chem Eng Data*, 1994, **39**, 611–614.
- 236 S. N. Sahasrabudhe, V. Rodriguez-Martinez, Meghan. O’Meara and B. E. Farkas, *Int J Food Prop*, 2017, **20**, 1–17.
- 237 H. Nouredini, B. C. Teoh and L. Davis Clements, *J Am Oil Chem Soc*, 1992, **69**, 1189–1191.
- 238 F. Irgens, *Rheology and Non-Newtonian Fluids*, Springer International Publishing, Cham, 2014.
- 239 F. Zuo, C. Carry, S. Saunier, S. Marinel and D. Goeuriot, *Journal of the American Ceramic Society*, 2013, **96**, 1732–1737.
- 240 J. Chen and L. Li, *Journal of Materials Research and Technology*, 2020, **9**, 13740–13748.
- 241 A. Centeno, V. G. Rocha, B. Alonso, A. Fernández, C. F. Gutierrez-Gonzalez, R. Torrecillas and A. Zurutuza, *J Eur Ceram Soc*, 2013, **33**, 3201–3210.
- 242 H. Xia, X. Zhang, Z. Shi, C. Zhao, Y. Li, J. Wang and G. Qiao, *Materials Science and Engineering A*, 2015, **639**, 29–36.

- 243 L. Zhou, J. Qiu, X. Wang, H. Wang, Z. Wang, D. Fang and Z. Li, *Ceram Int*, 2020, **46**, 19731–19737.
- 244 N. R. Wilson, P. A. Pandey, R. Beanland, R. J. Young, I. A. Kinloch, L. Gong, Z. Liu, K. Suenaga, J. P. Rourke, S. J. York and J. Sloan, *ACS Nano*, 2009, **3**, 2547–2556.
- 245 M. Wojtoniszak, X. Chen, R. J. Kalenczuk, A. Wajda, J. Łapczuk, M. Kurzewski, M. Drozdziak, P. K. Chu and E. Borowiak-Palen, *Colloids Surf B Biointerfaces*, 2012, **89**, 79–85.
- 246 H.-K. Jeong, Y. P. Lee, R. J. W. E. Lahaye, M.-H. Park, K. H. An, I. J. Kim, C.-W. Yang, C. Y. Park, R. S. Ruoff and Y. H. Lee, *J Am Chem Soc*, 2008, **130**, 1362–1366.
- 247 A. Romero, M. P. Lavin-Lopez, L. Sanchez-Silva, J. L. Valverde and A. Paton-Carrero, *Mater Chem Phys*, 2018, **203**, 284–292.
- 248 C. T. Alves, M. A. Peters and J. A. Onwudili, *J Anal Appl Pyrolysis*, 2022, **168**, 105766.
- 249 C.-J. Lin, I.-C. Lin and W.-H. Tuan, *J Mater Sci*, 2017, **52**, 1759–1766.
- 250 F. Gutiérrez-Mora, R. Cano-Crespo, A. Rincón, R. Moreno and A. Domínguez-Rodríguez, *J Eur Ceram Soc*, 2017, **37**, 3805–3812.
- 251 Z. Ni, Y. Wang, T. Yu and Z. Shen, *Nano Res*, 2008, **1**, 273–291.
- 252 T. Jawhari, A. Roid and J. Casado, *Carbon N Y*, 1995, **33**, 1561–1565.
- 253 N. Cao and Y. Zhang, *J Nanomater*, 2015, **2015**, 1–5.
- 254 H. Saleem, M. Haneef and H. Y. Abbasi, *Mater Chem Phys*, 2018, **204**, 1–7.
- 255 G. Lu, X. Zhou, H. Li, Z. Yin, B. Li, L. Huang, F. Boey and H. Zhang, *Langmuir*, 2010, **26**, 6164–6166.
- 256 Y. Tang, X. Yao, Y. Chen, Y. Zhou, D. Z. Zhu, Y. Zhang, T. Zhang and Y. Peng, *Granul Matter*, 2020, **22**, 37.
- 257 A. Kia, H. S. Wong and C. R. Cheeseman, *J Environ Manage*, 2017, **193**, 221–233.
- 258 J. P. Coughlin, C. D. Campbell and D. C. Mays, *J Hydrol Eng*, 2012, **17**, 68–73.
- 259 W. Chen, L. Yan and P. R. Bangal, *Carbon N Y*, 2010, **48**, 1146–1152.
- 260 P. Rivero-Antúnez, C. Zamora-Ledezma, F. Sánchez-Bajo, J. C. Moreno-López, E. Anglaret and V. Morales-Flórez, *J Eur Ceram Soc*, 2023, **43**, 1064–1077.
- 261 S. M. Walley, *Materials Science and Technology*, 2012, **28**, 1028–1044.
- 262 I. J. McColm, *Ceramic Hardness*, Springer US, Boston, MA, 1990.
- 263 M. Balog, J. Kečkéš, T. Schöberl, D. Galusek, F. Hofer, J. Křest'an, Z. Lenčėš, J.-L. Huang and P. Sajgalík, *J Eur Ceram Soc*, 2007, **27**, 2145–2152.
- 264 J. Gong, H. Miao, Z. Peng and L. Qi, *Materials Science and Engineering: A*, 2003, **354**, 140–145.
- 265 G. D. Quinn, 2008, pp. 45–62.
- 266 H. Porwal, P. Tatarko, S. Grasso, J. Khaliq, I. Dlouhý and M. J. Reece, *Carbon N Y*, 2013, **64**, 359–369.
- 267 S. Ghanizadeh, S. Grasso, P. Ramanujam, B. Vaidhyanathan, J. Binner, P. Brown and J. Goldwasser, *Ceram Int*, 2017, **43**, 275–281.
- 268 D. Liu, G. Zhang, K. Gui, W. Han, J. Niu and M. Wang, *Journal of Materials Research and Technology*, 2023, **24**, 5159–5164.
- 269 M. Boniecki, T. Sadowski, P. Gołębiewski, H. Węglarz, A. Piątkowska, M. Romaniec, K. Krzyżak and K. Łosiewicz, *Ceram Int*, 2020, **46**, 1033–1039.

- 270 S. Rowthu, F. Saeidi, K. Wasmer, P. Hoffmann and J. Kuebler, *Ceram Int*, 2018, **44**, 5193–5201.
- 271 B. Lee, M. Y. Koo, S. H. Jin, K. T. Kim and S. H. Hong, *Carbon N Y*, 2014, **78**, 212–219.
- 272 H. J. Kim, S.-M. Lee, Y.-S. Oh, Y.-H. Yang, Y. S. Lim, D. H. Yoon, C. Lee, J.-Y. Kim and R. S. Ruoff, *Sci Rep*, 2014, **4**, 5176.
- 273 D. Chakravarty, S. Bysakh, K. Muraleedharan, T. N. Rao and R. Sundaresan, *Journal of the American Ceramic Society*, 2007, **91**, 203–208.
- 274 J.-H. Shin, J. Choi, M. Kim and S.-H. Hong, *Ceram Int*, 2018, **44**, 8350–8357.
- 275 H. Miyazaki and Y. Yoshizawa, *Ceram Int*, 2014, **40**, 2777–2783.
- 276 Y. Çelik, A. Çelik, E. Flahaut and E. Suvaci, *J Eur Ceram Soc*, 2016, **36**, 2075–2086.
- 277 I. Ahmad, M. Islam, N. H. Alharthi, H. Alawadhi, T. Subhani, K. S. Munir, S. I. Shah, F. Inam and Y. Zhu, *J Compos Mater*, 2018, **52**, 417–428.
- 278 L. S. Walker, V. R. Marotto, M. A. Rafiee, N. Koratkar and E. L. Corral, *ACS Nano*, 2011, **5**, 3182–3190.
- 279 C. Ramirez and M. I. Osendi, *Ceram Int*, 2014, **40**, 11187–11192.
- 280 H. Shi, X. Wang, Y. Xiang, C. Zhang, X. Li, C. Xu, X. Hu and W. Gan, *Materials Science and Engineering: A*, 2023, **885**, 145619.
- 281 D. S. Smith, S. Fayette, S. Grandjean, C. Martin, R. Telle and T. Tonnessen, *Wiley Online Library*, 2003, **86**, 105–111.
- 282 D. S. Smith, F. Puech, B. Nait-Ali, A. Alzina and S. Honda, *Int J Heat Mass Transf*, 2018, **121**, 1273–1280.
- 283 J. Chen, X. Xu, J. Zhou and B. Li, *Rev Mod Phys*, 2022, **94**, 025002.
- 284 P. Rutkowski, P. Klimczyk, L. Jaworska, L. Stobierski and A. Dubiel, *J Therm Anal Calorim*, 2015, **122**, 105–114.
- 285 A. Schubert, H. Zeidler, R. Kühn and M. Hackert-Oschätzchen, *Journal of Ceramics*, 2015, **2015**, 1–9.
- 286 L. Liang, C. Huang, C. Wang, X. Sun, M. Yang, S. Wang, Y. Cheng, Y. Ning, J. Li, W. Yin and Y. Li, *Compos Part A Appl Sci Manuf*, 2022, **156**, 106871.
- 287 Y. Fan, L. Wang, J. Li, J. Li, S. Sun, F. Chen, L. Chen and W. Jiang, *Carbon N Y*, 2010, **48**, 1743–1749.
- 288 Y. Fan, W. Jiang and A. Kawasaki, *Adv Funct Mater*, 2012, **22**, 3882–3889.
- 289 R. Ivanov, I. Hussainova, M. Aghayan, M. Drozdova, D. Pérez-Coll, M. A. Rodríguez and F. Rubio-Marcos, *J Eur Ceram Soc*, 2015, **35**, 4017–4021.
- 290 K. Ahmad, W. Pan and H. Wu, *RSC Adv*, 2015, **5**, 33607–33614.
- 291 A. Weibel, A. Flaureau, A. Pham, G. Chevallier, J. Esvan, C. Estournès and C. Laurent, *J Eur Ceram Soc*, 2020, **40**, 5779–5789.
- 292 O. Jankovský, P. Šimek, D. Sedmidubský, Š. Huber, M. Pumera and Z. Sofer, *RSC Adv*, 2013, **4**, 7418–7424.
- 293 C. Manière, E. Nigito, L. Durand, A. Weibel, Y. Beynet and C. Estournès, *Powder Technol*, 2017, **320**, 340–345.
- 294 C. Manière, E. Torresani and E. Olevsky, *Materials*, 2019, **12**, 557.
- 295 V. Bharathi, A. R. Anilchandra, S. S. Sangam, S. Shreyas and S. B. Shankar, *Mater Today Proc*, 2021, **46**, 1451–1458.
- 296 H. Knoch and M. Fundus, *Sealing Technology*, 1995, **1995**, 6–14.
- 297 J. M. Carrapichano, J. R. Gomes, F. J. Oliveira and R. F. Silva, *Wear*, 2003, **255**, 695–698.

- 298 R. Flitney, in *Seals and Sealing Handbook*, Elsevier, 2014, pp. 7–103.
- 299 J. B. Wachtman Jr., *Structural ceramics*, Elsevier, 2012.
- 300 M. Turon-Vinas and M. Anglada, *Dental Materials*, 2018, **34**, 365–375.
- 301 R. C. Dante and C. K. Kajdas, *Wear*, 2012, **288**, 27–38.
- 302 J. Gong, J. Wu and Z. Guan, *Mater Lett*, 1998, **35**, 58–61.
- 303 B. Román-Manso, Y. Chevillotte, M. I. Osendi, M. Belmonte and P. Miranzo, *J Eur Ceram Soc*, 2016, **36**, 3987–3993.
- 304 D.-M. Liu and B.-W. Lin, *Ceram Int*, 1996, **22**, 407–414.
- 305 J. Rumble, *CRC Handbook of Chemistry and Physics*, CRC Press, 103rd edn., 2022.
- 306 N. Langenbrunner, M. Weaver, M. G. Dunn, C. Padova and J. Barton, *J Eng Gas Turbine Power*, DOI:10.1115/1.4028685.
- 307 W. A. Maxwell, R. S. Gurnick and A. C. Francisco, *Preliminary investigation of the 'freeze-casting' method for forming refractory powders*, 1954.
- 308 W. G. Fahrenholtz, G. E. Hilmas, I. G. Talmy and J. A. Zaykoski, *Journal of the American Ceramic Society*, 2007, **90**, 1347–1364.
- 309 W. G. Fahrenholtz and G. E. Hilmas, *Scr Mater*, 2017, **129**, 94–99.
- 310 S. Constable and C. J. Weiss, *Geophysics*, 2006, **71**, G43–G51.
- 311 W.-G. Shin and S.-H. Lee, *Journal of Mechanical Science and Technology*, 2010, **24**, 37–41.
- 312 K. Groth, F. Heidenfelder and R. Holinski, *Industrial Lubrication and Tribology*, 2001, **53**, 5–10.
- 313 A. Morina and A. Neville, *J Phys D Appl Phys*, 2007, **40**, 5476–5487.
- 314 A. Turel, J. Slavič and M. Boltežar, *Advances in Mechanical Engineering*, DOI:10.1177/1687814017694801.
- 315 F. Inam, B. R. Bhat, T. Vo and W. M. Daoush, *Ceram Int*, 2014, **40**, 3793–3798.
- 316 D. E. Bray, *Nondestructive Evaluation*, CRC Press, 2014.
- 317 S. Gholizadeh, *Procedia Structural Integrity*, 2016, **1**, 50–57.
- 318 W. Wunderlich, *Metals (Basel)*, 2014, **4**, 410–427.
- 319 J. S. Moya, S. Lopez-Esteban and C. Pecharromán, *Prog Mater Sci*, 2007, **52**, 1017–1090.
- 320 O. F. Ogunbiyi, T. Jamiru, E. R. Sadiku, O. T. Adesina, L. Beneke and T. A. Adegbola, *Procedia Manuf*, 2019, **35**, 1324–1329.
- 321 K. Zarebski and P. Putyra, *Advanced Powder Technology*, 2015, **26**, 401–408.